

**Non-equilibrium processes in strongly correlated
electron systems with multiple orbital degrees of
freedom**

Dissertation with the aim of achieving a doctoral degree
at the Faculty of Mathematics, Informatics
and Natural Sciences

Department of Physics
of Universität Hamburg

submitted by Malte Behrmann

2016 in Hamburg

Day of oral defense: 02.02.2016

The following evaluators recommend the admission of the dissertation:

Dr. Frank Lechermann

Prof. Dr. Alexander Lichtenstein

Prof. Dr. Michael Potthoff

Prof. Dr. Henning Moritz

Prof. Dr. Daniela Pfannkuche

Kurzfassung

In dieser Arbeit wird eine zeitabhängige (TD) Erweiterung der Slave Boson Mean-field Theory (SBMFT) basierend auf der TD-Gutzwiller Näherung (TD-GA) eingeführt. Sie wird angewandt auf das ein- und mehrorbitalige fermionische Hubbardmodell außerhalb des Gleichgewichts in verschiedenen Zusammenhängen. Zunächst wird der Einfluss von orbitalen Fluktuationen auf Prethermalisierung, frozen dynamics und den dynamischen Metall zu Isolator (Mott) Übergang untersucht. Während Prethermalisierung und frozen dynamics qualitativ intakt bleiben, verbreitert sich der dynamische Mott Übergang in eine Region kritischen Verhaltens mit oder ohne Hundscher Kopplung. Weiterhin werden magnetische Nichtgleichgewichtsreaktionen bei oder abseits von Halbfüllung unter Berücksichtigung mehrerer orbitaler Freiheitsgrade aufgedeckt. Zum Einen findet man einen magnetischen Nichtgleichgewichtsübergang zwischen antiferromagnetischen und paramagnetischen Zustand in einem großen Füllungsbereich. Zum Anderen werden longitudinale (temporäre) Spin Oszillationen entdeckt, wobei die temporäre Eigenschaft und die Füllungsabhängigkeit stark von dem Grundzustand abhängen. Diese Aspekte verschaffen einen Blick auf zu erwartende Multiorbitalphysik in zukünftigen Nichtgleichgewichtsexperimenten. Um die Anwendbarkeit von TD-SBMFT auf reale Materialien zu verdeutlichen wird V_2O_3 betrachtet. Kürzlich hat ein bis jetzt nicht publiziertes ultraschnelles Laser Experiment einen Nichtgleichgewicht Mott-Isolator zu Metall Übergang in diesem Material entdeckt. Ergebnisse dieses Experiments werden qualitativ reproduziert und der Übergang kann als Quench eines Korrelationsverstärkten Kristallfeldes verstanden werden. Außerdem wird eine Realraumformulierung von TD-SBMFT im Gleichgewicht angewandt auf die anspruchsvolle Physik von Sauerstoffleerstellen an der $LaAlO_3/SrTiO_3$ Grenzfläche. Auf diesem Weg wird die Konkurrenz von Ruderman-Kittel-Kasuya-Yosida(RKKY)-ähnlichen, double exchange-ähnlichen und superexchange Prozessen abhängig von der Anzahl der Leerstellen aufgedeckt. Schlüsselergebnisse von Experimenten an der $LaAlO_3/SrTiO_3$ Grenzfläche werden reproduziert, welches die wichtige Rolle von Sauerstoffleerstellen

für Magnetismus an der Grenzfläche unterstreicht. Außerhalb des Gleichgewichts wird Realraum-TD-SBMFT verwendet, um magnetische Anregungen des Hubbard-modells mit einem Orbital zu berechnen. Zunächst liegt der Fokus auf einer schwachen Störung des Systems. Im Grenzfall niedriger elektronischer Wechselwirkung werden Elektron-Loch-Anregungen (Stoner-Anregungen) produziert, während im entgegengesetzten Grenzfall kollektive Spin-Anregungen (Magnonen) aufgedeckt werden. Diese beiden Ergebnisse reproduzieren lineare Antwort Ergebnisse. Danach werden Stärken von Realraum TD-SBMFT benutzt. Stoner Anregungen *und* Magnonen bei mittlerer Wechselwirkungsstärke werden aufgedeckt und die Entwicklung dieser Anregungen in den Grenzfall niedriger und starker Wechselwirkung wird verfolgt. Anschließend wird die Störung des Systems verstärkt und der Einfluß von der Stärke der Störung auf das Magnonenspektrum betrachtet. Dies zeigt störungsabhängigen Magnonenzerfall außerhalb von linearer Antwort, der zuvor mittels selbstkonsistenter Born Approximation im Heisenberg Spin Modell bei starken Magnetfeldern entdeckt wurde.

Abstract

In this work a time-dependent (TD) extension of the slave boson mean-field theory (SBMFT) based on the TD-Gutzwiller approximation (TD-GA) is introduced. It is applied to the single- and multi-orbital fermionic Hubbard model out of equilibrium in different contexts. The influence of orbital fluctuations onto prethermalization, frozen dynamics and the dynamical metal to insulator (Mott) transition is investigated. While prethermalization and frozen dynamics remain qualitatively intact, the dynamical Mott transition broadens into an extended region of critical behavior. Additionally non-equilibrium magnetic responses with multiple orbital degrees of freedom at or away from half-filling are revealed. On the one hand a non-equilibrium magnetic transition from antiferromagnetic to a paramagnetic state is encountered in a wide range of fillings. On the other hand longitudinal (transient) spin oscillations are revealed, where transient property and filling dependence strongly depend on the specifics of the ground state. This provides a preview on multi-orbital physics to unveil by upcoming non-equilibrium experiments. To demonstrate the applicability of TD-SBMFT on real materials V_2O_3 is considered. Recently an up to now unpublished ultrafast laser experiment revealed a non-equilibrium Mott insulator to metal transition in this material. Results of this experiment are qualitatively reproduced and the transition is attributed to a quench in correlation enhanced crystal field. Furthermore a real-space formulation of TD-SBMFT is employed. It is applied in equilibrium on the challenging physics of oxygen vacancies at the $\text{LaAlO}_3/\text{SrTiO}_3$ interface. On this way the competition is revealed between Ruderman-Kittel-Kasuya-Yosida(RKKY)-like, double exchange-like and superexchange processes depending on the number of vacancies. Key results of experiments at the $\text{LaAlO}_3/\text{SrTiO}_3$ interface are reproduced underlining the vital role of oxygen vacancies concerning magnetism at the interface. Real-space TD-SBMFT is employed to compute magnetic excitations of the single-orbital Hubbard model. First a weak perturbation is considered. In the small interaction limit electron-hole excitations (Stoner excitations) are reproduced, while in the large interaction limit collective spin excitations

(magnons) are recapped, both known from previous linear-response results. Afterwards strengths of real-space TD-SBMFT are utilized. Stoner excitations *and* magnons at intermediate interaction are revealed and their evolution into small or large interaction limit is traced. Additionally the perturbation is enhanced and the influence of the perturbation onto the magnon dispersion is investigated. This reveals perturbation-dependent magnon decay away from linear-response previously known from results in self-consistent Born approximation of the Heisenberg Spin model in strong magnetic field.

Contents

1	Preface	1
2	Theoretical framework	3
2.1	Hubbard model	3
2.1.1	Single-orbital model	3
2.1.2	Multi-orbital model	4
2.2	Slave boson mean-field theory in equilibrium	5
2.3	Real-space slave boson mean-field theory in equilibrium	9
2.4	Time-dependent slave boson mean-field theory	10
2.4.1	Derivation of the time-dependent Gutzwiller approximation	11
2.4.2	Conserved quantities	15
2.4.3	Transfer of differential equations to momentum space slave boson formulation	17
2.4.4	Transfer of differential equations to real-space slave boson formulation	22
3	Metal-insulator transition in one-orbital case	27
3.1	Weak coupling	30
3.2	Critical point	32
3.3	Strong coupling	32
3.4	Interaction quenches away from half-filling	33
3.5	Interaction quenches from an initial interacting state at half-filling	34
3.6	Comparison to results of time-dependent Gutzwiller approximation	36
3.7	Summary of this chapter	37
4	Metal-insulator transition in two-orbital case	39
4.1	The equilibrium case	40
4.2	Interorbital interactions with zero Hund's coupling	42
4.2.1	Weak-coupling	43

4.2.2	Precursor and critical region	45
4.2.3	Strong-coupling	48
4.3	Interorbital interactions with finite Hund's coupling	49
4.3.1	Weak-coupling	49
4.3.2	Precursor and critical region	51
4.3.3	Strong-coupling	51
4.4	Summary of this chapter	52
5	Charge fluctuations in a realistic model for V_2O_3	55
5.1	Setting up the realistic model	56
5.2	Non-equilibrium results	57
5.3	Summary of this chapter	59
6	Impact of hole doping on magnetic fluctuations in the t_{2g}-shell	61
6.1	The equilibrium case	62
6.2	Interaction quenches from an antiferromagnetic state	64
6.3	Interaction quenches from an initial paramagnetic state	69
6.4	Total energy considerations	72
6.5	Summary of this chapter	77
7	Influence of oxygen vacancies on the $LaAlO_3/SrTiO_3$ interface	79
7.1	Testing real-space slave boson mean-field theory	80
7.1.1	Lattice size dependence of metal to insulator transition	81
7.1.2	Charge oscillations induced by non-magnetic defect	82
7.2	Dense-defect limit of oxygen vacancies as starting point	84
7.3	Modelling arbitrary numbers of oxygen vacancies in real-space	86
7.4	Small numbers of oxygen vacancies	89
7.5	Medium number of oxygen vacancies	92
7.6	High numbers of oxygen vacancies	93
7.7	Summary	94
8	Real-space magnetization dynamics	97
8.1	Equilibrium setup	98
8.2	Non-equilibrium setup	100
8.3	Testing the real-space time-dependent slave boson mean-field theory	102
8.3.1	Results in the Stoner limit (weak interaction)	102

8.3.2	Results in the Heisenberg limit (strong interaction)	108
8.4	Revealing strengths of real-space time-dependent slave boson mean-field theory	110
8.4.1	Magnetic excitations between Stoner and Heisenberg limit	110
8.4.2	Instability of magnons out of equilibrium	114
8.5	Summary of this chapter	116
9	Conclusion	119
A	Appendix	123
A.1	Runge-Kutta theory	123
A.1.1	Explicit Runge-Kutta methods	123
A.1.2	Error estimation of Runge-Kutta variables	125
A.2	Real-space magnetization dynamics-additional material	127
A.2.1	Stoner limit $n = 6$	127
A.2.2	Stoner limit-alternative non-equilibrium setup	129
A.2.3	Heisenberg limit $n = 6$	132
A.2.4	Magnetic excitations between Stoner and Heisenberg-Limit	134
A.2.5	Instability of magnons in effective high magnetic fields	136
B	List of publications and author contributions	139
C	Acknowledgments	141
	Bibliography	143

1 Preface

Experiments in ultracold gases have stimulated for the last decade ongoing research in non-equilibrium physics of fermionic or bosonic Hubbard models [15]. The connection between Hubbard models and ultracold gases is simple as the latter work as quantum simulators of the former [127]. Ultracold gases have in contrast to materials no impurities, purely local Coulomb interaction and nearly zero temperature [127]. The finding of the metal to insulator (Mott) transition in bosonic [37] and fermionic [57, 127] ultracold gases underlines this fact. Non-equilibrium physics after an external perturbation are accessible in ultracold gases by probing [57, 127] or in solids by femtosecond spectroscopy [113]. From the theory side a useful theoretical idealization is a so called quantum quench [20]. Studies on an interaction quenched single-orbital fermionic Hubbard model reveal intriguing non-equilibrium phenomena like prethermalization, frozen dynamics and the dynamical Mott transition [29, 96, 125]. Switching again to the experimental side, theoretical studies on how to incorporate orbital physics of models like the Kondo lattice model in ultracold fermionic atoms raised great interest [12, 34]. Experimental realization especially of magnetic states is a serious challenge in ultracold gases due to the required low temperatures and entropies needed to observe exchange-driven spin ordering effects [36]. Still progress has been made [36, 124] raising the impression that it is only a matter of time until non-equilibrium multi-orbital (magnetic) phenomena will be accessible in ultracold gases.

Definitely within reach of ultracold gases in the near future are magnetic states of the single-orbital fermionic Hubbard model, as already for example short-range magnetic order could be established in ultracold gases [36] or antiferromagnetic correlations measured [45]. The Hubbard model includes two complementary approaches toward magnetism in solid state systems worth investigating in ultracold gases. The strong interaction limit leads to the Heisenberg model, which describes magnetism as induced by local magnetic moments on atoms [109]. In the weak interaction limit the interaction term of the Hubbard model is well approximated by its mean-field

value leading to the Stoner model [109]. While the Heisenberg model contains only transverse low energy collective spin excitations (magnons), the Stoner model consists only of longitudinal magnetic excitations covering a broad energy range [103]. Therefore interesting and challenging are investigations of magnetic excitations in the intermediate interaction regime. Theoretical studies already discovered intriguing results [128, 152], but struggled with employing a high resolution of the Brillouin zone or taking into account high energy magnetic excitations.

The work is structured as follows. In chapter 2 the Hubbard model, equilibrium slave boson mean-field theory (SBMFT) and its time-dependent extension (TD-SBMFT) are introduced as well as their real-space formulations. As a testing case TD-SBMFT is applied to the single-orbital Hubbard model at half-filling in chapter 3 to recover time-dependent Gutzwiller approximation results. Afterwards the influence of orbital degrees of freedom on prethermalization, frozen dynamics and dynamical Mott transition using the two-orbital Hubbard model is investigated in chapter 4. TD-SBMFT is not limited to model applications, thus the origin of a non-equilibrium Mott insulator to metal transition in V_2O_3 is investigated in chapter 5. Additionally non-equilibrium magnetic fluctuations in the three t_{2g} orbitals at and away from half-filling are revealed in chapter 6. Then the real-space formulation of TD-SBMFT is employed. First the equilibrium part is applied to simple test cases and the intriguing interplay of correlations and oxygen vacancies at the $LaAlO_3/SrTiO_3$ interface in chapter 7. In chapter 8, before the strengths of real-space TD-SBMFT are utilized, it is tested displaying magnetic excitations in the interaction limits of the single-orbital Hubbard model. Still in the same chapter as strengths magnetic excitations at intermediate interactions are revealed and the magnon decay at high interaction in pulsed magnetic fields.

2 Theoretical framework

2.1 Hubbard model

2.1.1 Single-orbital model

The main problem of condensed matter theory is, that one knows the Hamiltonian (N electrons in the potential $V(\vec{r})$ of the ion cores with Coulomb interaction) [94]

$$\mathcal{H} = \sum_{j=1}^N \underbrace{\left(\frac{\mathbf{p}_j^2}{2m} + V(\mathbf{r}) \right)}_{E_{kin}^j} + \frac{1}{2} \sum_{j \neq k} \underbrace{\frac{e^2}{|\mathbf{r}_j - \mathbf{r}_k|}}_{E_C^{jk}}, \quad (2.1)$$

but can not solve the corresponding Schrödinger equation analytically. The Hubbard model [48] has established its place as standard model of condensed matter systems with strong Coulomb interaction in recent years. Assuming the electrons to be strongly localized near the atomic nucleus, atomic eigenstates (for N electrons and L lattice sites) $\{|\varphi_{i\sigma n}\rangle | i \in \{1, \dots, L\}, n \in \{1, \dots, N\}\}$ are used as second quantization basis. Greek letters represent in this subsection a spin index. In this basis the Hubbard model can be rewritten as

$$\mathcal{H} = \underbrace{\sum_{i,j=1}^L \sum_{\sigma} \left(\tau_{i\sigma j\sigma} c_{i\sigma}^{\dagger} c_{j\sigma} + \text{h.c.} \right)}_{\mathcal{H}^{kin}} + \frac{1}{2} \underbrace{\sum_{i=1}^L \sum_{\alpha\beta\gamma\delta} \left(U_{i\alpha i\beta i\gamma i\delta} c_{i\alpha}^{\dagger} c_{i\beta}^{\dagger} c_{i\delta} c_{i\gamma} + \text{h.c.} \right)}_{\mathcal{H}^{loc} = \sum_i \mathcal{H}_i^{loc}}, \quad (2.2)$$

where \mathcal{H}^{kin} denotes the kinetic part and \mathcal{H}^{loc} the local interaction. Here $\tau_{i\sigma j\sigma} = \langle \varphi_{i\sigma 1} | E_{kin}^1 | \varphi_{j\sigma 1} \rangle$ depicts the expectation value of the electrons' kinetic energy and ion cores' potential. $\tau_{i\sigma j\sigma}$ describes the probability for an electron with spin σ to move from lattice site j to site i . In the following τ is often called hopping or hopping matrix. $U_{i\alpha i\beta i\gamma i\delta} = \langle \varphi_{i\alpha 1} \varphi_{i\beta 1} | E_C^{12} | \varphi_{i\gamma 1} \varphi_{i\delta 1} \rangle$ is a **local** description of the Coulomb interaction between electrons at site i . Often only $U_{i\alpha i\alpha i\bar{\alpha} i\bar{\alpha}} n_{i\alpha} n_{i\bar{\alpha}}$ with

$n_{i\alpha} = c_{i\alpha}^\dagger c_{i\alpha}$ and $\bar{\alpha}$ the opposing spin index to α is considered (Hubbard-U). Meaning the following Hamiltonian is taken into account

$$\mathcal{H} = \underbrace{\sum_{i,j=1}^L \sum_{\sigma} \left(\tau_{i\sigma j\sigma} c_{i\sigma}^\dagger c_{j\sigma} + \text{h.c.} \right)}_{\mathcal{H}^{kin}} + \underbrace{\sum_{i\alpha} U_{i\alpha i\alpha \bar{\alpha} i\bar{\alpha}} n_{i\alpha} n_{i\bar{\alpha}}}_{\mathcal{H}^{loc} = \sum_i \mathcal{H}_i^{loc}}. \quad (2.3)$$

Compared to E_C^{ij} (Eq. 2.1) \mathcal{H}^{loc} (Eq. 2.2) and the Hubbard-U are simplifications, as they are only taking into account the Coulomb interaction between electrons at the same lattice site and no radial dependence. For all single-orbital applications considered in this work $U_{i\alpha i\alpha \bar{\alpha} i\bar{\alpha}}$ is not spin-dependent and set to $0.5U$. There are only few special cases, in which the Hubbard model can be solved analytically. In the case $U = 0$ the Hamiltonian reduces to \mathcal{H}^{kin} , which can be diagonalized in momentum space. This is called the itinerant limit, as the hopping of the electrons is not affected by Coulomb interaction and the eigenstates of the Hamiltonian are therefore Bloch states. In a similar way $\tau = 0$ can be solved analytically, too. There all lattice sites are isolated from each other, as there is no way for one electron to move between them. The Hamiltonian of a single site consists only of the Coulomb interaction at that site and can be diagonalized. As eigenstates the atomic eigenstates and the so called atomic limit are obtained. However the case $U \neq 0$ and $\tau \neq 0$ has in general no analytic solution. An overview considering solutions of the Hubbard model can be found in [81]. Numerically exact solutions with state of the art supercomputers are only possible for up to 20 lattice sites. So to obtain solutions in the thermodynamic limit ($N \rightarrow \infty$) approximations are needed.

2.1.2 Multi-orbital model

The presented Hubbard model in the last section (Eq. 2.2) takes only one orbital degree of freedom into account. The formulation of Eq. 2.2 is chosen in a way that a generalization to multiple orbital degrees of freedom is possible. For this purpose the greek index elements are $\in (m\sigma)$ instead of σ in \mathcal{H}^{loc} , where m is an orbital index. Additionally in \mathcal{H}^{kin} the index σ has to be replaced with $m\sigma$. The derived model is called n -orbital model (or n -band model), where n represents the number of orbitals. Considering multiple orbital degrees of freedom, Hund's rules [38] have to be ensured. They describe empirically the energetic order of atomic states for atoms with multiple electrons and multiple orbitals. There are three rules (sorted

by energetic relevance in descending order) and in the statement the z-component of the stated vector operators is taken, which is an arbitrary choice:

1. The total spin in z-direction of the electrons' spin vector operator ($S_z = \sum_i (S_z)_i$) of one atom is maximal. An asymmetric orbital part of the electrons' wavefunction is energetically favored, because this induces a smaller overlap of the spin part of the electrons' wavefunction resulting in a smaller Coulomb interaction.
2. The total angular momentum of the electrons' angular momentum vector operator ($L_z = \sum_i (L_z)_i$) is maximal for states with same S_z . Electrons with higher L_z tend to be further away from the atomic nucleus and by this also from each other reducing again the Coulomb interaction.
3. In atoms with multiple not fully occupied shells, the following holds: Is the shell filled less than half, the total momentum operator \mathbf{J} is $\mathbf{J} = |\mathbf{L} + \mathbf{S}|$ else $\mathbf{J} = |\mathbf{L} - \mathbf{S}|$. As in this work only single not fully occupied shells are considered, this rule is not relevant.

Accounting now for the Hund's rules and multiple orbitals in the Hubbard model leads to the following Hamiltonian (with J_H denoting the Hund's rule coupling)

$$\begin{aligned}
\mathcal{H} = & \underbrace{\mathcal{H}^{kin} + \sum_i \mathcal{H}_i^{loc}}_{\mathcal{H}^{loc}} - \underbrace{\sum_{\langle i,j \rangle mm'\sigma} \left(\tau_{imjm'} c_{im\sigma}^\dagger c_{jm'\sigma} + \text{h.c.} \right)}_{\mathcal{H}^{kin}} + U \sum_{im} n_{im\uparrow} n_{im\downarrow} + \\
& + \frac{1}{2} \sum_{i,m \neq m',\sigma} \left\{ U' n_{im\sigma} n_{im'\bar{\sigma}} + U'' n_{im\sigma} n_{im'\sigma} + \right. \\
& \left. + J_H \left(c_{im\sigma}^\dagger c_{im'\bar{\sigma}}^\dagger c_{im\bar{\sigma}} c_{im'\sigma} + c_{im\sigma}^\dagger c_{im'\sigma}^\dagger c_{im'\bar{\sigma}} c_{im\sigma} \right) \right\}. \tag{2.4}
\end{aligned}$$

As long as cubic symmetry is present regarding the orbital degrees of freedom $U' = U - 2J_H$, $U'' = U - 3J_H$ proves adequate [22, 33]. Note that the Hamiltonian of Eq. 2.4 is spin and orbital rotationally invariant [22].

2.2 Slave boson mean-field theory in equilibrium

Slave boson mean-field theory (SBMFT) aims at the qualitative and fast description of the low-energy and low-temperature physics of a Hubbard model tailored to a

specific physical scenario. The results are retrieved in the framework of Fermi-liquid theory, which allows access to bandstructure, quasiparticle weight, local eigenstates of the atoms, but neglects quantum fluctuations of the derived observables. Starting point is a multi-orbital Hubbard model $\mathcal{H} = \mathcal{H}^{kin} + \mathcal{H}^{loc}$ (see Eq. 2.4). In this section i denotes atoms in the unit cell and greek indices $|\alpha\rangle = |m\sigma\rangle$, where m labels orbitals and σ spin degrees of freedom. Additionally occasionally $|\tilde{\alpha}\rangle = |im\sigma\rangle$ is utilized. Note that in fact instead of the \mathcal{H}^{kin} in Eq. 2.4 the Fourier transformed version

$$\bar{\mathcal{H}}^{kin} = \sum_{\mathbf{k}\tilde{\alpha}\tilde{\beta}} \varepsilon_{\mathbf{k}\tilde{\alpha}\mathbf{k}\tilde{\beta}} \tilde{c}_{\mathbf{k}\tilde{\alpha}}^\dagger \tilde{c}_{\mathbf{k}\tilde{\beta}} \quad (2.5)$$

is used with \mathbf{k} denoting points in momentum space. In this section only translational invariant systems with respect to the unit cell are considered. The derivation of the formalism is now briefly sketched in a series of steps and afterwards characteristic SBMFT values are explained. Technical details regarding the mentioned steps and more details considering the method can be found in [25] and [77], respectively.

1. The multi-orbital Hubbard Hamiltonian is projected onto an extended Hilbert space $\underline{\mathbb{H}}$ using $c_{i\alpha}^\dagger = \mathcal{R}_{i\alpha i\beta} [\phi] f_{i\beta}^\dagger$, where f^\dagger represents a fermionic quasiparticle and ϕ_{iAn}^\dagger a bosonic creation operator. With this projection no intersite ϕ are used. In the index iAn of $\underline{\mathbb{H}}$, A stands for the bosonic and n for the fermionic part. Utilizing the constraints

$$\sum_{An} \phi_{iAn}^\dagger \phi_{iAn} = 1, \forall i \quad (2.6)$$

$$\sum_A \sum_{nn'} \phi_{iAn}^\dagger \phi_{iAn} \langle n | f_{i\alpha}^\dagger f_{i\alpha'} | n' \rangle = f_{i\alpha}^\dagger f_{i\alpha'} \forall i \quad (2.7)$$

only physical states remain in $\underline{\mathbb{H}}$. The first constraint norms the slave bosons ϕ_{iAn}^\dagger and the second one ensures that charge matches between original and extended Hilbert space. Both is ensured for all sites i of the unit cell. One representation of \mathcal{H} in $\underline{\mathbb{H}}$ is

$$\underline{\mathcal{H}} = \underbrace{\sum_{\mathbf{k}} \sum_{\tilde{\alpha}\tilde{\alpha}'} \sum_{\tilde{\beta}\tilde{\beta}'} \mathcal{R}_{\tilde{\alpha}\tilde{\alpha}}^\dagger \varepsilon_{\tilde{\alpha}\tilde{\alpha}\tilde{\beta}\tilde{\beta}} \mathcal{R}_{\tilde{\beta}\tilde{\beta}} f_{\mathbf{k}\tilde{\alpha}}^\dagger f_{\mathbf{k}\tilde{\beta}}}_{\bar{\mathcal{H}}_{*}^{SB}} + \underbrace{\sum_{iAA'} \langle iA | \mathcal{H}_i^{loc} | iA' \rangle \sum_n \phi_{iAn}^\dagger \phi_{iA'n}}_{\underline{\mathcal{H}}^{loc}}$$

In this representation the Hamiltonian is now quadratic in bosonic and quasi-fermionic operators. Note that ε is the Fourier transform of τ denoted in \mathcal{H}^{kin} (Eq. 2.4).

2. The path-integral formalism [102] is used, to calculate the partition function Z (with β as inverse temperature)

$$\begin{aligned}
Z &= \int D[\phi^\dagger \phi] D[\Lambda \lambda_{i0}] D[f^\dagger f] \exp \left[- \int_0^\beta dt (\mathcal{L}_1 + \mathcal{L}_2 + \mathcal{L}_3 + \mathcal{L}_4) \right]. \\
\mathcal{L}_1 &= \sum_{iAn} \sum_{A'n'} \phi_{iAn}^\dagger \left(\frac{\partial}{\partial t} + \lambda_0 \right) \phi_{iA'n'} - \lambda_0 \\
\mathcal{L}_2 &= \sum_{iAA'} \sum_{nn'} \phi_{iAn}^\dagger \left(\delta_{AA'} \delta_{nn'} \frac{\partial}{\partial t} - \delta_{AA'} \langle f_{in}^\dagger f_{in'} \rangle \Lambda_{inin'} \right) \phi_{iA'n'} \\
\mathcal{L}_3 &= \sum_{iAn} \sum_{A'n'} \phi_{iAn}^\dagger \left(\delta_{AA'} \delta_{nn'} \frac{\partial}{\partial t} + \delta_{nn'} \langle A | \mathcal{H}_i^{loc} | A' \rangle \right) \phi_{iA'n'} \\
\mathcal{L}_4 &= \sum_{inn'} f_{in}^\dagger \left(\frac{\partial}{\partial t} + \Lambda_{inin'} \right) f_{in'} + \sum_{\mathbf{k}} \sum_{\substack{\tilde{\alpha}\tilde{\alpha}' \\ \tilde{\beta}\tilde{\beta}'}} \mathcal{R}_{\tilde{\alpha}\tilde{\alpha}'}^\dagger[\phi] \varepsilon_{\mathbf{k}\tilde{\alpha}'\mathbf{k}\tilde{\beta}'} \mathcal{R}_{\tilde{\beta}\tilde{\beta}'}[\phi] f_{\mathbf{k}\tilde{\alpha}}^\dagger f_{\mathbf{k}\tilde{\beta}}
\end{aligned}$$

The constraints from Eqs. 2.6 and 2.7 are ensured at each site i of the unit cell by Lagrange multipliers λ_{i0} and $\Lambda_{inin'}$. The integration regarding \mathcal{L}_4 with respect to $[f^\dagger f]$ can be done now analytically [25]. Of particular interest is the renormalized Hamiltonian $\bar{\mathcal{H}}_*^{\text{SB}}$

$$\bar{\mathcal{H}}_*^{\text{SB}} = \sum_{\mathbf{k}} \sum_{\substack{\tilde{\alpha}\tilde{\alpha}' \\ \tilde{\beta}\tilde{\beta}'}} \mathcal{R}_{\tilde{\alpha}\tilde{\alpha}'}^\dagger[\phi] \varepsilon_{\mathbf{k}\tilde{\alpha}'\mathbf{k}\tilde{\beta}'} \mathcal{R}_{\tilde{\beta}\tilde{\beta}'}[\phi] f_{\mathbf{k}\tilde{\alpha}}^\dagger f_{\mathbf{k}\tilde{\beta}}, \quad (2.8)$$

especially later on, when turning to the non-equilibrium description (see section 2.4).

3. Applying a mean-field treatment by assuming ϕ_{iAn}^\dagger and ϕ_{iAn} as time independent and moving to the zero temperature limit leads to the following partition function

$$Z = \lim_{\beta \rightarrow \infty} \int D[\phi^\dagger \phi] D[\Lambda \lambda_0] \exp [-\beta (\mathcal{L}_1 + \mathcal{L}_2 + \mathcal{L}_3)]. \quad (2.9)$$

4. The corresponding free energy Ω to this partition function can be approx-

imated in the saddle-point approximation. In this approximation the free energy is estimated by evaluation the function inside the integral at the highest contribution, which is a complex saddle-point [94]. This point is indicated by the saddle-point equations

$$\frac{\partial \Omega}{\partial \phi_i} = 0, \quad \frac{\partial \Omega}{\partial \Lambda_{inin'}} = 0, \quad \frac{\partial \Omega}{\partial \lambda_{0i}} = 0. \quad (2.10)$$

5. In the end the numerical evaluation of Eq. 2.10 follows, leading to the following characteristic values of RISB (in matrix form)

$$Z = \mathcal{R}^\dagger \mathcal{R} \quad (2.11)$$

$$\Sigma = \omega (1 - (\mathcal{R}^\dagger \mathcal{R}))^{-1} + (\mathcal{R}^\dagger)^{-1} \Lambda \mathcal{R}^{-1} - \varepsilon^0 \quad (2.12)$$

$$\langle O_i \rangle = \sum_{AA'n} \langle iA | O_i | iA' \rangle \phi_{iAn}^\dagger \phi_{iA'n} \quad (2.13)$$

$$G_f^{-1}(\mathbf{k}, \omega) = \omega - \mathcal{R}^\dagger \varepsilon(\mathbf{k}) \mathcal{R} - \Lambda \quad (2.14)$$

Here Z denotes the quasiparticle weight, Σ the selfenergy, $\langle O \rangle$ the expectation value of a local operator and G_f the one-particle Green's function of the fermionic quasiparticles. These characteristic values are computed at low energies near the Fermi energy and low temperatures and are listed and described hereinafter.

Quasiparticle weight Z : The value $Z = 1$ indicates free, non-interacting electrons. $Z < 1$ describes a correlated system and correlations increase with decreasing value until at $Z = 0$ the systems transitions to an insulator.

Selfenergy Σ : The real part indicates the strength of many-particle interactions. The imaginary part describes, when the Green's function is evolved at least to second order in ω the finite lifetime of the quasiparticles.

Quasiparticle occupation $f_{i\alpha}^\dagger f_{i\alpha}$: Expresses the number of quasiparticles, which occupy the specified (by $i\alpha$) site, orbital and spin degree of freedom.

Slave-boson occupation: $\phi_{iAn}^\dagger \phi_{iAn}$: Occupation of the corresponding slave boson state. It is not directly related to the original system, as it is an unphysical auxiliary value. But the distribution and weights of the slave boson states often lead to important statements regarding the investi-

gated system.

2.3 Real-space slave boson mean-field theory in equilibrium

In the last section the evaluation of the important observables in SBMFT is sketched under the assumption, that a translational invariant system with a small unit cell is present. It is written in a general form, which allows for a multi-atom unit cell. A (minimum) two-atom unit cell is needed for example to describe antiferromagnetic order (see chapter 6). However when a (sufficiently large) inhomogeneous system is the focus of attention, this formulation reaches its limits quite fast. The main problem is the linear scaling of the number of saddle-point equations with sites in the unit cell i as shown in Eq. 2.10. Additionally the diagonalization of $\bar{\mathcal{H}}_*^{\text{SB}}$ at each \mathbf{k} point of each iteration to determine the Fermi level becomes numerically demanding. To consider a real-world example, let's take into account the calculation of chapter 7, which was done using the real-space SBMFT formulation, which is addressed in a few lines. If this would have been done inside the formulation of the last section the 10x10 lattice with two-orbitals on each site mean the following. For two orbitals there are 60 symmetry inequivalent slave bosons with one λ_0 and 16 (=4x4) $\Lambda_{nn'}$ present per site. This results in 7700 saddle-point equations in total for the 100 sites considered. Already numerically very demanding, the fact that some of the equations contain \mathbf{k} sums [25] complicates parallelization of the problem at hand. Furthermore $\bar{\mathcal{H}}_*^{\text{SB}}$ is a 400x400 matrix at each \mathbf{k} -point, which has to be diagonalized at each \mathbf{k} -point in each iteration step of the self-consistent calculation. This leads to the conclusion that a real-space formulation is beneficial.

The derivation of the real-space formalism is straightforward and analogue to the last section, only the following aspects have to be considered.

- As in the previous section no intersite slave bosons are considered. Inhomogeneous effects arise in the self-consistency cycle.
- All \mathbf{k} -sums vanish and the same holds for the appropriate \mathbf{k} indices.
- Instead of $\bar{\mathcal{H}}^{kin}$ (Eq. 2.5) the real-space formulation \mathcal{H}^{kin} (Eq. 2.4) is used utilizing periodic or open boundary conditions to enforce or neglect translational invariance.

- This leads to the following renormalized free Hamiltonian

$$\mathcal{H}_*^{\text{SB}} = \sum_{ijmm'nn'\sigma} \mathcal{R}_{imim'}^\dagger \tau_{im'jn'} \mathcal{R}_{jn'jn} c_{im\sigma}^\dagger c_{jn\sigma}, \quad (2.15)$$

where i, j label sites and m, m', n, n' denote orbitals.

- The index i now runs over all sites of the lattice using open/periodic boundary conditions. In the mentioned example $i \in 1, \dots, 100$.

This leads to the following advantages with respect to the formalism of the previous section

- In momentum space determination of the Fermi level needs diagonalization of $\overline{\mathcal{H}}_*^{\text{SB}}$ at each \mathbf{k} -point and each iteration. In contrast in real-space only a single diagonalization of $\mathcal{H}_*^{\text{SB}}$ per iteration is required. However $\overline{\mathcal{H}}_*^{\text{SB}}$ is a 4x4 matrix at each \mathbf{k} -point, while $\mathcal{H}_*^{\text{SB}}$ is a 400x400 matrix in the example.
- The (still) 7700 saddle-point equations can be parallelized over sites as no momentum-space sums are involved anymore.

One serious drawback is, that the system size considered (10x10 in the mentioned example) is ultimately linked to the accuracy of the whole calculation as it limits the dimension of the kinetic Hamiltonian. To elaborate on this, having a 400x400 kinetic Hamiltonian means that there are only 400 eigenvalues and eigenstates to resolve the energy dispersion. This limits the resolution of the density of states. Previously the momentum space grid limited the density of states and the number of atoms in the unit cell the resolution of spatial inhomogeneities. Now one grid has to be chosen to acquire a suitable resolution in both aspects. In section 7.1 the just presented real-space equilibrium formulation is tested by applying it to the homogeneous single-orbital Mott transition using various real-space lattice sizes (section 7.1.1). Furthermore a single non-magnetic defect scenario is considered to test also inhomogeneous qualities (section 7.1.2).

2.4 Time-dependent slave boson mean-field theory

It is important to realize that the Gutzwiller approximation is equivalent to the slave boson formulation in equilibrium [19]. For example, one Gutzwiller projector

in the mixed basis notation defined in some lines can be transformed by unitary transformation of the basis to a slave boson. The time-dependent slave boson mean-field theory (TD-SBMFT) is based on the time-dependent Gutzwiller Approximation (TD-GA) [125]. Hence the differential equations in the Gutzwiller framework are derived first in section 2.4.1. Then a look on conserved quantities in the time-dependent description is performed in section 2.4.2. Afterwards in section 2.4.3 the differential equations are transferred to slave boson formalism (compare equilibrium introduction in section 2.2). The equivalent transfer for the real-space description (see section 2.3) is done in section 2.4.4. In the appendix (section A.1.1) the Runge-Kutta methods are introduced, which are needed to solve the differential equations. Additionally the error estimation of variables obtained by Runge-Kutta methods is explained in section A.1.2.

2.4.1 Derivation of the time-dependent Gutzwiller approximation

In this section a review of TD-GA is followed [160]. The time-dependent Schrödinger equation describes the time evolution of a pure quantum state $|\Psi(t)\rangle$ by

$$i\frac{\partial}{\partial t}|\Psi(t)\rangle = \mathcal{H}(t)|\Psi(t)\rangle \quad (2.16)$$

This equation can be restated as being the stationary point of the following action functional

$$\mathcal{S}[|\Psi\rangle] = \int_0^{t_f} d\tau \left\langle \Psi(\tau) \left| i\frac{\partial}{\partial \tau} - \mathcal{H} \right| \Psi(\tau) \right\rangle. \quad (2.17)$$

The solution of the Schrödinger equation can be understood in this as a solution of the variational principle

$$\frac{\partial \mathcal{S}[|\Psi\rangle]}{\partial |\Psi(t)\rangle} \stackrel{!}{=} 0 \quad (2.18)$$

This reformulation allows to look for the best solution in a subclass of time-dependent wavefunctions out of which in the following the time-dependent Gutzwiller wavefunctions $\psi(t)$ are considered with

$$|\Psi(t)\rangle = \mathcal{P}(t)|\psi(t)\rangle. \quad (2.19)$$

$\mathcal{P}_i(t)$ denotes the time-dependent Gutzwiller projector at a given site i of the unit cell, which will be parametrized below. Furthermore the equilibrium Gutzwiller constraints are imposed to hold at each time t

$$\left\langle \psi(t) \left| \mathcal{P}_i^\dagger(t) \mathcal{P}_i(t) \right| \psi(t) \right\rangle \stackrel{!}{=} 1 \quad (2.20)$$

$$\left\langle \psi(t) \left| \mathcal{P}_i^\dagger(t) \mathcal{P}_i(t) d_{i\alpha}^\dagger d_{i\beta} \right| \psi(t) \right\rangle \stackrel{!}{=} \left\langle \psi(t) \left| d_{i\alpha}^\dagger d_{i\beta} \right| \psi(t) \right\rangle \quad (2.21)$$

These constraints ensure that the wavefunction Ψ is normalized and that calculations in the limit of infinite lattice coordination number can be done analytically. The action $\mathcal{S}(t)$ can be evaluated now exactly in this limit and reads¹ [160]

$$\begin{aligned} \mathcal{S} [|\Psi\rangle] &= \int_0^{t_f} d\tau \left[i \left\langle \psi(\tau) \left| \frac{\partial}{\partial t} \psi(\tau) \right\rangle + \right. \\ &\quad \left. + i \sum_i \left\langle \psi(\tau) \left| \mathcal{P}_i^\dagger(t) \frac{\partial}{\partial t} \mathcal{P}_i(t) \right| \psi(\tau) \right\rangle - E(\tau) \right] \end{aligned} \quad (2.22)$$

where $E(t) = \langle \Psi(t) | \mathcal{P}^\dagger(t) \mathcal{H}(t) \mathcal{P}(t) | \Psi(t) \rangle$ is the total energy. Assuming now that there exists operators \tilde{d}_a^\dagger and \tilde{d}_a , which are related to the previous ones (d_α^\dagger and d_α) by unitary transformation, and fulfill

$$\left\langle \psi(t) \left| \tilde{d}_{ia}^\dagger \tilde{d}_{ib} \right| \psi(t) \right\rangle = \delta_{iab} n_{ia}^0(t) \quad (2.23)$$

the Gutzwiller projector can be rewritten in a mixed basis notation. In this notation $|i, \Gamma\rangle$ indicates the basis introduced by d_α^\dagger and d_α and $|i, n\rangle$ is the new so called natural basis given by \tilde{d}_a^\dagger and \tilde{d}_a .

$$\mathcal{P}_i(t) = \sum_{\Gamma n} \frac{\Phi_{i,\Gamma n}(t)}{\sqrt{\mathcal{P}_{i,n}^0(t)}} |i, \Gamma\rangle \langle i, n| \quad (2.24)$$

with the Gutzwiller variational matrix Φ_i and the local uncorrelated probability $\mathcal{P}_{i,n}^0(t) = \langle \psi(t) | i, n \rangle \langle i, n | \psi(t) \rangle$. Utilizing the renormalization Matrix \mathcal{R} with

¹Note that an in depth calculation of Eqs. 2.22 and 2.28 can be found in the appendix of [121].

entries $n_b^{(0)}(t)$ of the (diagonal) $\mathcal{P}_{i,n}^0(t)$

$$\mathcal{R}_{iaib}^* = \frac{1}{\sqrt{n_b^{(0)}(t) (1 - n_b^{(0)}(t))}} \text{Tr} \left(\Phi_i^\dagger(t) d_{ia}^\dagger \Phi_i(t) \tilde{d}_{ib} \right) \quad (2.25)$$

the renormalized Hamiltonian $\mathcal{H}_*^{\text{GA}}$ can be defined as

$$\mathcal{H}_*^{\text{GA}} = \sum_{ij} \sum_{abcd} \mathcal{R}_{iaic}^\dagger \tau_{icjd} \mathcal{R}_{jdjb} \tilde{d}_{ia}^\dagger \tilde{d}_{jb}. \quad (2.26)$$

Its momentum-space formulation reads

$$\bar{\mathcal{H}}_*^{\text{GA}} = \sum_{\mathbf{k}} \sum_{abcd} \mathcal{R}_{ac}^\dagger \varepsilon_{\mathbf{k}ckd} \mathcal{R}_{db} \tilde{d}_{\mathbf{k}a}^\dagger \tilde{d}_{\mathbf{k}b}. \quad (2.27)$$

These two equations can be compared to Eqs. 2.15 and 2.8, where $\mathcal{H}_*^{\text{SB}}$ and $\bar{\mathcal{H}}_*^{\text{SB}}$ are defined, respectively. As they are related by unitary transform and from the context it is clear if Gutzwiller framework or slave boson description is used, they are denoted in the following as \mathcal{H}_* and $\bar{\mathcal{H}}_*$. Using \mathcal{H}_* the following form of action is obtained with² [160]

$$\begin{aligned} \mathcal{S} [|\Psi\rangle] = & \int_0^{t_f} d\tau \left[i \left\langle \psi(\tau) \left| \frac{\partial}{\partial \tau} \psi(\tau) \right. \right\rangle - \langle \psi(\tau) | \mathcal{H}_*(\tau) | \psi(\tau) \rangle \right. \\ & \left. + i \sum_i \text{Tr} \left(\Phi_i^\dagger(\tau) \frac{\partial}{\partial \tau} \Phi_i(\tau) \right) - \sum_i \text{Tr} \left(\Phi_i^\dagger(\tau) \mathcal{H}^{\text{loc}} \Phi_i(\tau) \right) \right] \quad (2.28) \end{aligned}$$

The best approximation to the real evolving state in the subclass of Gutzwiller wavefunctions can then be retrieved by requiring the stationary of this action with respect to the Slater determinant $\psi(t)$ and the Gutzwiller variational matrix Φ_i , as

²Note that an in depth calculation of Eq. 2.28 can be found in the appendix of [121].

well as its conjugate Φ_i^\dagger . Deriving the functional derivatives results in

$$i\frac{\partial}{\partial t}|\psi(t)\rangle = \mathcal{H}_*[\Phi(t)]|\psi(t)\rangle \quad (2.29)$$

$$i\frac{\partial}{\partial t}\Phi_i(t) = \mathcal{H}^{loc}(t)\Phi_i(t) + \left\langle \psi(t) \left| \frac{\partial \mathcal{H}_*[\Phi(t)]}{\partial \Phi_i^\dagger} \right| \psi(t) \right\rangle \quad (2.30)$$

$$-i\frac{\partial}{\partial t}\Phi_i^\dagger(t) = \Phi_i^\dagger(t)\mathcal{H}^{loc}(t) + \left\langle \psi(t) \left| \frac{\partial \mathcal{H}_*[\Phi(t)]}{\partial \Phi_i} \right| \psi(t) \right\rangle \quad (2.31)$$

By these first-order ordinary differential equations quasiparticle degrees of freedom (Slater determinants) $|\psi(t)\rangle$ are coupled to local degrees of freedom (Gutzwiller projectors) Φ . $|\psi(t)\rangle$ is evolved by an effective Schrödinger equation for the renormalized Hamiltonian \mathcal{H}_* . Note that TD-GA is similar to Gutzwiller with fluctuations accounted by random phase approximation (GA+RPA). The latter method was invented by Seibold *et al.* [128, 129], but the here presented method has the major advantage that the Gutzwiller projector Φ has its own time evolution. In GA+RPA the time evolution of Φ is only driven by the time evolution of the Slater determinant $|\psi(t)\rangle$. It is necessary to give Φ its own time evolution to be able to describe for example the dynamic metal to insulator transition [126].

Note that from Eqs. 2.30 and 2.31 using the Gutzwiller expression for $E(t)$ it is straightforward to show that

$$i\frac{\partial \Phi_i}{\partial t} = \frac{\partial E}{\partial \Phi_i^\dagger} \wedge -i\frac{\partial \Phi_i^\dagger}{\partial t} = \frac{\partial E}{\partial \Phi_i} \quad (2.32)$$

meaning Φ_i and Φ_i^\dagger work as classical conjugate variables and $E(t)$ as their effective Hamiltonian. This turns the whole description via Eqs. 2.29–2.31 into a semiclassical approach and will be used to proof energy conservation in section 2.4.2. In the following, discussion can be limited to Eqs. 2.29 and 2.30 as Eq. 2.31 is just the adjoint of Eq. 2.30.

The derivation of these differential equations is so far exact, done in the limit of infinite lattice coordination number. Applying these formulas to other cases then yields the time-dependent Gutzwiller approximation (TD-GA). Furthermore in most cases the enforcing of the constraints depicted by Eqs. 2.20 and 2.21 is not necessary, as it is proven in [160]. To be specific, these constraints hold for $t > 0$, if fulfilled at $t = 0$ and the local occupation matrix has a representation, in which it has only

diagonal elements.

2.4.2 Conserved quantities

In this section conserved quantities during the time evolution of TD-GA are depicted, which occur also in TD-SBMFT.

Theorem 1. *The occupation of an arbitrary bloch state $n_{\mathbf{k}'a'}$ is conserved during the time evolution as $[\bar{\mathcal{H}}_*, n_{\mathbf{k}'a'}]_-$ holds, where the commutator is defined as follows $[A, B]_- = AB - BA$.*

Proof. Using $[d_a^\dagger, d_b^\dagger]_- = 0 = [d_a, d_b]_-$ and $[d_a, d_b^\dagger]_- = \delta_{ab}$, as well as $[A, BC]_- = [A, B]_- C + B [A, C]_-$ leads to:

$$\begin{aligned} [d_{\mathbf{k}a}, n_{\mathbf{k}'a'}]_- &= [d_{\mathbf{k}a}, d_{\mathbf{k}'a'}^\dagger d_{\mathbf{k}'a'}]_- = [d_{\mathbf{k}a}, d_{\mathbf{k}'a'}^\dagger]_- d_{\mathbf{k}'a'} + \\ &\quad + d_{\mathbf{k}'a'}^\dagger [d_{\mathbf{k}a}, d_{\mathbf{k}'a'}]_- = \delta_{\mathbf{k}\mathbf{k}'} \delta_{aa'} d_{\mathbf{k}'a'} \\ [d_{\mathbf{k}a}^\dagger, n_{\mathbf{k}'a'}]_- &= [d_{\mathbf{k}a}^\dagger, d_{\mathbf{k}'a'}^\dagger d_{\mathbf{k}'a'}]_- = [d_{\mathbf{k}a}^\dagger, d_{\mathbf{k}'a'}^\dagger]_- d_{\mathbf{k}'a'} + \\ &\quad + d_{\mathbf{k}'a'}^\dagger [d_{\mathbf{k}a}^\dagger, d_{\mathbf{k}'a'}]_- = -\delta_{\mathbf{k}\mathbf{k}'} \delta_{aa'} d_{\mathbf{k}'a'}^\dagger \end{aligned}$$

These both equations are helpful when computing $[\bar{\mathcal{H}}_*, n_{\mathbf{k}'a'}]_-$. As $\bar{\mathcal{H}}_*$ is a one-particle operator,

$$\bar{\mathcal{H}}_* = \sum_{\mathbf{k}} \sum_{ab} \bar{\mathcal{H}}_{*ab}^{\mathbf{k}} d_{\mathbf{k}a}^\dagger d_{\mathbf{k}b} + \bar{\mathcal{H}}_{*ba}^{\mathbf{k}*} d_{\mathbf{k}b}^\dagger d_{\mathbf{k}a}$$

holds. Using the two identities

$$\begin{aligned} [d_{\mathbf{k}a}^\dagger d_{\mathbf{k}b}, n_{\mathbf{k}'a'}]_- &= - \left([n_{\mathbf{k}'a'}, d_{\mathbf{k}a}^\dagger]_- d_{\mathbf{k}b} + d_{\mathbf{k}a}^\dagger [n_{\mathbf{k}'a'}, d_{\mathbf{k}b}]_- \right) \\ &= - \left(\delta_{aa'} \delta_{\mathbf{k}\mathbf{k}'} d_{\mathbf{k}a}^\dagger d_{\mathbf{k}b} - \delta_{\mathbf{k}\mathbf{k}'} \delta_{ba'} d_{\mathbf{k}a}^\dagger d_{\mathbf{k}b} \right) \\ [d_{\mathbf{k}b}^\dagger d_{\mathbf{k}a}, n_{\mathbf{k}'a'}]_- &= \delta_{aa'} \delta_{\mathbf{k}\mathbf{k}'} d_{\mathbf{k}b}^\dagger d_{\mathbf{k}a} - \delta_{\mathbf{k}\mathbf{k}'} \delta_{ba'} d_{\mathbf{k}b}^\dagger d_{\mathbf{k}a} \end{aligned}$$

$[\bar{\mathcal{H}}_*, n_{\mathbf{k}'a'}]_-$ can be easily computed.

$$\begin{aligned}
[\bar{\mathcal{H}}_*, n_{\mathbf{k}'a'}]_- &= \left[\sum_{\mathbf{k}} \sum_{ab} \left(\bar{\mathcal{H}}_{*ab}^{\mathbf{k}} d_{\mathbf{k}a}^\dagger d_{\mathbf{k}b} + \bar{\mathcal{H}}_{*ba}^{\mathbf{k}*} d_{\mathbf{k}b}^\dagger d_{\mathbf{k}a} \right), n_{\mathbf{k}'a'} \right]_- \\
&= \sum_{\mathbf{k}} \sum_{ab} \bar{\mathcal{H}}_{*ab}^{\mathbf{k}} \left[d_{\mathbf{k}a}^\dagger d_{\mathbf{k}b}, n_{\mathbf{k}'a'} \right]_- + \sum_{\mathbf{k}} \sum_{ab} \bar{\mathcal{H}}_{*ba}^{\mathbf{k}*} \left[d_{\mathbf{k}b}^\dagger d_{\mathbf{k}a}, n_{\mathbf{k}'a'} \right]_- \\
&= \sum_{\mathbf{k}} \sum_{ab} \bar{\mathcal{H}}_{*ab}^{\mathbf{k}} \left(-\delta_{aa'} \delta_{\mathbf{k}\mathbf{k}'} d_{\mathbf{k}a}^\dagger d_{\mathbf{k}b} + \delta_{\mathbf{k}\mathbf{k}'} \delta_{ba'} d_{\mathbf{k}a}^\dagger d_{\mathbf{k}b} \right) \\
&\quad + \sum_{\mathbf{k}} \sum_{ab} \bar{\mathcal{H}}_{*ba}^{\mathbf{k}*} \left(\delta_{aa'} \delta_{\mathbf{k}\mathbf{k}'} d_{\mathbf{k}b}^\dagger d_{\mathbf{k}a} - \delta_{\mathbf{k}\mathbf{k}'} \delta_{ba'} d_{\mathbf{k}b}^\dagger d_{\mathbf{k}a} \right) \\
&= \sum_a \bar{\mathcal{H}}_{*aa'}^{\mathbf{k}'} d_{\mathbf{k}'a}^\dagger d_{\mathbf{k}'a'} - \sum_b \bar{\mathcal{H}}_{*a'b}^{\mathbf{k}'} d_{\mathbf{k}'a}^\dagger d_{\mathbf{k}'b} + \sum_b \bar{\mathcal{H}}_{*ba'}^{\mathbf{k}'*} d_{\mathbf{k}'b}^\dagger d_{\mathbf{k}'a'} \\
&\quad - \sum_a \bar{\mathcal{H}}_{*a'a}^{\mathbf{k}'*} d_{\mathbf{k}'a'}^\dagger d_{\mathbf{k}'a'} \\
&= 0
\end{aligned}$$

In the last step the hermiticity of $\bar{\mathcal{H}}_*$ was used. \square

Theorem 2. *The total Energy $E(t)$ is conserved, if the Hamiltonian is time-independent. If the Hamiltonian is explicitly time-dependent, only the explicit time-dependence remains.*

Proof.

$$\begin{aligned}
\frac{dE}{dt} &= \frac{d}{dt} \langle \Psi(t) | \mathcal{H} | \Psi(t) \rangle = \frac{d}{dt} \left[\langle \psi(t) | \bar{\mathcal{H}}_* | \psi(t) \rangle + \sum_i \text{Tr} \left(\Phi_i^\dagger \mathcal{H}^{\text{loc}} \Phi_i \right) \right] \\
&= \underbrace{\left\langle \frac{d\psi(t)}{dt} | \bar{\mathcal{H}}_* | \psi(t) \right\rangle}_{\textcircled{1}} + \underbrace{\left\langle \psi(t) | \bar{\mathcal{H}}_* | \frac{d\psi(t)}{dt} \right\rangle}_{\textcircled{2}} + \underbrace{\left\langle \psi(t) \left| \frac{d\bar{\mathcal{H}}_* [\Phi^\dagger(t), \Phi(t), t]}{dt} \right| \psi(t) \right\rangle}_{\textcircled{3}} \\
&\quad + \underbrace{\sum_i \text{Tr} \left(\frac{d\Phi_i^\dagger}{dt} \mathcal{H}^{\text{loc}} \Phi_i \right)}_{\textcircled{4}} + \underbrace{\sum_i \text{Tr} \left(\Phi_i^\dagger \mathcal{H}^{\text{loc}} \frac{d\Phi_i}{dt} \right)}_{\textcircled{5}} + \underbrace{\sum_i \text{Tr} \left(\Phi_i^\dagger \frac{d\mathcal{H}^{\text{loc}}}{dt} \Phi_i \right)}_{\textcircled{6}}
\end{aligned}$$

As Eq. 2.29 holds also with opposite sign for the corresponding bra vector contribution $\textcircled{1}$ and $\textcircled{2}$ negate each other and the contributions $\textcircled{3} - \textcircled{6}$ can be restated

using the chain rule.

$$\begin{aligned}
&= \frac{dE(\Phi^\dagger(t), \Phi(t), t)}{dt} = \frac{dE}{d\Phi} \frac{d\Phi}{dt} + \frac{dE}{d\Phi^\dagger} \frac{d\Phi^\dagger}{dt} + \frac{\partial E}{\partial t} \\
&= -i \frac{dE}{d\Phi} \frac{dE}{d\Phi^\dagger} + i \frac{dE}{d\Phi^\dagger} \frac{dE}{d\Phi} + \frac{\partial E}{\partial t} = \frac{\partial E}{\partial t},
\end{aligned} \tag{2.33}$$

where in the first step, Eq. 2.32 was utilized and in the second step it can be safely assumed that the energy E has continuous second order partial derivatives with respect to Φ and Φ^\dagger . Therefore $\frac{dE}{dt} = 0$ holds, if \mathcal{H} is not explicitly time-dependent. \square

2.4.3 Transfer of differential equations to momentum space slave boson formulation

After deriving TD-GA in section 2.4.1 and computing conserved quantities in the previous section, the interest lies now on the transfer of the differential equations 2.29 and 2.30 to the slave boson formalism. These differential equations control the time evolution in TD-GA. Since section 2.4.1 latin letters denote spin and orbital degrees of freedom in Gutzwiller space and in the following greek letters denote spin and orbital degrees of freedom in slave boson formalism. Starting from the first equation (Eq. 2.29)

$$i \frac{\partial}{\partial t} |\psi(t)\rangle = \bar{\mathcal{H}}_* |\psi(t)\rangle \tag{2.34}$$

and utilizing the unitary transform

$$d_{\mathbf{K}}^\dagger = \sum \nu_{\mathbf{K}} c_{\mathbf{K}}^\dagger \rightarrow d_{\mathbf{K}a}^\dagger \nu_{\mathbf{K}\beta a} = \nu_{\mathbf{K}\alpha\beta} c_{\mathbf{K}\beta}^\dagger \nu_{\mathbf{K}\beta a} \tag{2.35}$$

$$c_{\mathbf{K}\beta}^\dagger = \sum_a d_{\mathbf{K}a}^\dagger \nu_{\mathbf{K}\beta a}^\dagger$$

$$c_{\mathbf{K}\beta} = \sum_b \nu_{\mathbf{K}b\beta} d_{\mathbf{K}b}. \tag{2.36}$$

Let us look now at the left hand side first. Note that d^\dagger denotes the creator in Gutzwiller space and c^\dagger the one in slave boson space. Both are at each point \mathbf{K} in momentum space only a unitary transformation away from each other denoted by

$\nu_{\mathbf{K}}$. We start at

$$i \cdot \frac{\partial}{\partial t} |\psi\rangle = i \cdot \frac{\partial}{\partial t} \left(\prod_{\mathbf{K}_a}^{\text{occ}} \left(\sum_{\beta} \nu_{\mathbf{K}_a \beta} c_{\mathbf{K}_a \beta}^{\dagger} \right) |0\rangle \right)$$

Note that $|\psi\rangle$ is a Slater determinant, therefore only indices occupied by electrons are considered in products or sums denoted by 'occ'. The product is restructured in the following way, where an additional sign $P(\mathbf{K})$ is obtained related to shifting the specific contribution $\mathbf{K}' = \mathbf{K}$ at the end of the product

$$\prod_{\mathbf{K}_a}^{\text{occ}} (\dots) = P(\mathbf{K}) \prod_{\substack{\mathbf{K}' \neq \mathbf{K} \\ a}}^{\text{occ}} (\dots) \prod_{\substack{\mathbf{K}' = \mathbf{K} \\ b}}^{\text{occ}} (\dots).$$

This leads to

$$\begin{aligned} & i \cdot \frac{\partial}{\partial t} \left(\prod_{\mathbf{K}_a}^{\text{occ}} \left(\sum_{\beta} \nu_{\mathbf{K}_a \beta} c_{\mathbf{K}_a \beta}^{\dagger} \right) |0\rangle \right) \\ &= i \cdot \sum_{\mathbf{K}}^{\text{occ}} P(\mathbf{K}) \prod_{\substack{\mathbf{K}' \neq \mathbf{K} \\ a}}^{\text{occ}} \left(\nu_{\mathbf{K}' a \beta} c_{\mathbf{K}' \beta}^{\dagger} \right) \frac{\partial}{\partial t} \left(\prod_d^{\text{occ}} \left(\sum_{\beta} i \cdot \nu_{\mathbf{K}_d \beta} c_{\mathbf{K}_d \beta}^{\dagger} \right) |0\rangle \right) \\ &= \sum_{\mathbf{K}_a}^{\text{occ}} P(\mathbf{K}) P(a) \prod_{\substack{\mathbf{K}' \neq \mathbf{K} \\ b}}^{\text{occ}} \left(\nu_{\mathbf{K}' b \beta} c_{\mathbf{K}' \beta}^{\dagger} \right) \prod_{d \neq a}^{\text{occ}} \left(\sum_{\alpha} i \cdot \frac{\partial}{\partial t} \nu_{\mathbf{K}_a \alpha} \underbrace{c_{\mathbf{K}_a \alpha}^{\dagger}}_{\sum_c d_{\mathbf{K}_c}^{\dagger} \nu_{\mathbf{K}_a c}} \right) \\ & \cdot \underbrace{\left(\sum_{\beta'} \nu_{\mathbf{K}_d \beta'} c_{\mathbf{K}_d \beta'}^{\dagger} \right)}_{d_{\mathbf{K}_d}^{\dagger}} |0\rangle \end{aligned} \tag{2.37}$$

Let us look now at the right hand side

$$\begin{aligned}
\tilde{\mathcal{H}}|\psi\rangle &= \sum_{\mathbf{K}\alpha\beta} \bar{\mathcal{H}}_{*\alpha\beta}^{\mathbf{K}} c_{\mathbf{K}\alpha}^\dagger c_{\mathbf{K}\beta} |\psi\rangle = \sum_{\mathbf{K}\alpha\beta} \bar{\mathcal{H}}_{*\alpha\beta}^{\mathbf{K}} c_{\mathbf{K}\alpha}^\dagger c_{\mathbf{K}\beta} \prod_a^{\text{occ}} \left(\sum_{\beta'} \nu_{\mathbf{K}'a\beta'} c_{\mathbf{K}'\beta'}^\dagger \right) |0\rangle \\
&= \sum_{\mathbf{K}\alpha\beta} \underbrace{P(\mathbf{K}) \bar{\mathcal{H}}_{*\alpha\beta}^{\mathbf{K}} c_{\mathbf{K}\alpha}^\dagger c_{\mathbf{K}\beta}}_{\textcircled{1}} \underbrace{\prod_a^{\text{occ}} \left(\sum_{\beta'} \nu_{\mathbf{K}'a\beta'} c_{\mathbf{K}'\beta'}^\dagger \right)}_{\textcircled{2}} \prod_b^{\text{occ}} \left(\sum_{\beta'} \nu_{\mathbf{K}b\beta'} c_{\mathbf{K}\beta'}^\dagger \right) |0\rangle
\end{aligned}$$

① and ② can be swapped now as they share no common index.

$$\begin{aligned}
&= \sum_{\mathbf{K}} P(\mathbf{K}) \prod_a^{\text{occ}} \left(\sum_{\beta'} \nu_{\mathbf{K}'a\beta'} c_{\mathbf{K}'\beta'}^\dagger \right) \sum_{\alpha\beta} \bar{\mathcal{H}}_{*\alpha\beta}^{\mathbf{K}} c_{\mathbf{K}\alpha}^\dagger c_{\mathbf{K}\beta} \underbrace{\prod_b^{\text{occ}} \left(\sum_{\beta'} \nu_{\mathbf{K}b\beta'} c_{\mathbf{K}\beta'}^\dagger \right)}_{d_{\mathbf{K}b}^\dagger} |0\rangle \\
&= \sum_{\mathbf{K}} P(\mathbf{K}) \prod_a^{\text{occ}} \left(\sum_{\beta'} \nu_{\mathbf{K}'a\beta'} c_{\mathbf{K}'\beta'}^\dagger \right) \sum_{\alpha\beta cd} \bar{\mathcal{H}}_{*\alpha\beta}^{\mathbf{K}} d_{\mathbf{K}c}^\dagger \nu_{\mathbf{K}\alpha c}^\dagger \nu_{\mathbf{K}d\beta} d_{\mathbf{K}d} \underbrace{\prod_b^{\text{occ}} d_{\mathbf{K}b}^\dagger}_{P(d) \prod_{b \neq d}^{\text{occ}} d_{\mathbf{K}b}^\dagger} |0\rangle \\
&= \sum_{\mathbf{K}cd} P(\mathbf{K}) P(d) \prod_a^{\text{occ}} \left(\sum_{\beta'} \nu_{\mathbf{K}'a\beta'} c_{\mathbf{K}'\beta'}^\dagger \right) \sum_{\alpha\beta} \bar{\mathcal{H}}_{*\alpha\beta}^{\mathbf{K}} d_{\mathbf{K}c}^\dagger \nu_{\mathbf{K}\alpha c}^\dagger \nu_{\mathbf{K}d\beta} \prod_{b \neq d}^{\text{occ}} d_{\mathbf{K}b}^\dagger |0\rangle
\end{aligned}$$

Now some index changes $a \rightarrow b$, $d \rightarrow a$, $b \rightarrow d$:

$$= \sum_{\mathbf{K}ca} P(\mathbf{K}) P(a) \prod_b^{\text{occ}} \left(\sum_{\beta'} \nu_{\mathbf{K}'b\beta'} c_{\mathbf{K}'\beta'}^\dagger \right) \sum_{\alpha\beta} \bar{\mathcal{H}}_{*\alpha\beta}^{\mathbf{K}} d_{\mathbf{K}c}^\dagger \nu_{\mathbf{K}\alpha c}^\dagger \nu_{\mathbf{K}a\beta} \prod_{d \neq a}^{\text{occ}} d_{\mathbf{K}d}^\dagger |0\rangle \quad (2.38)$$

By comparing the result of the right hand side (Eq. 2.38) to the one of the left hand side (Eq. 2.37), we arrive at

$$\begin{aligned}
\sum_{\alpha\beta c} \bar{\mathcal{H}}_{*\alpha\beta}^{\mathbf{K}} d_{\mathbf{K}c}^\dagger \nu_{\mathbf{K}\alpha c}^\dagger \nu_{\mathbf{K}a\beta} &= \sum_{\alpha c} i \cdot \frac{\partial}{\partial t} \nu_{\mathbf{K}a\alpha} d_{\mathbf{K}c}^\dagger \nu_{\mathbf{K}\alpha c}^\dagger \\
\Leftrightarrow \sum_{\beta} \bar{\mathcal{H}}_{*\alpha\beta}^{\mathbf{K}} \nu_{\mathbf{K}a\beta} &= i \cdot \frac{\partial}{\partial t} \nu_{\mathbf{K}a\alpha} \quad \forall a \text{ occupied}, \forall \mathbf{K} \text{ occupied}, \forall \alpha. \quad (2.39)
\end{aligned}$$

Eq. 2.39 is the final result for the first differential equation.

Let us now take a look at the second equation (Eq. 2.30), where $\frac{\partial \langle \psi | \bar{\mathcal{H}}_*^{\mathbf{K}}[\phi(t)] | \psi \rangle}{\partial \phi^\dagger} = \langle \psi | \frac{\partial \bar{\mathcal{H}}_*^{\mathbf{K}}}{\partial \phi^\dagger} | \psi \rangle$ is the interesting part. In the other parts of Eq. 2.30, a simple replacement of the Gutzwiller projector Φ with the slave boson ϕ is sufficient. This is justified by the fact, that both operators are the same, when applying the mentioned unitary transformation (Eqs. 2.35 and 2.36) to the basis [19].

$$\begin{aligned}
 \frac{\partial \bar{\mathcal{H}}_*}{\partial \phi^\dagger} | \psi \rangle &= \frac{\partial \bar{\mathcal{H}}_*}{\partial \phi^\dagger} \prod_a^{\text{occ}} \left(\sum_{\beta'} \nu_{\mathbf{K}'a\beta'} c_{\mathbf{K}'\beta'}^\dagger \right) | 0 \rangle \\
 &= \sum_{\alpha\beta\mathbf{K}} \frac{\partial \bar{\mathcal{H}}_*^{\mathbf{K}}}{\partial \phi^\dagger} c_{\mathbf{K}\alpha}^\dagger \underbrace{c_{\mathbf{K}\beta}}_{\sum_b \nu_{\mathbf{K}b\beta} d_{b\mathbf{K}}} \prod_a^{\text{occ}} \left(\sum_{\beta'} \nu_{\mathbf{K}a\beta'} c_{\mathbf{K}'\beta'}^\dagger \right) | 0 \rangle \\
 &= \underbrace{\sum_{\alpha\beta\mathbf{K}} \sum_b \frac{\partial \bar{\mathcal{H}}_*^{\mathbf{K}}}{\partial \phi^\dagger} c_{\mathbf{K}\alpha}^\dagger \nu_{\mathbf{K}b\beta} d_{b\mathbf{K}}}_{\textcircled{1}} \underbrace{\prod_{\mathbf{K}' \neq \mathbf{K}}^{\text{occ}} P(\mathbf{K}) P(a)}_{\textcircled{2}} \left(\sum_{\beta'} \nu_{\mathbf{K}'a\beta'} c_{\mathbf{K}'\beta'}^\dagger \right) \cdot \prod_c^{\text{occ}} d_{\mathbf{K}c}^\dagger | 0 \rangle
 \end{aligned}$$

Again $\textcircled{1}$ and $\textcircled{2}$ can be swapped now.

$$\begin{aligned}
 &= \sum_{\alpha\beta\mathbf{K}} \prod_a^{\text{occ}} P(\mathbf{K}) P(a) \left(\sum_{\beta'} \nu_{\mathbf{K}'a\beta'} c_{\mathbf{K}'\beta'}^\dagger \right) \sum_b \frac{\partial \bar{\mathcal{H}}_*^{\mathbf{K}}}{\partial \phi^\dagger} c_{\mathbf{K}\alpha}^\dagger \nu_{\mathbf{K}b\beta} d_{b\mathbf{K}} \prod_c^{\text{occ}} d_{\mathbf{K}c}^\dagger | 0 \rangle \\
 &= \sum_{\alpha\beta\mathbf{K}} \prod_a^{\text{occ}} P(\mathbf{K}) P(a) \left(\sum_{\beta'} \nu_{\mathbf{K}'a\beta'} c_{\mathbf{K}'\beta'}^\dagger \right) \sum_b \frac{\partial \bar{\mathcal{H}}_*^{\mathbf{K}}}{\partial \phi^\dagger} c_{\mathbf{K}\alpha}^\dagger \nu_{\mathbf{K}b\beta} \prod_{c \neq b}^{\text{occ}} d_{\mathbf{K}c}^\dagger | 0 \rangle
 \end{aligned}$$

Together with

$$\langle \psi | = \langle 0 | \prod_{\mathbf{K}''e}^{\text{occ}} d_{\mathbf{K}''e} = \langle 0 | \prod_e^{\text{occ}} \left(\sum_{\beta'} \nu_{\mathbf{K}e\beta'} c_{\mathbf{K}''\beta'}^\dagger \right)$$

it follows with $\textcircled{3} = \langle \psi | \frac{\partial \bar{\mathcal{H}}_*}{\partial \phi^\dagger} | \psi \rangle$

$$\begin{aligned}
\textcircled{3} &= \langle 0 | \prod_e^{\text{occ}} d_{\mathbf{K}'' e} \sum_{\alpha\beta\mathbf{K}} \prod_{\mathbf{K}' \neq \mathbf{K}}^{\text{occ}} P(\mathbf{K}) P(a) \left(\sum_{\beta'} \nu_{\mathbf{K}' a \beta'} c_{\mathbf{K}' \beta'}^\dagger \right) \cdot \\
&\quad \cdot \sum_b \frac{\partial \bar{\mathcal{H}}_{*\alpha\beta}^{\mathbf{K}}}{\partial \phi^\dagger} c_{\mathbf{K}\alpha}^\dagger \nu_{\mathbf{K}b\beta} P(b) \prod_{c \neq b}^{\text{occ}} d_{\mathbf{K}c}^\dagger | 0 \rangle \\
&= \langle 0 | \sum_{\mathbf{K}} \prod_e^{\text{occ}} \left(\sum_{\beta'} \nu_{\mathbf{K}e\beta'}^\dagger c_{\mathbf{K}\beta'} \right) \cdot \\
&\quad \cdot \underbrace{\prod_d^{\text{occ}} P(\mathbf{K}) P(d) \left(\sum_{\beta'} \nu_{\mathbf{K}'' d \beta'}^\dagger c_{\mathbf{K}'' \beta'} \right) \sum_{\alpha, \beta} \prod_{\mathbf{K}' \neq \mathbf{K}}^{\text{occ}} P(\mathbf{K}) P(a) \left(\sum_{\beta'} \nu_{\mathbf{K}' a \beta'} c_{\mathbf{K}' \beta'}^\dagger \right)}_{=1} \\
&\quad \cdot \frac{\partial \bar{\mathcal{H}}_{*\alpha\beta}^{\mathbf{K}}}{\partial \phi^\dagger} \underbrace{c_{\mathbf{K}\alpha}^\dagger}_{\sum_f d_{f\mathbf{K}}^\dagger \nu_{\mathbf{K}\alpha f}^\dagger} \sum_b \nu_{\mathbf{K}b\beta} P(b) \prod_{c \neq b}^{\text{occ}} d_{\mathbf{K}c}^\dagger | 0 \rangle \\
&= \langle 0 | \sum_{\mathbf{K}} \prod_e^{\text{occ}} d_{e\mathbf{K}} \sum_f d_{f\mathbf{K}}^\dagger \nu_{\mathbf{K}\alpha f}^\dagger \frac{\partial \bar{\mathcal{H}}_{*\alpha\beta}^{\mathbf{K}}}{\partial \phi^\dagger} \sum_b \nu_{\mathbf{K}b\beta} P(b) \prod_{c \neq b}^{\text{occ}} d_{\mathbf{K}c}^\dagger | 0 \rangle \\
&= \langle 0 | \sum_{\mathbf{K}\alpha\beta} \sum_f \prod_{e \neq f}^{\text{occ}} d_{e\mathbf{K}} \nu_{\mathbf{K}\alpha f}^\dagger \frac{\partial \bar{\mathcal{H}}_{*\alpha\beta}^{\mathbf{K}}}{\partial \phi^\dagger} P(f) \sum_b P(b) \nu_{\mathbf{K}b\beta} \prod_{c \neq b}^{\text{occ}} d_{\mathbf{K}c}^\dagger | 0 \rangle
\end{aligned}$$

Note that this expression is zero for $f \neq b$, thus

$$= \langle 0 | \sum_{\mathbf{K}\alpha\beta} \sum_b \nu_{\mathbf{K}\alpha b}^\dagger \frac{\partial \bar{\mathcal{H}}_{*\alpha\beta}^{\mathbf{K}}}{\partial \phi^\dagger} \nu_{\mathbf{K}b\beta} | 0 \rangle, \quad (2.40)$$

which is the final expression for $\textcircled{3}$. Finally we can write up the slave boson equivalents of (Eqs. 2.29 and 2.30)

$$i \frac{\partial}{\partial t} \nu_{\mathbf{K}a\alpha} = \sum_{\beta} \bar{\mathcal{H}}_{*\alpha\beta}^{\mathbf{K}} \nu_{\mathbf{K}a\beta} \quad \forall a, \mathbf{K} \text{ occupied } \forall \alpha \quad (2.41)$$

$$i \frac{\partial \phi}{\partial t} = \mathcal{H}^{\text{loc}} \phi + \sum_{\mathbf{K}b} \sum_{\alpha\beta} \nu_{\mathbf{K}\alpha b}^\dagger \frac{\partial \bar{\mathcal{H}}_{*\alpha\beta}^{\mathbf{K}}}{\partial \phi^\dagger} \nu_{\mathbf{K}b\beta} \quad (2.42)$$

The unitary transformation $\nu_{\mathbf{K}}$ is the Slater determinant, which replaces ψ of the Gutzwiller formalism. $\nu_{\mathbf{K}a}$ are in fact the eigenvectors of the renormalized Hamiltonian $\bar{\mathcal{H}}_*$ (Eq. 2.8 regarding the eigenvalue a). The Gutzwiller projector Φ is replaced by the slave bosons ϕ . A central role in the differential equations 2.41 and 2.42 play the occupied points in momentum space and spin+orbital space. This is the reminder that $\nu_{\mathbf{K}}$ are Slater determinants and by definition only meaningful, when at least partially occupied.

2.4.4 Transfer of differential equations to real-space slave boson formulation

The calculation depicted here is analogous to the one of the last section. Instead of points in momentum space real-space lattice indices are considered. Starting from the first equation 2.29

$$i\frac{\partial}{\partial t} |\psi(t)\rangle = \mathcal{H}_* |\psi(t)\rangle \quad (2.43)$$

using the unitary transformation

$$c_{i\alpha}^\dagger = \sum_{jb} d_{jb}^\dagger \eta_{i\alpha jb}^\dagger \quad (2.44)$$

$$c_{j\beta} = \sum_{j'b} \eta_{j'b j\beta} d_{j'b}, \quad (2.45)$$

where i, j (and primed i, j) denote lattice sites. Orbitals with spin in Gutzwiller space are denoted by greek letters (and primed greek letters) and orbitals with spin in slave boson space by latin letters (and primed latin letters). Furthermore one state in real-space is characterized by both site and orbital (with spin) meaning one state in Gutzwiller real-space is $|\tilde{\alpha}\rangle = |i\alpha\rangle$. The right hand side of Eq. 2.43 can

now be turned into

$$\begin{aligned}
\tilde{H}|\psi\rangle &= \sum_{ij\alpha\beta} \mathcal{H}_{*i\alpha j\beta} c_{i\alpha}^\dagger c_{j\beta} \left(\prod_{i'a}^{\text{occ}} d_{i'a}^\dagger \right) |0\rangle \\
&= \sum_{ij\alpha\beta} \mathcal{H}_{*i\alpha j\beta} c_{i\alpha}^\dagger \left(\sum_{j'b} \eta_{j'b j\beta} d_{j'b} \right) \left(\prod_{i'a}^{\text{occ}} d_{i'a}^\dagger \right) |0\rangle \\
&= \sum_{j'b}^{\text{occ}} P(j') P(b) \sum_{ij\alpha\beta} \mathcal{H}_{*i\alpha j\beta} c_{i\alpha}^\dagger \eta_{j'b j\beta} \prod_{\substack{i' \neq j' \\ a \neq b}}^{\text{occ}} d_{i'a}^\dagger |0\rangle.
\end{aligned} \tag{2.46}$$

Working now on the left hand side of Eq. 2.43, leads to

$$\begin{aligned}
i \frac{\partial}{\partial t} |\psi\rangle &= i \frac{\partial}{\partial t} \left(\prod_{ib}^{\text{occ}} d_{ib}^\dagger \right) |0\rangle = i \frac{\partial}{\partial t} \left(\left(\prod_{\substack{i \neq i' \\ a \neq b'}}^{\text{occ}} d_{ia}^\dagger \right) \left(\prod_{b'}^{\text{occ}} d_{i'b'}^\dagger \right) \right) |0\rangle \\
&= i \sum_{i'b'}^{\text{occ}} P(i') P(b') \left(\prod_{\substack{i \neq i' \\ a \neq b'}}^{\text{occ}} d_{ia}^\dagger \right) \frac{\partial}{\partial t} d_{i'b'}^\dagger |0\rangle
\end{aligned}$$

Now apply the index changes: $i' \rightarrow j'$ $b' \rightarrow b$

$$= i \sum_{j'b}^{\text{occ}} P(j') P(b) \left(\prod_{\substack{i \neq j' \\ a \neq b}}^{\text{occ}} d_{ia}^\dagger \right) \frac{\partial}{\partial t} \left(\sum_{i\alpha} \eta_{j'bi\alpha} c_{i\alpha}^\dagger \right) \tag{2.47}$$

Comparing Eqs. 2.47 and 2.46 leads to

$$i \frac{\partial}{\partial t} \eta_{j'bi\alpha} = \sum_{j\beta} \mathcal{H}_{*i\alpha j\beta} \cdot \eta_{j'bj\beta}, \tag{2.48}$$

where j' and b run over occupied lattice sites and orbitals and i, α indicate any lattice site or orbital, respectively. Eqn. 2.48 is the real-space equivalent of Eq. 2.41. Turning now to the second equation 2.30, $\langle \psi(t) \left| \frac{\partial \mathcal{H}_*[\Phi(t)]}{\partial \Phi_i^\dagger} \right| \psi(t) \rangle$ is the part, which needs to be transformed. This is started by transforming $\frac{\partial \mathcal{H}_*}{\partial \Phi_i^\dagger} |\psi(t)\rangle$ (suppressing

site index of derivative to improve readability)

$$\begin{aligned}
\frac{\partial \mathcal{H}_*}{\partial \Phi^\dagger} |\psi(t)\rangle &= \frac{\partial \mathcal{H}_*}{\partial \Phi^\dagger} \left(\prod_{ia}^{\text{occ}} d_{ia}^\dagger \right) |0\rangle = \sum_{ij\alpha\beta} \frac{\partial \mathcal{H}_{*i\alpha j\beta}}{\partial \Phi^\dagger} c_{i\alpha}^\dagger c_{j\beta} \left(\prod_{i'a}^{\text{occ}} d_{i'a}^\dagger \right) |0\rangle \\
&= \sum_{ij\alpha\beta} \frac{\partial \mathcal{H}_{*i\alpha j\beta}}{\partial \Phi^\dagger} c_{i\alpha}^\dagger \left(\sum_{j'd} \eta_{j'dj\beta} d_{j'd} \right) \left(\prod_{i'a}^{\text{occ}} d_{i'a}^\dagger \right) |0\rangle \\
&= \sum_{j'd}^{\text{occ}} \sum_{ij\alpha\beta} P(d) P(j') \frac{\partial \mathcal{H}_{*i\alpha j\beta}}{\partial \Phi^\dagger} c_{i\alpha}^\dagger \eta_{j'dj\beta} \prod_{\substack{i' \neq j' \\ a \neq d}}^{\text{occ}} d_{i'a}^\dagger |0\rangle
\end{aligned}$$

using $\langle \psi(t) | = \langle 0 | \prod_{i''b} d_{i''b}$ results in

$$\begin{aligned}
\left\langle \psi(t) \left| \frac{\partial \mathcal{H}_*}{\partial \Phi^\dagger} \right| \psi(t) \right\rangle &= \langle 0 | \prod_{i''b} d_{i''b} \sum_{j'd}^{\text{occ}} \sum_{ij\alpha\beta} P(d) P(j') \frac{\partial \mathcal{H}_{*i\alpha j\beta}}{\partial \Phi^\dagger} c_{i\alpha}^\dagger \eta_{j'dj\beta} \prod_{\substack{i' \neq j' \\ a \neq d}}^{\text{occ}} d_{i'a}^\dagger |0\rangle \\
&= \sum_{j'd}^{\text{occ}} \sum_{ij\alpha\beta} P(d) P(j') \langle 0 | \prod_{i''b} d_{i''b} \left(\sum_{j''g} d_{j''g}^\dagger \eta_{i\alpha j''g}^\dagger \right) \frac{\partial \mathcal{H}_{*i\alpha j\beta}}{\partial \Phi^\dagger} \eta_{j'dj\beta} \prod_{\substack{i' \neq j' \\ a \neq d}}^{\text{occ}} d_{i'a}^\dagger |0\rangle \\
&= \sum_{j'd}^{\text{occ}} \sum_{i''b}^{\text{occ}} P(d) P(j') P(i'') P(b) \sum_{ij\alpha\beta} \langle 0 | \prod_{\substack{i'' \neq j'' \\ b \neq g}} d_{i''b} \eta_{i\alpha j''g}^\dagger \frac{\partial \mathcal{H}_{*i\alpha j\beta}}{\partial \Phi^\dagger} \eta_{j'dj\beta} \prod_{\substack{i' \neq j' \\ a \neq d}}^{\text{occ}} d_{i'a}^\dagger |0\rangle \\
&\quad \text{as } \langle 0 | \prod_{\substack{i'' \neq j'' \\ b \neq g}}^{\text{occ}} d_{i''b} \prod_{\substack{i' \neq j' \\ a \neq d}}^{\text{occ}} d_{i'a}^\dagger |0\rangle = 0, \text{ if } j'' \neq j' \text{ or } g \neq d \\
&= \sum_{j'd}^{\text{occ}} \sum_{ij\alpha\beta} \eta_{i\alpha j'd}^\dagger \frac{\partial \mathcal{H}_{*i\alpha j\beta}}{\partial \Phi^\dagger} \eta_{j'dj\beta} \quad (2.49)
\end{aligned}$$

This results in the second differential equation in real-space:

$$i \frac{\partial \phi_i}{\partial t} = \sum_i \mathcal{H}_i^{\text{loc}} \phi_i + \sum_{j'd}^{\text{occ}} \sum_{ij\alpha\beta} \eta_{i\alpha j'd}^\dagger \frac{\partial \mathcal{H}_{*i\alpha j\beta}}{\partial \phi_i^\dagger} \eta_{j'dj\beta}, \quad (2.50)$$

where the Gutzwiller projector Φ was replaced with the slave boson ϕ . Eqn. 2.50 is the real-space equivalent of Eq. 2.42. Finally let's write both equations in the

real-space formulation together

$$\begin{aligned}
i\frac{\partial}{\partial t}\eta_{j'bi\alpha} &= \sum_{j\beta} \mathcal{H}_{*i\alpha j\beta} \cdot \eta_{j'bj\beta}, \\
i\frac{\partial\phi_i}{\partial t} &= \sum_i \mathcal{H}_i^{\text{loc}}\phi_i + \sum_{j'd}^{\text{occ}} \sum_{i\alpha\beta} \eta_{i\alpha j'd}^\dagger \frac{\partial\mathcal{H}_{*i\alpha j\beta}}{\partial\phi_i^\dagger} \eta_{j'dj\beta},
\end{aligned}$$

where in the first equation j' and b run over occupied lattice sites and orbitals. i, α indicate any lattice site or orbital in the first equation. In the real-space formulation no intersite slave bosons are used (see section 2.3). Different sites are coupled via non-zero site-offdiagonal entries of the eigenvectors η_{ij} of the renormalized Hamiltonian \mathcal{H}_* . The derivative of the renormalized Hamiltonian with respect to the slave bosons acts as transfer matrix.

3 Metal-insulator transition in one-orbital case

Metal to insulator (Mott) transitions are well-known from transition metal oxides [54]. In recent years they were also found in bosonic [37] and fermionic ultracold quantum gases [57, 127]. These gases work as a quantum simulator of the appropriate Hubbard model, and in contrast to solids have no impurities, purely local Coulomb interaction and nearly zero temperature [127]. Non-equilibrium dynamics after an external perturbation of ultracold quantum gases or solids are experimentally accessible by probing the ultracold gas [57, 127] or in the case of solids by using femtosecond spectroscopy [113] and provide a new perspective. Indeed interacting quantum systems out of equilibrium can display intriguing dynamical behavior or be trapped in metastable states, which have no equilibrium counterpart [115, 119]. Although experimental perturbation happens at a finite rate a useful theoretical idealization is a so called quantum quench [20]. Here the system is prepared in an initial state given by the Hamiltonian \mathcal{H}_i and then evolved under a different Hamiltonian \mathcal{H}_f . This turns the initial state into a highly excited state of the final Hamiltonian. The (single-orbital) Hubbard model displays the simplest theoretical approach, which encodes strongly correlated physics like the metal to insulator (Mott) transition at equilibrium. Recent theoretical studies [29, 30, 96] have addressed this model out of equilibrium by inducing a quench from a non-interacting initial state to a state with stronger interactions. They encountered at half-filling for paramagnetic states a dynamical transition separating two regimes. At weak coupling (quenching to small interactions) observables like double occupation are thermalized to equilibrium values, but the momentum distribution resembles a zero temperature Fermi liquid and correlations are more pronounced [96]. Time-dependent dynamical mean-field theory (TD-DMFT) [7] confirmed this *prethermalization* [29] and revealed a dynamical transition towards a regime with pronounced oscillations in the dynamics of physical quantities. The questions, which arise naturally as time-dependent slave boson

mean-field theory (TD-SBMFT) was introduced in section 2.4. Is TD-SBMFT able to reproduce central results of these studies? Where are the limits of the semiclassical approach (compare section 2.4)? These questions were already addressed within TD Gutzwiller approximation (TD-GA) [125, 126], which is the basis of the TD-SBMFT formulation. So this chapter is a reproduction of central results of TD-GA within TD-SBMFT comparing to the mentioned previous studies [29, 30, 96].

The single-orbital Hubbard model (Eq. 2.3) is considered using a simple cubic dispersion in three dimensions. The results are restricted to paramagnetic states and the interaction quench will start from a non-interacting state ($U_i = 0$, if not mentioned otherwise) into a higher interacting state ($U_f > 0$) at half-filling. To achieve the best correspondence with TD-GA works [125, 126], it is mandatory to work in units of $U_c^{(1)}$, where $U_c^{(1)}$ is the critical interaction value to obtain the Mott transition in equilibrium. For simplicity in this chapter $U_c \equiv U_c^{(1)}$ is set for the figures. For a dispersion with bandwidth $2 eV$, meaning working in units of half-bandwidth W , $U_c^{(1)} = 2.65$ is obtained (see Fig. 3.1). By appropriate rescaling of

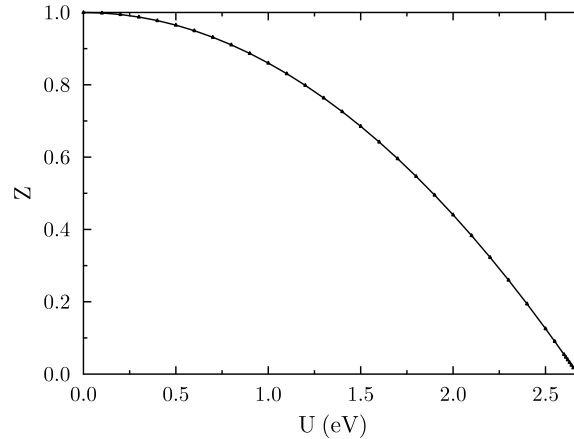


Figure 3.1: Quasiparticle weight as function of the on-site interaction U at half-filling depicting a metal-insulator transition at $U_c^{(1)} = 2.65$.

the hopping τ , the non-equilibrium calculation is done in units of $U_c^{(1)}$. Therefore the notation $u_f = U_f/U_c^{(1)}$ and $u_i = U_i/U_c^{(1)}$ is used. From the differential equations (see Eqs. 2.41 and 2.42), which are the basis of the time evolution in TD-SBMFT, it is known that not only slave bosons are evolved but also the eigenvectors $\nu_{\mathbf{K}}$ of the renormalized free Hamiltonian. Their evolution at three different points in momentum space is depicted as an example at $u_f = 0.40$ in Fig. 3.2. As the absolute value is unchanged during the time evolution, the eigenvectors acquire

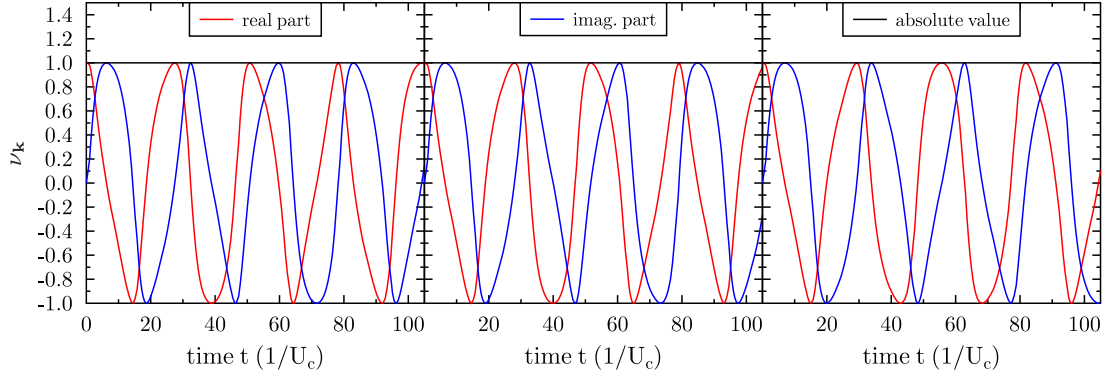


Figure 3.2: Time-dependent real and imaginary part of eigenvector $\nu_{\mathbf{k}}$ at three different \mathbf{k} -points for $u_f = 0.40$.

merely a phase. So their time evolution is trivial and they have no importance for the physics. In Fig. 3.3 time-dependent quasiparticle weight Z and slave boson occupation probabilities $|\phi|^2$ are depicted for an interaction quench to $u_f = 0.05$ (a), $u_f = 0.40$ (b) and $u_f = 0.70$ (c). Periodic, undamped oscillations in Z and in the local slave boson occupation probabilities $|\phi|^2$ are observed. This is clearly an artifact of the semi-classical approach (compare section 2.4). Especially for weak quenches $u_f \sim 0$ as the initial state is a metal, one would expect the system to quickly relax to one equilibrium state due to the continuum of low lying excitations. As half-filling and only paramagnetic ground states are considered double and zero occupation are degenerate. Furthermore both single occupied states are degenerate, too. Due to this symmetry, interpretation of local occupation can be restricted to the double occupation $D = |\phi_{\uparrow\downarrow}|^2$. Increasing the quenched interaction to $u_f = 0.4$ in Fig. 3.3 (b), leads to an increased amplitude and period of oscillations in Z and D . When $u_f = 0.7$ (Fig. 3.3 (c)) is reached, the quasiparticle weight oscillates between zero and one with *decreased* period and the amplitude of D *decreases* compared to $u_f = 0.4$. This indicates that somewhere between $u_f = 0.4$ and $u_f = 0.7$ a qualitative change of non-equilibrium dynamics has happened. Assuming this change to happen abruptly at one $u_f = u_{fc}^{(1)}$ a deeper look is now performed into the weak-coupling ($u_f < u_{fc}^{(1)}$), critical ($u_f = u_{fc}^{(1)}$) and strong coupling ($u_f > u_{fc}^{(1)}$) region. To analyze these three regions the period of the quasiparticle weight is computed by counting the number of oscillations and dividing by the total time $t_{tot} = 1000 / U_c^{(1)}$. Note that all physical quantities have the same period. Additionally the undamped periodicity of Z and D suggest to look at the averaged time integrated value to check if this

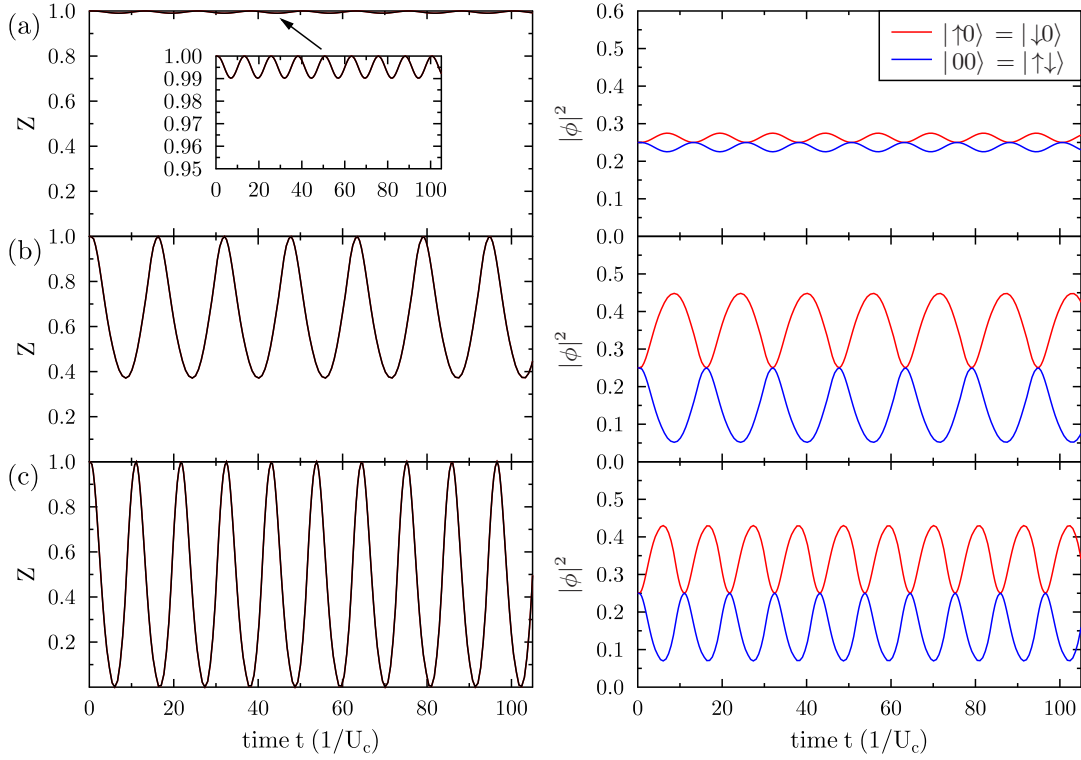


Figure 3.3: Time-dependent quasiparticle weight Z and time-dependent slave boson occupation probabilities $|\phi|^2$ for $u_f = 0.05, 0.40$ and 0.70 in (a), (b) and (c), respectively.

bears any physical meaning

$$\bar{O}_s = \frac{1}{s} \int_0^s dt \langle O(t) \rangle \quad (3.1)$$

with \bar{O} as representative for any local observable like \bar{Z} and $\overline{|\phi|^2}$. s will be in the following also set to $1000 \ 1/U_c^{(1)}$, if not mentioned otherwise.

3.1 Weak coupling

Z and $|\phi|^2$ show periodic and undamped oscillations, which increase in period T between $u_f = 0.05$ and $u_f = 0.40$ (see Fig. 3.3 (a) and (b)). Looking at the dependence on u_f in Fig. 3.4 shows that the period diverges from below approaching $u_f = 0.5$. To get an additional perspective onto the dynamics in the weak-coupling

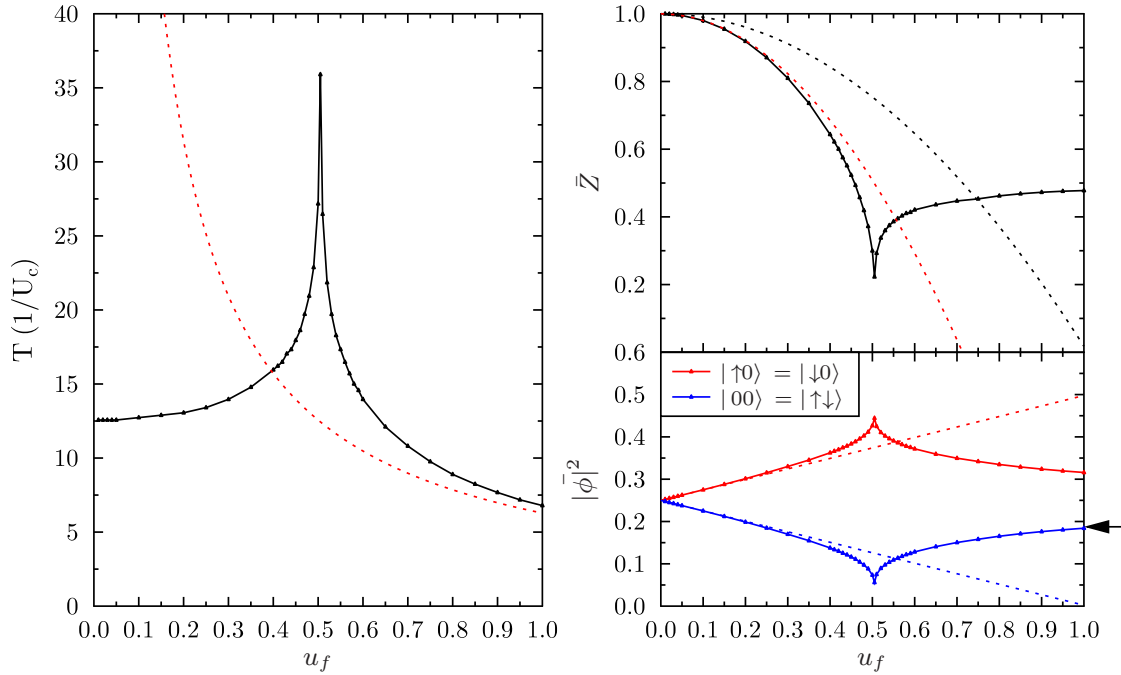


Figure 3.4: Left: Period of physical quantities with u_f . Red dotted lines denote collapse and revival period $2\pi/u_f$ discovered as approximate value by TD-DMFT in strong-coupling regime [29]. Top right: Time-averaged \bar{Z} as function of u_f . Black dotted line denote equilibrium values. Red dotted line depicts $1 - \bar{Z} = 2(1 - Z(t=0))$ known from a weak-coupling expansion using the flow-equation method [96]. Bottom right: Time-averaged occupation (straight lines) and equilibrium values (dotted lines). Black arrow indicates strong-coupling perturbative result from [29] computed at $u_f = 1.0$.

regime, Fig. 3.4 depicts also \bar{Z} and $|\phi|^2$ with u_f . The time-averaged double occupation follows the equilibrium value, meaning \bar{D} is thermalized. In contrast \bar{Z} deviates already for small values of u_f to the equilibrium value and follows the relation $1 - \bar{Z} = 2(1 - Z(t=0))$ known from a weak-coupling expansion using the flow-equation method [96]. These both observations characterize the *prethermalization* regime first recognized in [96] and then confirmed with TD-DMFT [29]. In this *prethermalization* regime momentum-averaged quantities like kinetic and potential energy are thermalized, but the momentum-distribution and related observables like the quasiparticle weight are not, but still well-defined. The relation $1 - \bar{Z} = 2(1 - Z(t=0))$ is a general result of an interaction quench to weak interac-

tions of a non-interacting Fermi liquid [97]. TD-SBMFT captures correctly the onset of prethermalization, but fails in describing its relaxation. Increasing u_f towards 0.5 shows a vanishing (numerical smeared) \bar{Z} and \bar{D} .

3.2 Critical point

At the point $u_f = 0.5$ the period diverges and time-averaged quasiparticle weight and double occupation vanish. The time-dependent Z and D is depicted in Fig. 3.5. Both show an exponential decay with revival, where the latter can be clearly attributed to the numerical handling of the system instead of analytic computation (dotted lines are analytic results). As \bar{Z} and \bar{D} both vanish at this point, it is natural to compare this steady state to the equilibrium Mott insulator, which has the same characteristics. An additional property of the equilibrium Mott insulator is that any finite doping is sufficient to transition into a metallic state. This will be discussed, when finite doping is applied to the non-equilibrium state in section 3.4. Intriguingly $u_{fc}^{(1)} = 0.5$ can be obtained solely from the energetic argument $E_0 = E_{\text{Mott}}$, where E_0 is the energy of the quenched state and E_{Mott} is the energy of the ideal $\tau = 0$ Mott-insulator (decoupled half-filled sites). Applied to the conditions of the TD-DMFT study this leads to $u_{fc}^{(1)} = 3.3$ [126] in very good agreement to the position of the DMFT critical point [29]. This is reason enough to call $u_{fc}^{(1)}$ the dynamic Mott transition.

3.3 Strong coupling

Between $u_f = 0.40$ and $u_f = 0.70$ period T and double occupation D decreases (see Fig. 3.3). The latter can also be seen in Fig. 3.4. The double occupation dynamics freeze out, as their energy is much higher than the kinetic energy, so a decay would need many-particle scattering processes [119]. Additionally \bar{D} approaches again the values of the initial state, leading to a trapping in the initial state at $u_f \rightarrow \infty$ [126]. In the limit of very strong couplings $u_f = 1$, $T \approx 2\pi/U_f$ is given by the dynamics in the atomic limit. In the latter limit the time propagator is $\exp(i\mathcal{H}^{\text{loc}}t)$, having the denoted periodicity. This period is also seen in TD-DMFT studies of the strong-coupling regime looking at collapse and revival oscillations of the double occupation [29, 30]. Furthermore looking again at Fig. 3.4 \bar{D} approaches its initial value, when increasing u_f and matches very well the strong-coupling perturbative result

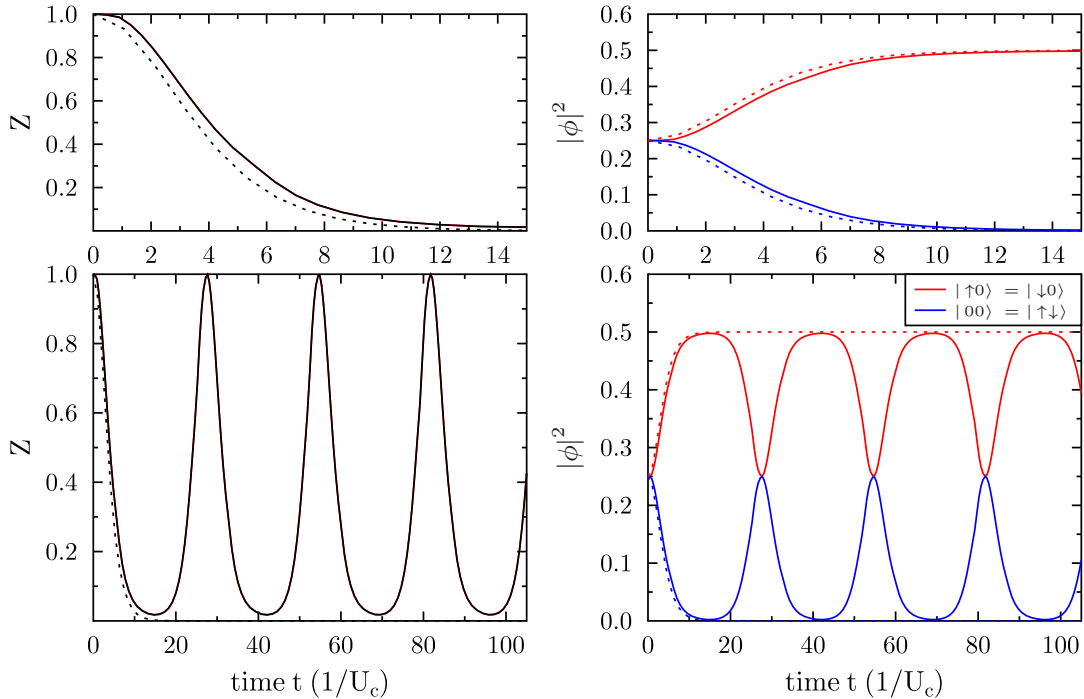


Figure 3.5: Bottom: Time-dependent quasiparticle weight Z (left) and time-dependent slave boson occupation probabilities $|\phi|^2$ (right) for $u_f = 0.5$ and until $t = 105$. Top: Same until $t = 15$. Dotted lines are analytic behavior obtained in TD Gutzwiller approximation [125, 126] (see Eqs. 3.3 and 3.4).

from Eckstein *et al.* [29] for the prethermalization plateau at $u_f = 1.0$. The time-averaged \bar{Z} saturates not at its initial value, but half of it, which can be explained by the periodic oscillation between zero and one (see Fig. 3.3).

3.4 Interaction quenches away from half-filling

To compare the dynamic Mott transition to the equilibrium Mott transition a small hole doping is applied. The derived $T(u_f)$ and \bar{Z} as well as $Z(t)$ is shown in Fig. 3.6. The only notable deviation is close to $u_f = u_{fc}^{(1)}$, where the divergence is smeared out both in period and time-averaged quasiparticle weight. Weak-coupling and strong-coupling prethermalization remain the same, doping does not affect \bar{Z} or T except very close to $u_f = u_{fc}^{(1)}$. This means that the previous description of both prethermal states still holds. Investigation of $Z(t)$ shows, that there is no

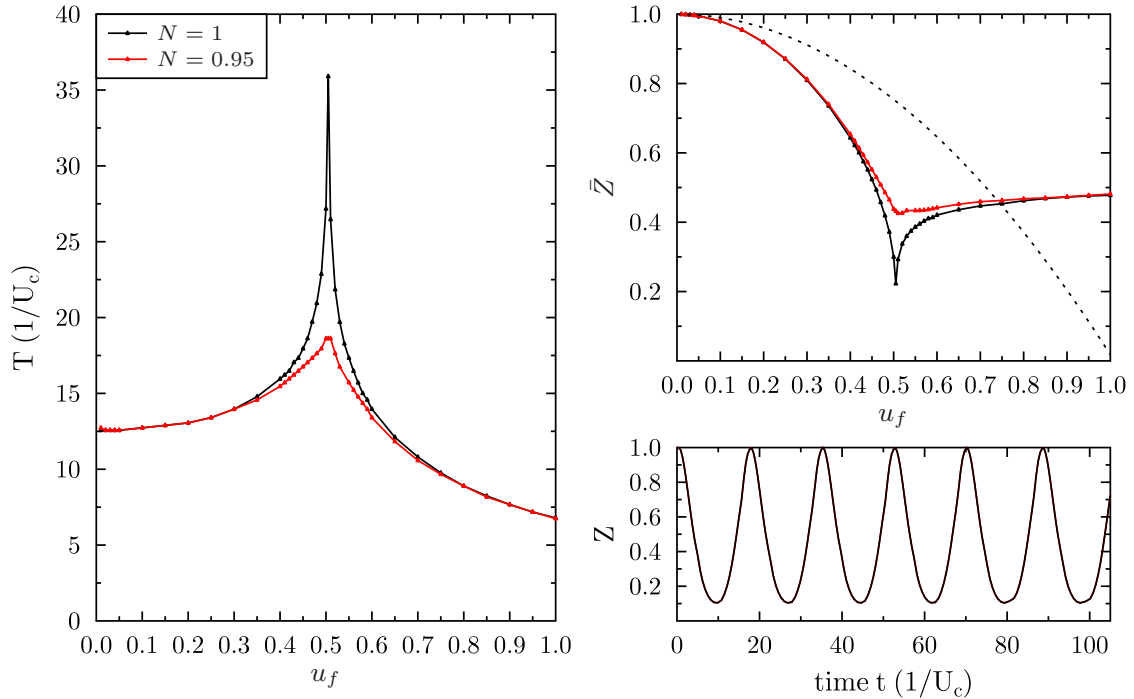


Figure 3.6: Left: Period of physical quantities with u_f at half-filling $N = 1$ and small hole doping. Top right: Time-averaged quasiparticle weight \bar{Z} at half-filling and small hole doping. Bottom right: Time-dependent quasiparticle weight at $u_f = u_{fc}^{(1)}$ with $N = 0.95$.

exponential relaxation of Z anymore to zero. This leads to the conclusion that the dynamical Mott transition is a unique feature of the half-filled case and a finite doping is enough (as in equilibrium) to render the sharp transition into a crossover.

3.5 Interaction quenches from an initial interacting state at half-filling

After considering a doping from half-filling at $u_i = 0$ another aspect is the dependence of prethermalized states and dynamical transition onto u_i . Hence half-filling is considered and all relevant physical quantities T , \bar{Z} and \bar{D} are computed also for $u_i = 0.25$. The results are depicted in Fig. 3.7. First one can compare the results to the shifted $u_i = 0.0$ ones, where the shift is equal to $\Delta u_f = 0.125$. As far as the period T is concerned the agreement is very good indicating that only the dynamical

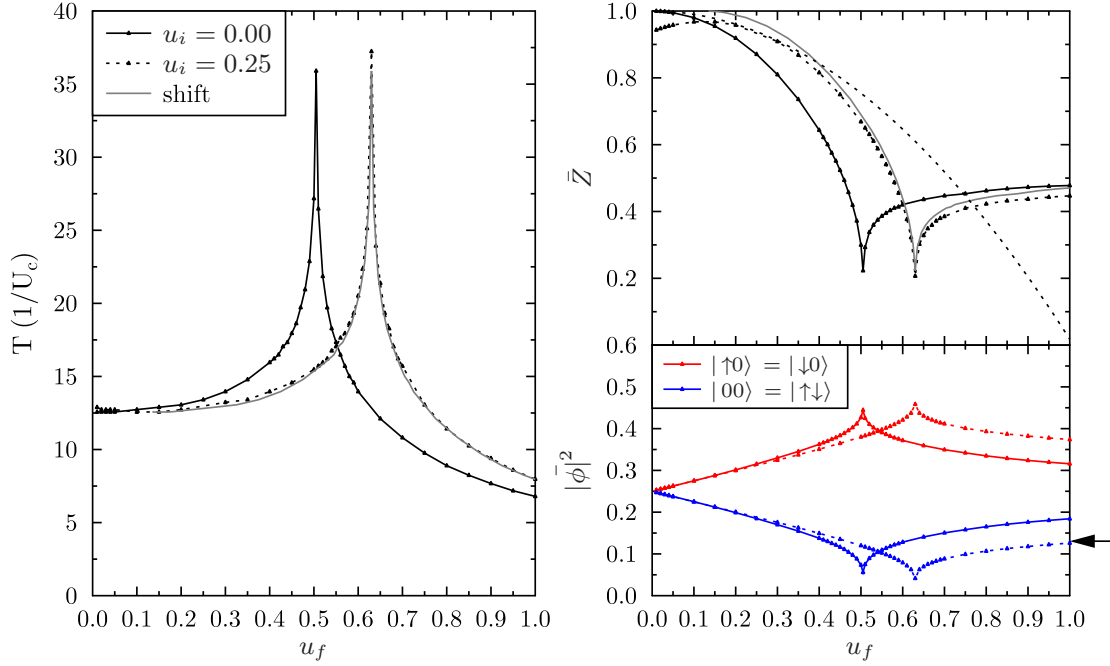


Figure 3.7: Left: Period of physical quantities with u_f and different u_i at half-filling. Top right: Time-averaged quasiparticle weight \bar{Z} at half-filling and different u_i with dotted line denoting equilibrium results. Bottom right: Time-dependent quasiparticle weight at $u_{fc}^{(1)}$ and different u_i . Shift denotes offset of $u_i = 0.0$ results by $\Delta u_f = 0.125$. Black arrow indicates strong coupling TD Gutzwiller approximation result from Eq. 3.2 evaluated at $u_f = 1.0$.

ical transition is shifted by Δu_f , but still present. The same can be seen in \bar{Z} and by the shift of the peak in \bar{D} . As the initial interaction is finite the corresponding quasiparticle weight is not exactly one, which explains the difference in slope to the shifted result in \bar{Z} . Note that results for $u_f < 0.25$ and $u_i = 0.25$ are not of interest here, as quenches should be investigated to higher interactions in this chapter. Second comparing now both u_i curves, the shift in $u_{fc}^{(1)}$ delays the strong coupling limit, but apparently roughly the same limits are reached in \bar{Z} and period. This does not hold for the time-averaged double occupation \bar{D} , which seems to be dependent on u_i in strong coupling. Conversely in weak-coupling it is independent on u_i and follows again the equilibrium results. The good agreement between equilibrium Z and $u_i = 0.25$ \bar{Z} results can be considered coincidental and solely related to the shift. To summarize, considering a weakly interacting initial state $u_i < u_{fc}^{(1)}$ leads to a shift of

$u_{fc}^{(1)}$ and with the two values computed, it could be assumed to be $u_{fc}^{(1)} = \frac{1+u_i}{2}$. The prethermalized state in weak-coupling remains unaltered, still the time-averaged double occupation follows the equilibrium results, while time-averaged quasiparticle weight is different. In strong coupling the atomic oscillation $T = 2\pi/u_f$ are delayed to higher u_f due to the shift of $u_{fc}^{(1)}$. The behavior of time-averaged double occupation is qualitatively different but matches very good the strong coupling TD-GA result from the next section, where some analytical results of previous TD-GA studies [125, 126] are mentioned. Note that the strong-coupling perturbative result for D in the prethermal state used before is only valid for the non-interacting initial state [29].

3.6 Comparison to results of time-dependent Gutzwiller approximation

In previous sections the numerical results of TD-SBMFT are shown. Now it is time to compare them to the results of TD-GA studies [125, 126]. In the following the results of Refs. [125, 126] are explained and references are made to the corresponding section or figures, which contain the appropriate TD-SBMFT results. Computations in TD-GA are done analytically, which is possible due to the high symmetry of the single-orbital Hubbard model considering only paramagnetic states. Two classical coupled differential equations of the two conjugated variables double occupation D and phase p describe the time evolution. As the Slater determinants have only a trivial time evolution, they can be assumed time-independent (compare beginning of chapter). In contrast to the equilibrium quasiparticle weight $Z(t)$ is dependent on D and on p . A critical point separating two regimes is found at $u_f = \frac{1+u_i}{2}$ (compare section 3.5). Analytical expressions for the period, long-time averaged double occupancy and quasiparticle weight written in terms of elliptic functions are retrieved. In the weak quench limit the time-averaged double occupation \bar{D} follows the equilibrium curve independent of u_i , however the time-averaged quasiparticle weight deviates from the equilibrium value following $1 - \bar{Z} = 2(1 - Z(t=0))$ (compare section 3.1 and [96]). In strong coupling $T \sim 2\pi/u_f$ matches smoothly the atomic limit (compare section 3.3 and [29]) and

$$\bar{D} \simeq D(t=0) \cdot \left(1 - \frac{u_{fc}^{(1)}}{2u_f}\right) \quad (3.2)$$

holds (compare Fig. 3.7), which equals the strong coupling perturbation result from [29]. At the critical point $u_f = u_{fc}^{(1)}$, D and Z relax exponentially with time scale $t_* = 4/Z(t=0)$ and

$$D = D(t=0) \cdot (1 - \tanh^2(t/t_*)) \quad (3.3)$$

$$Z = Z(t=0) \cdot (1 - \tanh^2(t/t_*)) \quad (3.4)$$

(compare Fig. 3.5). This leads to logarithmically divergence (in leading order) of T , \bar{D} and \bar{Z} , when approaching $u_{fc}^{(1)}$ from below or above (compare Fig. 3.7). To summarize, TD-SBMFT recovers all results from TD-GA well including position and characteristic of the dynamical transition and physical attributes of the prethermal states at weak and strong coupling. Even the comparison to analytic expressions done at the critical point in Fig. 3.7 are very good. The small deviations may be related to the fact that in TD-SBMFT a three-dimensional cubic dispersion is used, whereas in TD-GA a flat density of states is utilized.

3.7 Summary of this chapter

TD-SBMFT features the same dynamics for the single-orbital paramagnetic Hubbard model as already discovered within TD Gutzwiller approximation (TD-GA)[125, 126]. They are oversimplified meaning they lack relaxation due to neglecting quantum fluctuation in the semi-classical approach. Still TD-SBMFT is able to retrieve many interesting features. The prethermalized states at weak coupling [96] as well as in strong coupling [29] are correctly reproduced. In weak coupling the prethermalized state is characterized by thermalized double occupation but non-equilibrium quasiparticle weight. To be precise, interactions lead to twice as strong correlations in non-equilibrium as in equilibrium, when starting from the non-interacting ground state. This is a general result for an interaction quench of the Fermi sea [97]. On the strong coupling side the double occupations are far from being equal to the corresponding equilibrium value and display oscillations with period of approximate the atomic limit $2\pi/u_f$ [29]. These metastable states are wrongly predicted to have infinite lifetime. Additionally TD-SBMFT is able to capture the dynamical Mott transition first observed in TD-DMFT [29]. On the one hand the dynamical transition could be expected from the viewpoint that already in equilibrium the system undergoes a quantum phase transition, the Mott transition. On the other

hand as mentioned in [29] the pumped energy at $u_f = u_{fc}^{(1)}$ corresponds to an effective temperature of an equilibrium system, which is higher than the Mott ending point. Still comparing the energy of the quenched system to the one of the ideal perfect decoupled Mott insulator yields the right $u_f = u_{fc}^{(1)}$ in TD-SBMFT as well as in TD-DMFT [126]. This together with the fact that the transition turns into a crossover at finite doping is a clear indicator that the dynamic Mott transition is the non-equilibrium equivalent of the Mott transition. TD-SBMFT addresses well the short-time metastable states of the system both at weak and strong interaction quenches by time-averaged physical quantities. Additionally critical behavior like the dynamical phase transition is captured. Note that the notion "short-time" is relative, as it was shown that the decay of the metastable states is very sensitive to model parameters and can be substantially delayed [29, 30].

4 Metal-insulator transition in two-orbital case

In the last chapter the single-orbital Hubbard model was addressed out of equilibrium motivated by recent advances in ultracold gases and femtosecond spectroscopy of real materials. In materials orbital degrees of freedom play a central role giving rise to basic magnetic couplings like double exchange [156, 157] and superexchange [70]. To list a few examples orbital degrees of freedom induce ferromagnetism in transition metals like Fe and Ni [28, 80, 146] and multiple phenomena in transition metal oxides. Among them Ferro-orbital order in LaTiO_3 [5, 61, 108] and the Mott transition in V_2O_3 first discovered in [90]. Later it was found out that the single-orbital picture of the Mott transition does not hold in this material as the quasiparticle weight diverges only in the e_g orbital, but remains finite for the a_{1g} orbital [60]. Additionally in the series $\text{Ca}_{2-x}\text{Sr}_x\text{RuO}_4$ an orbital-selective Mott transition [4] and in one of the end members Sr_2RuO_4 unconventional spin triplet superconductivity [56] has been found. Due to these interesting effects orbital degrees of freedom recently attracted interest also in the ultracold gases community. In a first step it has been shown theoretically, how to realize orbital physics of models like the Kugel-Khomskii model [72] and Kondo Lattice model [3, 68] with ultracold fermionic atoms [12, 34]. Already some systems with orbital degrees of freedom has been experimentally realized [124, 136]. Another way is to consider also higher bands as part of the lattice formed in an ultracold gas leading to orbital-dependent phases [153]. From a model point of view already the two-orbital Hubbard model gives rise to new energy scales like the crystal field and Hund's rule coupling. The latter has not only tremendous effects regarding magnetization [6, 120], it also greatly increases correlation in paramagnetic systems. This increase of correlations leads to a substantial shift of the Mott transition to lower interaction values [66]. The crystal field is competing with Hund's rule coupling [75], while the former favors orbital ordering the latter likes to equally populate all orbitals. This competition

induces for example the high-spin to low-spin transition [149]. Additionally different bandwidths in a two-orbital framework can induce orbital selective Mott transitions [27, 55, 67, 83]. Treating of the Hund's rule coupling in a full rotational-invariant way regarding spin and orbital space is especially important not only for magnetism [6, 120], but also for paramagnetic phenomena like the Mott transition [148]. In this chapter the paramagnetic two-orbital case is investigated, where the effect of interorbital interactions and Hund's rule coupling on the dynamical Mott transition and the metastable states for weak and strong quenches discovered in the last chapter are of central interest. As mentioned ultracold gases are nowadays able to emulate orbital physics and might be able to simulate the Hubbard model used in this chapter soon.

We study interaction quenches in the canonical two-band Hubbard Hamiltonian $\mathcal{H} = \mathcal{H}^{kin} + \sum_i \mathcal{H}_i^{loc}$ with a nearest-neighbor hopping τ that defines the kinetic part \mathcal{H}^{kin} . In detail it is introduced in Eq. 2.4, which is formulated in a full rotational-invariant way regarding spin and orbital space. A three-dimensional simple-cubic dispersion is used and thus the parametrization $U' = U - 2J_H$, $U'' = U - 3J_H$ proves adequate [22, 33]. The value of the hopping τ is such that the half-bandwidth W is the energy unit. This is in contrast to the last chapter, where $U_c^{(1)}$, the Mott critical interaction value of the single-orbital Hubbard model, is used as energy unit. Again the initial state is the non-interacting ground state. In the following, the focus lies on the paramagnetic half-filled scenario and aims at general dynamic multi-orbital Mott transition mechanisms; thus antiferromagnetic fluctuations are neglected. The antiferromagnetic fluctuations will be of central interest in chapter 6. First equilibrium properties are shortly recapped in section 4.1. Afterwards interaction quenches starting from the non-interacting state are considered. In section 4.2 interaction quenches with interorbital coupling and $J_H = 0$ are investigated. Furthermore in section 4.3 the interorbital coupling with $J_H = 0.2U$ are analyzed. In the latter case the ratio is fixed before and after the quench. This means $J_{H,i} = 0.2U_i$ and $J_{H,f} = 0.2U_f$ holds, which is noted in the following as $J_H = 0.2U$. The chapter closes with a summary in section 4.4.

4.1 The equilibrium case

In the single-orbital case the Mott critical interaction is already evaluated in chapter 3. By decoupling the orbitals using $U' = U'' = 0$, $U_c^{(1)} = 2.65$ can be reproduced.

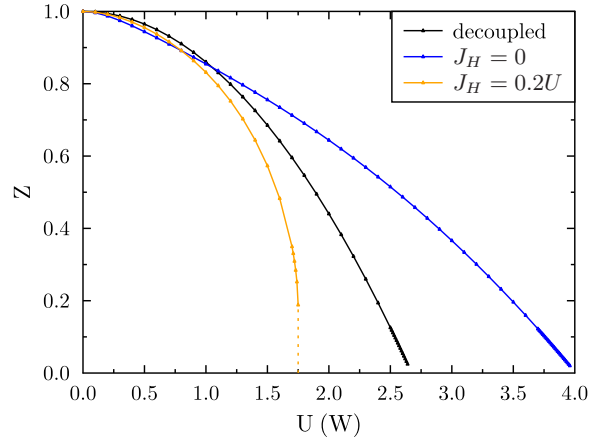


Figure 4.1: Quasiparticle weight as function of the on-site interaction U at half-filling depicting a metal insulator transition at $U_c^{(1)}=2.65$ eV for decoupled orbitals, $U_c^{(2, J_H=0)}=4.0$ eV for $J_H = 0$ and $U_c^{(2, J_H=0.2U)}=1.75$ eV for $J_H = 0.2U$.

Imposing a basic orbital coupling utilizing $U' = U'' = U$ (note $J_H = 0$) leads to a high degeneracy of local states (see Tab. 4.1). The local energy depends only on the number of electrons described by the Fock state. With finite J_H this degeneracy in the two-particle-sector is lifted as can be seen in Tab. 4.2. This decreases orbital fluctuations [55] and gives rise to local spin triplet and singlet states. Both effects greatly reduce the Mott critical value from $U_c^{(2, J_H=0)} = 4.0$ in the basic orbital coupling case to $U_c^{(2, J_H=0.2U)} = 1.75$ [66]. As a well-known fact (see for example [55]) the second order phase transition turns into a first-order one with finite J_H . The chemical potential shift $\sum_{im} (-\frac{3}{2}U + \frac{5}{2}J_H)(n_{im\uparrow} + n_{im\downarrow})$ added to the Hamiltonian renders the particle-hole symmetry obvious (see Tab. 4.1 and 4.2). Thus only six local states need to be computed, as this is the maximum number of non-degenerate eigenstates of \mathcal{H}^{loc} for finite J_H . Zero J_H has only three non-degenerate eigenstates. Furthermore the discussion of results can be restricted to the particle-sectors zero, one and two. With this in mind interaction quenches with $J_H = 0$ can be considered.

4.2 Interorbital interactions with zero Hund's coupling

Let us focus first on neglecting spin-flip and pair-hopping terms (e.g. setting $J_H = 0$). Note that still interorbital interactions are present. Then as elaborated in the last section all particle-sectors are degenerate. Therefor the presented occupation probabilities of a given particle-sector are the sum over all occupation probabilities of the corresponding states. Fig. 4.2 shows the time-dependent quasiparticle weight $Z(t)$ and occupation probability $\#p$ for different particle-sectors for the interaction quench to $U_f=0.2$. Additionally as an inset the Fourier transform of $Z(t)$ is depicted. This non-uniform Fourier transform is computed in the time interval $[0, 7500D^{-1}]$, which is also used for all upcoming Fourier transforms [35, 78]. Note that higher multiples of the relevant frequencies appear due to restricting the Fourier transform to a finite time interval. Contrary to the single-orbital case, where only one frequency shows up a second frequency ω_2 with sideband $\omega_1 - \omega_2$ appears (Fig. 4.4). This sideband is a clear indicator that ω_1 gets amplitude modulated by ω_2 . Hence ω_1 could be the frequency known from the single-orbital case and ω_2 arises due to the interorbital interactions. As in the single orbital case it is interesting to check, if there is some qualitative change in physical quantities with U_f like Z . In Fig. 4.3 $Z(t)$, $|\phi|^2$ and the Fourier transform of physical quantities are depicted at the four U_f values 0.4, 1.6, 1.8 and 2.6. Like in the single-orbital case the number of oscillations

Fock state	Particle-sector	Energy (eV)	Energy with shift (eV)
$ 0\rangle$	0	0	0
$ \uparrow 000\rangle, 0\downarrow 00\rangle$ $ 00\uparrow 0\rangle, 000\downarrow\rangle$	1	0	$-\frac{3}{2}U$
$ \uparrow\downarrow 00\rangle, \uparrow 0\uparrow 0\rangle$ $ \uparrow 00\downarrow\rangle, 0\downarrow\uparrow 0\rangle$ $ 0\downarrow 0\downarrow\rangle, 00\uparrow\downarrow\rangle$	2	U	$-2U$
$ \uparrow\uparrow\uparrow 0\rangle, \uparrow\downarrow 0\downarrow\rangle$ $ \uparrow 0\uparrow\downarrow\rangle, 0\downarrow\uparrow\downarrow\rangle$	3	$3U$	$-\frac{3}{2}U$
$ \uparrow\uparrow\uparrow\downarrow\rangle$	4	$6U$	0

Table 4.1: Local Fock states with appropriate particle-sector and energy with and without shift for orbital coupling $U = U' = U''$. Shift denotes a shift in chemical potential and is $\sum_{im} -\frac{3}{2}(n_{im\uparrow} + n_{im\downarrow})$, which is added to \mathcal{H}^{loc} . This allows to use the particle-hole symmetry.

Eigenstate	Particle-sector	Energy (eV)	Energy with shift (eV)
$ 0\rangle$	0	0	0
$ \uparrow 000\rangle, 0\downarrow 00\rangle$ $ 00\uparrow 0\rangle, 000\downarrow\rangle$	1	0	$-\frac{3}{2}U + \frac{5}{2}J_H$
$ \uparrow 0\uparrow 0\rangle, 0\downarrow 0\downarrow\rangle$ $\frac{1}{\sqrt{2}}(\uparrow 00\downarrow\rangle + 0\downarrow\uparrow 0\rangle)$	2 (triplet)	$U - 3J$	$-2U + 2J_H$
$\frac{1}{\sqrt{2}}(\uparrow 00\downarrow\rangle - 0\downarrow\uparrow 0\rangle)$ $\frac{1}{\sqrt{2}}(\uparrow\downarrow 00\rangle - 00\uparrow\downarrow\rangle)$	2 (singlet)	$U - J$	$-2U + 4J_H$
$\frac{1}{\sqrt{2}}(\uparrow\downarrow 00\rangle + 00\uparrow\downarrow\rangle)$	2 (singlet)	$U + J$	$-2U + 6J_H$
$ \uparrow\uparrow 0\rangle, \uparrow\downarrow 0\downarrow\rangle$ $ \uparrow 0\uparrow\rangle, 0\downarrow\uparrow\rangle$	3	$3U - 5J_H$	$-\frac{3}{2}U + \frac{5}{2}J_H$
$ \uparrow\uparrow\uparrow\rangle$	4	$6U - 10J_H$	0

Table 4.2: Eigenstates and energy eigenvalues in atomic limit with finite J_H [77]. Energy eigenvalues are denoted with and without shift. Shift denotes a shift in chemical potential and is $\sum_{im}(-\frac{3}{2}U + \frac{5}{2}J_H)(n_{im\uparrow} + n_{im\downarrow})$, which is added to \mathcal{H}^{loc} . This allows to use the particle-hole symmetry.

visible in $Z(t)$ and $|\phi|^2$ first *decreases* and then *increases* by increasing U_f , going from $U_f = 0.4$ to $U_f = 1.6$ and then from $U_f = 1.8$ to $U_f = 2.6$, respectively. But in contrast to the single-orbital case there is an intermediate *region* of U_f showing other qualitative behavior. There a continuous and broad Fourier spectrum can be observed. This hints towards a qualitative different physics in three regions, which are called from now on weak-coupling (I), precursor and critical region (II) and strong-coupling (III). Region II is uniquely characterized by a broad and continuous Fourier spectrum. To investigate these three regions, the same physical quantities, that proved helpful in the single-orbital case are considered again, namely period T , time-averaged \bar{Z} and local occupations shown in Fig. 4.4 (compare Fig. 3.4). Orbital decoupled case $U' = U'' = 0$ and coupled case $U' = U'' = U$ are compared, too. These results will be used to interpret the three regions, starting with the weak-coupling one.

4.2.1 Weak-coupling

Already from lowest U_f values on, there are two instead of one dominant frequencies/periods (Fig. 4.2 and 4.4). Because $T_1 = T_{1S}$ holds in the limit $U_f \rightarrow 0$, T_1 seems to be the period already known from the single-orbital case, which gets modified by interorbital interactions. Additionally the interorbital interactions give rise

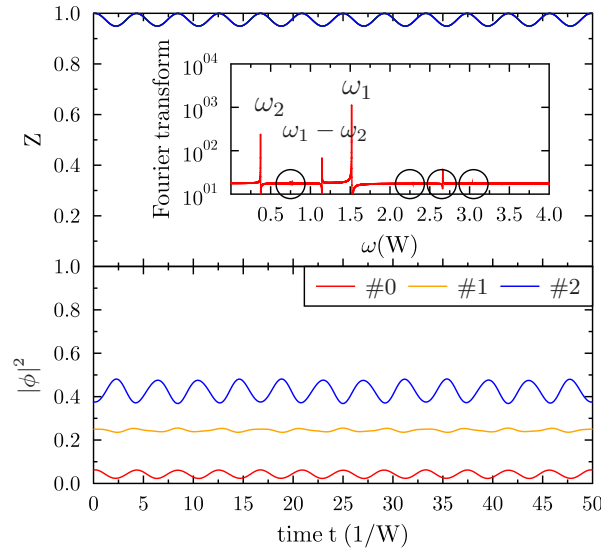


Figure 4.2: QP weight $Z(t)$ and occupation probability $\#p$ of local sectors with particles $p=0,1,2$ for the interaction quench to $U_f=0.2$. Dotted lines denote period of local states oscillations. The inset shows the Fourier transform (absolute value of Fourier coefficients in logarithmic units) of $Z(t)$.

to a new period T_2 starting from approximately six times the period of T_1 . Like in the single-orbital case time-averaged local slave boson occupation probabilities $|\phi|^2$ are the same as equilibrium ones, but \bar{Z} is substantially different from the equilibrium counterpart. As an additional common feature the relation $1 - \bar{Z} = 2(1 - Z(t=0))$ holds with an overall good agreement, but increasing deviations close to the critical region. Interestingly, just before entering the critical region the agreement to the mentioned relation becomes *better*, when the interorbital interacting systems is weaker correlated than the decoupled one. The level diagram in Fig. 4.5 shows in this region quite substantial development from one frequency and sidebands to a splitting of sidebands followed by ground state and excited state having sidebands. Furthermore T_2 shows huge changes like splitting into two periods and deviations of factor 5 inside this region. Despite these two last aspects the prethermalized state can be described in the same way like in the single-orbital model [29, 96] in a very good approximation. The defining aspects of equilibrated occupation probabilities and non-equilibrated quasiparticle weight as $1 - \bar{Z} = 2(1 - Z(t=0))$ are still in place. Approaching $U_f = 1.15$ T_2 diverges and a drop in \bar{Z} is visible signaling critical behavior.

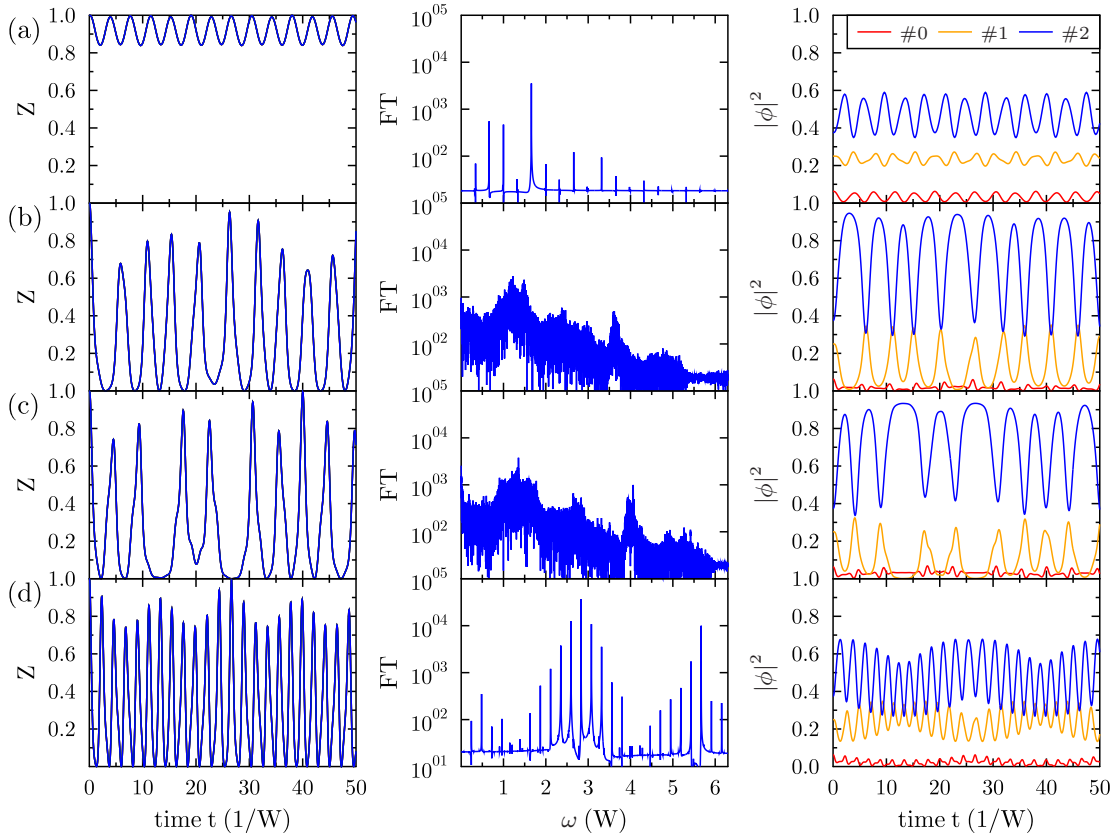


Figure 4.3: Time-dependent quasiparticle weight Z (left), Fourier transform of physical quantities (middle) and slave-boson occupation probability $|\phi|^2$ (right) for $U_f = 0.4, 1.60, 1.80$ and 2.60 in (a), (b), (c) and (d), respectively.

4.2.2 Precursor and critical region

A better understanding of the dynamical transition can be gained by an Ising-spin representation of the model that is fully equivalent to slave-bosons and reads [160]

$$\mathcal{H}_S = -\frac{J}{S^2} \frac{2}{r} \sum_{\langle i,j \rangle} S_{ix} S_{jx} + \frac{U}{2} \sum_i (S_{iz})^2 \quad . \quad (4.1)$$

Here the spin $S=2$ is used and $r=6$ is the lattice coordination number, while $-J=-2/3$ is the energy per site of the non interacting ground state. Within mean-field, i.e., assuming a variational wave function $\prod_i |\Phi(S_{iz})\rangle$, the spin model above becomes identical to the slave boson mean-field theory at half-filling if $|\Phi(S_{iz})\rangle =$

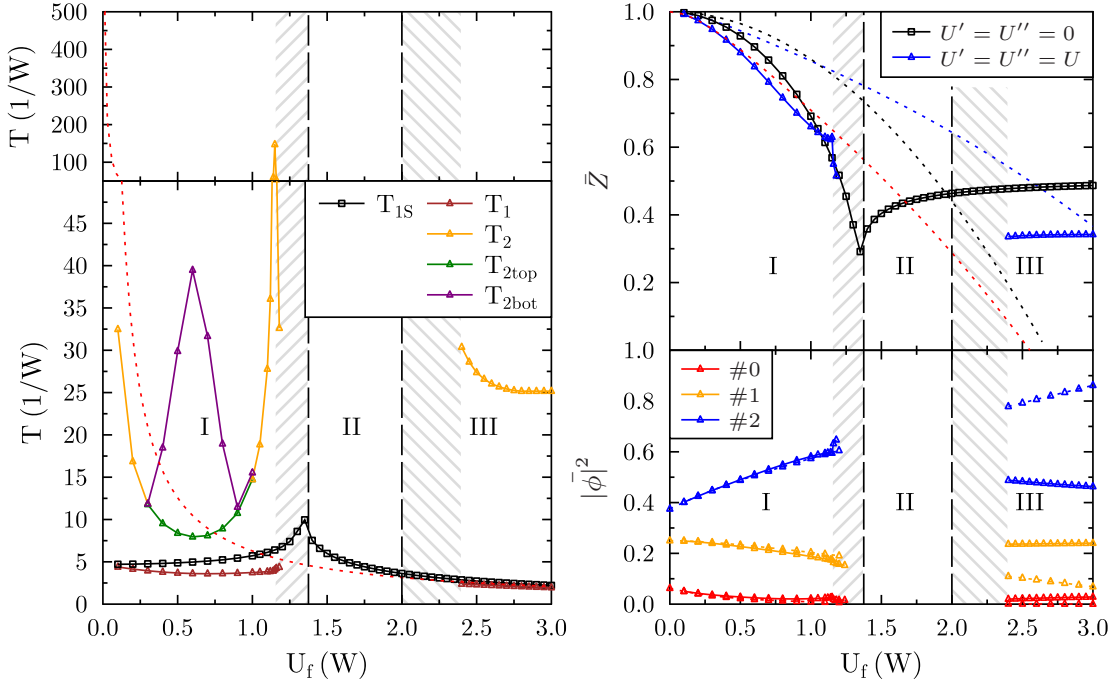


Figure 4.4: Left: Period of physical quantities with U_f . Without interorbital interaction only T_{1S} shows up, else the others. Red dotted lines denote period $2\pi/U_f$ from single-orbital strong-coupling regime [29]. Top right: time-averaged \bar{Z} as function of U_f with interorbital interactions (blue) and without (black). Dotted lines denote equilibrium values. Red dotted line depicts $1 - \bar{Z} = 2(1 - Z(t=0))$ for values with interorbital interaction. This relation is known from single orbital weak-coupling expansion [96]. Bottom right: Local occupation probabilities with corresponding equilibrium values as dotted lines. Dashed lines separate three regions (see text) and grey hashed area marks precursor behavior. This figure is the two-orbital $J_H = 0$ equivalent of Fig. 3.4.

$\sum_{p=0}^4 \phi_p |S_{iz} = p - 2\rangle$, where ϕ_p is the original slave boson at site in particle-sector p . Because of half-filling, $\phi_p = \phi_{4-p}$, so that $\langle S_{iz} \rangle = 0$. Metallic coherence is signaled in the spin model by a finite Ising order parameter $\langle S_{ix} \rangle = \Re \left[\sqrt{6} (\phi_3^* \phi_2 + \phi_2^* \phi_1) + 2(\phi_4^* \phi_3 + \phi_1^* \phi_0) \right] \equiv M_1 + M_2$, while the incoherent Mott insulator has $\langle S_{ix} \rangle = \langle S_{iz}^2 \rangle = 0$. The initial non-interacting state is characterized by $\langle S_{ix} \rangle = 2$ and $\langle S_{iz}^2 \rangle = 1$, i.e. energy per site $E = -2/3 + U/2$, conserved during the unitary evolution. If, like in the single-band case [125], the dynamical Mott transition is assumed to occur when the energy equals that of the Mott insulator, i.e., $E = 0$, then $U_{fc}^{(2, J_H=0)} = 4/3$ is expected. This is

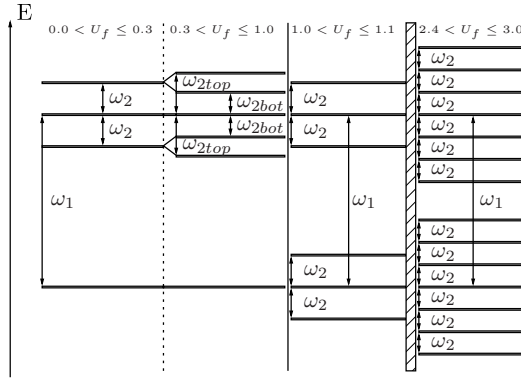


Figure 4.5: Level diagram for the active frequencies in the case $U'=U''=U$ within the different regimes dictated by U_f .

also equal to the single-band value for the dynamical Mott transition. In fact, this argument predicts one and the same value $U_{fc}^{(N, J_H=0)}=4/3$ for any N -band simple, i.e., $J_H=0$, Hubbard model at half-filling, indeed close to the numerical value. Figure 4.6 exhibits the quantity $\overline{\langle S_x \rangle}$ revealing characteristics of an order parameter. In the case of vanishing interorbital interactions equivalent to considering a single-orbital model on the left side of Figure 4.6, there are two regions as also revealed in chapter 3. Weak-coupling (I) with finite $\overline{\langle S_x \rangle}$ describing metallic behavior and strong-coupling (III) with zero value signaling insulating properties with $U_{fc}^{(1)}=1.325=U_c^{(1)}/2=u_{fc}^{(1)}$. The contributions \overline{M}_1 and \overline{M}_2 depict the time-averaged correlations between different particle-sectors. Similar to equilibrium an increasing U_f favors the transition towards a Mott insulator, decreasing $\overline{\langle S_x \rangle}$. Both contributions decrease linearly with increasing interaction, with \overline{M}_1 being the larger contribution due to the filling induced higher occupation of the two-particle-sector. This picture is substantially different in the case with interorbital interactions shown in the right panel of Figure 4.6. At $U_f=0.1$ \overline{M}_1 and \overline{M}_2 are nearly the same as in the decoupled case, but increasing the interaction with interorbital terms effects \overline{M}_1 greatly in contrast to \overline{M}_2 , which is nearly unaffected in weak-coupling. This leads to a crossover of these contributions. It seems as the interorbital terms (note that $J_H = 0$) on the one hand pronounce the occupation dependence of \overline{M}_1 , but on the other hand lead to an unnoticeable occupation dependence of \overline{M}_2 . At $U_f = 1.15$ a precursor regime starts with increasing fluctuations visible in \overline{M}_1 and \overline{M}_2 . In the region $1.375 \leq U_f \leq 2.0$ the order parameter vanishes only after averaging over a longer time, which is shown in the inset. This extended Mott insulating transition (EDMT) is characterized by

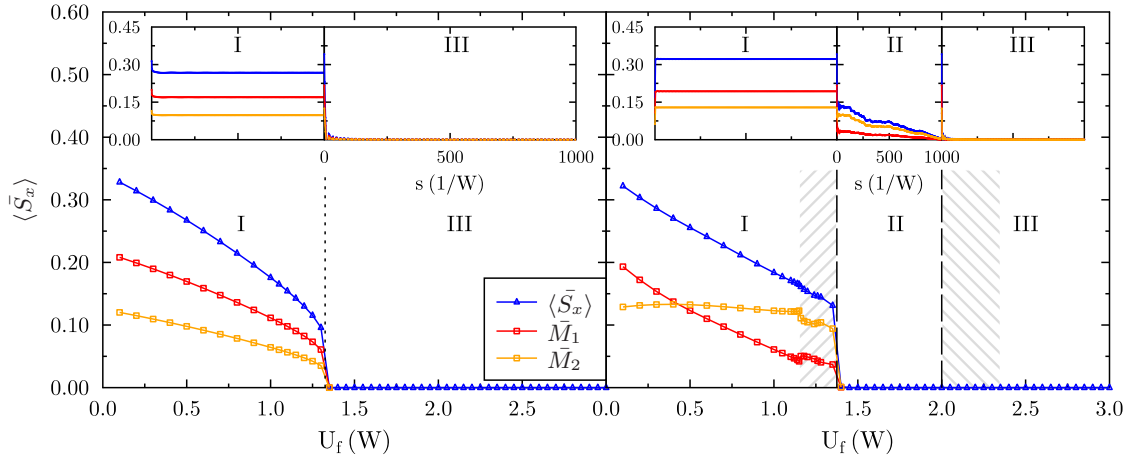


Figure 4.6: Order parameter $\langle \bar{S}_x \rangle$ without interorbital couplings (left) and with interorbital couplings ($J_H = 0$) (right). Inset shows $\langle \bar{S}_x \rangle (s)$ (see Eq. 3.1) in the three different regions. The decoupled two-band case (left) stabilizes only in regions I and III (divided by the vertical dashed line). Region II appears with interorbital terms. The precursor regime is visualized by the gray hashed area.

noisy Fourier spectra. Note that in equilibrium the Mott critical value is increased (from 2.65 to 4.0) by including interorbital interactions with $J_H = 0$ due to the high induced degeneracy of local states. Similarly in the non-equilibrium case the insulating strong-coupling region (III) appears for higher U_f with the EDMT between pure metallic and pure insulating non-equilibrium state.

4.2.3 Strong-coupling

In the strong-coupling limit T_1 approaches like T_{1S} the value $2\pi/U_f$ measured for oscillations in the strong-coupling single-orbital case [29]. This is an intuitive result, as it is also the period of the time propagator in the atomic limit. T_2 saturates at ~ 25 $1/W$, which equals 0.25 W . Additionally the slave boson occupations $|\phi|^2$ approach their initial values, where at $U_f = 3.0$ only two-particle-sector has not yet reached it. Furthermore the amplitude of $|\phi|^2$ decreases in the strong-coupling limit with higher U_f (see Fig. 4.3). Thus for $U_f \rightarrow \infty$ locally frozen dynamics are induced, which are trapped in the initial state. Furthermore \bar{Z} saturates due to the interorbital couplings not at 0.5 but at 0.33.

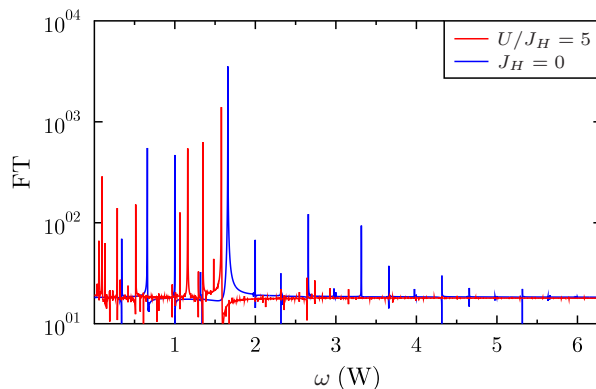


Figure 4.7: Comparison of Fourier transforms at $U_f = 0.4$ with and without finite Hund's rule coupling.

4.3 Interorbital interactions with finite Hund's coupling

Turning to the case $J_H = 0.2U$ renders the whole picture more complicated. Instead of one low frequency multiple arise (see Fig. 4.7). The following considerations are limited to the highest and lowest dominant frequency determined at $U_f = 0.1$. It is assumed that both frequencies evolve continuously with U_f . Then period T , time-averaged \bar{Z} and time-averaged $|\bar{\phi}|^2$ are investigated for $U_f/J_H = 5$ shown in Fig. 4.8. Note that with finite J_H the previous degenerate two-particle-sector turns into two singlets and one triplet. The former having the energy $U - J_H$ (multiplicity 2) and $U + J_H$ (multiplicity 1). The latter yields $U - 3J_H$ with multiplicity 3. Additionally the finite J_H leads to a drastically increase in correlation shifting the Mott critical interaction from 4.0 to 1.75 in equilibrium. In the following weak-coupling, critical region and strong-coupling are discussed.

4.3.1 Weak-coupling

In comparison to $J_H = 0$ (Fig. 4.4) the highest period has shifted from the average value ~ 20 to ~ 100 . This is in line with the fact that previously the interorbital interaction scaled with $U' = U'' = U$, where now the lowest energy scale are spin-flip and pair-hopping, which scale with $J_H = U/5$. As already shown for $J_H = 0$, T_1 substantially deviates from the single-orbital values for moderate U_f . Still the single-orbital picture of the prethermalized state holds. Time-averaged

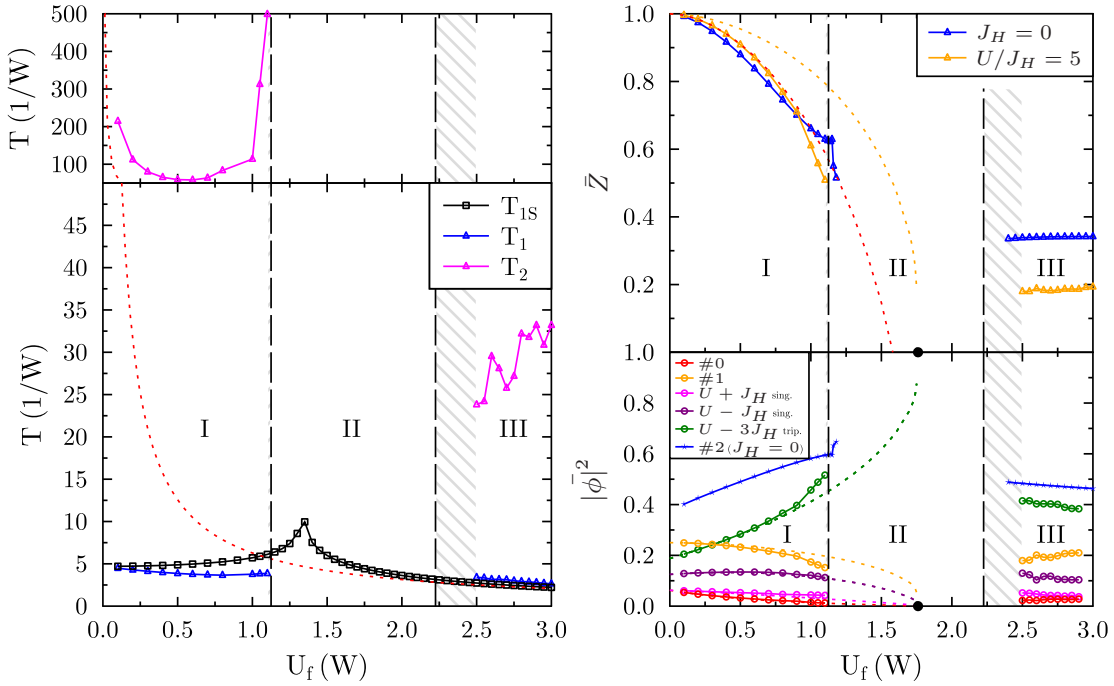


Figure 4.8: Left: Period of physical quantities with U_f and $U_f/J_H = 5$ (see text). Red dotted lines denote period $2\pi/U_f$ from single-orbital strong-coupling regime [29]. Top right: Time-averaged \bar{Z} as function of U_f with $J_H = 0.2U_f$ (orange) and with $J_H = 0$ (blue). Dotted lines denote equilibrium values with $J_H = 0.2U_f$. Red dotted line depicts $1 - \bar{Z} = 2(1 - Z(t=0))$ for values with $J_H = 0.2U_f$. This relation is known from single orbital weak-coupling expansion [96]. Bottom right: Time-dependent local occupation probabilities (straight lines) and equilibrium values (dotted lines). Dashed lines separate three regions (see text) and grey hashed area marks precursor behavior. Black circle marks Mott critical interaction in equilibrium. This figure is the two-orbital $J_H \neq 0$ equivalent of Fig. 3.4.

local occupation probabilities are equal to their equilibrium values. Furthermore $1 - \bar{Z} = 2(1 - Z(t=0))$ [96] is fulfilled. This is quite astonishing as the impact of J_H is quite severe by giving rise to (local) singulet and triplet formation, as well as a very low energy scale. The deviations in \bar{Z} between zero J_H and non-zero case are overall quite small, but become bigger when approaching the critical region. A notable change is the smoothing of the abrupt decrease of \bar{Z} close to the critical region with finite J_H . Additionally the low frequency T_2 shows diverging tendencies similar to the T_2 in the $J_H = 0$ case.

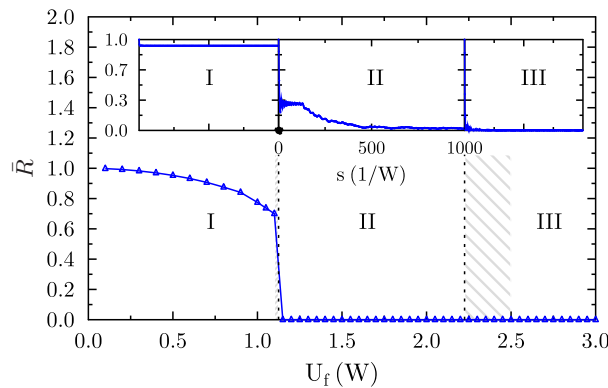


Figure 4.9: Time-averaged diagonal renormalization \bar{R} for $U/J = 5$. Insets show $\bar{R}(s)$ in the three different regions.

4.3.2 Precursor and critical region

It is important to note that the EDMT is not an artifact of $J_H = 0$. The mapping to a spin model proves elusive to add an additional point of view to the picture, but is not needed to access an order parameter. In fact, the renormalization matrix depicted in Fig. 4.9 shows the same characteristics. Comparing Fig. 4.6 and Fig. 4.9 introducing a finite Hund's coupling *broadens* the EDMT (from $1.375 \leq U_f \leq 2.0$ to $1.125 \leq U_f \leq 2.225$).

4.3.3 Strong-coupling

As shown in Fig. 4.8, T_1 approaches again the atomic-like oscillation limit $2\pi/U_f$, known already from the single-orbital [29] and $J_H = 0$ case. The other defining characteristic of the large U_f metastable state in the single-orbital case is the approaching of initial values regarding the time-dependent $|\phi|^2$ leading to frozen doublon dynamics. The argument is that for high U doublons have a very high energy compared to the kinetic energy, so a decay would need many-particle scattering processes [119]. However with interorbital interaction this does not hold for all local states. Without Hund's coupling it is the two particle-sector, which shows highest deviations from its initial state at the considered maximum interaction quench (see Fig. 4.4). With finite J_H as can be seen in $|\phi|^2$ for $U_f = 3.0$ (Fig. 4.8) all local states are already quite close to their initial values with small amplitudes (close to frozen dynamics), but not the triplet (see Fig. 4.10). The scattering channels between singulets and triplets does not scale with U , but with $J_H = U/5$ and the triplet is the lowest

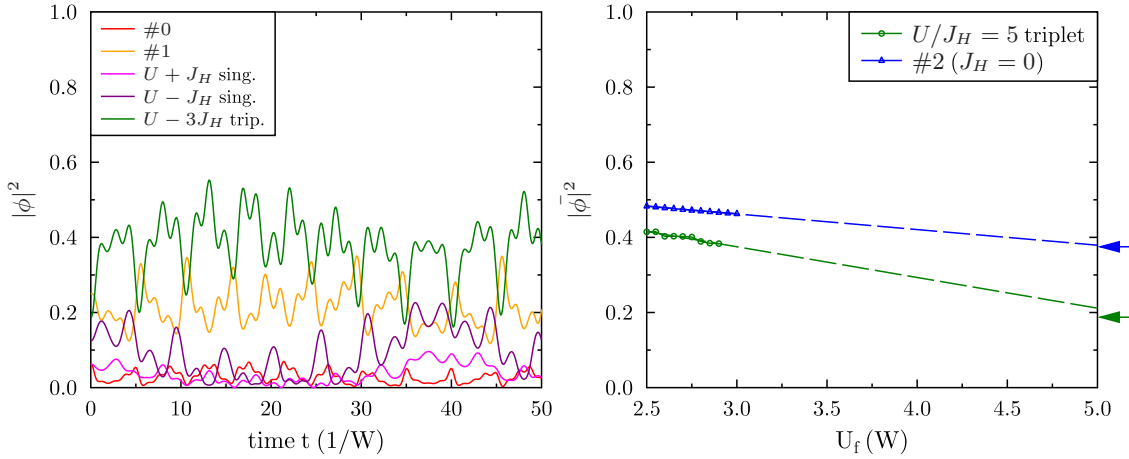


Figure 4.10: Time-dependent local occupation probability $|\phi|^2$ at $U_f = 3.0$ with $J_H = 0.2U$ (left). Right panel displays time-averaged triplet occupation ($J_H = 0.2U$) compared to twoparticle-sector for $J_H = 0$ and linear fits as dashed lines. Colored arrows mark equilibrium values.

energy state. This means the triplet is the highest occupied state at large U_f and the decrease with U_f is smaller. This results in a delay of frozen dynamics for the triplet to higher U_f compared to the doublons in the single-orbital case or the two-particle-sector in the $J_H = 0$ case (see Fig. 4.10). While the twoparticle-sector for $J_H = 0$ has reached its initial occupation already at $U_f = 5.0$, the triplet needs $U_f > 5.0$ to reach it. Therefore J_H discriminates the triplet state from all other local states regarding the freezing of dynamics in strong-coupling. The fluctuations and linear increase of T_2 could be related to the unfrozen triplet, as in the $J_H = 0$ case with local states closer to the frozen dynamic limit the higher period is already saturated (compare Fig. 4.4 and 4.8). Note that the strong-coupling metastable state is not similar to the equilibrium insulating state. While in the former finite singlet occupation are visible, the latter is characterized by a vanishing singlet and an only occupied triplet state.

4.4 Summary of this chapter

This chapter deals with an interaction quench in the canonical two-orbital Hubbard model at half-filling restricted to paramagnetic states. The non-interacting state is the initial state. When weak interaction quenches are applied the time-averaged

local occupation probabilities coincide with the equilibrium values. Furthermore the non-equilibrium time-averaged quasiparticle weight is reduced twice with interaction compared to the equilibrium value. These are the characteristics of the single-orbital weak-coupling metastable state (prethermalization state) and even with interorbital interactions, they still apply with or without J_H . This is surprising as interorbital interactions lead to one ($J_H = 0$) or multiple ($J_H \neq 0$) low frequencies, which already for $J_H = 0$ and weak quenches show frequency splitting meaning non-trivial behavior. Additionally the high frequency known from the single-orbital case is still present, but is only equal to the single-orbital values for small interaction quenches. The deviation to single-orbital values increases with stronger quenches. Increasing the interaction quench to intermediate values leads not to a sharp dynamical Mott transition, but a broadened extended dynamic Mott transition (EDMT). In the finite J_H case results are focused on the lowest and highest dominant frequency determined at small interaction. As a continuous dependence of these two frequencies on the final interaction is assumed, they can easily be traced. With $J_H = 0$ interorbital interactions have the energy scale U , however with finite J_H the lowest energy scale is J_H introduced by spin-flip and pair hopping. As the lowest frequency decreases by the factor J_H/U , when going from the former to the latter case, a clear relation between lowest frequency and lowest energy scale of interorbital interactions can be extracted. A divergence of the lowest frequency signals the transition into the EDMT. The EDMT is characterized by a low frequency switching between metallic and insulating state, so the insulating state appears only after an extended period of time. Another indicator are the noisy Fourier spectra. Compared to vanishing Hund's coupling a broadening of the EDMT appears with finite J_H . For even stronger interaction quenches a clear structure of Fourier spectra can be derived again and the insulating state appears already after small times giving rise to a strong-coupling region. In this region the highest frequency approaches independent of J_H the atomic limit $U_f/2\pi$ like in the single-orbital case. Similarly to the single-orbital case time-averaged local occupation probabilities approach their initial value and freeze out then (vanishing amplitude). In contrast to the orbitally decoupled case there is effectively not only one local state and the interaction quench scale to reach the initial state depends on the local state. The highest occupied state reaches its initial state at considerably higher interaction quenches than other states. In the $J_H = 0$ case this affects the two-particle-sector and for finite Hund's coupling the local triplet state. As the finite J_H triplet needs an even higher U_f than

the two-particle-sector in the $J_{\text{H}} = 0$ case one can see that the introduction of an additional low energy scale delays the freezing of the highest occupied state. In the end the highly affected regions by interorbital coupling are the former dynamical Mott transition and the strong-coupling regime.

5 Charge fluctuations in a realistic model for V_2O_3

Vanadium sesquioxide (V_2O_3) has fascinated researchers for decades [41, 42, 46, 89, 91, 114] and the reason for its popularity is mainly the Metal insulator transition with Chromium doping, which is the archetypical Mott transition in the Hubbard model picture (see Fig. 5.1). For the Mott insulating state only three orbitals are

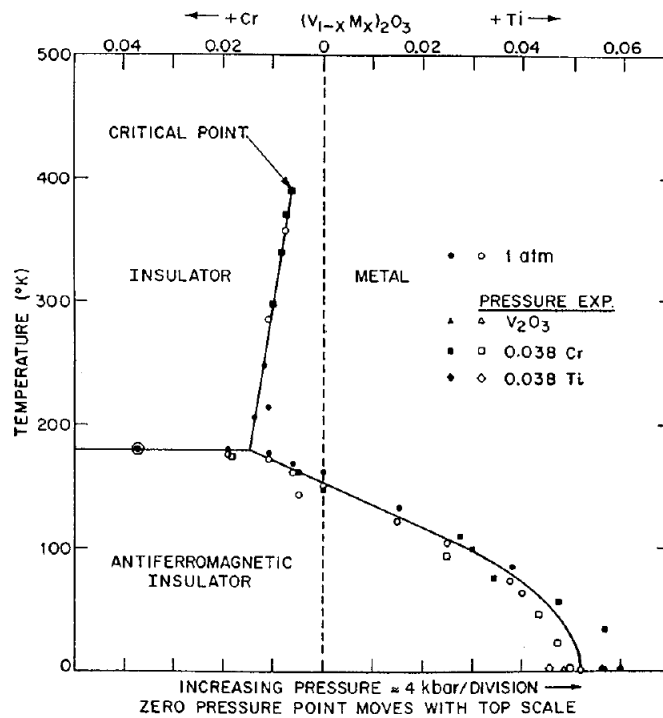


Figure 5.1: Experimental phase diagram of V_2O_3 [89, 91].

important, one a_{1g} and two energy degenerate e'_g [46]. The characteristics of the Mott insulating state in V_2O_3 are a non-occupied a_{1g} orbital with two electrons for the other two e'_g orbitals per atom [114]. A recent study showed that the Mott insulating

character of V_2O_3 in equilibrium is driven by a correlation enhanced crystal field splitting between a_{1g} and e'_g orbital [114]. Additionally up to now unpublished experimental results show that a femtosecond laser excitation is able to turn the unoccupied a_{1g} orbital in the Mott insulating ground state to a finite occupied state [40]. On this way V_2O_3 is turned into a metal. This chapter is intended as a small example that TD-SBMFT is not limited to model calculations, but can also describe non-equilibrium physics in real materials. The focus lies on a simple modeling of the effect of the laser excitation by a crystal field quench.

5.1 Setting up the realistic model

Details to the equilibrium modeling of paramagnetic V_2O_3 can be found in [39], here just some important facts are stated. The crystal structure is depicted in Fig. 5.2. Density functional theory (DFT) leads to the following density of states (DOS)

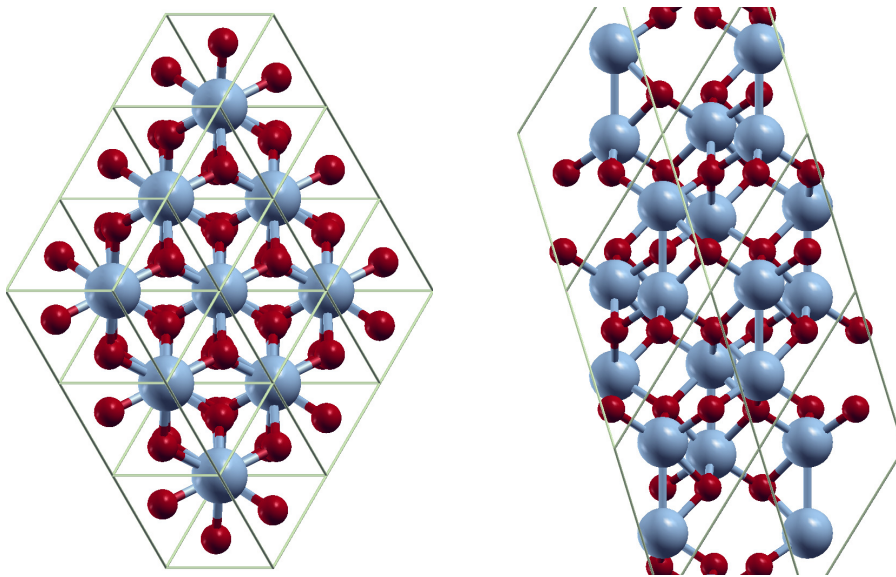


Figure 5.2: Crystal structure of paramagnetic V_2O_3 seen along the z -axis (left) and along the y -axis (right). The larger blue spheres symbolize Vanadium, the smaller red spheres symbolize Oxygen atoms. Images taken from [39].

depicted in Fig. 5.3. The challenge is now to find a minimum number of orbitals, which describe the low energy part of this DOS sufficiently. Important is that the low energy part of the DOS can not be simply described by cubic harmonics as

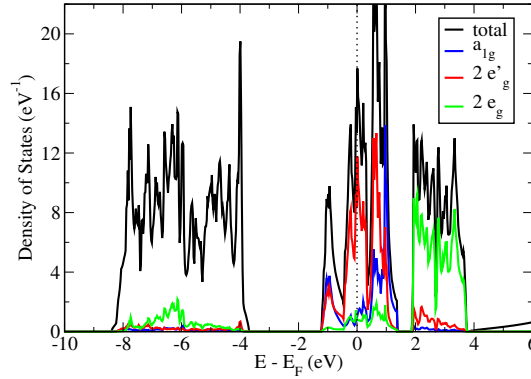


Figure 5.3: Total one-particle density of states of V_2O_3 from LDA at the equilibrium volume and local density of states of Vanadium projected onto symmetry-adapted $l = 2$ cubic harmonics. Image taken from [39].

nearly all of them have non-negligible weight. Instead, these orbitals have to be projected [2] onto the following effective t_{2g} orbitals, which have the same symmetry as normal t_{2g} orbitals [41]

$$\begin{aligned}
 t_{2g}^1 &= d_{3z^2-r^2} & t_{2g}^2 &= \sqrt{\frac{2}{3}} \cdot d_{xy} \pm \sqrt{\frac{1}{3}} \cdot d_{xz} \\
 t_{2g}^3 &= -\sqrt{\frac{2}{3}} \cdot d_{x^2-y^2} \mp \sqrt{\frac{1}{3}} \cdot d_{yz}.
 \end{aligned} \tag{5.1}$$

The signs in Eq. 5.1 are related to the multiple Vanadium atoms in the unit cell. In the following t_{2g}^1 is named as a_{1g} and the other t_{2g}^2 and t_{2g}^3 are two energy degenerate e'_g . These three orbitals are also depicted in Fig. 5.3 and reproduce the low energy DOS quite well. The unit cell of the crystal structure (Fig. 5.2) can be modeled as four symmetry-equivalent Vanadium atoms with each having two electrons and three orbitals, one a_{1g} and two e'_g .

5.2 Non-equilibrium results

The multi-orbital Hubbard model with Hubbard U and Hund's coupling J_H is used depicted in Eq. 2.4. The hopping term τ is computed by the DFT results and includes many hopping orders (not only nearest-neighbor) to get a close to material dispersion. To model the Mott insulating ground state, which will be the initial state of the non-equilibrium study, the parameters $U = 5.0$ and $J_H = 0.93$ taken

$\Delta_{add}(eV)$	occupation (e'_g)	occupation (a_{1g})	Z (e'_g)	Z (a_{1g})
0.00	0.38	0.24	0.34	0.56
0.35	0.46	0.08	0.14	0.61

Table 5.1: Orbital occupation and quasiparticle weight Z at $U=5.0$ and $J_H=0.93$ depending on the additional crystal field Δ_{add} . $\Delta_{add} = 0.00$ means only DFT crystal field is used.

from a previous study [46] are used. As the ground state of Cr-doped V_2O_3 is a Mott insulator with zero a_{1g} orbital occupation [114], the Hamiltonian parameters has to be chosen accordingly. For this reason the DFT crystal field is increased by an additional crystal field Δ_{add} , which mimics the expected correlation enhancement [114]. As depicted in Tab. 5.1, $\Delta_{add} = 0.35$ is inducing a state with very small quasiparticle weight of 0.14 in e'_g and a near vanishing occupation of 0.08 in the a_{1g} orbital, so very close to the real ground state. Note that SBMFT can only describe a paramagnetic close to Mott insulating state, not the Mott insulating state itself [77]. The idea is to quench $\Delta_{add}=0.35$ to lower values to induce charge fluctuations

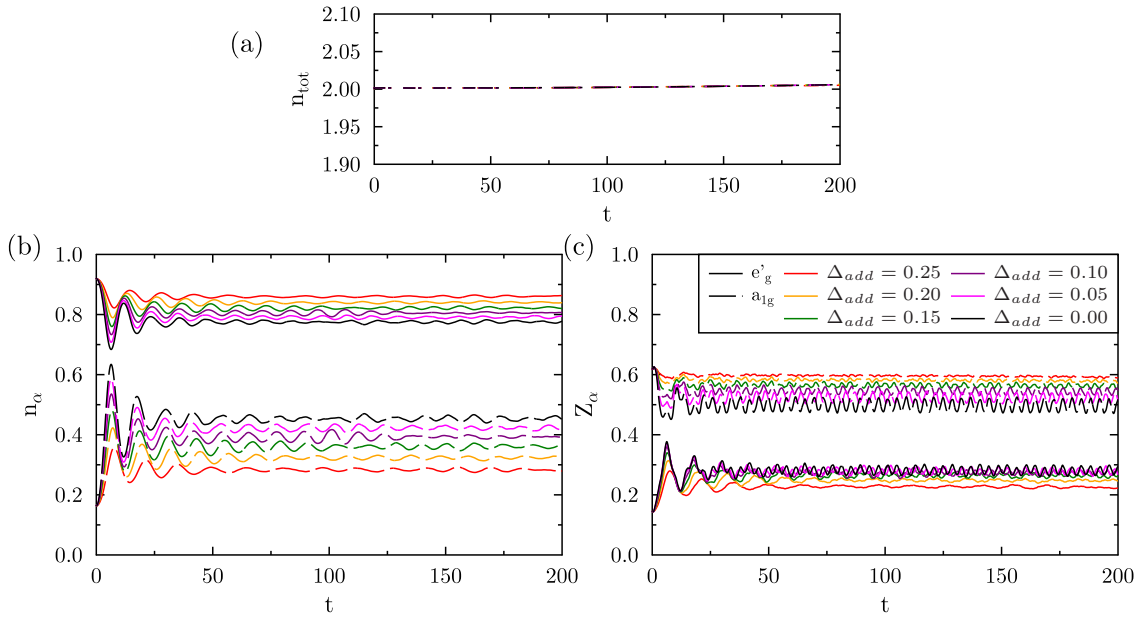


Figure 5.4: Impact of quench in additional crystal field $\Delta_{add} \equiv \Delta_{add,f}$ (initial value 0.35) on time-dependent orbital occupation and quasiparticle weight. (a) total electron occupation of one atom n_{tot} , (b) orbital occupation n_α and (c) quasiparticle weight Z_α .

and with these a metallic state displaying an occupation of the a_{1g} orbital greater than the equilibrium value of 0.08. The results are depicted in Fig. 5.4. As expected the quench to lower crystal fields induces time-dependent charge transfer from the e'_g to the a_{1g} orbital as the total number of electrons per atom is unchanged. Shortly after the quench the orbital occupations displays large fluctuations, which quickly stabilizes to a quite time-independent value. The same behavior can also be seen in the quasiparticle weight Z , where the increased number of electrons in the before almost empty a_{1g} orbital leads to an increase of correlations. Similarly the decrease of electrons in the e'_g orbital induces a decrease of correlations. This proportional relation is expected as both orbitals are less than half-filled. Note that a higher $\Delta_{add,f} - \Delta_{add}$ increases the fluctuations shortly after the quench and the charge transfer between the orbitals.

5.3 Summary of this chapter

This chapter focuses on the Mott insulating state of V_2O_3 . The low energy density of states can be reproduced using a projection on three effective t_{2g} orbitals in a four atom unit cell. The three orbitals are two energy degenerate e'_g and one a_{1g} . The Mott-insulating state has the characteristic property of vanishing quasiparticle weight and vanishing a_{1g} orbital occupation. SBMFT is able to approximate this state by a finite but very small quasiparticle weight and very small occupation in the a_{1g} orbital. To reach this, a three-orbital Hubbard model with interaction parameters of a previous study [46] and an increased crystal field with respect to the DFT value is considered. The crystal field increase is expected as correlations enhance the crystal field [114]. An up to now unpublished experiment uses a femtosecond laser to induce a Mott insulating to metal transition in which course the a_{1g} orbital obtains a finite occupation [40]. Increased occupation in the a_{1g} orbital is induced by quenching the correlation enhanced crystal field splitting to lower values within TD-SBMFT. This leads to a charge transfer from the e'_g orbitals to the a_{1g} orbital decreasing correlations e.g. a weaker correlated metallic state. One should stress the fact that TD-SBMFT is able to handle this complex realistic model. The complexity is expressed by the four (symmetry-equivalent) atoms per unit cell and three orbital per atom. For this close to material model results with excellent numerical quality are derived. An example is the well conserved total charge during the course of the time evolution.

6 Impact of hole doping on magnetic fluctuations in the t_{2g} -shell

The importance of orbital degrees of freedom and the Hund's rule coupling for magnetism is already explained in chapter 4. In ultracold gases the interest for multiorbital physics includes magnetic phenomena. Models like the Kondo Lattice model [3, 68] can be experimentally realized in ultracold gases [34]. The Kondo Lattice model hosts not only paramagnetic (PM) phenomena like Kondo singlet formation, but also antiferromagnetic (AFM) or ferromagnetic (FM) phases. However the experimental realization has not been done so far, as it is a serious challenge to obtain ultralow temperatures and entropies [36]. These are needed to observe exchange-driven spin ordering effects. Still progress has been made by for example establishing short-range AFM ordering with a single orbital degree of freedom [36] or setting up spin-exchanging contact interactions with two orbital degrees of freedom [124]. This arises the impression, that it is only a matter of time until multiorbital magnetic phenomena will be accessible in ultracold gas systems. Conversely in solid state systems since the discovery of ultrafast demagnetization of ferromagnetic Nickel [11] multiorbital magnetic phenomena and especially demagnetization in ferromagnets are accessible and have attracted wide interest [62–64, 139]. A focus lies on switching spin orientations in a deterministic way on shortest (femtosecond) time scales. This is critical for data storage as it sets the bit-recording time limit in magnetic memory devices [106]. Many theoretical mechanisms have been proposed to explain the ultrafast demagnetization and a way to control FM order. These include the Elliot-Yafet mechanism [69, 132], superdiffusive spin transport [10] and processes driven by the Coulomb interaction [71]. As the exchange-bias effect can be used to employ ultrafast FM order via manipulation of an adjacent antiferromagnet [74], addressing ultrafast dynamics in antiferromagnets prove relevant. Often AFM order is tied to strong correlations inducing AFM tendencies via superexchange. A basic question is, if Coulomb interactions are enough to obtain ultrafast

demagnetization in antiferromagnets. From a model point of view this question has recently been addressed in a single-orbital Hubbard model concerning demagnetization of an AFM state after an interaction quench [123, 138]. In this chapter the t_{2g} (three-orbital) Hubbard model with a general dispersion, chosen as simple cubic is considered. Additionally a wide range of fillings is investigated. Accounting in the modeling for the t_{2g} shell the investigation is relatively close to real materials like high-Néel-temperature SrTcO₃ [117] (half-filled $N = 3$), nearly-AFM SrCrO₃ [105] ($N = 2$) and PM Sr₂MoO₄ [52] ($N = 2$). Note that for the last two materials there is no crystal field in the t_{2g} shell in agreement with the model in this chapter [53, 105].

To be specific, the three-orbital Hubbard model is investigated using t_{2g} orbital degrees of freedom on a three-dimensional cubic lattice with rotational-invariant Coulomb interaction in Slater-Kanamori parametrization as stated in Eq. 2.4. A two-site unit cell is utilized to be able to model AFM order. In the following a bandwidth of 2 eV is used, therefore the half-bandwidth W sets the energy scale. Using an interaction quench the initial state has U_i and $J_{H,i}$ and the final state U_f and $J_{H,f}$. As the ratio q is utilized as $q \equiv J_H/U$, $q = q_i = q_f$ holds in the following. In the single-orbital case at half-filling time-dependent Gutzwiller approximation (TD-GA) has proven to recap qualitatively the AFM demagnetization dynamics with critical points obtained with time-dependent dynamical mean-field theory (TD-DMFT) [123, 138]. This holds not only for non-thermal but also thermal critical points [122, 144]. The focus in this chapter lies on non-equilibrium magnetization dynamics and non-thermal critical points in a wide range of hole dopings after an interaction quench. In section 6.1 equilibrium properties like the magnetic phase diagram are revealed. Afterwards an interaction quench from an initial AFM state at $U_i = 2.0$ to $U_f < U_i$ in a wide range of hole-dopings is discussed in section 6.2. Then a kind of vice versa scenario is considered starting from an initial PM state and performing interaction quenches to $U_f > U_i$ in section 6.3. The total energy before and shortly after the quench is the matter of interest in section 6.4 and is checked for a relation to the observed time-dependent phenomena. Finally the results will be summarized in section 6.5.

6.1 The equilibrium case

First the equilibrium magnetic phase diagram is the focus of attention. In Fig. 6.1 the magnetic phase diagram obtained by equilibrium SBMFT utilizing hole-doping

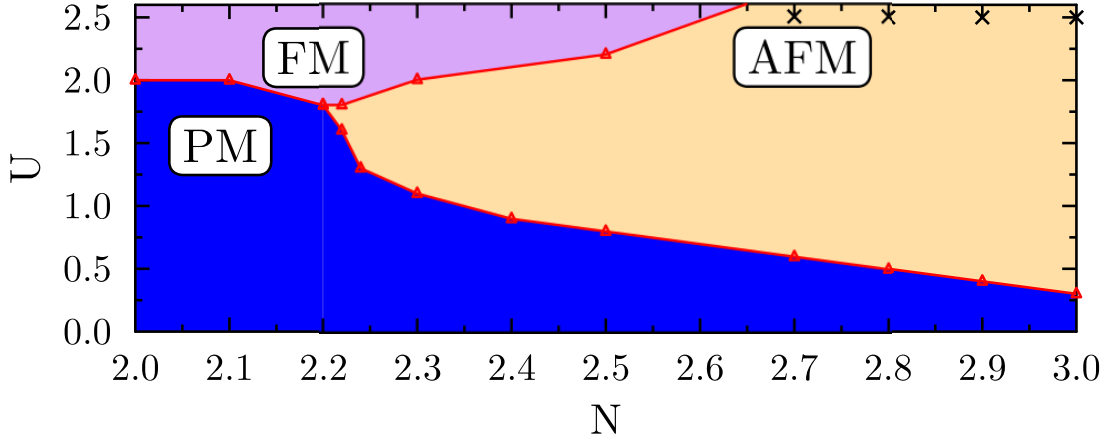


Figure 6.1: Equilibrium SBMFT magnetic phase diagram for the hole-doped three-orbital Hubbard model on the cubic lattice with $q = 0.2$. Black crosses mark stable AFM solutions within DMFT using an CT-QMC impurity solver [16, 43, 107] at $\beta\tau = 50$ and $q = 0.167U$.

and $q = 0.2$ is shown. $N = 3$ marks half-filling and black crosses mark stable AFM solutions within DMFT using an continuous-time quantum Monte Carlo (CT-QMC) impurity solver [16, 43, 107] at $\beta\tau=50$ and $q = 0.167U$ (with β inverse temperature). A previous study [24] found no AFM order away from half-filling at same β , q and U using a Bethe lattice in contrast to our 3D simple cubic dispersion. Within our setup we are able to stabilize AFM order in the hole-doped regime (see Tab. 6.1 and Fig. 6.1). For the DMFT calculations we use $U = 15\tau$, which equals $2.5D$ as the band width is 12τ . The equilibrium phase diagram in Fig. 6.1 determined by free-energy comparison of the competing phases, consists of a FM, PM and AFM phase. The FM phase is only the ground state for high interaction values and moderate hole-doping, conversely the AFM phase is stable over a wide range of fillings. Of key interest is the AFM-PM phase boundary as the used Hamiltonian (Eq. 2.4) in the two-site unit cell conserves the total spin S_z (summed over both sites). Therefore

N	3.0	2.9	2.8	2.7
S_z	-1.45	-1.24	-0.94	-0.12

Table 6.1: Total S_z (summed over orbitals) for appropriate filling N in a 3D simple cubic lattice with $\beta t_h = 50$, $q = 0.167$ and $U = 2.5D$ derived by DMFT using an CT-QMC impurity solver [16, 43, 107].

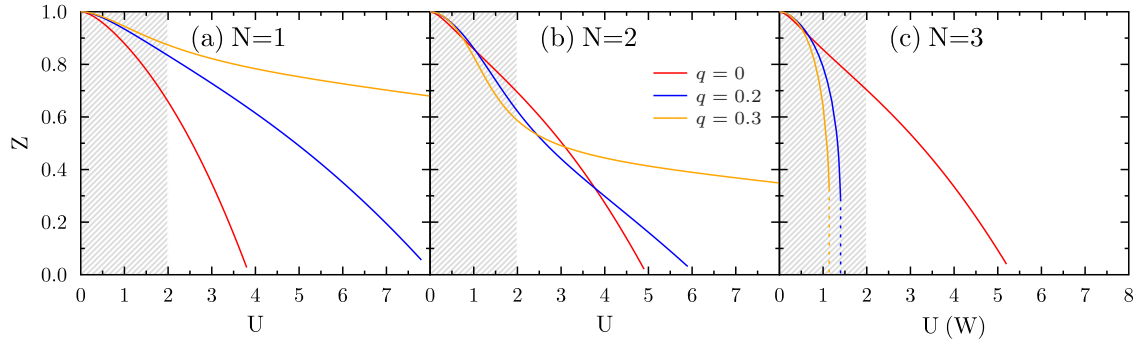


Figure 6.2: Equilibrium quasiparticle weight for different U , q , and fillings $N = 1, 2, 3$. Grey shaded areas mark the interaction regime covered by the non-equilibrium study in the subsequent quench scenarios.

no transition between FM and one of the other phases is observable.

The Hund's rule coupling J_H is known to be a key feature in the three-orbital t_{2g} Hubbard model. It substantially effects the stability of magnetic phases [6, 120, 149] and is for example needed to trigger ferromagnetism away from half-filling [47]. Additionally it has substantial influence in the PM state onto the Mott transition at half-filling [66, 148]. In the half-filled case $N = 3$ the Mott transition is shifted towards lower values by increasing J_H contrary to lower integer fillings, where it is shifted to higher values by increasing J_H . This Janus-faced behavior [92] is accessible within SBMFT and can be observed in Fig. 6.1. The non-equilibrium studies are restricted to $U_f \leq 2.0$, where the AFM state is the stable groundstate over a wide range of dopings ($2.2 \leq N \leq 3.0$). So no strong influence of the Janus-faced behavior onto non-equilibrium physics is expected. Note that it is an open question so far, in which way this Janus-faced physics effect magnetic states.

6.2 Interaction quenches from an antiferromagnetic state

An initial AFM state at $U_i = 2.0$ is quenched to lower interaction values at different fillings in the range of $2.0 \leq N \leq 3.0$. Looking at the equilibrium phase diagram in Fig. 6.1 the expectation is that at a specific U_f a transition into a paramagnetic state occurs as the equilibrium phase boundary is crossed. To connect with previous single-orbital studies [123, 138, 150], the half-filled case is considered first. The

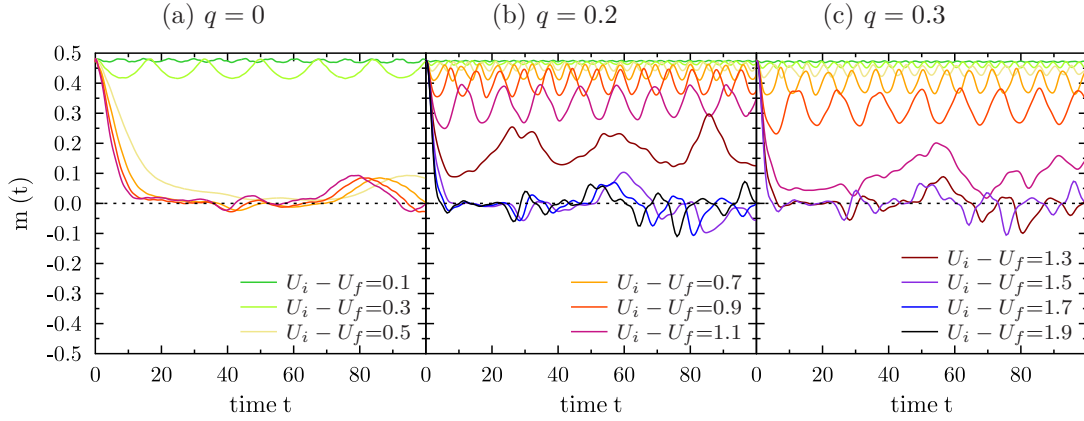


Figure 6.3: Time-dependent magnetization for different q at half-filling after the quench. The chosen U_i ensure equal initial magnetization: (a) $U_i = 3.0$, (b) $U_i = 2.0$, (c) $U_i = 1.6$.

result is shown in Fig. 6.3, depicting the time-dependent magnetic moment $m(t)$ for weak quenches (small $\Delta U = |U_i - U_f|$) in green to high quenches ($\Delta U \sim 2.0$) in black. The three panels denote different q . Zero Hund's rule coupling establishes the transition to a PM non-equilibrium state ($\Delta_{fc}^{(3,PM)} = U_i - U_{fc}^{(3,PM)}$) already at very weak quenches. Increasing q to $q = 0.2$ considerably increases $\Delta_{fc}^{(3,PM)}$, which is lowering a bit going to $q = 0.3$. The equilibrium phase diagram (Fig. 6.1) suggests that $\Delta_{fc}^{(3,PM)}$ is lowered by decreasing the filling N , assuming that $\Delta_{fc}^{(3,PM)}$ follows the equilibrium phase boundary. Consequently the state with highest $\Delta_{fc}^{(3,PM)}$ is taken, $q = 0.2$ to be able to witness an AFM-PM non-equilibrium transition in a wide filling range. Changes observed by using $q = 0.3$ are also discussed.

The quench scenario depicted in Fig. 6.3 at half-filling is now extended to the hole-doped case. The AFM ground state at $U_i = 2.0$ is utilized at all fillings and quenched to lower interaction values keeping $q = 0.2$. The occurring non-equilibrium demagnetization response is plotted as a color coded square at the corresponding U_f in Fig. 6.4 (a), where a comparison to the equilibrium magnetic phases at $U = U_f$ is drawn in (b). Furthermore the quench setup is sketched for three examples in (c). For each non-equilibrium response small graphs depict the magnetization dynamics at both sites of the unit cell (with straight and dotted lines) and below each graph the spin dynamic is sketched in the unit cell. $U_{fc}^{(3,PM)}$ increases with hole-doping as expected by the equilibrium phase diagram. It is located near the equilibrium AFM-PM phase boundary, when going to lower fillings. However at $N = 2.6$ and

below until the AFM equilibrium state breaks down at $N < 2.3$ a new kind of non-equilibrium response shows up, a spin oscillation. This can be analyzed by taking into account the case $N = 2.4$, where the time-dependent magnetic moment for different U_f is depicted in Fig. 6.5 (b). For small ΔU an AFM non-equilibrium state is discovered, where neighboring sites of the unit cell (denoted by straight and dotted lines) have the same absolute value of magnetic moment $m(t)$ but opposite signs. $m(t)$ shows small oscillations but remains finite. The oscillation's amplitude and period increases by increasing ΔU until around $\Delta U = 0.9$, where the amplitude is large enough to reverse the sign at each site periodically leading to a spin oscillation. Increasing ΔU further *decreases* the amplitude and period of the oscillation resulting in the transition to a PM non-equilibrium state. This is reminiscent of a non-thermal critical point found in the single-orbital case, where the frequency of the amplitude mode tends to zero from above [123, 138]. Note that thermalization is delayed near such a (non-thermal) critical point in the single-orbital case [138]. The U_f range, where the spin oscillations occur, broadens towards $N = 2.3$. Looking at the time-averaged quasiparticle weight \bar{Z} shown in Fig. 6.5 (a) renders two as-

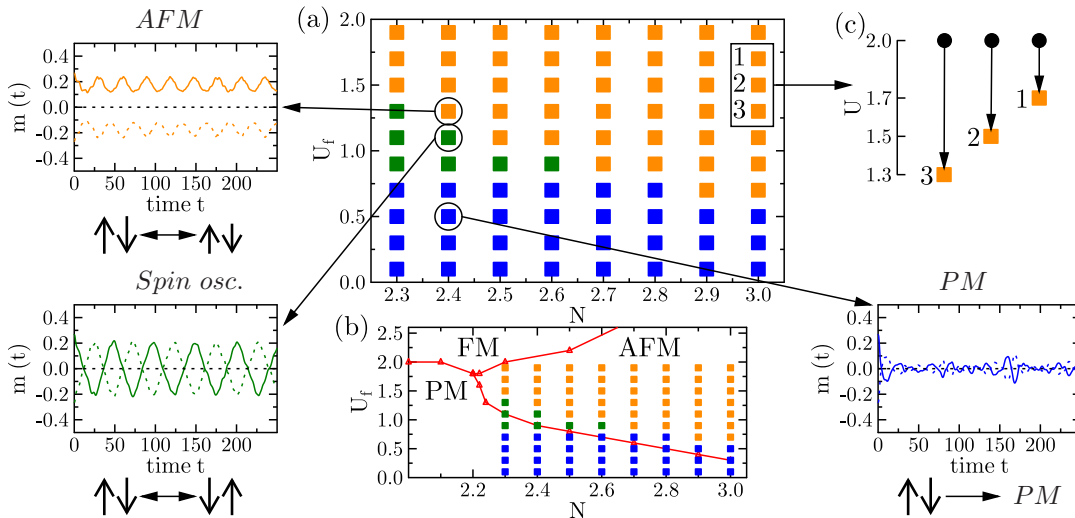


Figure 6.4: (a) Non-equilibrium demagnetization response diagram for $q = 0.2$. Type of response is color-coded and corresponding magnetization dynamics are depicted for one example each in separate graphs. Dynamics of spins in unit cell is also sketched below the corresponding graphs. Comparison to equilibrium phases separated by full lines and described by labels in (b). Sketch of the utilized interaction quench in (c), where filled circles mark fixed $U_i = 2$ and squares the different U_f indicating the position in (a).

pects clear. On the one hand equilibrium AFM states lift the spin degeneracy of the quasiparticle weight and correlations increase linearly with U . The transition to PM states for $U_f = 0.9$ marks the point, where spin degeneracy is established. On the other hand only the non-equilibrium AFM state shows a time-averaged quasiparticle weight with linear dependence on U_f (with closest resemblance to equilibrium Z at $U = U_f$). In contrast spin oscillation and PM state have a time-averaged quasiparticle weight with a nearly constant value with strong difference from the equilibrium Z at $U = U_f$. The resemblance to equilibrium correlation values at high U_f is expected as higher U_f means also lower ΔU in this quench setup. So $U_f = 1.9$ is effectively the weak quench limit, where $\bar{Z}(U_f) \sim Z(U=U_f)$ is retained. Additionally the spin degeneracy in \bar{Z} is established already, when spin oscillations occur. This is *before* the PM state at lower U_f is observed in the non-equilibrium case. Therefore spin oscillations resemble the non-equilibrium PM state correlation-wise and can be regarded as fluctuations around the latter.

To get a grip on these spin oscillations the dominant local multiplets prove insightful. From Tab. 6.2 the conclusion can be drawn, that only two multiplets expressed in eigenvalues of the squared angular momentum \hat{L}^2 and spin operator \hat{S}^2 dominantly contribute. To be precise near half-filling the maximal S state ($L = 0$, $S = \frac{3}{2}$), a spin-quartet, is the highest occupied state. Considering the S_z eigenvalue the maximal value obtains all occupation indicating a high magnetic polarization. Increasing the hole-doping decreases the spin-quartet's occupation (three-electron state) and increases the ($L = S = 1$) spin-triplet's (two-electron state) occupation. This induces a decrease in magnetic polarization. Below $N = 2.5$ the occupation hierarchy of spin-triplet and spin-quartet reverses.

One thus can define a threshold parameter η via ratios between the maximal amplitude of the TD magnetic fluctuations for the spin triplet ($\phi_{L_z,1,S_z}$) /quartet ($\phi_{\frac{3}{2},S_z}$)

$\{L, S\} (S_z)$	$N=2.3$	$N=2.5$	$N=2.8$	$N=3.0$
$\{1,1\} (1)$	0.50 (0.32)	0.41 (0.35)	0.22 (0.21)	0.05 (0.05)
$\{0, \frac{3}{2}\} (\frac{3}{2})$	0.31 (0.17)	0.44 (0.35)	0.69 (0.66)	0.88 (0.88)

Table 6.2: Initial occupation at $t = 0$ of selected single-site multiplets for different fillings N and $U = 2.0$ with $q = 0.2$.

and the initial (equilibrium) spin polarization, i.e.

$$\eta = \frac{w_1 \cdot (A_1^1 - A_0^1)}{|\phi_{1,1}^{(t=0)}|^2 - |\phi_{1,0}^{(t=0)}|^2} + \frac{w_{\frac{3}{2}} \cdot (A_{\frac{3}{2},\frac{3}{2}}^{\frac{3}{2}} + A_{-\frac{3}{2},-\frac{3}{2}}^{\frac{3}{2}}) / 2}{|\phi_{\frac{3}{2},\frac{3}{2}}^{(t=0)}|^2 - |\phi_{\frac{3}{2},-\frac{3}{2}}^{(t=0)}|^2}, \quad (6.1)$$

$$w_S = \sum_{S_z=\pm S, \pm S-1} |\phi_{S,S_z}^{(t=0)}|^2, \quad A_{S_z}^S = \text{Max} \left(|\phi_{S,S_z}^{(t)}|^2 \right).$$

As the spin triplet is L_z degenerate, the L_z -summed values $\phi_{1,S_z} = \sum_{L_z=\pm 1,0} \phi_{L_z,1,S_z}$ are the focus of attention. The maximum amplitudes A are computed from the maximum value (Max) of the slave bosons in the time interval [10, 250] beyond the initial drop in m from dephasing. The first term in Eq. (6.1) arises from the difference in A between $S_z = 1$ and $S_z = 0$ of the triplet. As the quartet has no $S_z = 0$ state, the second term originates from the average amplitude of states with largest S_z difference, since those are most susceptible to magnetic fluctuations. In order to normalize the different filling scenarios, both contributions are weighted with the initial multiplet occupation. Therefore Eq. 6.1 provides a measure of magnetic fluctuations, whereby a value of $\eta \geq 0.5$ indicates the onset of spin oscillations. In Figure 6.5 η is plotted dependent on U_f with different colors from blue to green

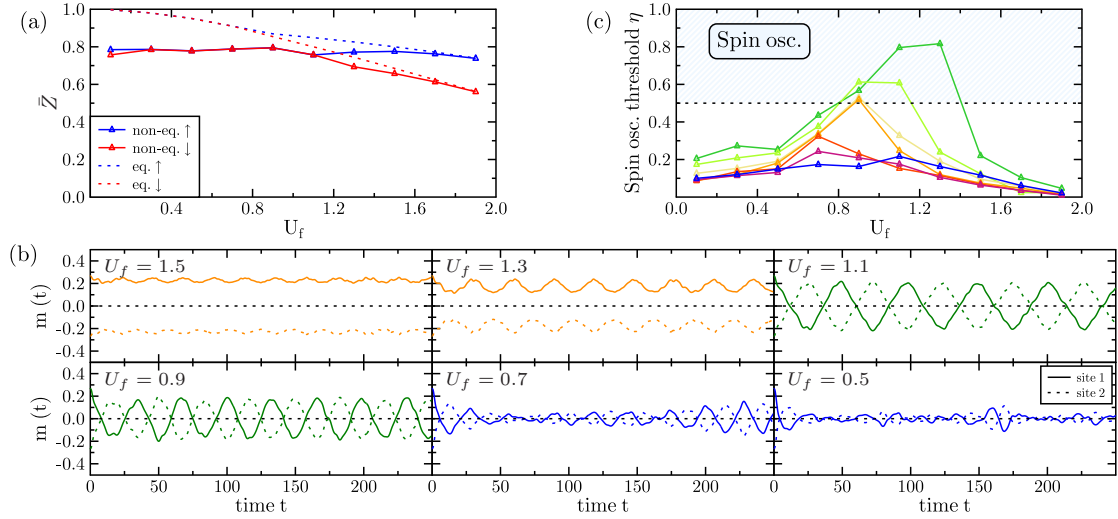


Figure 6.5: Time-averaged Z as straight lines and equilibrium values as dotted lines (a) and magnetisation dynamics at $N = 2.4$ (b). Spin oscillation threshold η for various U_f and fillings $N = 3.0, \dots, 2.3$ (from blue to green) for the quenched AFM state (c).

denoting the fillings N from 3.0 to 2.3. As one can see these two multiplets are able to signal the onset of spin fluctuations for all calculated fillings, meaning Eq. 6.1 provides a consistent measure of magnetic fluctuations for all considered fillings. A quick look at Tab. 6.2 confirms that an equal share of occupation regarding spin triplet and quartet or lesser share of spin quartet seems to be needed to establish spin oscillations. Considering $q = 0.3$ leads to small shifts of the spin oscillation's region of appearance with qualitative identical filling dependence.

6.3 Interaction quenches from an initial paramagnetic state

A kind of vice versa quench scenario is considered now. Starting from an equilibrium paramagnetic state close to the equilibrium PM-AFM phase boundary an interaction quench to higher interaction values at fixed q is performed. As this phase boundary is filling dependent the U_i becomes $U_i = U_i(N)$ (see Tab. 6.3). U_i increases linear with hole-doping except for $N = 2.9$. This is in contrast to the previous quench scenario, where U_i remained constant. The occurring non-equilibrium demagnetization response is plotted as a color coded square at the corresponding U_f in Fig. 6.6 (a). The equilibrium phase boundaries are plotted as straight red lines and labeled for $U = U_f$ in Fig. 6.6 (b). Additionally the quench setup is sketched for $N = 2.9$ in Fig. 6.6 (c). For each non-equilibrium response small graphs depict the magnetization dynamics at both sites of the unit cell (with straight and dotted lines) and below each graph the spin dynamics is sketched in the unit cell. Only initial interaction values close to the equilibrium AFM-PM phase boundary lead to a finite time-dependent magnetic moment indicating a relation between the non-equilibrium magnetic fluctuations and the equilibrium phase boundary. Small ΔU result in a non-equilibrium AFM state with \bar{Z} close to equilibrium correlation values as can be seen in Fig. 6.7. High ΔU triggers a highly correlated PM non-equilibrium state reasoned by the large energy transfer, which puts the system's energy above any reasonable Néel scale. At intermediate quenches transient spin oscillations ap-

	$N=2.3$	$N=2.4$	$N=2.5$	$N=2.6$	$N=2.7$	$N=2.8$	$N=2.9$
$U_i(N)$	0.9	0.7	0.6	0.5	0.4	0.3	0.2

Table 6.3: $U_i(N)$ in PM \rightarrow AFM interaction quench setup.

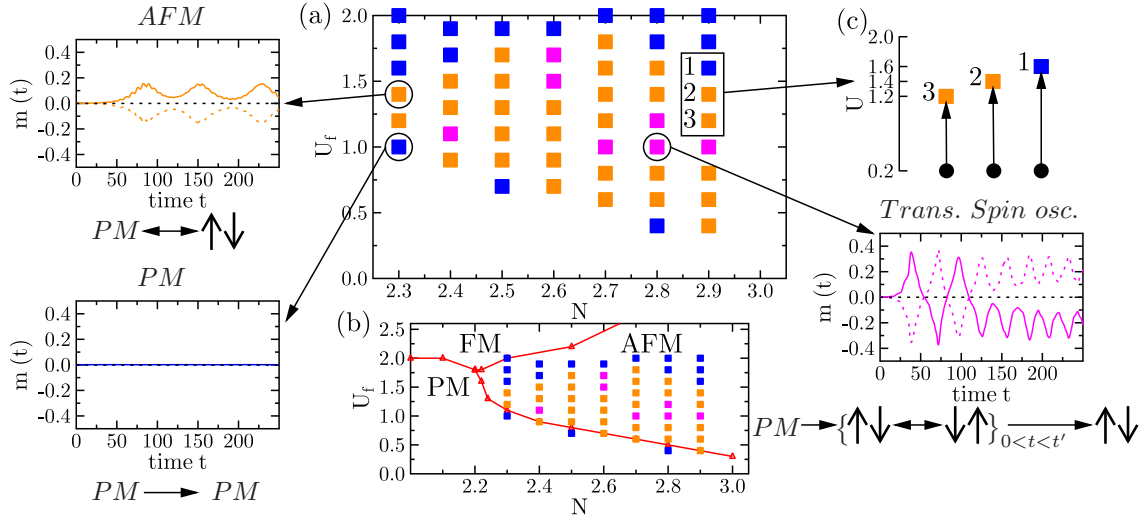


Figure 6.6: (a) Non-equilibrium magnetization response diagram for $q = 0.2$. Type of response is color-coded and corresponding magnetization dynamics are depicted for one example each in separate graphs. Dynamics of spins in unit cell is also sketched below the corresponding graphs. Comparison to equilibrium phases separated by full lines and described by labels in (b). Sketch of the utilized interaction quench in (c), where filled circles mark $U_i(N=2.9) = 0.2$ and squares the different U_f indicating the position in (a).

pear. They show for a limited period of time the periodic sign changes at each site known from the spin oscillations of the previous quench scenario. However then result ultimately into a non-equilibrium AFM state. Their occurrence is different from the spin oscillations in the AFM to PM quench case. They appear also at low hole doping values and remain vital in the whole filling range showing no obvious dependence thereof. Additionally there is no striking relation to the equilibrium AFM-PM phase boundary. Turning to the non-interacting ground state for small hole doping ($2.6 \leq N \leq 2.9$) reveals a hidden dependence. In this non-interacting ground state case the U_f displaying transient spin oscillations are lying on top of the equilibrium AFM-PM phase boundary. This indicates that finite U_i and q_i for these small hole dopings shift the transient spin oscillations away from the equilibrium phase boundary.

The influence of thermalization onto these transient spin oscillations can be estimated from a paramagnetic single-orbital TD-DMFT study [29]. There, weak interaction quenches from a noninteracting initial state lead to no thermalization on

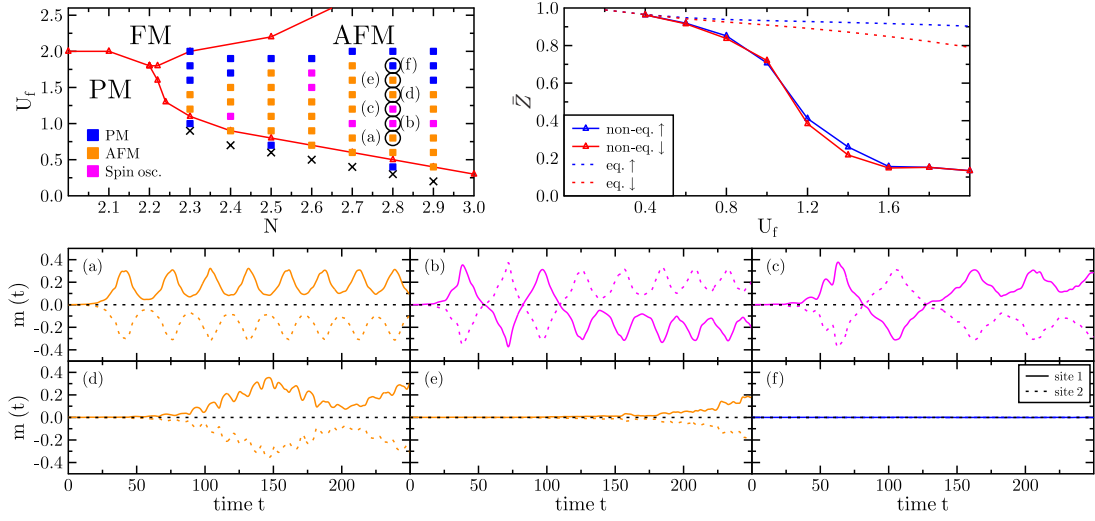


Figure 6.7: Top left: Non-equilibrium magnetization response diagram for $q = 0.2$ as in Fig. 6.6. Black crosses denote U_i . Top right: Time-averaged \bar{Z} denoted by straight and equilibrium values by dotted lines at $N = 2.8$. Bottom panels depict magnetization dynamics for different U_f at $N = 2.8$.

intermediate time scales. This suggests that the present transient spin oscillations should be observable shortly after the quench, before thermalization sets in. The threshold parameter η derived in the previous section is not applicable here, as there is no initial spin polarization. Looking again at the same multiplets as considered in the previous quench case provides helpful to distinguish between three different types of spin oscillations. In Fig. 6.8 the types are denoted by magenta symbols and the lower panels depict the time-dependent multiplet occupation to distinguish them. Let us focus on the states with extremal S_z to make it obvious. For $N = 2.4$, the spin quartet has a higher maximal time-dependent occupation as the spin triplet. As the former has only finite S_z projections, it is more susceptible to net spin polarization since the triplet has one nonmagnetic state ($S_z = 0$). So the dynamic change in occupation amplitude triggered by magnetic fluctuations has to be higher for a dominant spin quartet than for the spin triplet. Thus, a quench strength $U_f - U_i = 0.4$ is sufficient for $N = 2.4$. Instead for $N = 2.8$ an amount $U_f - U_i = 0.7$ is necessary to render the system susceptible to these transient states. The near-degenerate case at $N = 2.6$ demands an even higher quench strength.

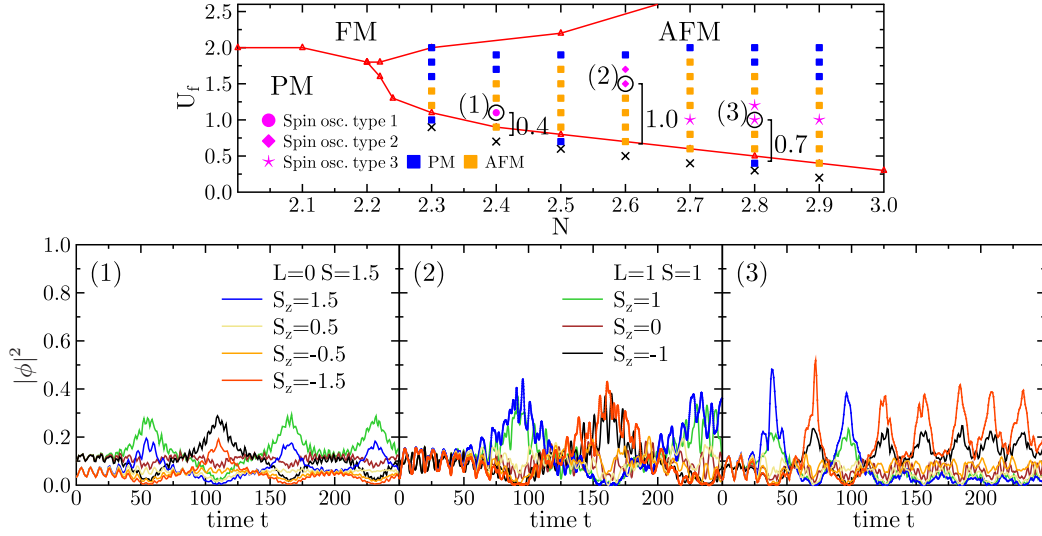


Figure 6.8: Top: Distinction between three types of transient spin oscillations when quenching the PM phase. Bottom: Time-dependent slave boson occupations for local spin quartet and triplet within these types: (1) $|\phi_t|^2 > |\phi_q|^2$, (2) $|\phi_t|^2 \sim |\phi_q|^2$ and (3) $|\phi_q|^2 < |\phi_t|^2$, with t : triplet and q : quartet. All other markers/labels as Fig. 6.6.

6.4 Total energy considerations

In this section, a closer look is taken at the interplay between the initial total energy $E_i^{tot} := \langle i | H(U_i) | i \rangle$ and the final total energy one time step after the quench E_f^{tot} in view of the obtained physics. The time evolved parameters (slave bosons ϕ and eigenvectors ν_a^k) have only acquired changes way below accuracy in the first time step. So, E_f^{tot} is a good approximation to $\langle i | H(U_f) | i \rangle$, namely, the total energy of the Hamiltonian after the quench in the initial state. Note that when the Coulomb interaction is quenched $\mathcal{H}_i^{loc} \neq \mathcal{H}_f^{loc}$ holds. Hence the potential energy changes abruptly $E_f^{pot} \neq E_i^{pot}$. In contrast, the kinetic energy is time dependent via the renormalization matrix R . The latter is a functional of the time-dependent slave bosons, and evolves from the initial value E_i^{kin} [77]. This means that one time step after the quench E_f^{kin} has acquired only changes way below accuracy leading to $E_f^{kin} = E_i^{kin}$. Note that these considerations are only valid one time step after the quench and that the total energy remains conserved during the time evolution after the quench.

First, let us inspect the evolution of both total energies with U_f and filling for

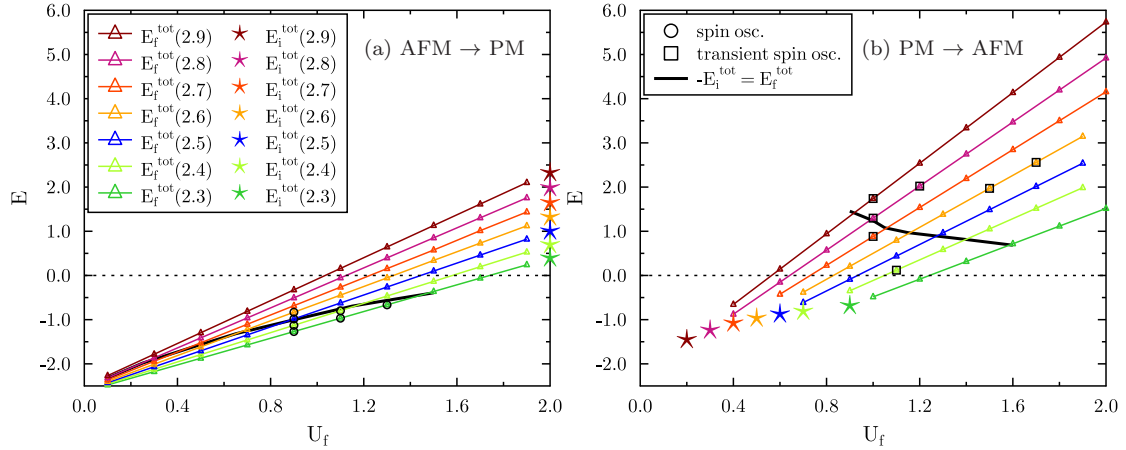


Figure 6.9: Total energies $E_i^{\text{tot}}(N)$ and $E_f^{\text{tot}}(N)$ dependent on filling N and U_f with $q = 0.2$. For $E_f^{\text{tot}}(N) < -E_i^{\text{tot}}(N)$ spin oscillations set in as long as AFM fluctuations are present in AFM \rightarrow PM case and for $E_f^{\text{tot}}(N) \approx -E_i^{\text{tot}}(N)$ transient spin oscillations for $N = 2.7-2.9$ in PM \rightarrow AFM case.

the quench scenario AFM \rightarrow PM in Fig. 6.9(a). E_f^{tot} exhibits a linear dependence on U_f , where the slope of the curve decreases with lower fillings N . Note that $E_i^{\text{tot}} = E_f^{\text{tot}}(U_f=2.0)$ holds. Due to the setup of the quench ($U_f < U_i$) the final total energy is always lower than the initial. A peculiarity is arising as spin oscillations occur, when $E_f^{\text{tot}} < -E_i^{\text{tot}}$ is reached and an AFM magnetic response is still present (beside the case $N = 2.6$). This is not surprising as the kinetic energy remains unchanged $E_i^{\text{kin}} = E_f^{\text{kin}}$, but the potential energy is lowered by decreasing U_f leading to phase instability. This behavior appears reminiscent of physics contained in the virial theorem, which is, however, not strictly applicable to Hubbard models [21]. Nonetheless, it is intuitive to assume that a strongly lowered potential energy with unchanged kinetic energy eventually drives the system towards instabilities. Now a straightforward correspondence between spin oscillation frequencies and total energies is investigated (see Tab. 6.4). This could prove a simple picture describing these spin oscillation in terms of energy scales introduced by both of the total energies. Extraction of the frequencies uses a nonuniform Fourier-transform scheme [35, 78], where the frequency resolution is limited by the maximum time of 250. All spin oscillations lie between 0.10 ± 0.03 and 0.20 ± 0.03 , which equals 18 to 51 fs (as natural units are utilized). This corresponds to frequencies in the THz regime. The frequency decreases linearly with increasing E_f^{tot} at $N = 2.3$ with $\omega_{\text{osc}}/E_f^{\text{tot}} \sim -0.15$.

$(\mathbf{N}, \mathbf{U}_i) =$	ω_{osc}	T_{osc} (fs)	E_i^{tot}	E_f^{tot}
(2.3,2.0)				
$U_f = 1.3$	0.10 ± 0.03	41 ± 10	0.39	-0.67
$U_f = 1.1$	0.15 ± 0.03	27 ± 5	0.39	-0.97
$U_f = 0.9$	0.20 ± 0.03	21 ± 3	0.39	-1.27
(2.4,2.0)				
$U_f = 1.1$	0.13 ± 0.03	33 ± 7	0.69	-0.80
$U_f = 0.9$	0.20 ± 0.03	21 ± 3	0.69	-1.13
(2.5,2.0)				
$U_f = 0.9$	0.18 ± 0.03	24 ± 3	1.00	-0.98
(2.6,2.0)				
$U_f = 0.9$	0.13 ± 0.03	33 ± 7	1.32	-0.83

Table 6.4: Spin oscillation frequencies and their period compared to initial and final total energy in the AFM→PM quench scenario. Frequencies calculated by nonuniform Fourier transform [35, 78].

But, already at $N = 2.4$ no linear behavior can be derived. Furthermore, the frequency decreases with increasing filling (E_i^{tot}) at constant U_f . Here again, ω_{osc}/E_f^{tot} or $\omega_{osc}/(E_f^{tot} - E_i^{tot})$ behave nonlinearly. To conclude, the spin oscillations cannot be explained solely by linear behavior upon E_f^{tot} or $E_f^{tot} - E_i^{tot}$.

Let us now turn to the case of quenches from the PM phase. Looking at Fig. 6.9 (b), E_f^{tot} exhibits again a linear dependence on U_f , where the slope of the curve decreases with lower fillings. As U_f is higher than U_i , $E_f^{tot} > E_i^{tot}$ holds in this case. For fillings close to half-filling ($N \in [2.7, 2.9]$) transient spin oscillations near $E_f^{tot} = -E_i^{tot}$ are observed, indicating like in the other quench case a phase instability upon increasing the potential energy above a critical value. Again, linking the occurring frequencies (transient and oscillatory) as well as the transient length to E_i^{tot} and E_f^{tot} provides additional insight into the importance of these energy scales. Transient spin oscillations are evolving into stable AFM oscillations (see Fig. 6.6). The number of periods of both oscillations is in most cases not sufficient to get an accurate Fourier transform. Instead, the frequencies are derived by inspecting the time-dependent magnetization $m(t)$ and counting the number of periods (Tab. 6.5, 6.6 and 6.7). Error estimation is done by considering the largest deviation of $m(t)$ from a sine function ($A \sin(\omega(x - B))$) with the stated frequency. The transient spin oscillations have in most cases much lower frequencies than the following stable counterpart (compare Tab. 6.5 and 6.6). The transient length is varying between

$(\mathbf{N}, \mathbf{U}_i) =$ (2.4,0.7)	ω_{tr}	L_{tr} (fs)	E_i^{tot}	E_f^{tot}
$U_f = 1.1$	0.05 ± 0.00	77 ± 3	-0.81	0.12
(2.6,0.5)				
$U_f = 1.5$	0.04 ± 0.00	98 ± 4	-0.97	1.97
$U_f = 1.7$	0.02 ± 0.00	92 ± 7	-0.97	2.56
(2.7,0.4)				
$U_f = 1.0$	0.08 ± 0.00	25 ± 1	-1.08	0.88
(2.8,0.3)				
$U_f = 1.0$	0.10 ± 0.01	60 ± 8	-1.24	1.30
$U_f = 1.2$	0.07 ± 0.00	64 ± 3	-1.24	2.02
(2.9,0.2)				
$U_f = 1.0$	0.11 ± 0.00	19 ± 1	-1.46	1.74

Table 6.5: Transient AFM spin oscillation frequencies and transient length compared to initial and final total energy in the PM→AFM quench scenario. Frequency derived by inspecting $m(t)$.

$(\mathbf{N}, \mathbf{U}_i) =$ (2.4,0.7)	ω_{osc}	T_{osc} (fs)	E_i^{tot}	E_f^{tot}
$U_f = 1.1$	0.11 ± 0.02	36 ± 8	-0.81	0.12
(2.6,0.5)				
$U_f = 1.5$	-	-	-0.97	1.97
$U_f = 1.7$	-	-	-0.97	2.56
(2.7,0.4)				
$U_f = 1.0$	0.22 ± 0.09	19 ± 7	-1.08	0.88
(2.8,0.3)				
$U_f = 1.0$	0.23 ± 0.07	18 ± 5	-1.24	1.30
$U_f = 1.2$	0.13 ± 0.03	32 ± 7	-1.24	2.02
(2.9,0.2)				
$U_f = 1.0$	0.27 ± 0.08	15 ± 5	-1.46	1.74

Table 6.6: Stable AFM spin oscillation frequencies and period compared to initial and final total energy in the PM→AFM quench scenario. Frequency derived by inspecting $m(t)$. '-' indicates that frequency could not be measured due to too long transient length.

18 and 102 fs (if one does not respect the defined transient oscillation types of Fig. 6.8). However, there seems to be a link to these different types as it is easier to spin polarize a dominant spin triplet ($N \in [2.7, 2.9]$) as a roughly equal populated spin

triplet and quartet ($N = 2.6$). Thus resulting in much lower transient lengths in the former case. For the same initial conditions, the transient lengths depend differently on E_f^{tot} according to the spin oscillation type. For type 3 ($N = 2.7$ to $N = 2.9$) there is a proportional behavior and for type 2 an antiproportional behavior. The stable oscillations are given by periods between 12 and 44 fs, so the spin oscillation period region is shifted to lower values compared to the AFM→PM case. Furthermore, the qualitative behavior of the stable oscillations with filling is different. Increasing the filling (increasing E_f^{tot}) at constant $U_f = 1.0$ increases ω_{osc} instead of decreasing it. To clarify the influence of different initial states onto transient and oscillatory behavior, let us look at Tab. 6.7. Starting from an initial noninteracting state the transient behavior moves to quenched interaction values right on top of the equilibrium AFM-PM phase boundary. This reveals an intricate connection between this phase boundary and the transient fluctuations. It is not possible to estimate ω_{osc} in two of the three cases here, as the number of periods is too low. The transient length lies between 50 and 181 fs. Comparing these to Tab. 6.5, there are drastic changes for $N = 2.6$ and $N = 2.9$ leading to an increased transient length moving towards half-filling. This is the opposite behavior for $N = 2.8$ to $N = 2.9$ and the case $U_i \neq 0$, which shows that initial correlations and generally speaking the initial state have a high influence onto the transient length.

$(\mathbf{N}, \mathbf{U}_i) =$	ω_{tr}	L_{tr} (fs)	ω_{osc}	E_i^{tot}	E_f^{tot}
(2.6,0.0) $U_f = 0.8$	0.04 ± 0.00	52 ± 5	0.12 ± 0.02	-1.90	0.80
(2.8,0.0) $U_f = 0.6$	0.07 ± 0.01	140 ± 23	-	-1.95	0.40
(2.9,0.0) $U_f = 0.6$	0.05 ± 0.01	181 ± 20	-	-1.98	0.54

Table 6.7: Transient and stable AFM spin oscillation frequencies and transient length compared to initial and final total energy in the PM→AFM quench scenario. Initial state is non-interacting ($U_i = 0$). Frequency derived by inspecting $m(t)$. '-' indicates that frequency could not be measured due to too long transient length.

6.5 Summary of this chapter

This chapter considers two types of interaction quenches at half-filling and with hole-doping for the t_{2g} -shell (three-orbital) Hubbard model with a two-site unit cell. One of the two types addresses a strongly correlated antiferromagnetic (AFM) ground state quenched to lower interaction values. This eventually results in a non-equilibrium paramagnetic (PM) state. The other addresses the vice versa scenario starting from an PM state close to the AFM-PM phase boundary quenched to higher interaction values. By this eventually an AFM non-equilibrium state is reached. The calculated equilibrium phase diagram reveals the wide filling range, in which the AFM-PM phase boundary is present. The famous Janus-face of the Hund's rule at integer fillings in the considered Hubbard model is accessible within SBMFT. However, the interaction values used for interaction quenches are too low to expect a pronounced influence on the results. At half-filling quenching from an AFM state to lower interaction values, previous results from the single-orbital case are qualitatively reproduced. A finite Hund's rule coupling is obligatory to investigate the shift of the non-equilibrium AFM-PM state boundary with hole-doping. At zero Hund's rule coupling the magnetic fluctuations are unstable and damped towards a non-equilibrium PM state already for small interaction quenches. Extending now the view to all accessible values of hole-dopings leads to two main results in this AFM to PM quench scenario. First, as expected non-equilibrium AFM states are retrieved for small interaction quenches and non-equilibrium PM states for high interaction values. The boundary of these two types of states is filling-dependent and lies close to the equilibrium counterpart. Second, at high hole doping near the non-equilibrium AFM-PM state boundary a new non-equilibrium state appears characterized by large-amplitude spin oscillations. This new state covers a higher range of final interaction values as hole doping is increased. To get a better understanding of these large-amplitude spin oscillations a threshold parameter is introduced. This signals the appearance of this state, when exceeding a critical value. This parameter is defined solely in terms of the two dominantly populated local states, a spin triplet and a spin quartet. The spin quartet has the highest occupation close to half-filling and the spin triplet close to the maximal considered hole-doping. Turning to the other quench scenario (PM to AFM) small interaction quenches not exceeding the equilibrium AFM-PM phase boundary result in no magnetic response. This means the non-equilibrium PM state remain paramagnetic. High interaction quenches result again in the same state as the transferred energy into the system is higher than

any Néel scale. Intermediate interaction quenches lead to a non-equilibrium AFM state or a new non-equilibrium state called transient large-amplitude spin oscillations. It has the same physical appearance as the large-amplitude spin oscillations from the first quench scenario but only for a limited period of time. Afterwards it changes to a non-equilibrium AFM state. In this way it is a transient state. This state shows no obvious filling dependence in contrast to the large-amplitude spin oscillation. It is vital over the full filling range. The threshold parameter can not be applied here as the initial spin polarization is zero, which acts as a weight factor in the denominator. But the considered multiplets for this parameter can be used to distinct between three types of transient spin oscillations taking into account, which of both has the higher maximal value of time-dependent occupation. Additionally a hidden relation to the equilibrium AFM to PM phase boundary can be found. Looking at the non-interacting ground state as the initial state for small hole doping shifts the final interaction values, where the transient spin oscillations occur, onto this equilibrium AFM-PM phase boundary. This leads to the conclusion that in both quench scenarios non-equilibrium state and equilibrium phase are intimately linked. Some conclusions can be drawn, when comparing equilibrium total energy to the total energy shortly after the quench. Then the kinetic energy is unchanged and only the potential energy has greatly changed due to the interaction quench. The frequency of the spin oscillation has no simple relation to the mentioned total energies. This means in neither of the quench scenarios (AFM \rightarrow PM, PM \rightarrow AFM) the frequencies scale with the total energy after the quench or the difference of the latter to the equilibrium total energy. However, in both quench cases spin oscillations and transient spin oscillations occur near the point, when both total energies are equal in absolute value with opposite sign. This is reminiscent of the virial theorem, which is, however, not strictly applicable to Hubbard models.

7 Influence of oxygen vacancies on the $\text{LaAlO}_3/\text{SrTiO}_3$ interface

After the discovery of the electron gas at the $\text{LaAlO}_3/\text{SrTiO}_3$ (LAO/STO) heterostructure interface [104] a vast number of experiments revealed phenomena like superconductivity [23, 79, 116], magnetism [8, 17, 79] and high mobility [104]. Yet, the question why there is a conducting layer between two insulating compounds is an outstanding puzzle. It is known, that growth conditions are severely impacting the oxide interface conductivity [100, 137, 145]. As oxygen vacancies (OVs) are known to act as electron donors in SrTiO_3 [58], the mentioned growth sensitivity supports the fact that OVs play a crucial role for interface conductivity. A general agreed mechanism to explain the conducting layer is coined polar-catastrophe [58], which basically means that charge transfer is preventing a strong polar discontinuity at the oxide interface. Another astonishing fact is the magnetism revealed at the LAO/STO interface, especially as both parent compounds do not share this property [17]. Studies revealed for example ferromagnetic (FM) hysteresis up to room temperature and coexisting with paramagnetic and diamagnetic susceptibilities indicating multiple coexisting phases [8] and coexistence of magnetic order and superconductivity [79]. Up to now two scenarios exist explaining the emergence of FM moments at the interface [134]. In the first scenario a special $t_{2g}(xy)$ energy band is split off to lower energies and is more localized than the other interface bands. It resides only in the first TiO plane adjacent to the interface [112]. This band is expected to accommodate most of all carriers. As the polar catastrophe leads to 0.5 electrons per Ti atom at the interface, this band turns into a quarter filled band insulator. The susceptibility of the localized carriers towards spin-polarization is then explained by a Stoner-like mechanism [112] or interaction with conduction electrons [95]. In the other scenario OVs are the main actors giving rise to magnetic phenomena. Supporting this scenario are facts like the observation of randomly distributed FM patches within the sample [13], high sensitivity to strain [59], large variability

between samples [13, 59] and dependence on oxygen growth pressure [8, 17]. Indeed density field theory (DFT) results show that Ti atoms around OVs develop large magnetic moments [111]. In DFT an OV induces a crystal-field lowered e_g -like state on neighboring Ti atoms. One can now think of two limiting scenarios. In the dilute defect limit with only few OVs e_g -like local moments form on Kondo impurities [84, 85]. These couple ferromagnetically via Ruderman-Kittel-Kasuya-Yosida (RKKY) interaction mediated by t_{2g} electrons. In the dense defect limit the physics is close to a minimal two-orbital ($e_g, t_{2g}(xy)$) Hubbard model near quarter-filling [76, 110]. In a recent DFT+dynamical mean field theory study [76] it was shown, that Zener double-exchange [156, 157] can be held responsible for FM order at the interface. In this chapter the focus lies on exchange processes induced by OVs at the LAO/STO interface in a broad concentration range. To allow for an arbitrary number and ordering of OVs the real-space formulation of slave boson mean-field theory (SBMFT) is employed (see section 2.3). This has the advantage compared to usual DFT studies, that it incorporates several many-body hallmarks as quasiparticle (QP) formation, paramagnetic local moments and band narrowing. In general DFT+DMFT would be the best method, but a unit cell like the here considered 10×10 one is numerically at present out of reach using that method. To start the real-space formulation of SBMFT is tested in section 7.1 on a homogeneous example (section 7.1.1) and an inhomogeneous one in section 7.1.2. Afterwards the problem of oxygen vacancies at the LAO/STO interface can be studied. This is initiated with a previous DFT+DMFT investigation, which reveals the impact of Hund's coupling J_H on the magnetic order in the n-type LAO/STO interface [49] in the limit of high OV concentration in section 7.2. Based on this a real-space model can be constructed in the next section 7.3, which is applied first to the dilute defect limit in section 7.4. According to the results two other OV concentration regions can be discriminated discussed in section 7.5 and 7.6. In section 7.2 until section 7.6 all energies are given in electron volts. Finally the section 7.7 summarizes this chapter.

7.1 Testing real-space slave boson mean-field theory

In the real-space SBMFT the lattice size is directly related to the dimension of the hopping matrix and therefore influences the precision of the obtained results. This is evident in the homogeneous example depicted in the following section 7.1.1.

7.1.1 Lattice size dependence of metal to insulator transition

As a simple example a single-orbital Hubbard model is considered (Eq. 2.3) at half-filling with a two-dimensional simple cubic dispersion. The hopping is chosen such that the half-bandwidth W is the energy unit and the aim is to resolve the metal to insulator (Mott) transition for various real-space lattices (with periodic boundary conditions) compared to the momentum space formulation. Therefore the same \mathcal{H}^{loc} is applied to each atom of the lattice. In momentum-space formulation a grid of 50×50 \mathbf{k} -points is used and a single atom in the unit cell. In Fig. 7.1 the behavior of quasiparticle weight Z , local spin-spin correlations and free energy Ω with interaction U can be seen. To compare the free energy Ω for different lattice sizes and numbers of electrons corresponding to half-filling the normalization $(\Omega + \mu N)/M$ is chosen, where μ is the chemical potential, N the number of electrons per unit cell and M the total number of atoms per unit cell. In general the result is as expected, the difference to the \mathbf{k} -space results shrinks the larger the real-space lattice. For a 10×10 lattice the Mott critical interaction value is in close agreement with the \mathbf{k} -space value. In contrast a 2×2 lattice predicts a critical value of about 2.0, which is 50 % off. It is interesting to see that small real-space lattices tend to overestimate the influence of correlations, which is surely related to the fact that the density of states is poorly reproduced by the small number of eigenvalues. For example a 2×2 lattice has four sites. When including spin-degrees of freedom this means only eight states (including energy degenerate ones) are available to approximate the two-dimensional simple cubic density of states in the whole energy range of 2 eV. The dependence of the number of energy eigenvalues on the lattice size in the real-space formulation is depicted in Tab. 7.1. In principle this testing case is quite artificial as this is a purely homogeneous case, where the \mathbf{k} -space formulation is better suited than using large lattices with periodic boundary conditions in real-space. To account for this in the following section an inhomogeneous testing case is exploited with a (non-magnetic) defect in the middle of the lattice.

	2x2	4x4	6x6	8x8	10x10
N_{EV}	8	32	72	128	200

Table 7.1: Number of energy eigenvalues N_{EV} to approximate density of states with lattice size in real-space.

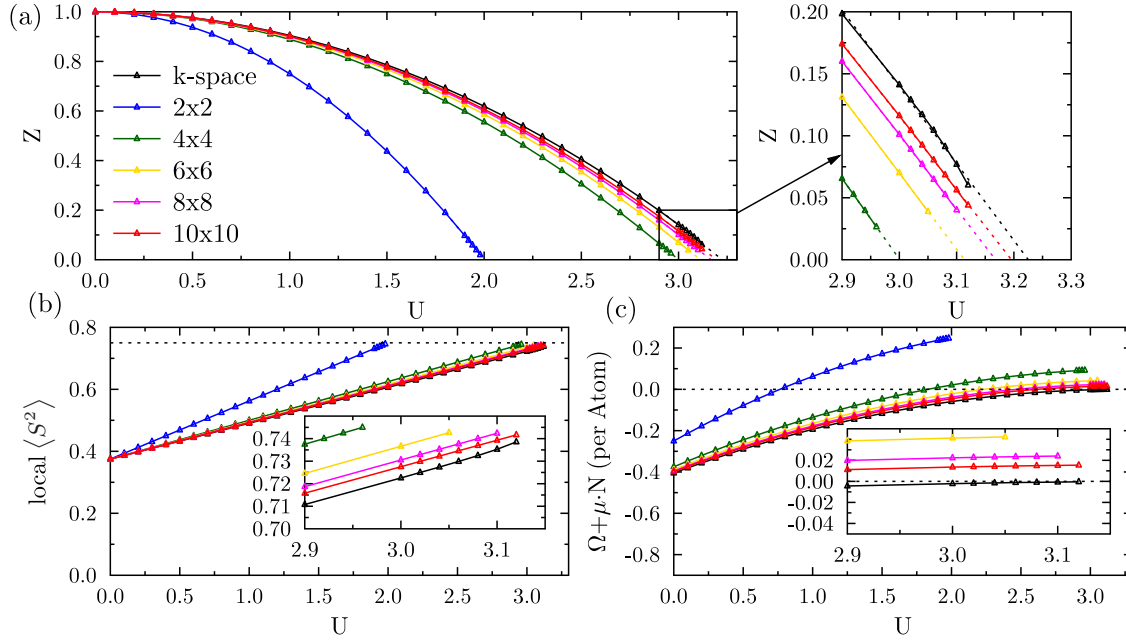


Figure 7.1: Dependence of various physical quantities on real-space unit cell size (with periodic boundary conditions) and interaction U . (a) Quasiparticle weight and position of Mott transition (right), where tail has been fitted linearly denoted by dotted points. (b) Local spin-spin correlation with maximum value 0.75 depicted by dotted points. (c) Free energy $\Omega + \mu N$ per atom with zero value denoted by dotted points, which is the asymptotic value in \mathbf{k} -space reached at the Mott transition. μ is the chemical potential and N the number of electrons per unit cell.

7.1.2 Charge oscillations induced by non-magnetic defect

As in the previous section a single-orbital Hubbard model is considered. This time a little twist is added.

$$\mathcal{H} = \sum_{i,j=1}^{10} \sum_{\sigma} \left(\tau_{i\sigma j\sigma} c_{i\sigma}^{\dagger} c_{j\sigma} + \text{h.c.} \right) + \sum_i U n_{i\uparrow} n_{i\downarrow} + V_0 \sum_{\sigma} n_{1\sigma}. \quad (7.1)$$

At the first site (origin) of the lattice the energies are shifted by the spin-independent potential V_0 . This is a simple modeling of a non-magnetic impurity. A 10x10 simple cubic lattice with in total 83 electrons is utilized with a bandwidth of 8 eV. These parameters are chosen to be in line with a previous study [159]. In the following some of the results of this study are reproduced. The impurity at the origin attracts

charge, when $V_0 < 0$ is set and leads to charge oscillations in the lattice. In Fig. 7.2 the radial modification of the charge density induced by the δ potential is visible for different V_0 . The results are in good agreement with [159]. Decreasing V_0 increases

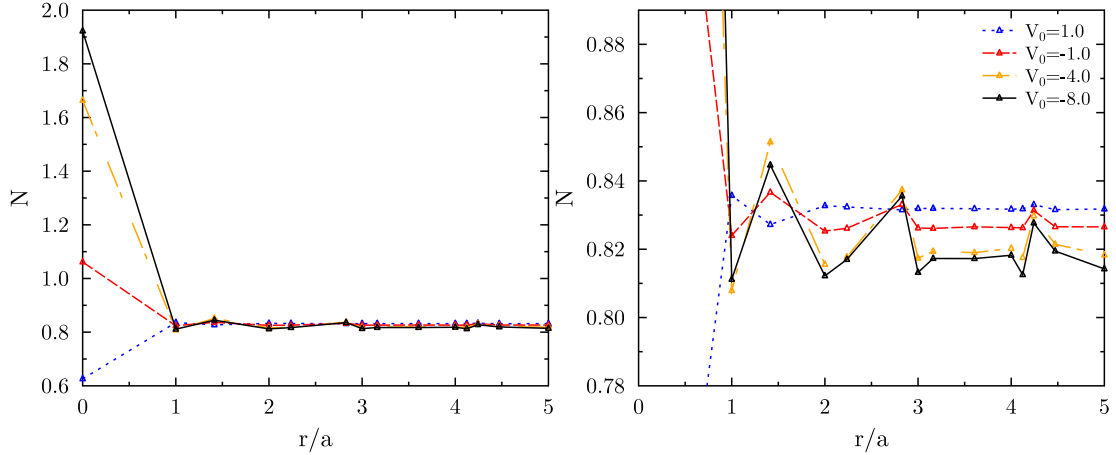


Figure 7.2: Radial modification of the charge density caused by a δ -potential with different V_0 at $r = 0$. All sites have $U = 4$. a is interatomic distance.

the amplitude of the charge oscillations and attracts more charge to the impurity site ($r=0$) until the impurity is filled ($N = 2$). Conversely a positive V_0 corresponds to an energy penalty for electrons at the impurity, which leads to a charge decrease at the impurity. Finally another central result of the study [159] is captured in Fig. 7.3, namely the charge density and the local magnetic moment (=local spin-spin correlation as we are in the paramagnetic case) at the impurity for different V_0 . This figure is again in good agreement with Fig. 7 from [159]. It displays the tendency of the system to form a magnetic state at $V_0 \sim -1.0$, where the impurity is half-filled and the local magnetic moment is maximal. In this calculation it is not exactly at $V_0 = -1.0$ like in [159], but at a slightly higher value.

To summarize, also in a inhomogeneous setting our real-space SBMFT formalism is able to reproduce results of a previous study. Minor differences could be related for example to the usage of a different dispersion, where the study to which we compared our results did not mention their lattice geometry.

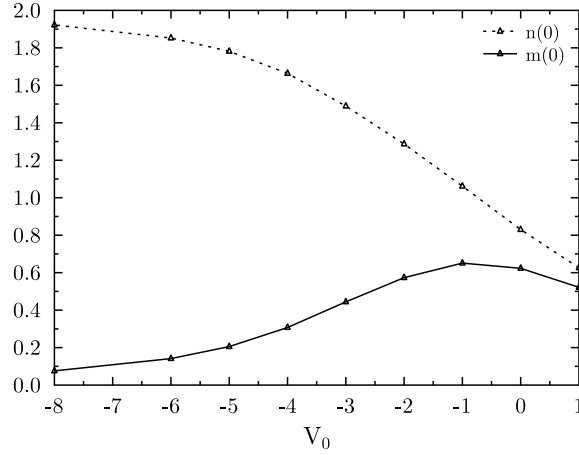


Figure 7.3: Charge density and local magnetic moment at the impurity for different δ -potentials. All sites have $U = 4$.

7.2 Dense-defect limit of oxygen vacancies as starting point

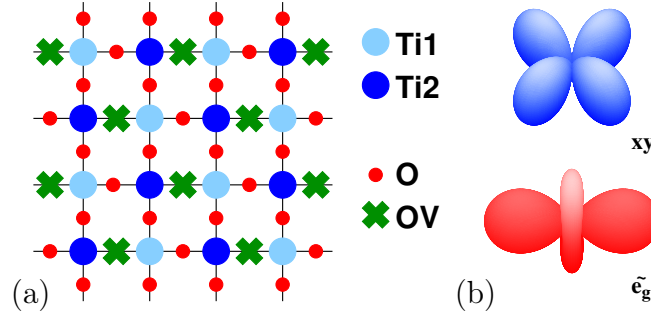


Figure 7.4: (a) TiO_2 interface layer of n-type LAO/STO with 25% oxygen vacancies (OV) utilized in supercell DFT+DMFT calculations [76]. Ions Ti1 and Ti2 form the basis in the $\sqrt{2} \times \sqrt{2}$ primitive cell. (b) minimal relevant Ti orbitals with $|\tilde{e}_g\rangle \sim 0.55|z^2\rangle \pm 0.84|x^2 - y^2\rangle$ [76].

The results of a charge self-consistent DFT+DMFT work [76] provide the starting point for the real-space model of OVs at the LAO/STO interface. The setting and results are shortly recapped in this section. The DFT+DMFT study has been performed in the limit of 25% OVs in the TiO_2 interface layer [76]. The OVs are solely located in the interface and within this chapter there are only Ti atoms with

a maximum of one OV as neighbor considered. For 25% OVs each Ti atom has one OV as neighbor (see Fig. 7.4). For the DFT part a mixed basis pseudopotential framework is utilized and continuous-time quantum Monte Carlo (CT-QMC) solves the DMFT impurity problem. Two orbitals ($\tilde{e}_g, t_{2g}(xy)$) with $U = 2.5$ and $J_H = 0.5$ are taken within a Slater-Kanamori parametrization. A variation of J_H is utilized to consider the importance of double-exchange-like effects. For LAO/STO a Hund's coupling of $J_H = 0.5$ - 0.6 is expected. Figure 7.5(a) depicts the spin and orbital dependent occupations in the magnetically ordered phase with J_H . The Ti

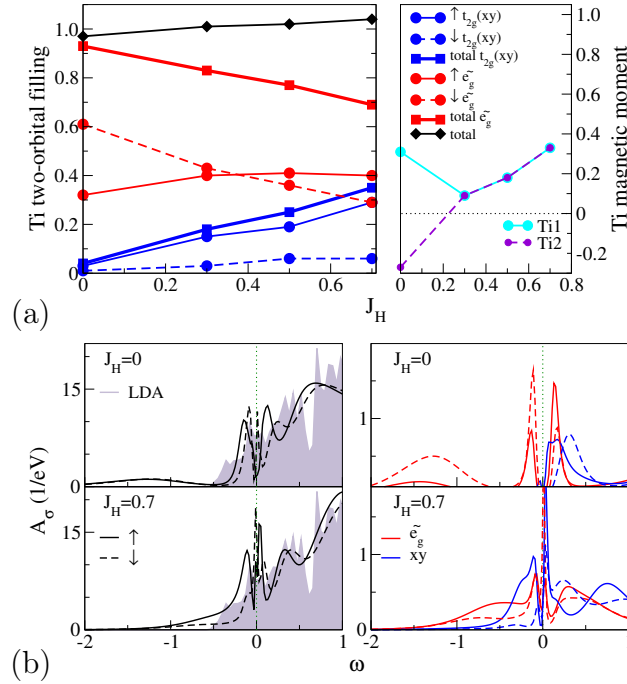


Figure 7.5: DFT-DMFT results depending on J_H for the dense-defect LAO/STO interface with magnetic order ($T=180\text{K}$) [76]. (a) Orbital occupations (left) and Ti magnetic moment (right). (b) total (left) and local (right) spectral function.

atoms at the interface layer are quarter filled ($n_{Ti1}, n_{Ti2} \sim 1$). At $J_H = 0.7$ the less occupied xy orbital has a higher spin polarization than the dominantly occupied \tilde{e}_g orbital and the system is ferromagnetically ordered. In contrast the case $J_H = 0.0$ reveals the vice versa case in respect to spin polarization and the xy is nearly empty. For $J_H = 0.0$ the system is antiferromagnetically ordered. This non-trivial Hund's coupling dependence indicates a double-exchange-like mechanism stabilizing FM or-

der at $J_H = 0.7$. Furthermore Fig. 7.5(b) shows the k -integrated spectral function $A_\sigma(\omega) = \int d\mathbf{k} A_\sigma(\mathbf{k}, \omega)$ for the limits $J_H = 0.0, 0.7$, as well as its orbital contributions. The correlation strength reproduces the known Janus-faced influence of J_H with filling in two-orbital model systems [92]. At quarter-filling lesser Hund's coupling increases correlation strength, resulting in a prominent Hubbard Peak at ~ -1.4 at $J_H = 0.0$. Only the \tilde{e}_g orbital contributes to this incoherent excitation and the Hubbard peak resembles photoemission data [88, 93]. The low metallicity of the system is provided by sites far from the interface. Going to $J_H = 0.7$ the interface has a prominent quasiparticle peak indicating pronounced metallic behavior, but a lower Hubbard band is missing. For intermediate values both features, Hubbard peak and quasiparticle peak are seen [76].

Keeping these results in mind the perspective is broadened to lower OV concentrations in the TiO_2 interface layer. As this requires a sufficient large enough unit cell, calculations are nowadays still too numerical expensive to be treated within DFT+DMFT. Instead, the DMFT results will provide a basis for a model Hamiltonian investigated within the real-space formulation of SBMFT.

7.3 Modelling arbitrary numbers of oxygen vacancies in real-space

A two-orbital Hubbard Hamiltonian based on the vacancy-induced effective \tilde{e}_g state and the in-plane $t_{2g}(xy)$ state, is acting on a 10×10 square lattice with $N_{\text{Ti}}=100$ titanium ions, mimicking the interface TiO_2 layer (see Fig. 7.6). Only the Ti sublattice is treated explicitly and the oxygen degrees of freedom are integrated out within the chosen Hamiltonian form. Only intraorbital NN hoppings are considered in the model and periodic boundary conditions are applied. To explain the model, the dense-defect limit is the focus of attention first. In this limit each Ti site is affected by a nearby OV. In line with Ref. [76], the NN hoppings $t_{\tilde{e}_g}=t_{xy}=0.2$ are used. In contrast to a different modeling by Pavlenko *et al.* [110] the hoppings from the projected-local-orbitals method [2] for larger OV concentration are not strongly orbital dependent. The crystal-field splitting Δ between xy and vacancy-induced \tilde{e}_g is the key-parameter from a noninteracting point of view. Note that Δ is not the usual octahedral crystal-field splitting, which although vital in the stoichiometric compound is not part of the present defect model. From Ref. [76] $\Delta=0.3$ is utilized.

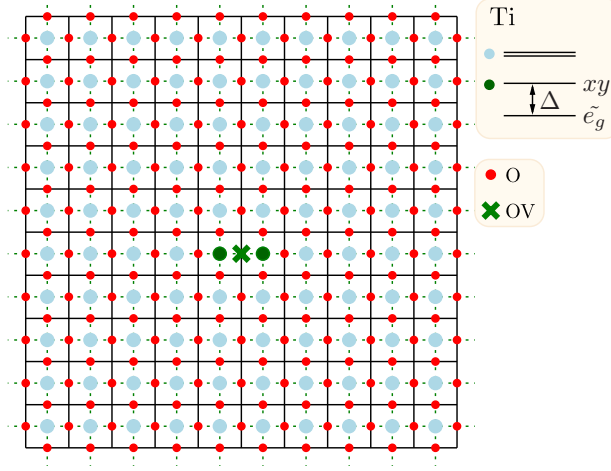


Figure 7.6: Real-space two-orbital modeling on a 10×10 TiO_2 square lattice for the n-type LAO/STO interface.

When applying Coulomb interaction via Hubbard U and Hund's coupling J_{H} at all Ti sites the interacting Hamiltonian reads (similar to Eq. 2.4)

$$\begin{aligned}
 H = & -\tau \sum_{\langle i,j \rangle \alpha \sigma} c_{i\alpha\sigma}^\dagger c_{j\alpha\sigma} - \Delta_i \sum_{i\sigma} (n_{i,\beta,\sigma} - n_{i,xy,\sigma}) + U \sum_{i\alpha} n_{i\alpha\uparrow} n_{i\alpha\downarrow} + \\
 & + \frac{1}{2} \sum_{i,\alpha \neq \alpha',\sigma} \left\{ U' n_{i\alpha\sigma} n_{i\alpha'\bar{\sigma}} + U'' n_{i\alpha\sigma} n_{i\alpha'\sigma} + \right. \\
 & \left. + J_{\text{H}} \left(c_{i\alpha\sigma}^\dagger c_{i\alpha'\bar{\sigma}}^\dagger c_{i\alpha\bar{\sigma}} c_{i\alpha'\sigma} + c_{i\alpha\sigma}^\dagger c_{i\alpha\bar{\sigma}}^\dagger c_{i\alpha'\bar{\sigma}} c_{i\alpha'\sigma} \right) \right\}, \quad (7.2)
 \end{aligned}$$

i, j are site indices, $\alpha, \alpha' = \beta, xy$ and $\sigma = \uparrow, \downarrow$ marks the spin projection, using $U' = U - 2J_{\text{H}}$, $U'' = U - 3J_{\text{H}}$. For the same Hubbard U , the strength of electronic correlations is usually weaker within slave boson theory than within CT-QMC. If not otherwise stated the Hubbard U is thus set to $U=3$ in all calculations. The Hund's coupling is set to $J_{\text{H}}=0.55$, again with variations to smaller/larger values to trace its relevance. In the dense-defect limit $\beta = \tilde{e}_g$ and the same crystal field can be applied at all Ti sites meaning $\Delta_i = \Delta$. By reducing the number of OV Ti ions without neighboring OV come into play. In that case the e_g orbitals are strongly bound to $\text{O}(2p)$ and don't contribute to neither states at the Fermi level nor to local moment formation. So defect-free Ti sites (having no neighbored OV) have no e_g contribution to the low-energy model of Eq. 7.2. To keep the modeling simple the following approximations are utilized:

- (i) the model Hamiltonian (Eq. 7.2) is used for the whole lattice
- (ii) Δ_i is parametrized in the following way

$$\Delta_i = \begin{cases} \Delta, \beta = \tilde{e}_g & : \text{ if OV nearby} \\ 0, \beta = xz/yz & : \text{ if no OV nearby} \end{cases} \quad (7.3)$$

- (iii) multiple OV around a Ti site are forbidden

The second aspect can be justified by the considerable hybridization between \tilde{e}_g and xz, yz in the dense-defect case [76], meaning the \tilde{e}_g degree of freedom takes the role of an additional t_{2g} orbital for Ti sites without nearby OV. The hoppings are neither dependent on the number of OV nor dependent on being neighbor to an OV or not. Such parametrization are not easy to setup and in this study a quite canonical setting should be utilized. Last but not least the OV concentration dependent electron filling needs to be fixed. The electron count considers only the interface layer, the model is not able to describe charge fluctuations to other distant layers. In the dense-defect limit DFT+DMFT retrieved a filling of one electron per Ti site in the interface layer. The defect free case resulted within DFT in 0.5 electrons per Ti site in the interface layer [76], in line with polar-catastrophe avoidance. Putting these two numbers into a linear interpolation scheme yields $n_{tot} = N_{Ti}/2 + N_{vac}$ with N_{vac} the number of OVs and $N_{Ti} = 100$ the number of Ti sites. Note that the vacancy concentration c is defined as $c = N_{vac}/N_O$, where N_O is the number of oxygen sites ($N_O = 200$).

In the following, the ordered magnetic moment m , the orbital moment v , the paramagnetic local spin moment m_{PM} and the orbital polarization ζ are defined as

$$\begin{aligned} m &= \sum_{\alpha} m_{\alpha} = \sum_{\alpha} (\bar{n}_{\alpha\uparrow} - \bar{n}_{\alpha\downarrow}) \quad , \quad v = \sum_{\sigma} (\bar{n}_{\tilde{e}_g, \sigma} - \bar{n}_{xy, \sigma}) \\ m_{PM} &= \left(\sum_{\alpha} S_{\alpha} \right)^2 \quad , \quad \zeta = \frac{\sum_{\sigma} \bar{n}_{\tilde{e}_g, \sigma}}{\sum_{\sigma} \bar{n}_{xy, \sigma}} \quad , \end{aligned} \quad (7.4)$$

where S denotes the local spin operator and $\bar{O} = \langle O \rangle$. Lattice-averaged values Q_{lat} of these quantities Q are computed by $Q_{lat} = Q/N_{Ti}$. The results indicate that three OV concentration regions has to be discriminated.

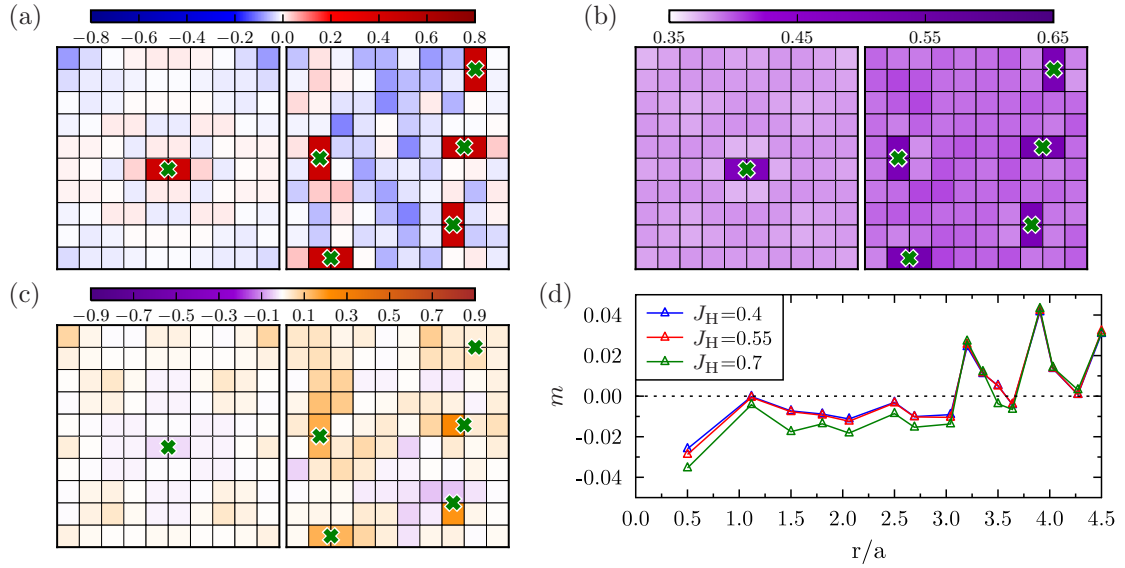


Figure 7.7: Site-resolved quantities of interest for one OV (left) and five OVs (right) in the TiO_2 layer. (a) PM orbital moment v at $J_H = 0.55$, (b) PM local spin moment m_{PM} at $J_H = 0.55$ and (c) ordered magnetic moment m at $J_H = 0.55$. (d) depicts distance-dependent averaged magnetic moment for single defect at $r = 0$ with a interatomic distance.

7.4 Small numbers of oxygen vacancies

It proves instructive to consider first the case of few OVs placed on the lattice. In Fig. 7.7 (a)-(c) important physical quantities are depicted for one OV (left) and five OVs (right). Additionally the radial distance-dependent averaged magnetic moment $m(r)$ is shown in Fig. 7.7 (d) for the single OV case, where the OV is placed at $r = 0$. Already with only one OV oscillations of v and local spin moment in the PM state or ordered magnetic moment show up on the lattice depending on the distance to the OV. As expected the OV induced crystal field leads to an increased v at the OV neighbored sites. Furthermore the OV induced crystal field attracts charge in the energy-lowered \tilde{e}_g orbital. This leads to a higher filling, moving the affected sites closer to half-filling increasing m_{PM} . In close distance to the OV the magnetic order favors antiferromagnetic (AFM) alignment due to the strong correlation induced kinetic exchange τ^2/U . In contrast, the long-range order is ferromagnetic (FM). The exchange order switches from FM to AFM at $r \sim 2.5$. Assuming a Fermi-wave vector k_F modulated RKKY exchange with $J(d) \sim \cos(2k_F d)$ in the low-density limit for the conduction electrons [95], $k_F \sim \pi/10$ is retrieved. This is more or less in

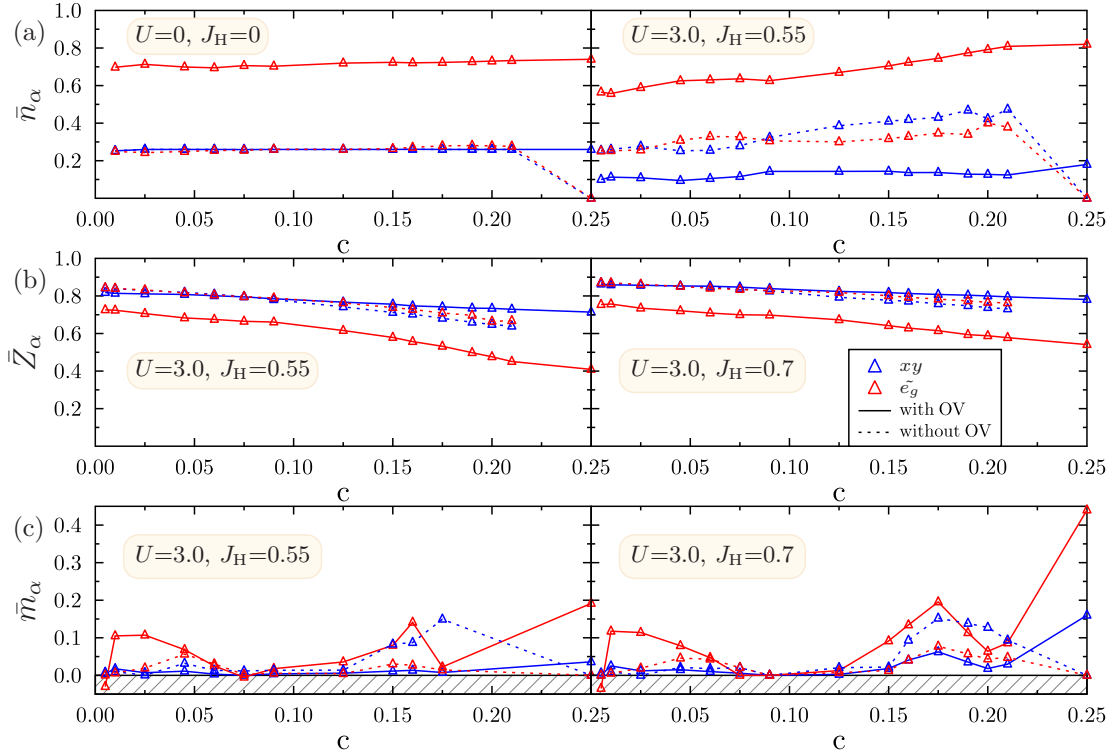


Figure 7.8: Site-averaged orbital-resolved quantities of interest per site type. Discriminated are Ti sites with (straight line) and without neighboring OV (dotted line) as well as xy (blue) and \tilde{e}_g orbital (red). (a) Average occupations (PM state), (b) average quasiparticle weight (PM state) and (c) average ordered magnetic moment (magnetic state).

agreement with the $1/8$ filling. As the local moments are small for a single OV this type of RKKY-like exchange is non-standard. Fig. 7.7 for the five OV setup shows that between the OVs regions form with decreased v or m . Regarding m two types of OV-neighbored sites magnetic orderings can be identified, namely sites ordering antiferromagnetically or ferromagnetically. It proves instructive to discriminate OV-neighbored sites and sites away from OV. The orbital-resolved occupation \bar{n}_α , quasiparticle weight \bar{Z}_α and magnetic ordered moment \bar{m}_α are averaged regarding these two types of sites and shown in Fig. 7.8 (a), (b) and (c), respectively. We focus on $c \leq 0.08$. As expected the crystal field drastically increases the \tilde{e}_g orbital's occupation of OV-neighbored sites. Finite interactions transfer this effect also to sites away from OVs in the considered concentration range $c \leq 0.08$. In contrast, without interaction the orbital occupation away from OVs is degenerate and equal to

the xy occupation near OVs. Because without interaction no exchange mechanism is available, the energy-lowered \tilde{e}_g orbital drains the same amount of electrons from the xy orbital near OV as from each orbital away from the OV. Due to the initial low number of electrons without OVs (50 electrons or $1/8$ filling) \bar{Z}_α starts near the uncorrelated value 1.0. Increasing c , meaning the number of OVs, the number of electrons is increased and more electrons are attracted to the \tilde{e}_g orbital near OVs. This results in an increased correlation in this orbital, while correlations in the xy orbital near OVs and the other orbitals away from OVs are rather concentration independent. The small number of OVs is not enough to see an effect of J_H on \bar{Z}_α . Fig. 7.8 (c) shows that the \tilde{e}_g orbital near OVs carries the dominant contribution to the magnetic moment on the lattice. To estimate now the influence of OVs on the lattice orbital moment ν_{lat} , quasiparticle weight Z_{lat} and ordered magnetic moment m_{lat} these are depicted in Fig. 7.9. Again the focus lies on $c \leq 0.08$. Increasing the

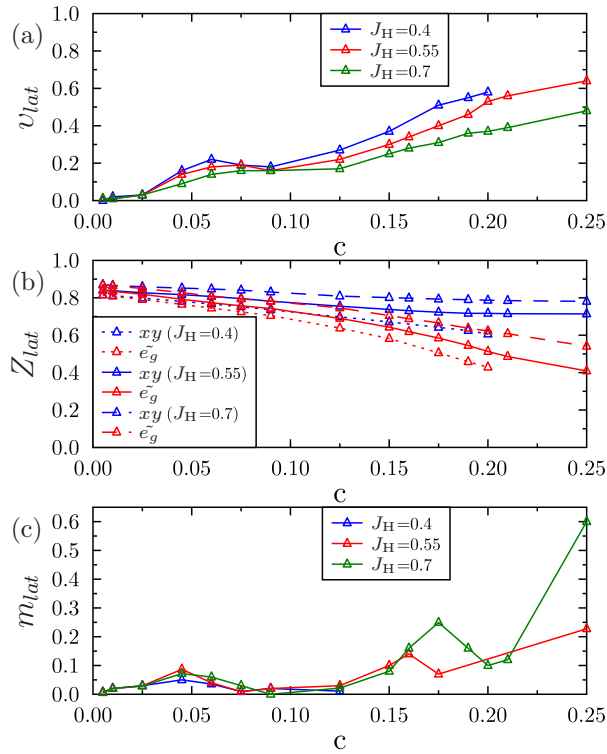


Figure 7.9: Lattice-averaged quantities of interest. (a) Averaged orbital moment ν_{lat} (PM state), (b) averaged orbital-resolved quasiparticle weight Z_{lat} (PM state) and (c) averaged ordered magnetic moment m_{lat} (magnetic state).

number of OVs leads to a monotonically increase of v_{lat} as more sites are affected by the crystal field. Interestingly, the mentioned fact of J_H counteracting the crystal field is already visible for small c in v_{lat} and Z_{lat} . The difference in correlations between orbitals is small in Z_{lat} due to the small number of crystal field affected sites. Regardless the small number of OVs a sizeable FM state arises on the lattice with maximum m_{lat} at $c = 0.045$. Apparently, the RKKY-like mechanism is strong enough to induce a FM state on the whole lattice given only few OVs with preferred FM long-range ordering. Now Fig. 7.8 and 7.9 are used also to understand the other concentration regions in section 7.5 and 7.6.

7.5 Medium number of oxygen vacancies

As before it proves instructive to look at the real-space picture for two concentrations in this regime. In Fig. 7.10 v (a), m_{PM} (b) and m (c) are shown like in Fig. 7.7 before, but now for 18 (left) and 25 OVs (right). At 18 OVs ($c = 0.09$) the transfer of

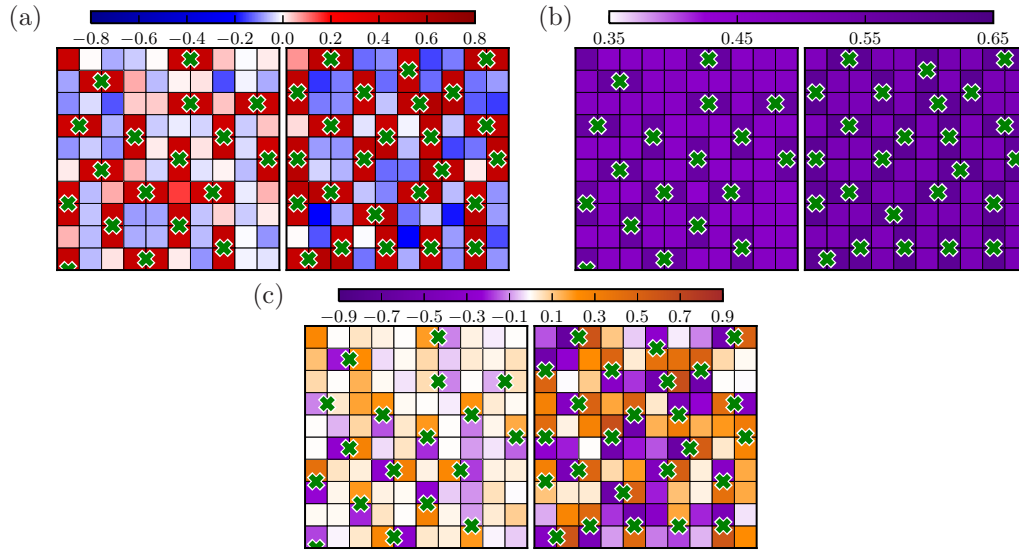


Figure 7.10: Site-resolved quantities of interest for 18 OVs (left) and 25 OVs (right) in the TiO_2 layer. (a) PM orbital moment v at $J_H = 0.55$, (b) PM local spin moment m_{PM} at $J_H = 0.55$ and (c) ordered magnetic moment m at $J_H = 0.55$.

the crystal-field induced $v > 0$ to sites away from OVs is still active. Increasing the number of OVs further to 25 ($c = 0.125$) leads to dramatic changes. The lattice is

almost bipartite in the sense that only sites near OVs have $v > 0$ and all other $v < 0$. The number of OVs is large enough and the number of electrons small enough that all \tilde{e}_g near OVs are preferably occupied. This qualitative change can also be seen in Fig. 7.8 (a), where away from OVs now the xy orbital has a higher occupation than the other orbital for $c > 0.08$. This leads to a shoulder in the lattice-averaged orbital moment (see Fig. 7.9 (a)). Additionally in this concentration region the local spin moment m_{PM} becomes quite homogeneous discriminating only sites near and away from OVs as expected. Most interestingly the lattice displays only a very weak FM state (see Fig. 7.9 (c)), due to the dominating AFM kinetic exchange. This exchange turns nearly all sites near OVs into AFM pairs (see Fig. 7.10 (c)).

7.6 High numbers of oxygen vacancies

Finally turning to the dense OV case, starting as before with a real-space picture for two selected OV configurations, this time 30 and 35 OVs are shown in Fig. 7.11. The local spin moment away from OV is even higher than in the concentration region before (compare 7.11 (b) and Fig. 7.10 (b)). Differences in v and m between these two OV numbers are small and subtle. Above $c = 0.125$ non-local double exchange between \tilde{e}_g orbital near OVs and xy orbital away from defects (see Fig. 7.8 (c)) leads to a FM state with sizeable m_{lat} . The latter is depicted in Fig. 7.9 (c). Between 30 and 35 OVs (for $J_{\text{H}} = 0.55$) the kinetic exchange is restrengthened as filling gets closer to half-filling. This leads to a formation of additional AFM pairs, decreasing m_{lat} , as can be also revealed by closer inspection of Fig. 7.9 (c). Considering $J_{\text{H}} = 0.7$ in Fig. 7.9 (c) shifts the minimum in m_{lat} to higher c . Again as Fig. 7.8 (c) reveals, the competition between non-local double-exchange and kinetic exchange can be held responsible. The higher J_{H} enforces the double-exchange and the kinetic exchange has to be even closer to half-filling to induce the reformation of some AFM pairs. Additionally in this concentration region the competition between J_{H} and the crystal field also becomes obvious in the quasiparticle weight \bar{Z}_α (see Fig. 7.8 (b)) or lattice-averaged orbital moment (see Fig. 7.9 (a)). This is due to the fact that in this region most of the sites of the lattice are neighbored to an OV and therefore affected by a crystal field.

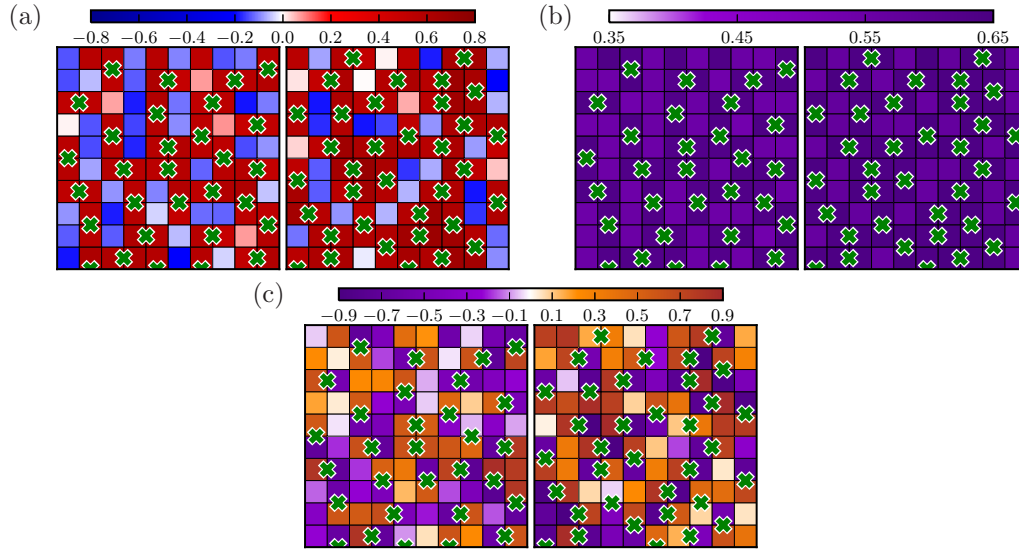


Figure 7.11: Site-resolved quantities of interest for 30 OVs (left) and 35 OVs (right) in the TiO_2 layer. (a) PM orbital moment v at $J_{\text{H}} = 0.55$, (b) PM local spin moment m_{PM} at $J_{\text{H}} = 0.55$ and (c) ordered magnetic moment m at $J_{\text{H}} = 0.55$.

7.7 Summary

Charge self-consistent DFT+DMFT for LAO/STO supercells depicts the competition of magnetic processes related to the orbital fillings of \tilde{e}_g and xy orbital. Using $J_{\text{H}} = 0$ an AFM state is obtained at the interface induced by a dominant \tilde{e}_g orbital, where the xy orbital is nearly empty. Conversely at $J_{\text{H}} = 0.7$ the xy orbital shows a higher spin polarization inducing a FM state, although it is still weaker populated than the \tilde{e}_g orbital. This already shows the importance of double-exchange (DE) processes to induce FM. Note that the system remains itinerant regardless J_{H} , where metallicity is provided by sites far from the interface for vanishing J_{H} and by sites at the interface at finite Hund's coupling. Additionally the strongly correlated dense-defect limit is depicted by a lower Hubbard band of \tilde{e}_g kind. Considering now a broad range of oxygen vacancy (OV) concentrations on a 10×10 TiO_2 model interface renders further magnetization processes induced by Coulomb interactions clear. Relevant for the discussion of these processes is the distinction of Ti sites near and away from OVs. Already a single defect induces oscillations in magnetic and orbital moment throughout the lattice. The distance-dependent magnetic moment can be explained in a RKKY-like picture, where a standard application is not possible due

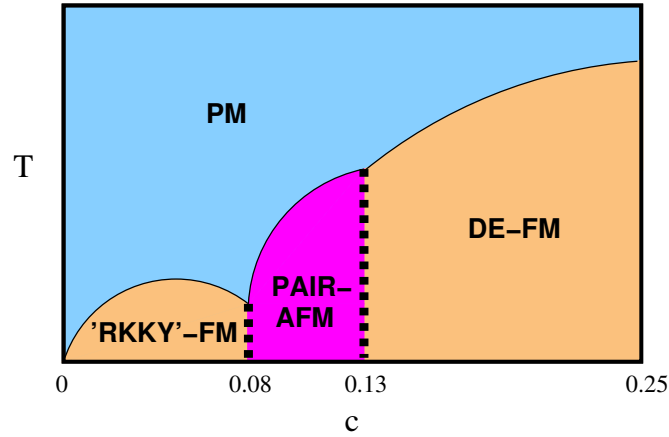


Figure 7.12: Rough sketch of a finite-temperature (T) magnetic phase diagram for OV-concentrations c based on the real-space slave boson mean-field theory modeling of the LAO/STO interface.

to small local moments. One or five vacancies are already enough to impose a weak FM state, where the stoichiometric interface does not show magnetic order. The five OV case also displays AFM ordering on Ti sites neighboring OVs induced by kinetic exchange due to strong correlations. So far this means two types of Ti sites near OVs are revealed, one favors AFM and the other FM alignment. Going from the dilute to the dense-defect limit Fig. 7.12 summarizes the main results. For small amounts of OVs the RKKY-like mechanism weakly FM polarizes the lattice. The expected Curie temperature T_c is rather low due to the delicate exchange mechanism. Above $c_p = 0.08$ pairs of AFM aligned Ti sites near OVs dominate the lattice and no spin polarization is present on Ti sites away from OVs. Increasing the concentration of OVs further above $c_p \sim 0.13$ strengthens DE local processes to switch these AFM pairs to FM alignment. DE non-local processes are also enforced inducing FM spin-polarization in the 'interstitial' region (Ti sites without near OV). This robust FM order has supposedly a relatively high T_c . The Hund's coupling influences the competition between AFM-like kinetic exchange and DE processes near OVs. Possible phase transitions between these three phases were not considered in this study. Having no coherent order parameter and symmetry distinction first-order (-like) phase transitions with coexistence regions are expected. The obtained behavior with OV concentration agrees with several features from experimental results. Generally it is in line with the found key-dependence of magnetism on electron doping in STO-based materials. Interplay of AFM and FM tendencies has recently been identified

in Bi *et al.* [14]. Experimentally LAO/STO ferromagnetism has been observed in different ranges of temperature. This may be linked to substantial differences in the number of vacancies in the respective samples. While low defect numbers are imposing RKKY-like FM low T_c behavior [32, 118], high defect concentrations stabilize the DE-FM phase with high T_c near room temperature [8, 14]. Another explanation to such different types of ferromagnetism could be inhomogeneous samples. This would need theoretical treatment by even larger supercells, which is numerically hard to achieve. From a theoretical point of view this chapter shows that real-space SBMFT can not only be applied to single-orbital homogeneous and single defect cases, but also to a complex three-orbital Hamiltonian on a large lattice. The application leads to a physical sound description sharing experimentally observed features, where the used setup is at present numerically out of reach for technically more advanced methods like DFT+DMFT.

8 Real-space magnetization dynamics

The Hubbard model [48] contains two approaches towards magnetism in solid state systems. The first is the explanation of magnetism as induced by local magnetic moments on atoms first expressed in the Langevin-Weiss theory and described in the Weiss model for ferromagnets [73, 147]. Quantum mechanics is necessary to reason the occurrence of these local moments (Bohr-van Leewen theorem, [140]). This first approach is contained in the Hubbard model, as the large interaction limit leads to a spin Hamiltonian [109], the Heisenberg Hamiltonian with the Weiss model being its mean-field approximation [103]. The second approach towards magnetism is itinerant electron focused. A central result of this approach is the Stoner model [133], which has found numerous quite successful applications to ferromagnets like Iron and Nickel (among them [31, 87]). However the model is not constrained to explaining ferromagnetic (FM) order, it can also describe for example antiferromagnetic (AFM) order. The Stoner model is the mean-field approximation of the Hubbard model [109], which is a reasonable approximation for small interaction. Both limits Stoner and Heisenberg model (called in the following also Stoner and Heisenberg limit) suffer from limitations. The former contains only longitudinal magnetic excitations [109] leading to problems like overestimation of Curie temperatures [103]. The latter contains only transversal magnetic excitations [109] and can't describe for example magnetic order in some transition metals [1]. So in principle the Hubbard model has the ingredients to provide a complete picture of for example magnetic excitations in an arbitrary sufficiently correlated solid state system. The problem is, that there are only few exact solutions like for example the magnetic excitation spectrum of an one-dimensional Hubbard chain [9, 155], obtained by using the Bethe ansatz [82]. In this chapter the focus lies on magnetic excitations in the two-dimensional Hubbard model, where up to now no exact solution is available. TD-SBMFT in its real-space formulation is utilized. First the equilibrium (section 8.1) and non-equilibrium

setup (section 8.2) is explained. Then in section 8.3 real-space TD-SBMFT is tested by computing magnetic excitations of an AFM ground state in the Stoner limit (small U , section 8.3.1) and Heisenberg limit (large U , section 8.3.2). The results are compared to the well-known collective spin excitations (magnons) of an AFM ground state in the Heisenberg model [50, 51, 131] and the electron-hole excitations of the Stoner model known as Stoner excitations [65, 98, 130, 142]. Even though the Stoner model is primarily used to describe ferromagnets, Stoner excitations are known to occur also in antiferromagnets [130]. Afterwards two strengths of real-space TD-SBMFT are revealed in section 8.4. Magnetic excitations between Stoner and Heisenberg limit are addressed and the results are connected to the both interaction limits in section 8.4.1. As real-space TD-SBMFT operates on the Hubbard model also intermediate interaction values can be considered. As a second strength going away from linear response the influence of a pulsed stronger magnetic field onto the magnon dispersion is revealed in section 8.4.2. The chapter concludes with a summary in section 8.5.

8.1 Equilibrium setup

We operate on the generic single-orbital half-filled Hubbard model on a two-dimensional 6x6 or 8x8 simple cubic lattice. Periodic boundary conditions and units of half-bandwidth W are used. In addition to hopping τ and Hubbard- U a site-dependent magnetic field $\mathbf{B}(\mathbf{r})$ is utilized. This leads to the following Hamiltonian

$$\mathcal{H} = \underbrace{\sum_{i,j} \sum_{\sigma} \tau_{i\sigma j\sigma} d_{i\sigma}^{\dagger} d_{j\sigma}}_{\mathcal{H}^{kin}} + \text{h.c.} + \underbrace{\sum_i U n_{i\uparrow} n_{i\downarrow} - \sum_i \mathbf{B}(\mathbf{r}_i) \cdot \mathbf{S}_{\mathbf{p}}}_{\mathcal{H}^{loc}}, \quad (8.1)$$

where i, j label sites, σ is a spin index and $\mathbf{S}_{\mathbf{p}}$ the spin operator. $\mathbf{B}(\mathbf{r})$ is needed to enforce the AFM ground state at different U depicted in Fig. 8.1 or 8.2. Note that numerical calculations indicate that the AFM state is indeed the ground state of the two-dimensional Hubbard model at half-filling [18, 152]. However a small magnetic field of $|\mathbf{B}(\mathbf{r})| = 0.002$ is sufficient to establish this. In the following the short-hand notation site 1=(0,1,1) and 2=(0,2,1) for (x,y,z) in Fig. 8.1 is used. Important physical quantities from the equilibrium AFM results are shown in Tab. 8.1. Note that $|m|$ is equal at each site. If not mentioned otherwise, the 6x6 lattice is used. At $U = 0.4$ a band magnetism Stoner limit is observed, in which magnetic moment and

local spin-spin correlation are quite small. For $U = 0.4$ instead of Fig. 8.1 the Fig. 8.2 describes the emerging AFM order. The exchange interaction splits the density

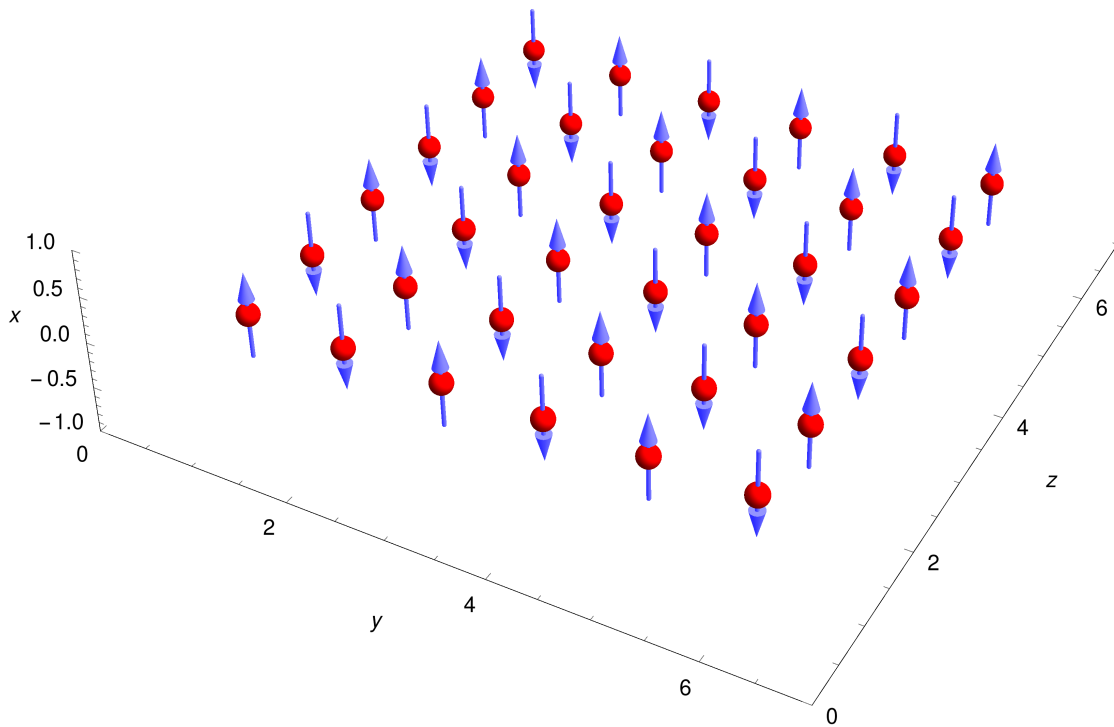


Figure 8.1: Sketch of the antiferromagnetic ground state as spin state in the Heisenberg limit. Blue arrows indicate spins, red balls atoms. Note that the x-axis is pointing out-of-plane, while y- and z-axis are residing in plane.

Lattice	U	$ \langle m \rangle $ (max. 1.0)	$\langle S^2 \rangle$ (max. 0.75)	Energy gap
6x6	0.4	0.39	0.46	0.06
	1.0	0.62	0.56	0.33
	2.0	0.86	0.67	2.40
	3.0	0.94	0.71	3.22
8x8	0.4	0.34	0.45	0.06

Table 8.1: Important quantities from equilibrium antiferromagnetic results with equal $|m|$ for each site of the lattice. In detail, Hubbard- U , magnetic moment m , local spin-spin correlation S^2 and energy-gap around the Fermi level are listed.

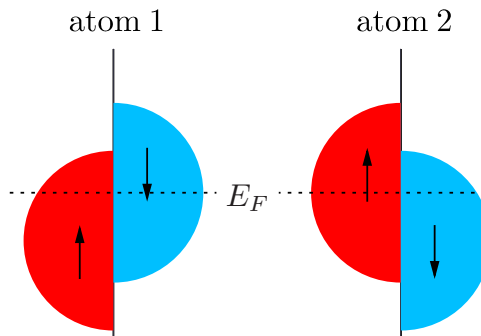


Figure 8.2: Sketch of the antiferromagnetic ground state as itinerant electron state of a two-atom unit cell in the Stoner limit. Half-circles denote spin-dependent density of states and E_F denotes Fermi level shown as dotted line.

of states into two spin-dependent parts, which are shifted with respect to each other. Therefore more spin-up than spin-down states are occupied on atom 1 and vice versa on atom 2 leading to an AFM state. Increasing U increases magnetic moment and local spin-spin correlation until at $U = 3.0$ the spins are almost full polarized and the Hamiltonian can be approximated by a Heisenberg model of spins. In this limit Fig. 8.1 describes the ground state in an exact way. Note that for all values of U a finite energy gap at the Fermi level persists, meaning the equilibrium ground state is an AFM insulator [151]. As the paramagnetic Mott transition is at about 3.05, the value of $U = 3.0$ resides in the highly correlated limit of the Hubbard model supporting the approximation by a Heisenberg model. The shift of the paramagnetic Mott transition in contrast to chapter 4 can be explained solely by the fact, that here a two-dimensional lattice is used, where in chapter 4 a three-dimensional lattice is utilized.

8.2 Non-equilibrium setup

The focus lies on the recovery of linear-response results obtained at large U (Heisenberg limit) and small U (Stoner limit) especially the corresponding magnetic excitations. To stay within the linear-response regime, when exciting the system, a kick instead of a quench is used (see Fig. 8.3 (c)). In the quench case there is a sudden switch of the equilibrium Hamiltonian \mathcal{H}_i to \mathcal{H}_f at $t > 0$ and then \mathcal{H}_f acts for all $t > 0$. Contrary in the kick case \mathcal{H}_f acts for all $t' > t > 0$ with kick time t' and for

$t > t'$ the Hamiltonian is switched back to \mathcal{H}_i . The expectation is that tuning the kicktime a smooth transition from linear-response to non-linear response regime can be obtained. The aim is now to find a suitable \mathcal{H}_f to destroy the high equilibrium symmetry of the lattice (effective two-atom unit cell, see Fig. 8.1) and generate all possible magnetic excitations in one calculation. A kick of the system to a state, where to each site i a random magnetic field vector $\mathbf{B}_f(\mathbf{r}_i)$ in y - z plane is applied with zero x component and fixed absolute value $|\mathbf{B}_f| = |\mathbf{B}_f(\mathbf{r}_i)| \forall i$ should induce all possible magnetic excitations. As a finite lattice is considered, it is beneficial to consider only a discrete number of magnetic field $\mathbf{B}_f(\mathbf{r}_i)$ configurations in the y - z plane for each site i . We consider the angle α to the y -axis in the y - z plane and the discrete configurations $\alpha = m \cdot \frac{2\pi}{n}$, where n is the number of total configurations and $m \in \{1, 2, \dots, n\}$. In the following a on this way generated $\mathbf{B}_f(\mathbf{r})$ is characterized by n and $|\mathbf{B}_f|$. In Fig. 8.3 (a) is sketched, which magnetic field configurations

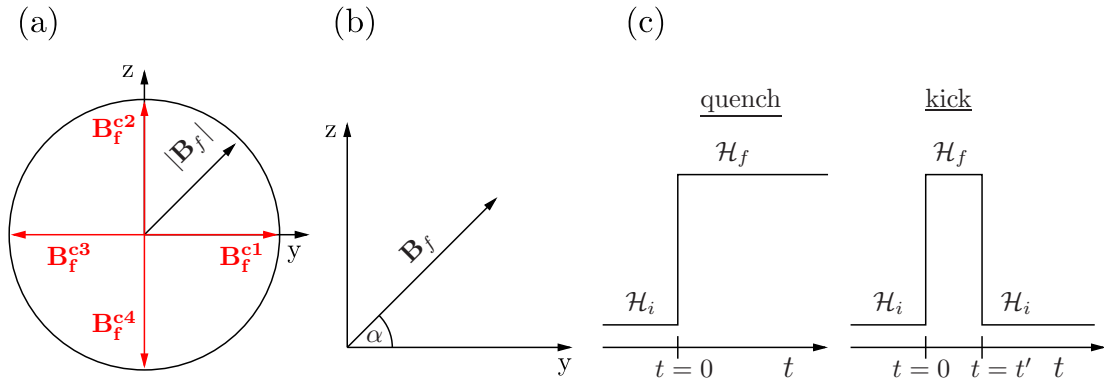


Figure 8.3: (a) Sketch of the possible magnetic field configurations ($\mathbf{B}_f^{c1}, \dots, \mathbf{B}_f^{c4}$) of $n = 4$ applied during the kick in \mathcal{H}_f at one given site. (b) Definition of the angle α and the magnetic field \mathbf{B}_f . (c) Sketch of a quench and a kick with kick time t' .

($\mathbf{B}_f^{c1}, \dots, \mathbf{B}_f^{c4}$) are possible for $n = 4$ at one site and in (b) the definition of α and the corresponding $\mathbf{B}_f(\mathbf{r}_i)$. Furthermore in (c) the difference between quench and kick is sketched. Again as the linear-response regime is most interesting at first, small magnetic fields $|\mathbf{B}_f|$ are considered. To compute the magnetic excitations of a system the Fourier transform $\tilde{\mathbf{m}}$ of the magnetic moment $\mathbf{m}(\mathbf{r}, t)$ is computed via

$$\tilde{\mathbf{m}}(\mathbf{q}, \omega) = \frac{1}{(2\pi)^3} \int d\mathbf{r} \int dt \mathbf{m}(\mathbf{r}, t) e^{-i\mathbf{q}\mathbf{r}} e^{-i\omega t}, \quad (8.2)$$

where \mathbf{q} is a point in momentum space. Note that the vector structure is left intact by this Fourier transform, meaning $\tilde{\mathbf{m}}$ has like \mathbf{m} a x -, y - and z -component. This enables a separation of longitudinal (x -direction) and transverse (y - and z -direction) modes (compare Fig. 8.1). The real-space grid limits the resolution in $\mathbf{q} = (q_y, q_z)$ and leads to the following sampling of the Brillouin zone shown in Fig. 8.4. In the following $\tilde{\mathbf{m}}(\mathbf{q}, \omega)$ is depicted along the shown way through the Brillouin zone with high symmetry points $\Gamma = (0,0)$, $X = (\pi,0)$ and $M = (\pi, \pi)$. Until stated otherwise the time evolution captures times until $t_{tot}=1800$. This provides a suitable high energy resolution of the magnetic excitations of $\Delta\omega = 0.003$.

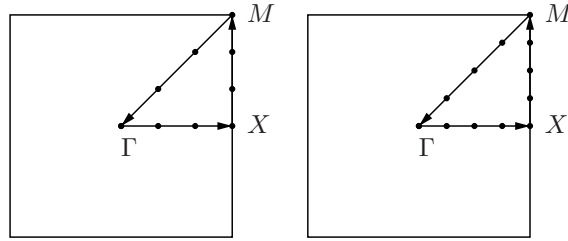


Figure 8.4: Accessible $\mathbf{q} = (q_y, q_z)$ -point in simple cubic Brillouin zone denoted as black circles for 6x6 (left) and 8x8 lattice (right). Arrow indicate the way through the Brillouin zone with high-symmetry points $\Gamma = (0,0)$, $X = (\pi,0)$, $M = (\pi, \pi)$ used for plotting $\tilde{\mathbf{m}}(\mathbf{q}, \omega)$ (see Eq. 8.2).

8.3 Testing the real-space time-dependent slave boson mean-field theory

8.3.1 Results in the Stoner limit (weak interaction)

To obtain results in the Stoner limit $U = U_i = U_f = 0.4$ is selected. The AFM ground state (Fig. 8.2) is kicked using $\mathbf{B}_f(\mathbf{r})$ with $n = 4$, $|\mathbf{B}_f|=0.002$ and a small kicktime $t'=5.0$ to be in the linear-response regime. The obtained magnetization dynamics at site 1 and 2 are shown in Fig. 8.5 (left) and (right), respectively. As these sites are neighbored the magnetization along x has opposite sign. The observed dynamics render no clear picture if there is a longitudinal mode excited or not. In all components the amplitudes are really small. So all components of $\tilde{\mathbf{m}}$ have to be checked now. Looking at \tilde{m}_x in the Brillouin zone in Fig. 8.6, we see that the magnetic excitations cover a broad range of energies up to ~ 2.0 . Note that the left

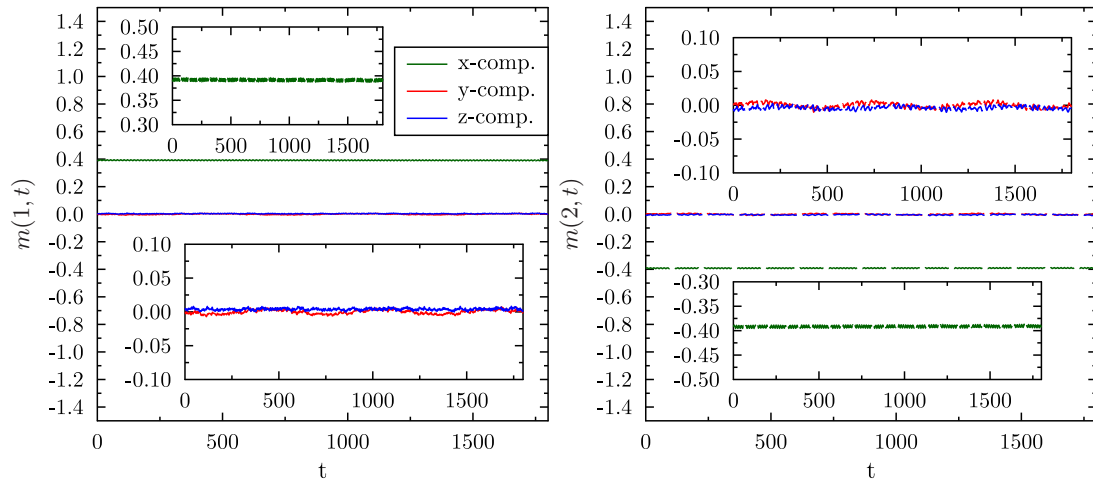


Figure 8.5: Magnetization dynamics at site 1 (left) and 2 (right) at $U=0.4$, $n=4$ with kick time 5.0 and $|\mathbf{B}_f|=0.002$.

image has a smaller energy range than the right one to increase visibility of the magnetic excitations. As the spin nature of the electrons at 0.4 is weak (compare section 8.1) and the itinerant nature strong the magnetic excitations are not describable by magnon formation. Instead electron-hole excitations arise called Stoner excitations [65, 98, 130, 142], which can have a high energy in the order of eV . In contrast

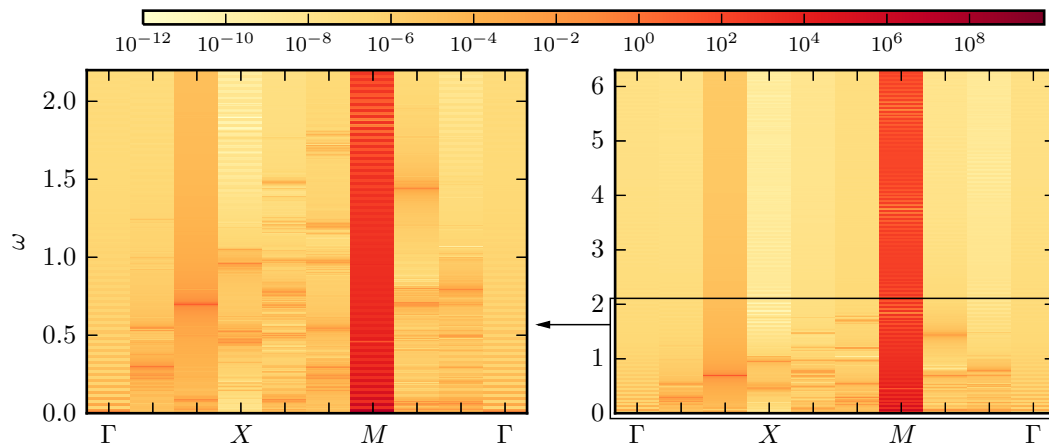


Figure 8.6: \tilde{m}_x along a path through the Brillouin zone with the high symmetry points Γ , X and M at $U=0.4$, $n=4$ with kick time 5.0 and $|\mathbf{B}_f|=0.002$. The left image is just a blowup of the right image indicated by the boxed area.

magnons have smaller energies. In the non-equilibrium setup a magnetic field in the y-z plane is applied during the kick, meaning transverse modes are the primary focus. Non-surprisingly, this non-equilibrium setup destabilizes the AFM longitudinal order seen in the strong incoherent excitation at the M -point, which is just the magnetic order symmetry of the system. In contrast the magnetic excitations at all other \mathbf{q} -points are only weakly contributing as the transverse focused setup only weakly affects the x -component. With this in mind, we can turn now to \tilde{m}_y and \tilde{m}_z depicted in Fig. 8.7. In \tilde{m}_y the magnetic excitations have stronger weight at \mathbf{q} -points away from $\mathbf{q} = M$ compared to \tilde{m}_x due to the chosen non-equilibrium setup. There is initially no $\mathbf{q} = M$ ordering mode in y-direction, consequently no

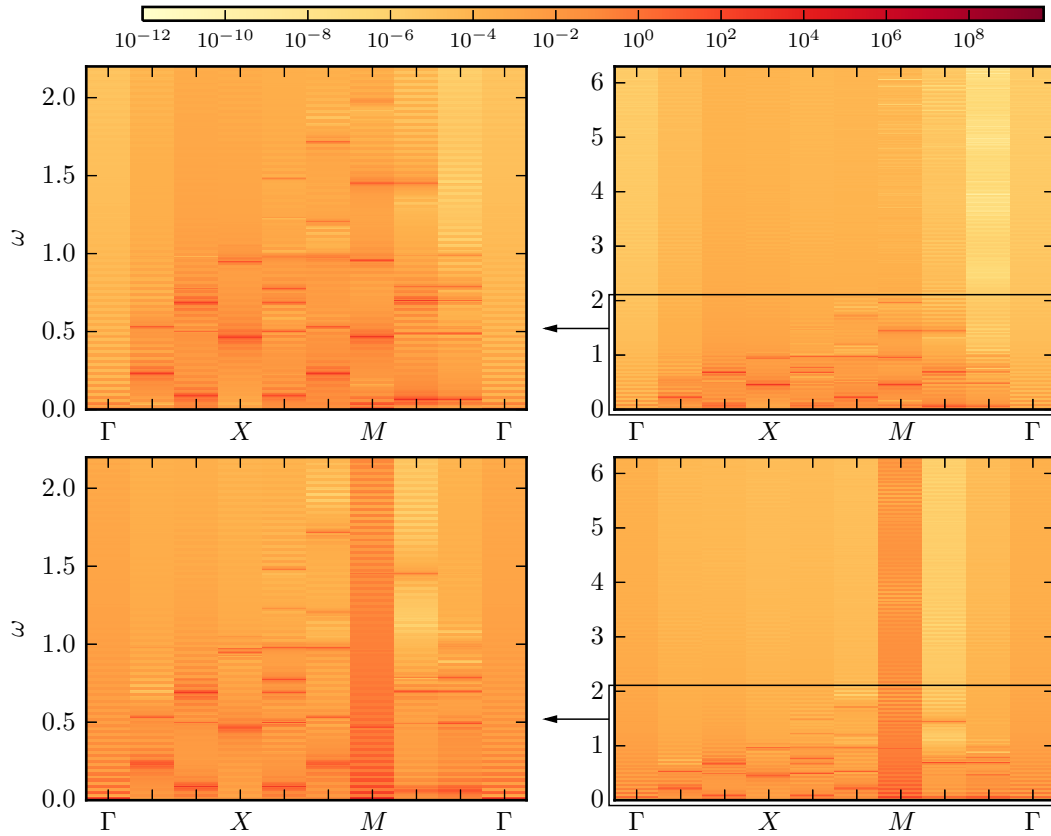


Figure 8.7: \tilde{m}_y (top) and \tilde{m}_z (bottom) along a path through the Brillouin zone with the high symmetry points Γ , X and M at $U=0.4$, $n=4$ with $t'=5.0$ and $|\mathbf{B}_F|=0.002$. The left image in each row is just a blowup of the right image indicated by the boxed area.

inhomogeneous excitation shows up at $\mathbf{q} = M$. The distribution of magnetic excitations over the same energy range of ~ 2.0 eV is similar to \tilde{m}_x , yet not identical. As the non-equilibrium setup prefers transverse modes, while the system is close to the Stoner limit preferring longitudinal modes, an anisotropy regarding longitudinal (x) and transversal (y, z) direction is expected. Due to the used small magnetic field and kicktime to remain in linear-response the anisotropy is small. Finally \tilde{m}_z renders the same results as \tilde{m}_y apart from a inhomogeneous excitation at $\mathbf{q} = M$ similar but weaker as seen in \tilde{m}_x . This is due to a numerical reason. TD-SBMFT is only able to time-evolve matrix elements, which are at equilibrium non-zero. Due to this fact at equilibrium also a very small (1 % of x -component) magnetic field in z -direction is applied to make sure that the matrix elements are generated such that magnetic order in z -direction can show up for $t > 0$. This generates a very weak AFM order also in z -direction ($m \sim 0.003$), which induces this weak inhomogeneous excitation (compare to \tilde{m}_x , which is about 10 orders of magnitude higher). In general the discovered magnetic excitations are in qualitative agreement with Stoner excitations observed in magnetic systems [65, 98, 130, 142]. Additionally the evolution of the maximum magnetic excitation energy along $\Gamma - M$ is in agreement with a previous study [152]. A crucial point however is that Stoner excitations show up in energy bands meaning a quasi-continuum of states in a certain energy range. So the question is, whether more magnetic excitations in the same energy range are seen for a larger lattice. This would indicate a quasi-continuum of states in the thermodynamic limit. It is also possible to compute $\tilde{\mathbf{m}}$ for a 8x8 lattice using the same equilibrium and non-equilibrium setup. As depicted in Tab. 8.1 the equilibrium state at $U = 0.4$ on the 8x8 lattice shows a slightly smaller magnetic moment than the 6x6 lattice, all other physical quantities are very similar. Additionally the Brillouin zone is slightly better resolved (see Fig. 8.4) than on the 6x6 lattice. Turning now to $\tilde{\mathbf{m}}$ shown in Fig. 8.8 proves the Stoner excitations picture. An increased number of magnetic excitations show up in an unchanged energy range of maximal ~ 2.0 . Additionally a weak inhomogeneous excitation at the M point is present for \tilde{m}_y . As no AFM order occurs in m_y at equilibrium, only in the other components, this result indicates that dynamically an inhomogeneous excitation in the y -direction evolves. Such dynamical evolution could also be supported by the increased number of Stoner excitations strengthening fluctuations in the system. Note that another $\mathbf{B}_f(\mathbf{r})$ was generated for the 8x8 lattice compared to the 6x6 lattice indicating that qualitatively the same results can be obtained regardless the concrete structure of $\mathbf{B}_f(\mathbf{r})$ used during the

kick. Furthermore in the appendix section A.2.1 qualitatively the same magnetic

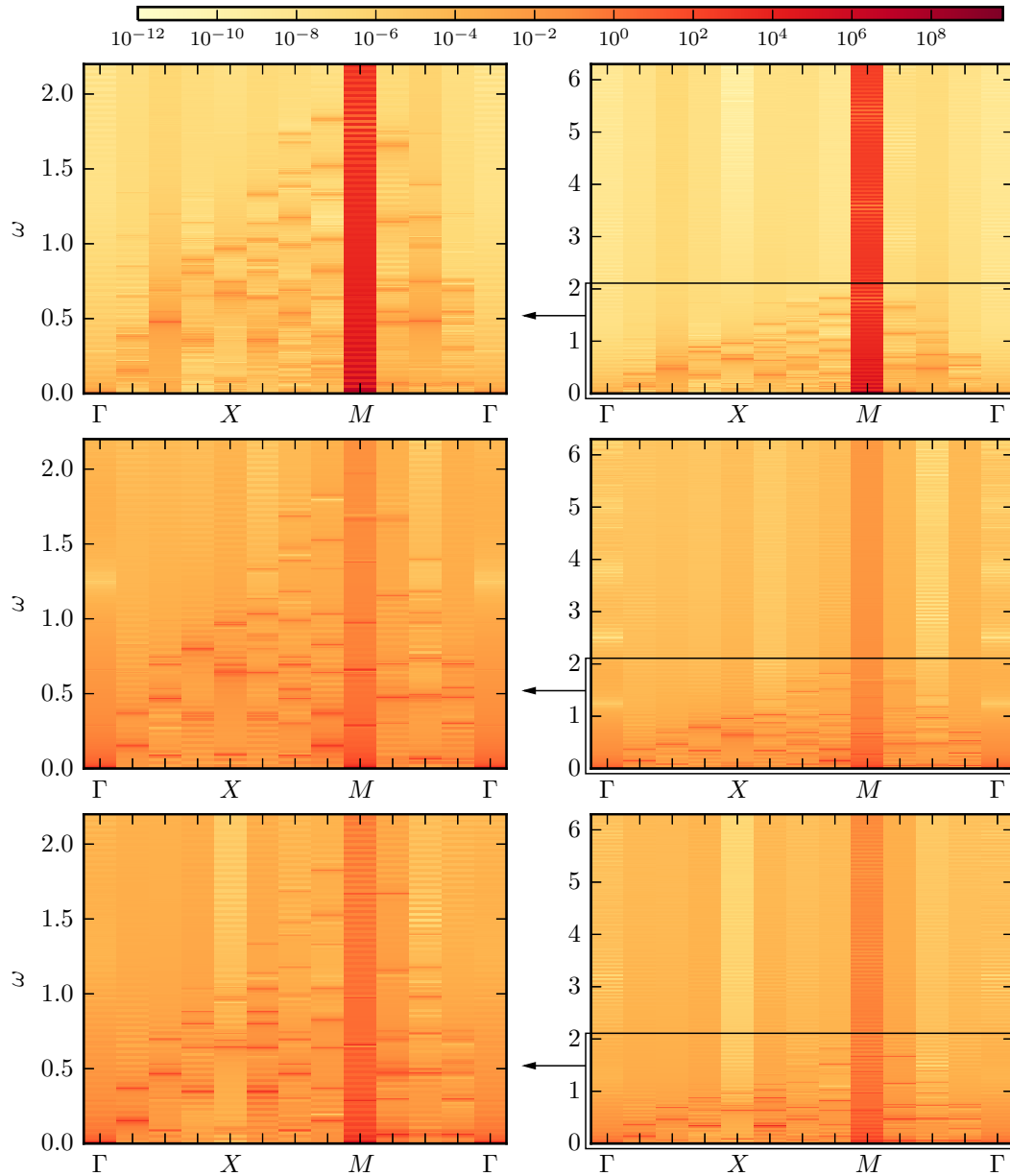


Figure 8.8: \tilde{m}_x (top), \tilde{m}_y (middle) and \tilde{m}_z (bottom) along a path through the Brillouin zone with the high symmetry points Γ , X and M at $U=0.4$, $n=4$ with $t'=5.0$ and $|\mathbf{B}_f|=0.002$ for 8×8 lattice. The left image in each row is just a blowup of the right image indicated by the boxed area.

excitations are retrieved using another $\mathbf{B}_f(\mathbf{r})$ with $n = 6$. Finally, it is interesting how much the results depend on the fact, that $\mathbf{B}_f(\mathbf{r})$ is applied in the y-z plane (see section 8.2). As the AFM order is established along the x-direction in equilibrium and the Stoner limit favors longitudinal modes the y-z plane magnetic field is not optimal to generate longitudinal magnetic excitations. For this reason the same setup as described in section 8.2 is used with the difference of applying the magnetic field in the x-z plane. The results are depicted in the appendix section A.2.2. They show that the small kicktime and small magnetic field during the kick are not sufficient to generate locally longitudinal magnetic excitations. Additionally the $\tilde{\mathbf{m}}$ retrieved by kicking in the x-z plane qualitatively agrees with the $\tilde{\mathbf{m}}$ kicked in the y-z plane previously discussed. So also globally no additional longitudinal magnetic excitations are generated. All components show Stoner excitations in the range of up to ~ 2 . The AFM order is destabilized into an inhomogeneous excitation for \tilde{m}_x .

8.3.2 Results in the Heisenberg limit (strong interaction)

As the Heisenberg limit is considered, $U = U_i = U_f = 3.0$ is utilized. The AFM ground state (Fig. 8.1) is kicked with $\mathbf{B}_f(\mathbf{r})$ (not the same as in the Stoner limit) with $n = 4$, $|\mathbf{B}_f|=0.002$ and a kicktime $t'=5.0$ to be in the linear-response regime. The obtained magnetization dynamics for $n = 4$ at site 1 and 2 are shown in Fig. 8.9 (left) and (right), respectively. These two sites are neighbored leading to opposite sign in the AFM order direction x . There is no visible dynamics in the x-component only small numeric deviations over the whole time frame. The dynamics in y- and z-direction are expected as in the Heisenberg Limit only transverse modes can be excited. Additionally the absolute value $|m|$ does nearly not change over time as m_y and m_z show only small amplitudes. This is also in good agreement with using

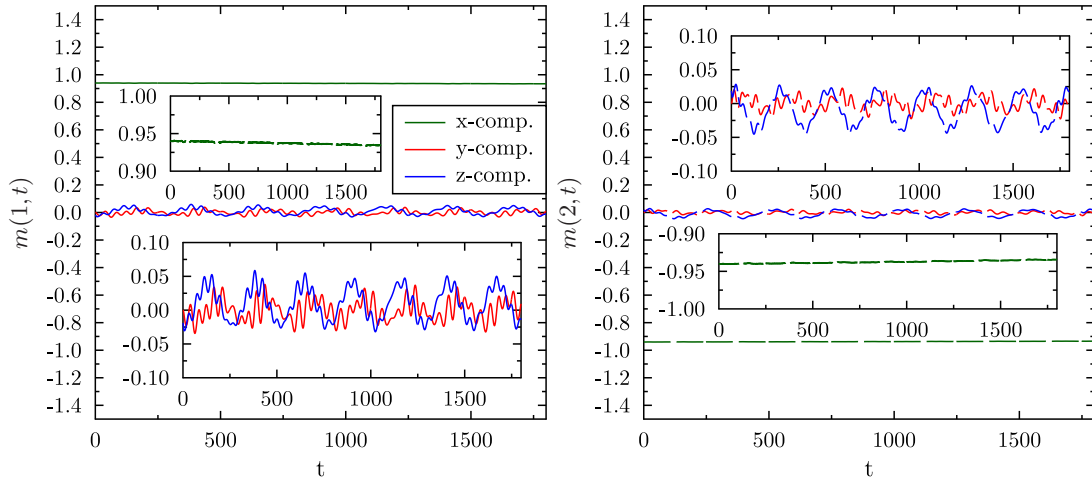


Figure 8.9: Magnetization dynamics at site 1 (left) and 2 (right) at $U=3.0$, $n = 4$ with $t'=5.0$ and $|\mathbf{B}_f|=0.002$.

a Heisenberg spin Hamiltonian, because there the spin is constant over time. Thus transverse modes can be focused, when computing $\tilde{\mathbf{m}}$. Accordingly in Fig. 8.10 \tilde{m}_y (top) and \tilde{m}_z (bottom) are depicted in the Brillouin zone. Note the different energy ranges used in the left compared to the right image to enhance the visibility of the low energy magnetic excitations. One can recognize in both figures the low energy magnetic excitations known as magnon excitations from spin-wave theory [50, 51]. The height of 0.175 eV is in agreement with previous model works [51], where the result was $\sim 1.0 \tau S_z$ leading here to a value of 0.20. Note that the displacement from zero is consistent with a small energy scale J_{exc}/ζ , where J_{exc} is the exchange

coupling and ζ the correlation length. Due to the Goldstone theorem [101], magnons must have zero energy at $\mathbf{q} = \Gamma$. It is important to note, that the so far discussed results do not depend on the choice of $\mathbf{B}_f(\mathbf{r})$ (see section 8.2). Of course, the magnetization dynamics are changed at a given site, when changing $\mathbf{B}_f(\mathbf{r})$, but the magnon dispersion remains the same. This can be seen in the Appendix A.2.3, where the same magnon dispersion and qualitative magnetization behavior is retrieved using another $\mathbf{B}_f(\mathbf{r})$ with $n = 6$ and $|\mathbf{B}_f|=0.002$.

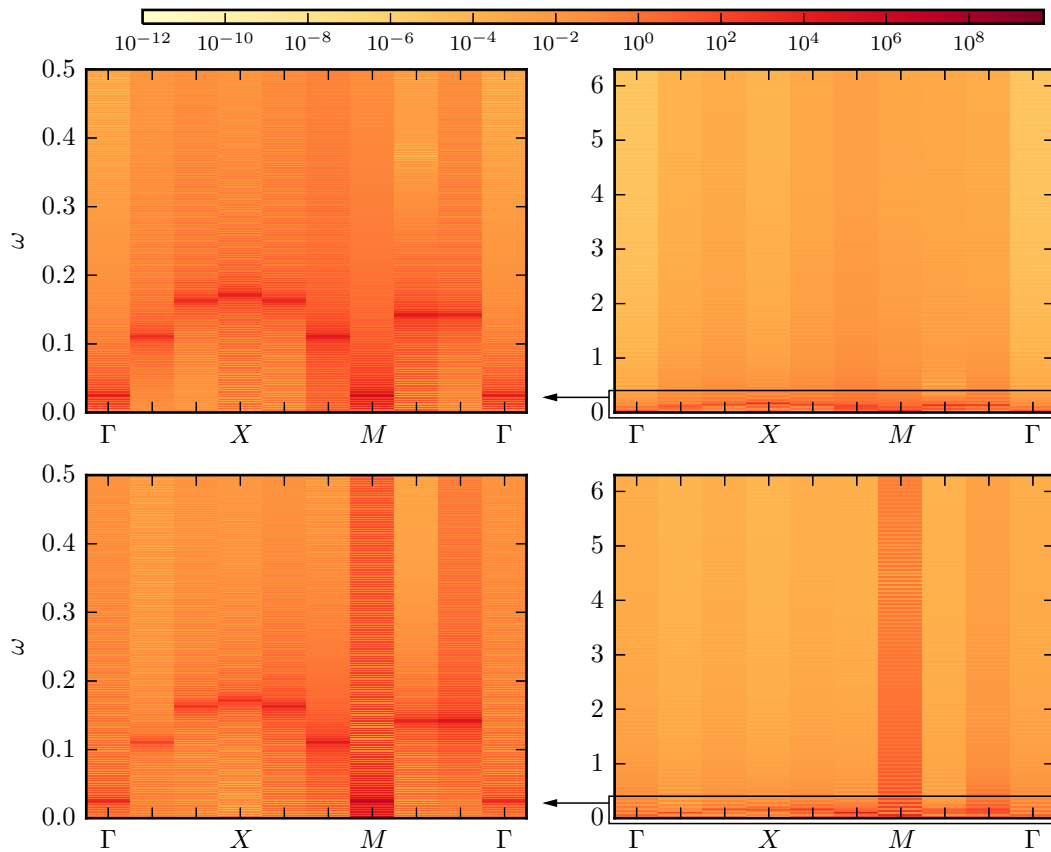


Figure 8.10: \tilde{m}_y (top) and \tilde{m}_z (bottom) along a path through the Brillouin zone with the high symmetry points Γ , X and M at $U=3.0$, $n = 4$ with $t'=5.0$ and $|\mathbf{B}_f|=0.002$. The left image in each row is just a blowup of the right image indicated by the boxed area.

8.4 Revealing strengths of real-space time-dependent slave boson mean-field theory

8.4.1 Magnetic excitations between Stoner and Heisenberg limit

As the Hubbard model is not only able to reproduce the Stoner and Heisenberg models in the appropriate small and large U limit, but to handle also intermediate U values, TD-SBMFT is also able to address these. An interesting question is now, how the magnetic excitations from the Stoner limit computed in section 8.3.1 evolve into the magnon dispersion of the Heisenberg limit of section 8.3.2, when intermediate U values are considered. The same setup as explained in section 8.1 and 8.2 is used. Therefore the limits $U = 0.4$ and $U = 3.0$ are just the previous results shown in section 8.3.1 and 8.3.2 and additionally $U = U_i = U_f = 1.0$ and $U = U_i = U_f = 2.0$ are investigated. As depicted in Tab. 8.1 the $U = 1.0$ ground state is an intermediate state between Stoner and Heisenberg limit, having only medium spin polarization and medium local spin-spin correlation. This indicates that the itinerant as well as the spin-nature of electrons are important. In contrast, the $U = 2.0$ ground state is already quite close to full spin polarization and maximum local spin-spin correlation. Hence a mixture of Stoner and Heisenberg magnetic excitations for $U = 1.0$ is expected and qualitative similar magnetic excitations of $U = 2.0$ compared to $U = 3.0$. The non-equilibrium setup triggers in the Heisenberg limit only transverse modes, so only these are considered now. Due to the fact that \tilde{m}_y and \tilde{m}_z display the same results only \tilde{m}_y is shown in Fig. 8.11 and \tilde{m}_z in the appendix section A.2.4 for completeness. Note that each column displays the same data only in different energy ranges. Again the time evolution is performed until $t_{tot}=1800$, with a suitable high energy resolution of $\Delta\omega = 0.003$. Fig. 8.11 shows a couple of intriguing features. In principle the magnetic excitations can be visually decoupled into a Heisenberg part in the energy range of 0 to 0.5 (top row), where the magnon dispersion at $U = 3.0$ is excellently visible and a Stoner part in the energy range of 0 to 2.2 (middle row), where the Stoner excitations at $U = 0.4$ are recognizable. The bottom row is only to show that there are no other magnetic excitations above 2.2. Of course, one can not speak of a magnon dispersion at $U = 0.4$ or 1.0 in the energy range of 0 to 0.5, still this visual decoupling is useful to see how the magnon dispersion at $U = 3.0$ evolves.

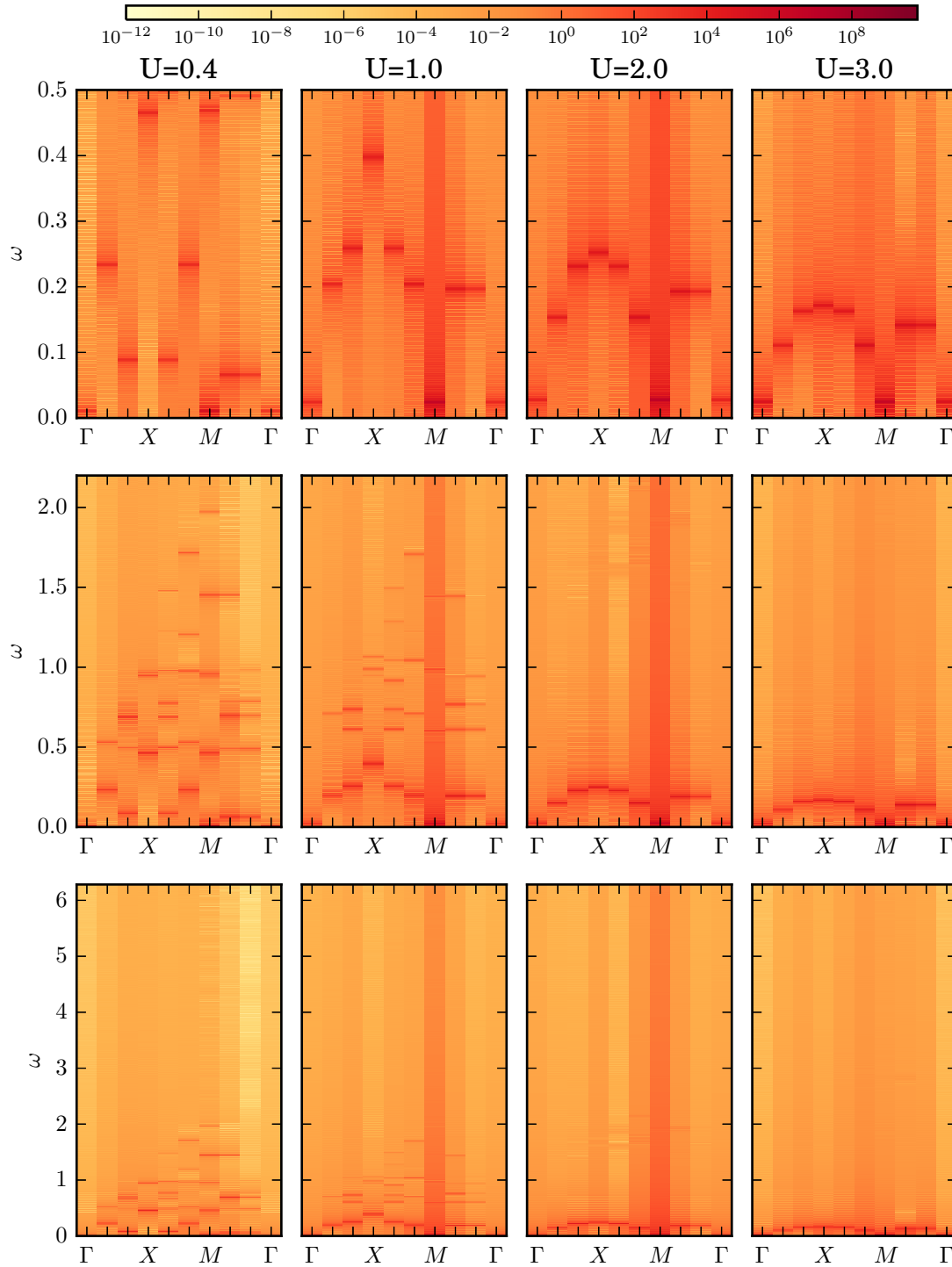


Figure 8.11: \tilde{m}_y along a path through the Brillouin zone with the high symmetry points Γ , X and M , $n = 4$ with $t'=5.0$ and $|\mathbf{B}_f|=0.002$. Note that each column displays the same data at different interactions U .

Let us focus first on the $\Gamma - X - M$ direction and the energy range 0 to 0.5. At $U = 1.0$ even though far away from the spin limit of the Hubbard model a Heisenberg-magnon-like dispersion is discovered with X at ~ 0.4 . Increasing U to 2.0 and then to 3.0 decreases the energy of the magnetic excitations along this direction and X moves to ~ 0.25 at $U = 2.0$ and then to ~ 0.175 at $U = 3.0$. This reminds of a similar shift in the energy of magnetic excitations with U in a half-filled Hubbard chain (1D) [9, 155], obtained by an analytical solution using the Bethe ansatz [82]. In contrast to the half-filled Hubbard chain this shift depends on \mathbf{q} , as can be seen for example by looking at the direction $M - \Gamma$. Indeed the \mathbf{q} values $(\pi/3, \pi/3)$ and $(2\pi/3, 2\pi/3)$ are only weakly shifted between $U = 1.0$ and 2.0 and stronger when turning to $U = 3.0$. This behavior seems to be qualitative the same to the points closest to the X point. Before analyzing the \mathbf{q} -dependence of the shift further, a closer look at the energy range 0.5 to 2.2 is performed. As expected $U = 1.0$ shows also Stoner excitations, while $U = 2.0$ does not. But the Stoner excitations at $U = 1.0$ are not the same as for $U = 0.4$ as they are partially restructured and disappear. Let us now turn to the \mathbf{q} -dependent influence of U on the lowest energy magnetic excitations between 0 and 0.5 and obtain a quantitative picture. Fig. 8.12 depicts the U -dependent positions of the lowest energy magnetic excitations of \tilde{m}_y at all symmetry-inequivalent points of the Brillouin zone. The positions are determined by analyzing the Fourier transform and the error is the full width at half maximum. As one can see in Fig. 8.11, there are multiple symmetry-equivalent points for example in $\Gamma - X$ and $X - M$ direction. The used 6x6 lattice equals six symmetry-inequivalent Brillouin points, where in Fig. 8.12 apart from the high-symmetry points $\mathbf{q}_1 = (\pi/3, 0)$, $\mathbf{q}_2 = (2\pi/3, 0)$ and $\mathbf{q}_3 = (2\pi/3, 2\pi/3)$ are displayed. First of all a comparison to a previous study of Seibold *et al.* [128] is drawn using the right side of Fig. 8.12. In that study Gutzwiller with fluctuations in random phase approximation (GA+RPA, see section 2.4.1) is used on a 4x4 lattice to compute magnetic excitations. This gives rise to two symmetry inequivalent \mathbf{q} -points apart from the antiferromagnetic wave vector $\mathbf{q} = M$ and high symmetry point Γ . The depicted results in Fig. 8.12 are in good agreement with that study observing the same transition from a spin-density wave gap in the order of U between the two depicted \mathbf{q} -points at small U to the low lying energy excitations of the Heisenberg model at large U . In contrast to Seibold *et al.* [128], real-space TD-SBMFT is not focused on low energy magnetic excitations and has a more consistent formalism, addressing the time evolution of local and itinerant degrees of freedom on equal

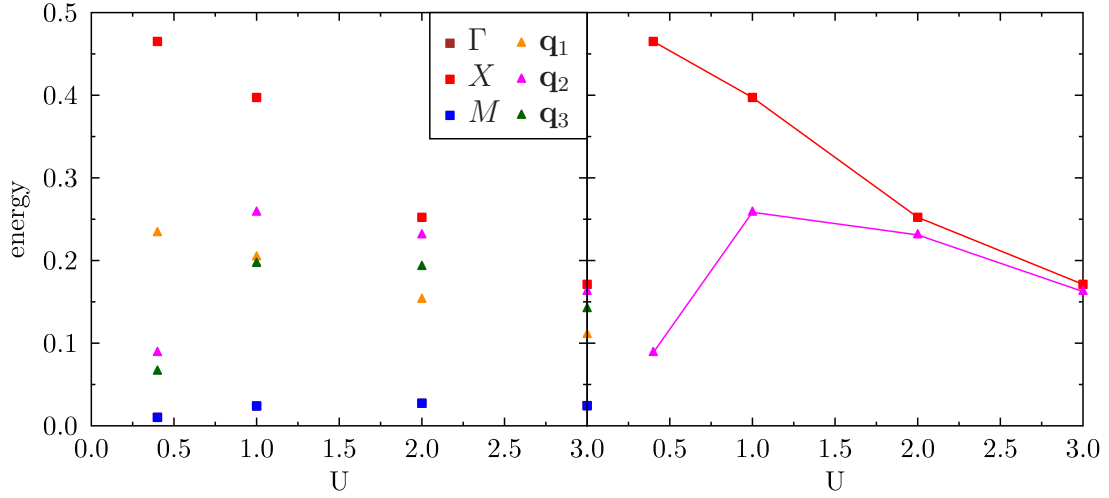


Figure 8.12: Positions of lowest energy magnetic excitations in \tilde{m}_y for all (left) and selected two (right) symmetry inequivalent \mathbf{q} with U . Lines are only as guide to the eye for better comparison with [128]. Errors determined by full width at half maximum and are equal or less the marker size. Again $n = 4$ with $t' = 5.0$ and $|\mathbf{B}_f| = 0.002$ is utilized. $\mathbf{q}_1 = (\pi/3, 0)$, $\mathbf{q}_2 = (2\pi/3, 0)$ and $\mathbf{q}_3 = (2\pi/3, 2\pi/3)$ is used. Γ and M are energy degenerate.

footing (see section 2.4.1). Therefore the influence of Stoner excitations on the qualitative behavior of the low energy excitations is addressed by looking at the left side of Fig. 8.12 and Fig. 8.11. The influence of U is twofold. On the one hand it just decreases the energy at X and q_2 similar to the effect observed in Hubbard chains [9, 155]. On the other hand it *increases* first the energy between $U = 0.4$ and $U = 1.0$ at the other \mathbf{q} -points and then decreases it, when increasing U further. This different behavior generates low energy Heisenberg-like magnetic excitations already at $U = 1.0$. The behavior of the excitation spectrum between $U = 1.0$ and $U = 3.0$ indicates, that high energy Stoner and low energy magnetic excitations do not mix and the high energy Stoner part just disappears. In this way, the excitations can then just act like in the Hubbard Chain [9, 155]. Furthermore it also means that the decoupling of these two parts of the excitation spectrum happens just between $U = 0.4$ and $U = 1.0$ visible as \mathbf{q} -dependent magnetic excitation change.

8.4.2 Instability of magnons out of equilibrium

Another strength of TD-SBMFT is, that it is not limited to small magnetic fields $|\mathbf{B}_f|$ and small kicktimes t' studied previously. In fact, this section is devoted to the investigation of a higher magnetic field and longer kicktimes. On this way, the linear-response regime is left. As the focus lies on changes in the magnon dispersion the Heisenberg limit $U = U_i = U_f = 3.0$ is considered with the same ground state used before (Tab. 8.1). Furthermore the same non-equilibrium setup as described in section 8.2 is used even the same $\mathbf{B}_f(\mathbf{r})$ with $n = 4$ is utilized as before for $U = 3.0$. The only notable difference is the increased magnetic field amplitude by a factor of 10 resulting in $|\mathbf{B}_f| = 0.020$. Fig. 8.13 depicts the influence of kicktime t' onto the magnon dispersion \tilde{m}_z . Same qualitative behavior can be seen also in \tilde{m}_y , which is depicted in the appendix section A.2.5 for completeness. Simply increasing $|\mathbf{B}_f|$ by a factor of 10, but keeping the small kicktime $t' = 5$ does not modify the magnon dispersion (compare Fig. 8.10), as can be seen in the leftmost column. Increasing t' affects the magnon dispersion drastically. At $t' = 40$ each magnon at every \mathbf{q} -point aside from $\mathbf{q} = \Gamma$ acquires multiple sidebands reminiscent of Zeeman splittings, where the splitting scales with $1/t'$. At $t' = 80$ almost all \mathbf{q} -points aside from Γ and M display a broadened, quite featureless distribution of energy around their original peaks. Turning to even higher kicktimes $t' = 320$ the original magnon dispersion is retrieved again, but with splittings. However with the used energy resolution of $\Delta\omega = 0.003$ induced by $t_{tot} = 1800$, it is unclear if the splitting still scales with $1/t'$. This feature of a broadening (destruction) of magnons and then reformation was first seen by Zhitomirsky *et al.* [158], when they investigated the non-equilibrium AFM magnon spectrum using self-consistent Born approximation in a Heisenberg model subject to a high magnetic field. To be able to compare with this study even better \tilde{m}_y is depicted in Fig. 8.14 at the four \mathbf{q} -points also computed in that study for $t' = 80$ (destruction of magnons) and $t' = 320$ (reformation). Additionally the sharp magnon peaks at $t' = 5$ are shown as grey lines for better comparison. The results are in good agreement to Zhitomirsky *et al.* [158], where between $\Gamma - M$ the magnon peak is first destroyed at $t' = 80$ and then reformed at $t' = 320$. As a slight difference in the depicted results a splitting of the peak at Γ and M is visible at $t' = 80$, which turns into a single peak at $t' = 320$. A double-peak structure was also seen in another study of the high-field magnon behavior in equilibrium [135] at $\mathbf{q} = (\pi/2, \pi/2)$, which is not accessible in the used lattice as it lies between (b) and (c) of Fig. 8.14. They interpreted this two-peak structure at two edge states

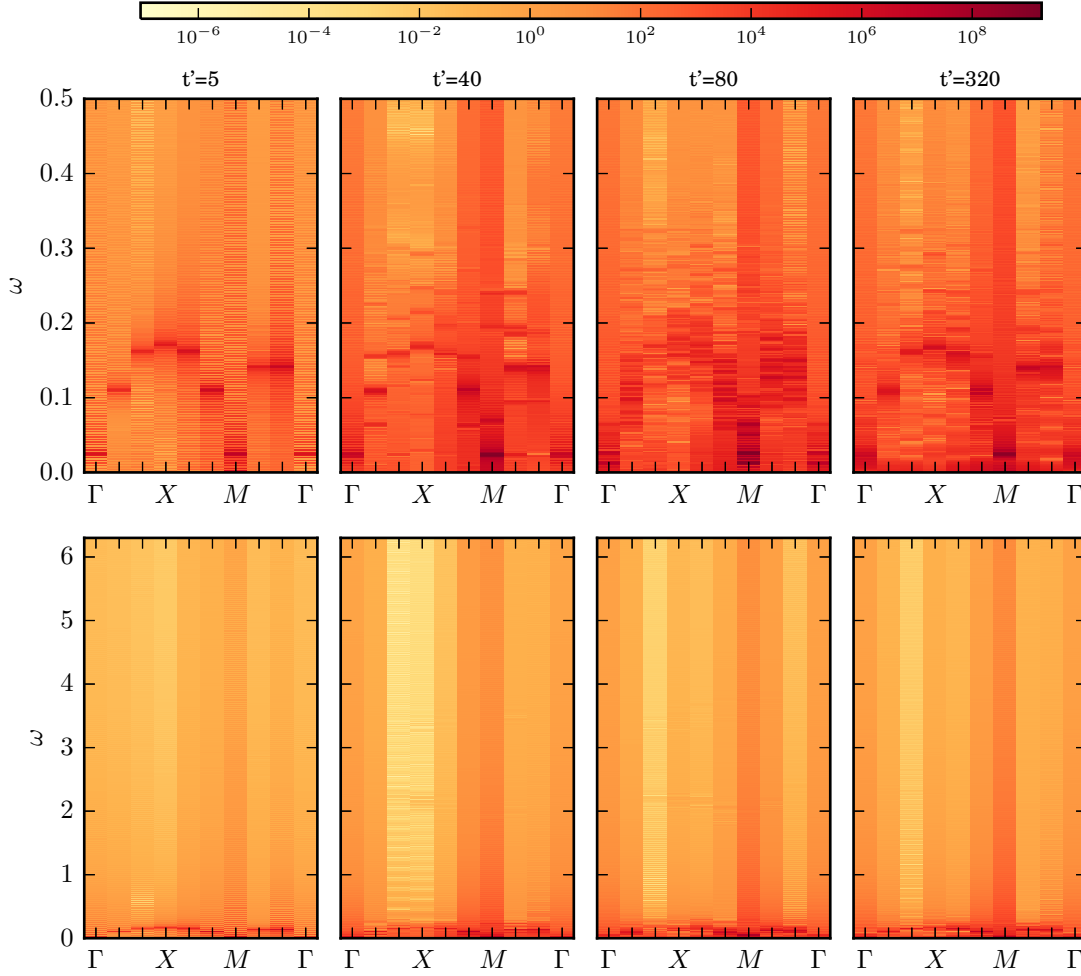


Figure 8.13: \tilde{m}_z along a path through the Brillouin zone with the high symmetry points Γ , X and M at $U=3.0$, $n = 4$ with different t' and $|\mathbf{B}_f|=0.020$. Note that each column display the same data, only in different energy ranges.

of a continuum, where the role of the magnetic field is the transfer of weight from the lower to upper edge. This is also in line with Fig. 8.14 looking at $t' = 80$ and $t' = 320$ for $\mathbf{q} = \Gamma$ and $\mathbf{q} = M$. The destruction and reappearance of the magnon peaks at equilibrium was explained by field-induced hybridization of single magnon states and two-magnon continuum [158]. Looking at Fig. 8.14, the results indicate that an increase of t' with the *same* magnetic field $|\mathbf{B}_f|$ during the pulse, has the same effect. Therefore a hybridization of single and two-magnon state can

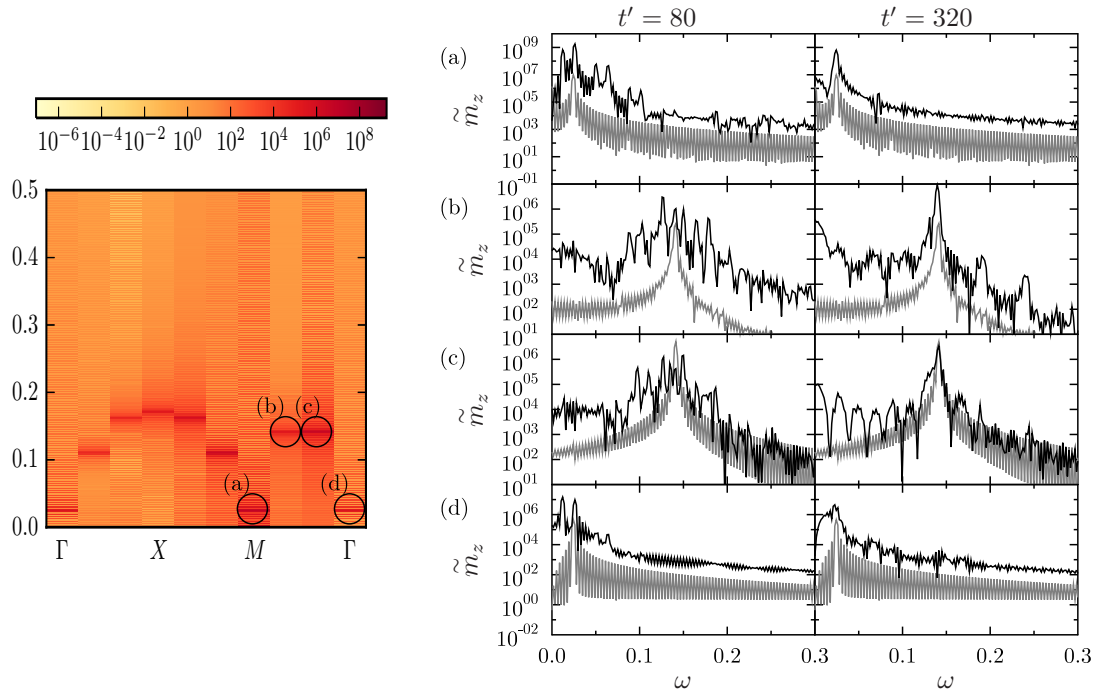


Figure 8.14: \tilde{m}_z along a path through the Brillouin zone with the high symmetry points Γ , X and M at $U=3.0$, $n = 4$, $|\mathbf{B}_F|=0.020$ for $t' = 5$ (left) and for four selected \mathbf{q} -points at $t' = 80$ and $t' = 320$ in black (right). Grey lines indicate \tilde{m}_z at $t' = 5$.

also be induced by pulsed magnetic field and is maybe already visible there at smaller magnetic fields when using large kicktimes. Note that in linear spin-wave theory magnons are stable at any momentum and any magnetic field as it does not describe the decay of single-magnon states into two magnon states [86].

8.5 Summary of this chapter

This chapter concerns the real-space magnetization dynamics of the single-orbital Hubbard model at half-filling. Focus of attention is an antiferromagnetic (AFM) insulating ground state at different interaction values. The real-space formulation of TD-SBMFT is employed to access first the well-known magnetic excitations in linear-response in the small interaction and large interaction limit. This is modeled by utilizing a site-dependent magnetic field with small amplitude, which excites the

system during a short pulse (called kick). On this way at small interaction electron-hole (Stoner) excitations are retrieved in agreement with the small interaction approximation of the Hubbard model, the Stoner model. These excitations have the characteristic tendency to form a quasi-continuum of states in the thermodynamic limit and range up to energies of the order of electron volts. At large interaction collective spin excitations (magnons) in agreement with the large interaction limit of the Hubbard model, the Heisenberg model, are discovered. They display the characteristic dispersion known for linear spin-wave theory. After these testing cases magnetic excitations between Stoner and Heisenberg limit are revealed. Starting at the small interaction limit displaying Stoner excitations an increase in interaction separates the magnetic excitations in a Stoner-like high energy and magnon-like low energy part. At the same time \mathbf{q} -dependent energy shifts of the magnetic excitations appear. Increasing the interaction further the low energy part is renormalized similar to magnetic excitations in a 1D Hubbard chain, while Stoner excitations disappear. The low energy magnetic excitation behavior is in agreement with a previous study [128], but could before not related to its high energy counterpart. Finally as another strength of real-space TD-SBMFT, the Hubbard model is kicked out of equilibrium with a site-dependent magnetic field. A higher magnetic field and longer kicks are utilized to observe effects on the magnon dispersion of the Heisenberg limit. With increasing kick a magnon decay (broadening of magnon peaks) and reformation is encountered. This is reminiscent of a non-equilibrium Heisenberg Spin model study utilizing self-consistent Born approximation, where similar features are seen, when increasing the magnetic field. The explanation in equilibrium is that the magnetic field induces a hybridization of single magnon states with the two magnon continuum opening decay channels. This indicates that real-space TD-SBMFT is able to describe this hybridization, which is out of reach of linear spin-wave theory. It would be interesting to look at larger lattices or utilize more kicks to see if the momentum-dependence of the magnon decay stated in a recent study [86] can be retrieved.

9 Conclusion

In this work the time-dependent extension to slave boson mean-field theory (TD-SBMFT) was introduced and applied in a wide range of applications using the fermionic multi- and single-orbital Hubbard model. As TD-SBMFT is based on the time-dependent Gutzwiller approximation (TD-GA), it was tested on interaction quenches in the single-orbital Hubbard model to recover TD-GA results. At and away from half-filling TD-GA results are regained, which are in very good agreement to the numerical more intricate time-dependent dynamical mean-field theory (TD-DMFT). In detail, TD-SBMFT was able to reproduce qualitatively the metastable states encountered, when quenching from a noninteracting state to weak or strong interactions at half-filling. Furthermore it was also able to reveal the dynamical metal insulator (Mott) transition in between. However as semi-classical method it does not contain quantum fluctuations and is therefore not able to display thermalization. On the other hand the small numerical footprint is an advantage as it allowed to cover a wide range of applications, where the focus then lied on the discovered metastable states and not their thermalization. Most of these applications are up to now numerical inaccessible for methods like TD-DMFT. A first example in the single-orbital case was the investigation of the dynamical Mott transition away from half-filling, where TD-GA (TD-SBMFT) predicted a vanishing of the dynamical transition similar to the behavior of the equilibrium Mott transition with doping.

Another example was the consideration of additional orbital degrees of freedom and magnetic states. The influence of an additional orbital coupled to the other via interorbital coupling with or without Hund's coupling was considered regarding its effects on the dynamical Mott transition. The critical influence of Hund's coupling on the Mott transition in equilibrium was recapped. Then interaction quenches from the noninteracting state with or without Hund's coupling but in any case a finite interorbital coupling were considered. Excitations of the system were slightly more complicate than in the single-orbital case consisting now of at least two modes and

superpositions instead of only a single mode. Still interaction quenches to small interaction values left the single-orbital prethermalized state description qualitatively intact. The same held for one of the modes for quenches to strong interaction. There it displayed again oscillations expected in the atomic limit. However the freezing was revealed to be dependent on the local state. This dependence is not accessible in the single-orbital case as due to the high symmetry only one effective state exists. The biggest change is certainly the broadening of the dynamical Mott transition into a region of critical behavior seen as strong incoherent excitation. Finite Hund's coupling left the metastable state description quite intact, but the broadening of the dynamical Mott transition was enhanced.

Afterwards magnetic states were the focus of interest looking at the orbitals of the t_{2g} shell, which are known to host already a plethora of intriguing physical effects in equilibrium [92, 99, 141]. Starting from a well-established point with considering a highly correlated antiferromagnetic (AFM) ground state at half-filling and quenching to lower interaction values single-orbital results [123, 138] were generalized to three-orbitals. Additionally a wide range of hole-dopings was considered. The dynamical transition between an AFM and paramagnetic (PM) non-equilibrium state was discovered in three-orbitals under moderate hole doping. Even stronger doping unveiled a longitudinal large amplitude spin oscillation replacing this transition. As a new viewpoint the vice versa case was investigated meaning the interaction quench from a PM ground state close to the equilibrium AFM-PM phase boundary to higher interactions. On this way not only an AFM state appears out of equilibrium, but also a transient spin oscillation, which displays periodic AFM spin switching for a limited period of time. This transient spin oscillation was vital for nearly all considered fillings, which could hint on experimental realization in a broad class of materials close to the utilized ground states and dominating t_{2g} shell.

To show that TD-SBMFT is not restricted to a model context, a small application regarding the Mott transition in Chromium doped V_2O_3 was done. The Mott transition in Chromium doped V_2O_3 is an archetypical example, as it displays features predicted by the Hubbard model. To get a good material description the density field theory (DFT) results were projected onto a unit cell with four atoms having each three-orbitals. This projection was incorporated in the hopping term of the used Hubbard model. Unpublished experimental results [40] display that a femtosecond laser excitation is able to populate a in the Mott insulating state unoccupied orbital. On this way an insulator to metal transition is induced. TD-SBMFT was able to

approximate the Mott insulating ground state. It described the Mott insulator to metal transition as an effect of a quenched correlation enhanced crystal field. This quench led to charge transfer and correlation changes in qualitative agreement with the experiment.

Translational symmetry is one of the basic symmetries in solid state systems, but there are circumstances, where this symmetry is broken for example when vacancies come into play. As a testing case of the capabilities of real-space SBMFT the influence of oxygen vacancies in the metallic interface of $\text{LaAlO}_3/\text{SrTiO}_3$ was revealed. For this a model Hamiltonian was developed first, approximating an oxygen vacancy by a modified electron number on the lattice and a crystal field on neighboring atoms. With this approach an intricate magnetic phase diagram was unfolded crafted from the competition among Ruderman-Kittel-Kasuya-Yosida(RKKY)-like, non-local double-exchange-like and superexchange interactions. This magnetic phase diagram was in qualitative agreement with experimental findings. It would be interesting to expand this investigation by considering even larger lattices. On this way the effects of clustered vacancies could be investigated, as here only one atom was neighbored to a single vacancy. Additionally a cluster formalism would allow to treat also singlet states regarding two coupled sites, which could replace the AFM coupled neighboring sites observed here.

Finally this work climaxed in the description of real-space magnetism in the single-orbital Hubbard model with real-space TD-SBMFT. The real-space formulation established an access to real-time momentum dependent magnetic excitations in linear-response and away from linear-response. Utilizing an AFM ground state and a pulsed site-dependent magnetic field linear-response results could be recovered in the limit of small pulse length and small magnetic field. To be specific, in the weak interaction limit Stoner (electron-hole) excitations of the Stoner model and in the strong interaction limit collective spin excitations (magnons) of the Heisenberg model were encountered. As real-space TD-SBMFT operates on the Hubbard model intermediate interactions could be investigated. The momentum-dependent magnetic excitation change with interaction could be related to the decoupling of Stoner-like and magnon-like excitations. Additionally the evolution of the low energy magnetic excitations with interaction is in agreement with a previous study [128]. Afterwards the non-equilibrium setup was changed to address effects away from linear response. With a higher magnetic field the effect of the pulse length on the magnon dispersion in the strong interaction limit was the focus of attention.

Thus magnon decay and magnon reformation depending on the applied magnetic field first revealed in a non-equilibrium self-consistent Born approximation study of the Heisenberg Spin model in high magnetic fields [158] could be qualitatively recovered using magnetic field pulses. To achieve this in the non-equilibrium setup only an increase of pulse length at constant magnetic field was necessary. Very high magnetic fields of orders of multiple $10 T$ are required to display the magnon decay in some of the materials displaying Heisenberg model physics [26, 154]. Therefore it is interesting to answer the question in the future whether a smaller magnetic field with longer pulse length out of equilibrium could display the same effect. This would make this type of magnon decay also available in other materials previously not accessible. Especially as the needed magnetic fields in high temperature superconductor parent compounds are unaccessible high (order of $1000 T$) [26], this approach seems to be worth pursuing. Another interesting result was the observation of edge states at high symmetry points of the Brillouin zone, which were previously only seen at non high symmetry points [135]. In this respect it is also interesting to investigate the importance of these edge state onto magnetization dynamics in the system. Another intriguing possibility opens by utilizing doping. As the AFM ground state is insulating, this would induce metallicity leading to an interplay of correlations and magnetic excitations especially interesting in the high interaction case.

A Appendix

A.1 Runge-Kutta theory

In the following section A.1.1 explicit Runge-Kutta methods are introduced, which are used to solve non-linear differential equations. In this work the non-linear differential equations describe the time evolution within time-dependent slave boson mean-field theory (TD-SBMFT) and are depicted for example in Eqs. 2.41 and 2.42. Furthermore in section A.1.2 error estimation of Runge-Kutta solutions is described.

A.1.1 Explicit Runge-Kutta methods

Starting point are the differential equations 2.41 and 2.42 (or in real-space formulation Eqs. 2.48 and 2.50). Explicit examples in this and the next section refer to the first two equations, the other two can be handled in the same way. To solve these ordinary first-order non-linear differential equations, one option is an explicit Runge-Kutta (RK) method [44]. Having a differential equation (DE) of the form $\dot{y}(t) = f(t, y(t))$ the central idea is to obtain a solution $y(t_{n+1})$ by interpolating m known slopes of $y(k_i)$ with $k_i \in [t_n, t_{n+1})$. The number m is called the order of the RK method. The classic RK method of order 4 works in the following way. Let $t_{n+1} - t_n = h$ and $f(t_n, y(t_n)) := K_1$ be known. Then the second slope $f(t_n + \frac{h}{2}, y_1) := K_2$ is computed at the point $y_1 = y(t_n) + \frac{h}{2} \cdot K_1$. So the initial slope is used to linear interpolate to the half of the time interval and compute a new slope K_2 there. With K_2 this process is repeated to compute a more precise value, meaning $K_3 := f(t_n + \frac{h}{2}, y_2)$ with $y_2 = y(t_n) + \frac{h}{2} \cdot K_2$. Finally K_3 is used to interpolate to the end of the time interval and compute K_4 there $K_4 := f(t_n + h, y_3)$ with $y_3 = y(t_n) + h \cdot K_3$. To obtain $y(t_{n+1})$ a weighted average is performed by $y(t_{n+1}) = y(t_n) + \frac{1}{6} \cdot K_1 + \frac{1}{3} \cdot K_2 + \frac{1}{3} \cdot K_3 + \frac{1}{6} \cdot K_4$. As already mentioned this is the classic order 4 RK method. There are different explicit RK methods. They differ in

$$\frac{\alpha^T}{\mid} \mid \frac{B}{a}$$

Table A.1: Butcher Array

0				
$\frac{1}{2}$	$\frac{1}{2}$			
$\frac{1}{2}$	0	$\frac{1}{2}$		
1	0	0	1	
	$\frac{1}{6}$	$\frac{2}{6}$	$\frac{2}{6}$	$\frac{1}{6}$

0				
$\frac{1}{3}$	$\frac{1}{3}$			
$\frac{2}{3}$	$-\frac{1}{3}$	1		
1	1	-1	1	
	$\frac{1}{8}$	$\frac{3}{8}$	$\frac{3}{8}$	$\frac{1}{8}$

Table A.2: Butcher array for classic RK method of order 4 [44]**Table A.3:** Butcher array for 3/8 method of order 4 [44]

order, choice of points where the slopes are computed

$$K_i = f \left(t_n + h \cdot \alpha_i, y(t_n) + h \cdot \sum_{j=1}^m \beta_{ij} k_j \right) \quad (\text{A.1})$$

and the weights when averaging at the end of one RK step are

$$y(t_{n+1}) = y(t_n) + h \cdot \sum_{i=1}^m a_i K_i. \quad (\text{A.2})$$

The characteristic coefficients $a_i, \alpha_i, \beta_{ij}$ are often represented in an object coined Butcher array (Tab. A.1, with $\alpha = (\alpha_1, \dots, \alpha_m), a = (a_1, \dots, a_m)$ and $B = [\beta_{ij}]$). In Tab. A.2 and A.3 the just explained classic RK method of order 4 and the more precise 3/8 method of same order are shown, respectively. Note that to evaluate a time step with the shown RK method of order 4 it is sufficient to compute the right hand side of the differential equation at three points. To derive the DE (Eqs. 2.41 and 2.42), the present procedure has to be extended to more than one variable. This is done by $y(t) \rightarrow \vec{y}(t) = (y_1, y_2, \dots, y_n)$ and $f(t_n, y(t_n)) \rightarrow \vec{f}(t_n, \vec{y}(t_n))$ with $\vec{f} = (f_1(t_n, \vec{y}(t_n)), \dots, f_n(t_n, \vec{y}(t_n)))$. The variables consist in this case of the eigenvectors v_a^K for occupied Bloch orbitals a and momentum points \mathbf{K} . Additionally the non-zero slave boson amplitudes ϕ_{AB} are variables, too. Both form the vector \vec{y} . However the stability and reliability of the results with RK methods depend critically on the time step size h . This leads to the question, if there is a procedure

to estimate the error of variables computed with a certain h and adapt it to keep this error estimate below a specified tolerance. This is addressed in the next section A.1.2.

A.1.2 Error estimation of Runge-Kutta variables

There are various ways to derive the error of one variable obtained with a Runge-Kutta method [44]. One often used procedure is to derive the variable with two RK methods of order m and $m + 1$. Hence two variables y_m and y_{m+1} are obtained. One approximation to the local error of y_m is $y_{m+1} - y_m$. But in many cases the local error occurring at each time step is not related to the global error, which arises after n time steps. This is the reason the local error is often only used to compute an optimal time step size and the calculation is continued only with y_{m+1} . This is called local extrapolation. A good technique to get the results of two different RK methods which differ only by one order, is to calculate the method of order $m + 1$ in the way already explained and to look for a RK method of order m , which uses the K_i and results of the method of order $m + 1$. To put it in other words to obtain the RK method of order m just one additional K_i is needed compared to the calculation of the RK method of order $m + 1$. As error estimate err is utilized from the following formula [44]

$$err = \sqrt{\frac{1}{n} \sum_{i=1}^n \left(\frac{y_i - \tilde{y}_i}{sc_i} \right)^2}, \quad (\text{A.3})$$

$$sc_i = Atol_i + \max(y_i(t_0), y_i) \cdot Rtol_i. \quad (\text{A.4})$$

Here y_i and \tilde{y}_i are the results from the order $m + 1$ and m method of the present time step, respectively. sc_i specifies the upper limit of the difference of absolute values of y_i and \tilde{y}_i . This value is composed of relative and absolute tolerances ($Rtol_i$ and $Atol_i$), which has to be set before starting the Runge-Kutta method. Applying

Eq. A.4 to the mentioned variables (eigenvectors v_a^K and slave-bosons ϕ), results in

$$err = \sqrt{\frac{1}{n} \left[\sum_{A,B} \left(\frac{|\phi_{AB} - \tilde{\phi}_{AB}|}{sc_{AB}} \right)^2 + \sum_{K,a} \left(\frac{|v_a^K - \tilde{v}_a^K|}{sc_a^K} \right)^2 \right]} \quad (\text{A.5})$$

$$sc_{AB} = Atol_{AB} + max(|\phi_{AB}(t_0)|, |\phi_{AB}|) \cdot Rtol_{AB} \quad (\text{A.6})$$

$$sc_a^K = Atol_a^K + max(|v_a^K(t_0)|, |v_a^K|) \cdot Rtol_a^K. \quad (\text{A.7})$$

A nine stage RK method of order 6 and 5 called IIIXb+6(5) [143] is utilized within TD-SBMFT and its real-space formulation. The Butcher array is displayed in Tab. A.4.

0									
$\frac{9}{50}$	$\frac{9}{50}$								
$\frac{1}{6}$	$\frac{29}{324}$	$\frac{25}{324}$							
$\frac{1}{4}$	$\frac{1}{16}$	0	$\frac{3}{16}$						
$\frac{53}{100}$	$\frac{79129}{250000}$	0	$-\frac{261347}{250000}$	$\frac{19663}{15625}$					
$\frac{3}{5}$	$\frac{1336883}{4909125}$	0	$-\frac{25476}{30875}$	$\frac{194159}{185250}$	$\frac{8225}{78546}$				
$\frac{4}{5}$	$-\frac{2459386}{14727375}$	0	$\frac{19504}{30875}$	$\frac{2377474}{13615875}$	$-\frac{6157250}{5773131}$	$\frac{902}{735}$			
1	$\frac{2699}{7410}$	0	$-\frac{252}{1235}$	$-\frac{1393253}{3993990}$	$\frac{236875}{72618}$	$-\frac{135}{49}$	$\frac{15}{22}$		
1	$\frac{11}{144}$	0	0	$\frac{256}{693}$	0	$\frac{125}{504}$	$\frac{125}{528}$	$\frac{5}{72}$	
1	$\frac{28}{477}$	0	0	$\frac{212}{441}$	$-\frac{312500}{366177}$	$\frac{2125}{1764}$	0	$-\frac{2105}{35532}$	$\frac{2995}{17766}$

Table A.4: Butcher array for IIIXb+6(5), a robust nine stage RK method of order 6 and 5 [143] used in TD-SBMFT and its real-space formulation. The last line depicts the a coefficients for the method of order 5 and the one before for the one of order 6.

A.2 Real-space magnetization dynamics-additional material

In this section some additional results are depicted concerning the real-space magnetization dynamics of chapter 8. These additional results are not needed to understand the discussion depicted in chapter 8, they are denoted here for completeness and to provide an additional viewpoint.

A.2.1 Stoner limit $n = 6$

To obtain results in the Stoner limit $U = U_i = U_f = 0.4$ is selected. The AFM ground state (Fig. 8.2) is kicked using $\mathbf{B}_f(\mathbf{r})$ with $n = 6$, $|\mathbf{B}_f|=0.002$ and a kicktime $t'=5.0$ to be in the linear-response regime. Concerning the local magnetization dynamics small differences can be seen between $n = 4$ in Fig. 8.5 and $n = 6$ in Fig. A.1. Still it has the same qualitative result that the observed dynamics render no

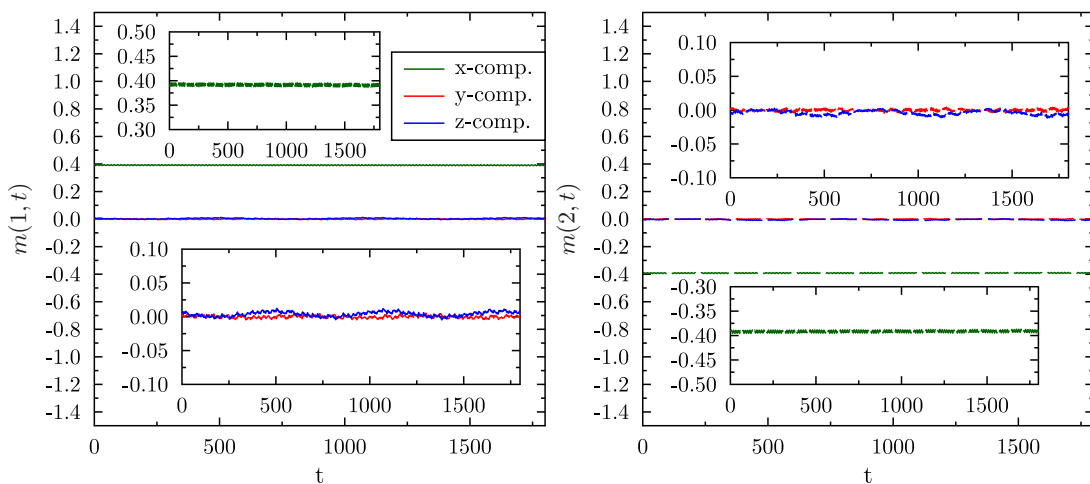


Figure A.1: Magnetization dynamics at site 1 (left) and 2 (right) at $U=0.4$, $n = 6$ with kick time 5.0 and $|\mathbf{B}_f|=0.002$ for 6x6 lattice.

clear picture if there is a longitudinal mode excited or not. In all components the amplitudes are really small. So all component of $\tilde{\mathbf{m}}$ has to be checked now. In Fig. A.2 \tilde{m}_x (top), \tilde{m}_y (middle) and \tilde{m}_z (bottom) are depicted in the Brillouin zone for $n = 6$ and $U = 0.4$. This figure can be compared to its $n = 4$ equivalents in Fig. 8.6 and 8.7. It shows a strong inhomogeneous excitation for the x-component and a

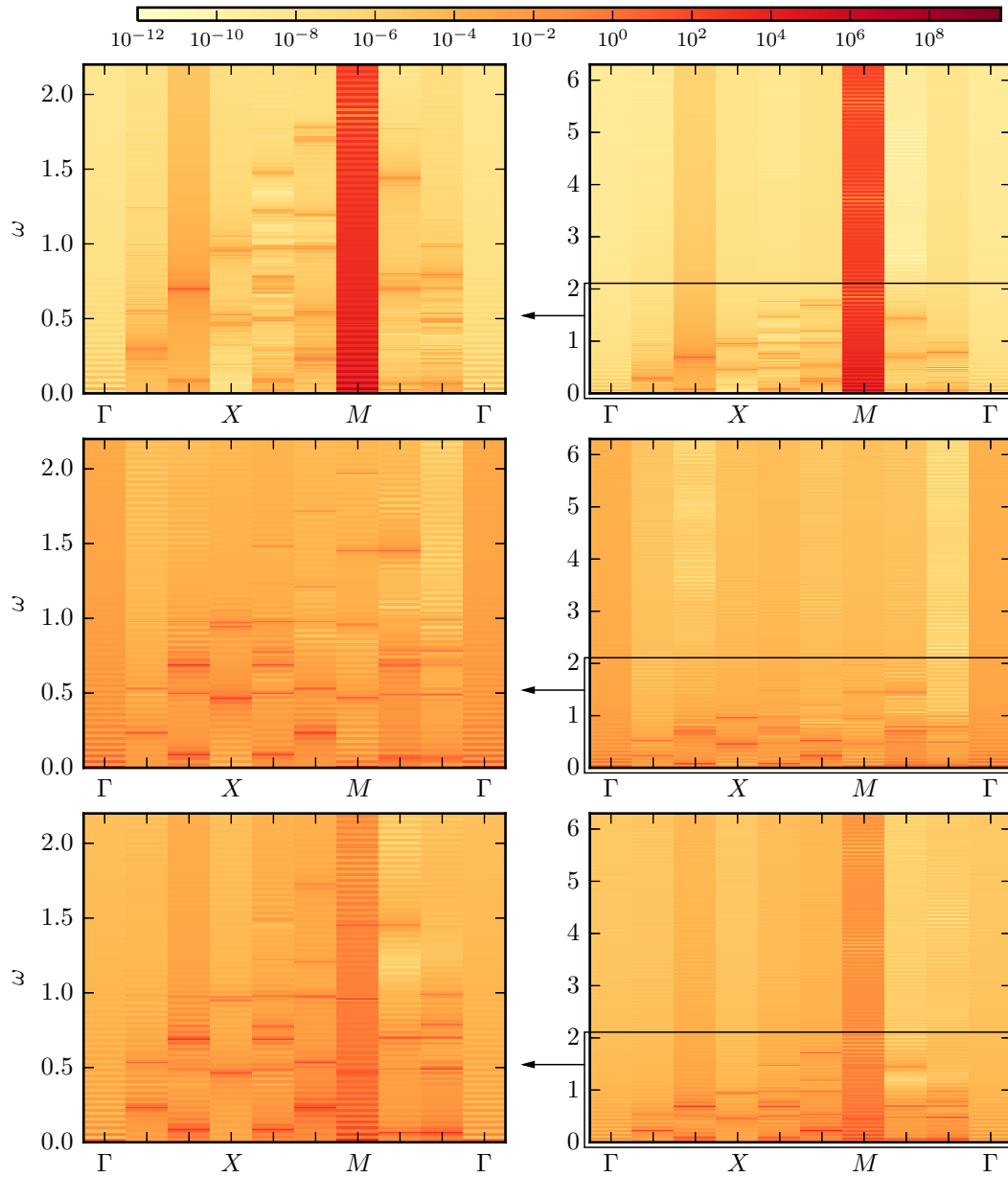


Figure A.2: \tilde{m}_x (top), \tilde{m}_y (middle) and \tilde{m}_z (bottom) along a path through the Brillouin zone with the high symmetry points Γ , X and M at $U=0.4$, $n = 6$ with kick time 5.0 and $|\mathbf{B}_f|=0.002$ for 6x6 lattice. The left image is just a blowup of the right image indicated by the boxed area.

weak inhomogeneous excitation for the z-component at the M point. The magnetic excitations cover a broad energy range up to ~ 2.0 eV, which can not be explained

by magnon formation. Instead electron-hole excitations named Stoner excitations arise. There is the quantitative agreement to Fig. 8.6 and 8.7, that almost all components of $\tilde{\mathbf{m}}$ and \mathbf{q} points have the same magnetic excitations. Only \tilde{m}_x shows some minor difference at two \mathbf{q} points concerning additional magnetic excitations.

A.2.2 Stoner limit-alternative non-equilibrium setup

In this section a small modification of the kick setup explained in section 8.2 is made. Namely, instead of the y-z plane, the x-z plane is used with $n = 4$ to apply the site-dependent magnetic field. The angle α is in this section measured to the x axis and the same $\alpha(\mathbf{r})$ configuration as in the calculations for $n = 4$ in the y-z plane is utilized. This should address the question if such a modified setup is better suited to generate longitudinal magnetic excitations (magnetic excitations along the x-direction) expected to be dominant in the Stoner limit [109]. All other parameters stay the same meaning $U = U_i = U_f = 0.4$ is selected. The AFM ground state (Fig. 8.2) is kicked using $|\mathbf{B}_f|=0.002$ and a kicktime $t'=5.0$ to be in the linear-response regime. In Fig. A.3 (compare to Fig. 8.5 for y-z plane) the local magnetization dynamics at site 1 and 2 are depicted. The differences to the results of the previous

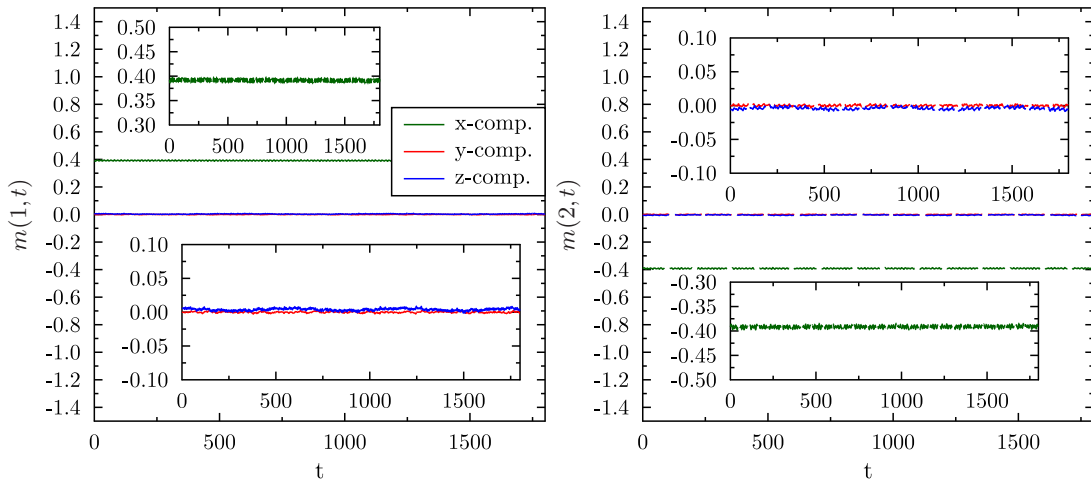


Figure A.3: Magnetization dynamics at site 1 (left) and 2 (right) at $U=0.4$, $n = 4$ with kick time 5.0 and $|\mathbf{B}_f|=0.002$.

setup (Fig. 8.5) are really small, especially there is still no visible dynamic along the x-direction. This indicates that the used magnetic field of 2 meV and small kicktime is not sufficient to excite longitudinal modes. $\tilde{\mathbf{m}}$ for the changed setup

shown in Fig. A.4 has the same qualitative features as for the previous setup (Fig. 8.6 and 8.7). All components show Stoner excitations in the range of up to ~ 2.0 . The AFM order is destabilized into an inhomogeneous excitation for \tilde{m}_x .

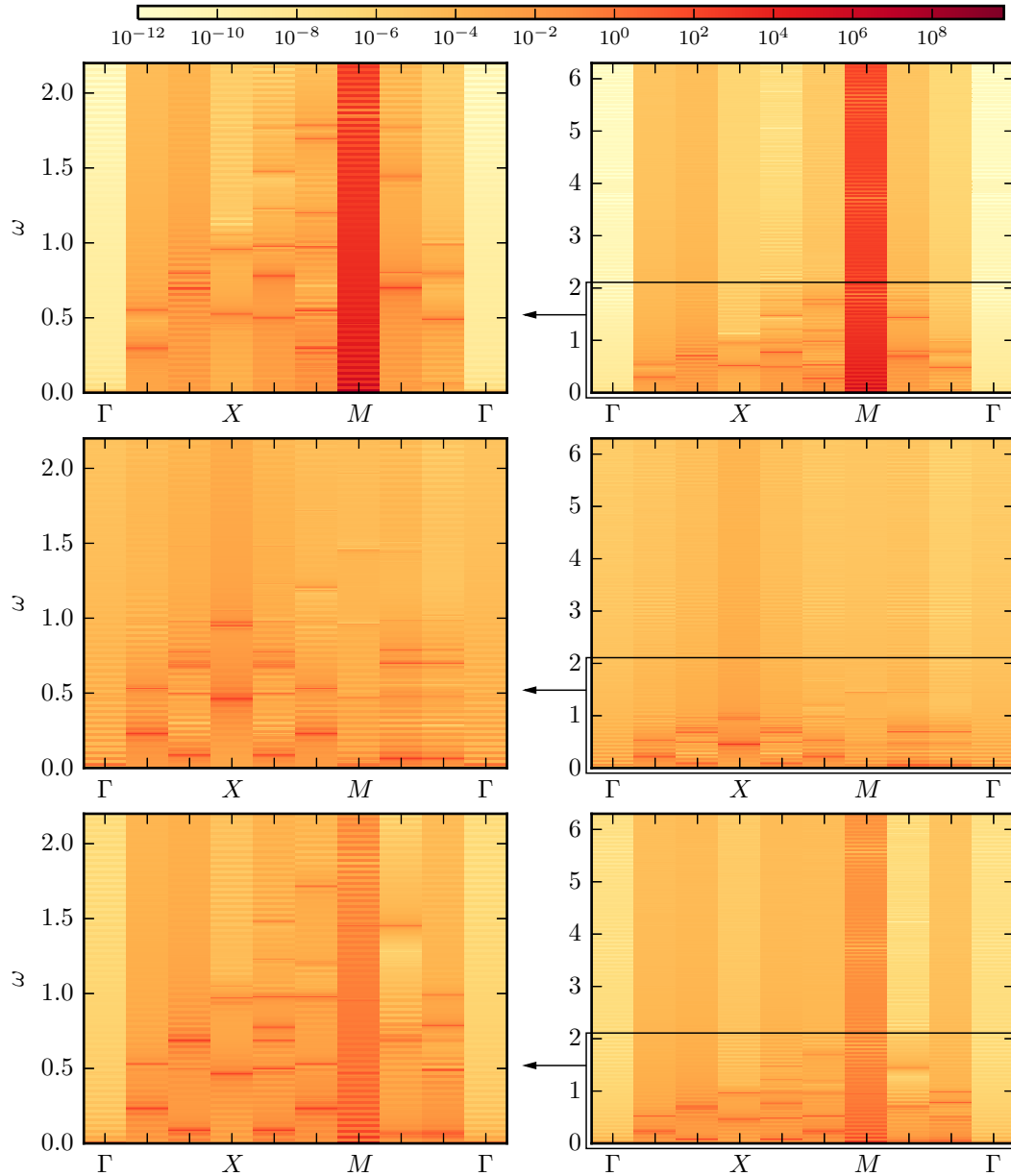


Figure A.4: \tilde{m}_x (top), \tilde{m}_y (middle) and \tilde{m}_z (bottom) along a path through the Brillouin zone with the high symmetry points Γ , X and M at $U=0.4$, $n = 4$ with kick time 5.0 and $|\mathbf{B}_F|=0.002$. The left image in each row is just a blowup of the right image indicated by the boxed area. The magnetic field during the kick is applied in the x-z plane instead of y-z plane.

A.2.3 Heisenberg limit $n = 6$

The same discussion as done in section 8.3.2 can be repeated here using $n = 6$. $U = U_i = U_f = 3.0$ is utilized and the AFM ground state (Fig. 8.1) is kicked using $|\mathbf{B}_f| = 0.002$ and a kicktime $t' = 5.0$ to be in the linear-response regime. The obtained magnetization dynamics for $n = 6$ at site 1 and 2 are shown in Fig. A.5 (left) and (right), respectively. Again the x -component displays the AFM order with no visible dynamic considering the computed time frame and only small numeric deviations. The absolute value $|m|$ remains nearly constant due to the small amplitudes in m_y and m_z . This enables us to restrict the discussion to the transverse modes. In

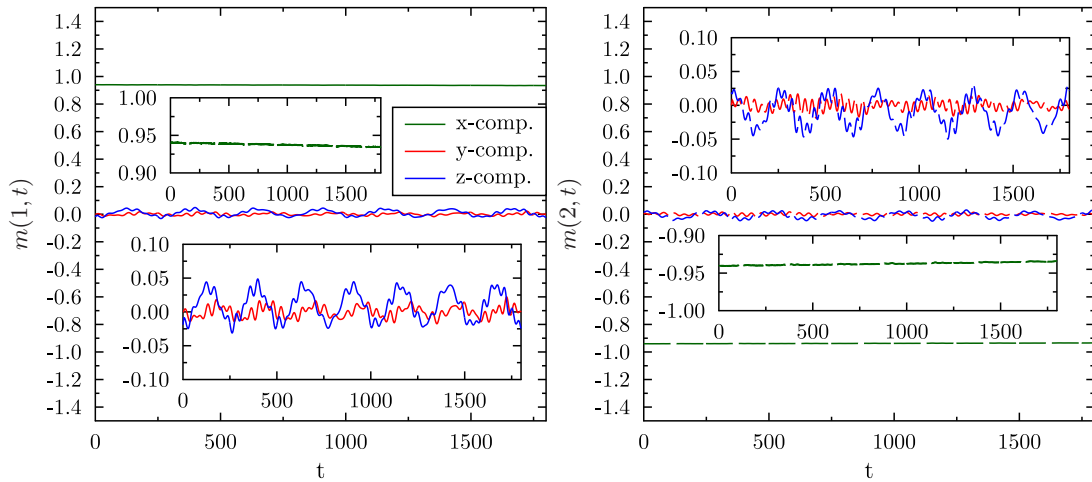


Figure A.5: Magnetization dynamics at site 1 (left) and 2 (right) at $U=3.0$, $n = 6$ with kick time 5.0 and $|\mathbf{B}_f|=0.002$ for 6x6 lattice.

Fig. A.6 \tilde{m}_y (top) and \tilde{m}_z (bottom) are depicted. Again both figures display the magnetic excitations known as magnon dispersion from spin-wave theory [50, 51]. Note that the position of the spin-excitations is exactly the same as in the $n = 4$ case (compare Fig. A.6 and 8.10). This renders clear that the specifics of the chosen site-dependent magnetic field applied during the kick are not important to obtain the magnon dispersion for the used small kicktime and weak magnetic field.

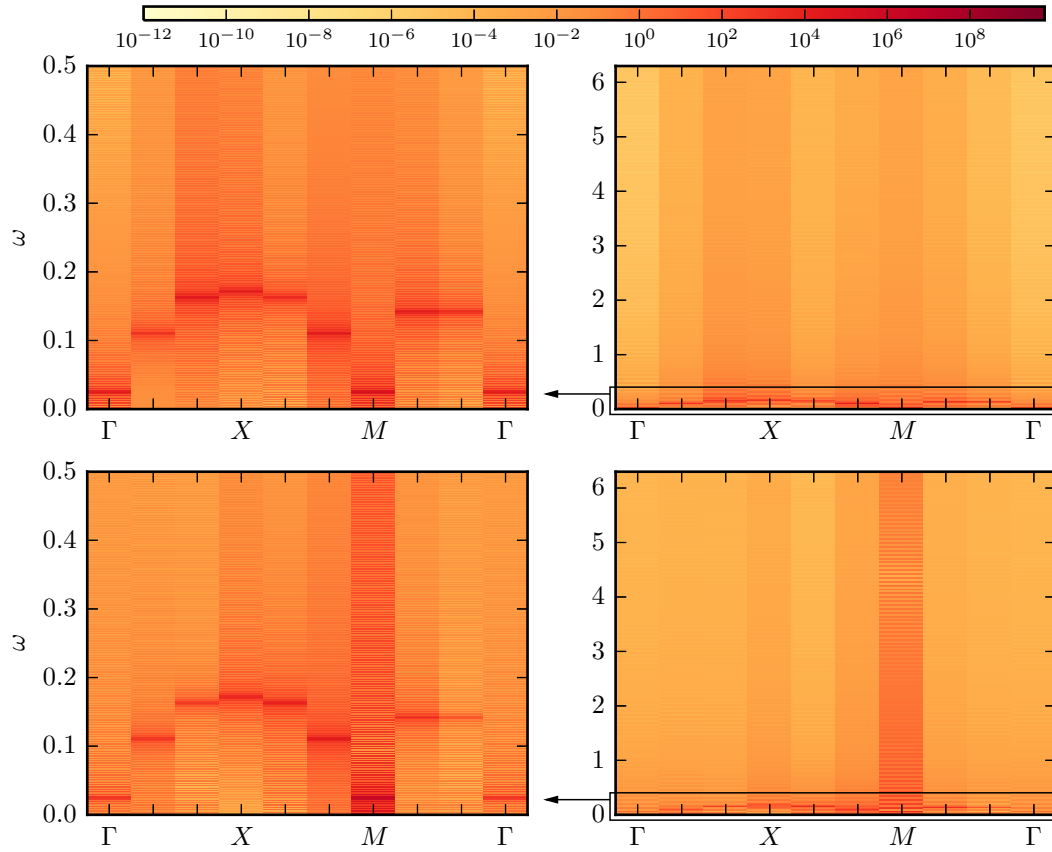


Figure A.6: \tilde{m}_y (top) and \tilde{m}_z (bottom) along a path through the Brillouin zone with the high symmetry points Γ , X and M at $U=3.0$, $n = 6$ with $t'=5.0$ and $|\mathbf{B}_f|=0.002$. The left image in each row is just a blowup of the right image indicated by the boxed area.

A.2.4 Magnetic excitations between Stoner and Heisenberg-Limit

Note that exactly the same setup is used as in section 8.4.1. However instead of \tilde{m}_y , \tilde{m}_z is depicted in A.7. \tilde{m}_z displays the same features as \tilde{m}_y of Fig. 8.11. So the discussion done in section 8.4.1 also holds for the picture of this section. The only difference between the two figures is the U -independent inhomogeneous magnetic excitation at $\mathbf{q} = M$, which is due the small AFM equilibrium order in the z -direction as explained in section 8.3.1.

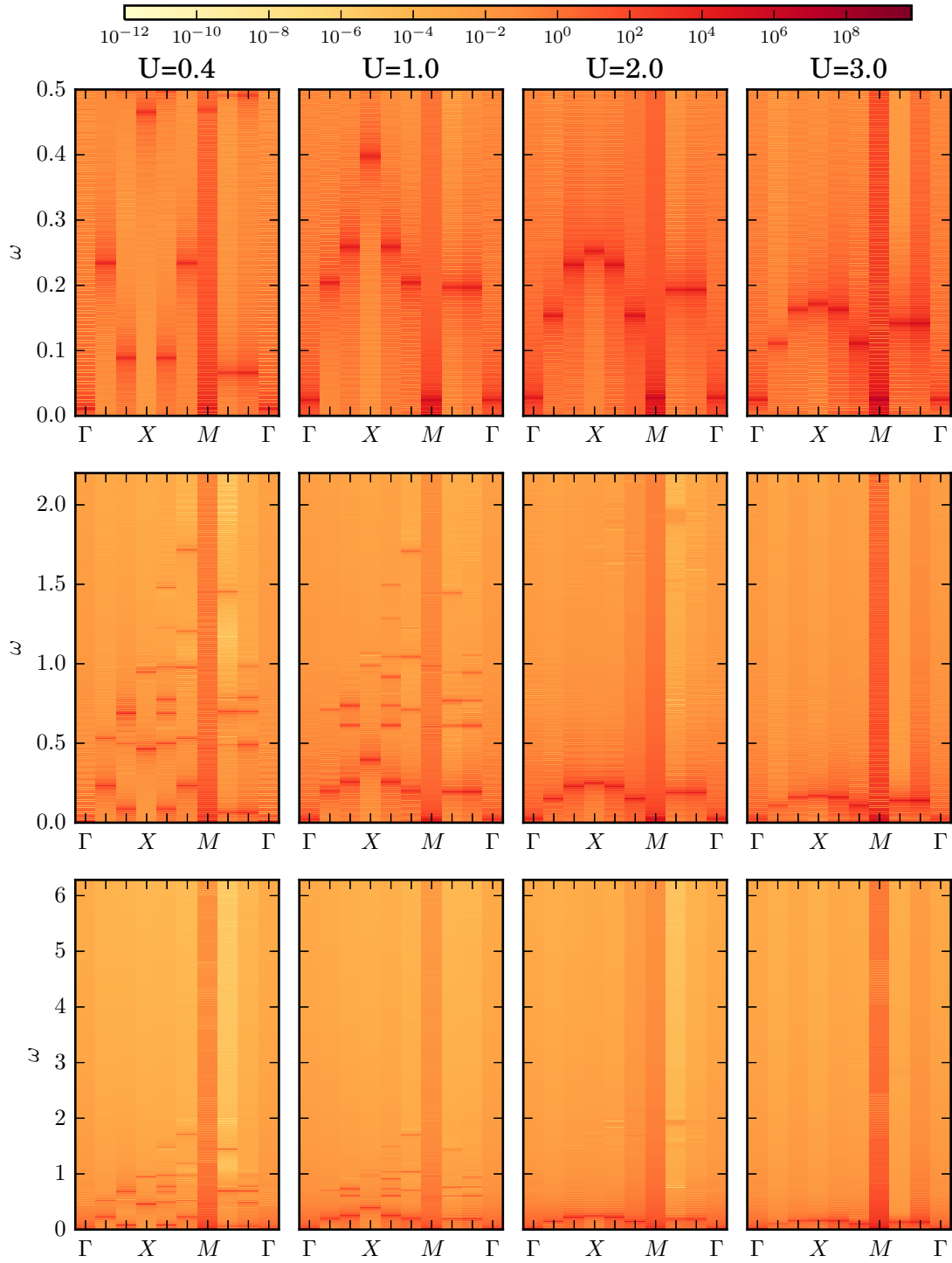


Figure A.7: \tilde{m}_z along a path through the Brillouin zone with the high symmetry points Γ , X and M $n = 4$ with kick time 5.0 and $|\mathbf{B}_f|=0.002$. Note that each column displays the same data at different interactions U .

A.2.5 Instability of magnons in effective high magnetic fields

Here the same discussion as done in section 8.4.2 can be repeated using \tilde{m}_y instead of \tilde{m}_z . First the influence of kicktime t' onto the magnon dispersion for $n = 4$, $|\mathbf{B}_f|=0.020$ and $U = 3.0$ is shown in Fig. A.8 and then a comparison to a previous non-equilibrium Heisenberg Spin model study utilizing self-consistent Born approximation [158] can be drawn using Fig. A.9.

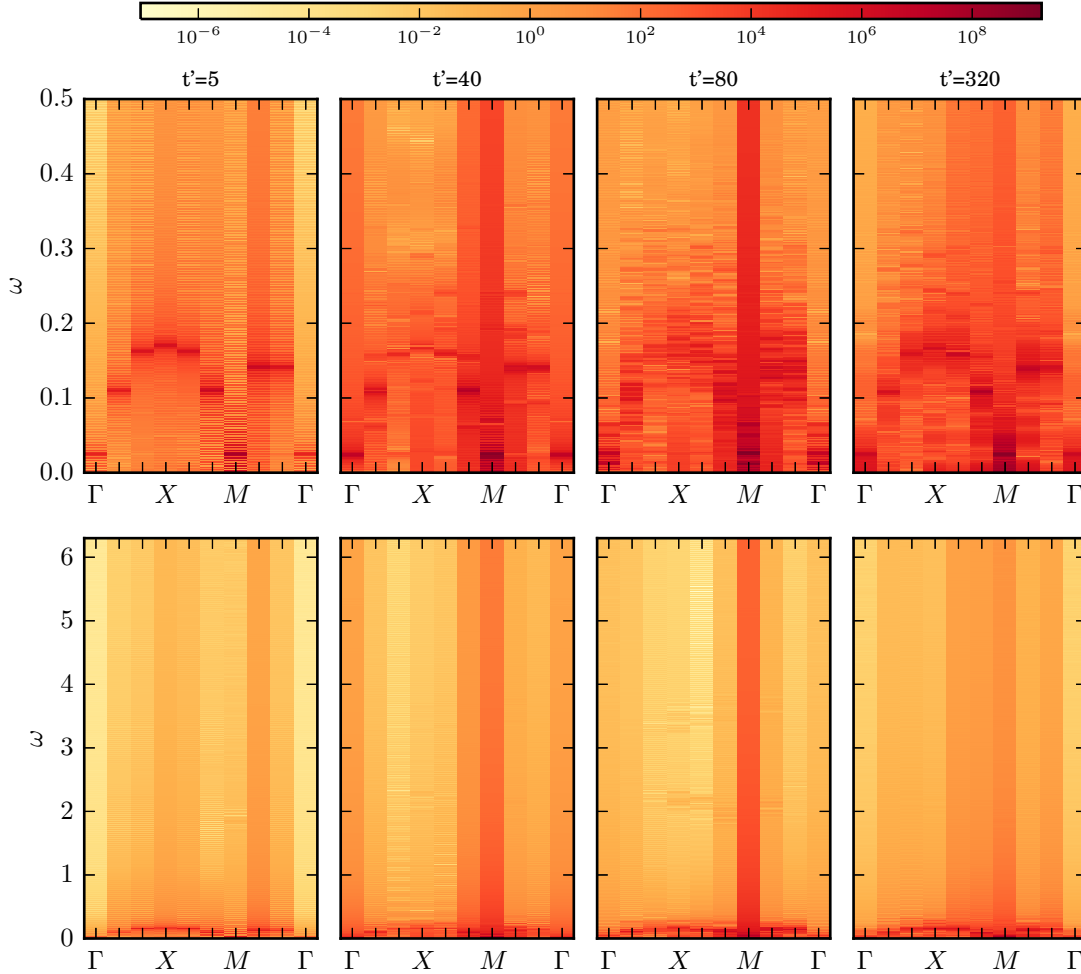


Figure A.8: \tilde{m}_y along a path through the Brillouin zone with the high symmetry points Γ , X and M at $U=3.0$, $n = 4$ with different t' and $|\mathbf{B}_f|=0.020$. Note that each column display the same data, only in different energy ranges.

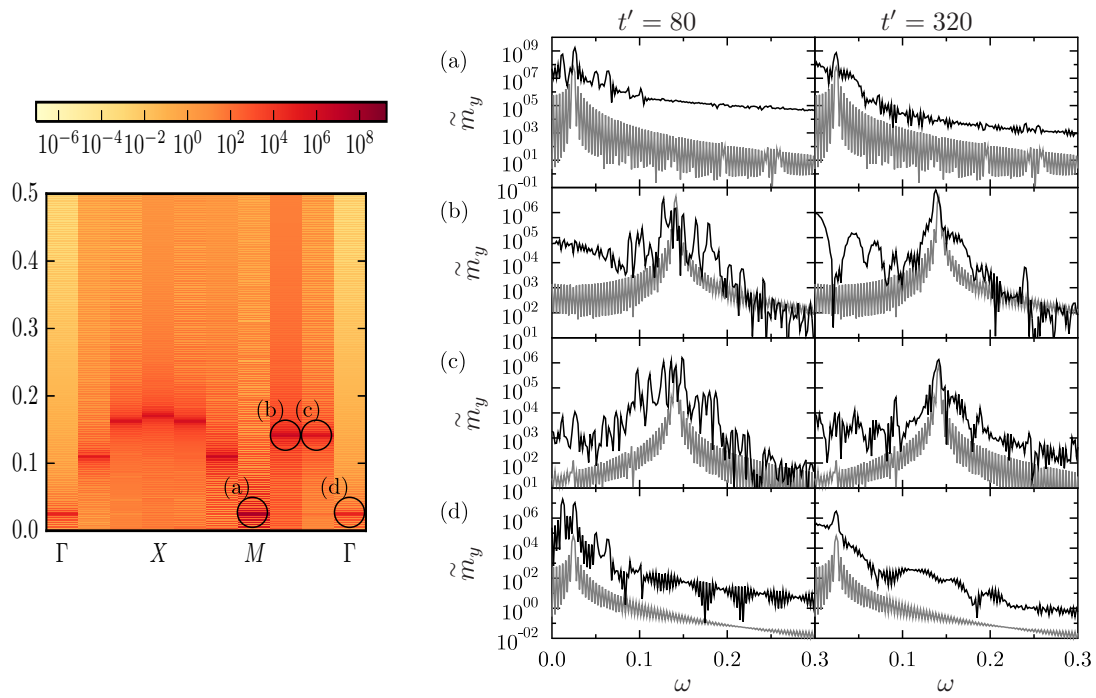


Figure A.9: \tilde{m}_y along a path through the Brillouin zone with the high symmetry points Γ , X and M at $U=3.0$, $n = 4$, $|\mathbf{B}_f|=0.020$ for $t' = 5$ (left) and for four selected \mathbf{q} -points at $t' = 80$ and $t' = 320$ in black (right). Grey indicates \tilde{m}_y at $t' = 5$.

B List of publications and author contributions

- Extended dynamic Mott transition in the two-band Hubbard model out of equilibrium

Malte Behrmann, Michele Fabrizio, and Frank Lechermann

Physical Review B **88**, 035116 – Published 15 July 2013

The content of this work is discussed in chapter 4.

This author transferred the time-dependent formalism from the Gutzwiller to the Slave-boson framework, implemented it, performed all calculations and contributed to the analysis and preparation of the manuscript.

- Large-amplitude spin oscillations triggered by nonequilibrium strongly correlated t_{2g} electrons

Malte Behrmann and Frank Lechermann

Phys. Rev. B **91**, 075110 – Published 11 February 2015

The content of this work is discussed in chapter 6.

This author generalized the implementation to include a multiple atom unit cell, performed all calculations and contributed to the analysis and preparation of the manuscript.

- Interface exchange processes in $\text{LaAlO}_3/\text{SrTiO}_3$ induced by oxygen vacancies

Malte Behrmann and Frank Lechermann

Phys. Rev. B **92**, 125148 – Published 28 September 2015

The content of this work is discussed in chapter 7.

This author transformed a former implementation to a real-space formulation, performed all calculations and contributed to the analysis and preparation of the manuscript.

C Acknowledgments

First of all i would like to thank my supervisor Frank Lechermann for his patience and endurance throughout the three and a half years of my PhD thesis. He had almost always time for questions and if he could not answer them immediately, he would know a direction to look for an answer. This has proven helpful for me numerous times. I think that our work was very successful regarding the content and number of interesting results presented in the publications and this thesis. Then i would like to thank Alexander Lichtenstein for reviewing this thesis and for numerous discussions especially in the last couple of month due to our common project. In the course of this project i also asked many questions to Misha Katsnelson and i thank him for his kind and helpful responses. Additionally i would like to thank Michael Potthoff, Henning Moritz and Daniela Pfannkuche for taking part in the examining board of my thesis. Daniela Pfannkuche as head of the examining board i have to thank also for the additional organizational duties. Then i would like to thank Michele Fabrizio for his kind introduction to the world of non-equilibrium physics in the Gutzwiller formalism and helping me to transfer the time-dependent Gutzwiller method to the slave boson formalism during my visit in Trieste. Additionally i found the collaboration during the work on our common publication a very interesting experience. During the stay in Trieste i also got to know Matteo Sandri, who i would like to thank for many discussions at that time and later on. I am indebted to my colleagues at the first institute of theoretical physics in Hamburg. Christoph Piefke with whom i had countless discussions on physical and non-physical topics of any kind. He helped me often and i could always count on him especially when time was short to find a solution. Lewin Boehnke the one who always had an answer on any technical or numerical question and stimulated interesting discussions by mentioning controversial point of views. Daniel Grieger with whom it was very nice to share the room. He provided helpful coding knowledge if needed or some time for off-topic discussions. The latter i can repeat for Michael Obermayer, who shared the room with me after Daniel left to work in Trieste. Apart from that

i would like to thank Raphael Richter, Alexander Hampel, Sergej Schuwalow for providing a nice working atmosphere and being open for discussions about physics, politics or economics. Furthermore i have to thank Holger Niehus, who helped me improving my knowledge about Mathematica and how one can generate useful and good-looking images. Similarly, i am obliged to Felix Hofmann, who introduced me to matplotlib, which proved as a very helpful tool to analyze and visualize data.

Bibliography

- [1] Al-Zubi, A.: *Ab Initio Investigations of Magnetic Properties of Ultrathin Transition Metal Films on 4d Substrates*, Forschungszentrum Jülich (2010), ISBN 978-3-89336-641-5.
- [2] Amadon, B., F. Lechermann, A. Georges, F. Jollet, T. O. Wehling und A. I. Lichtenstein: *Plane-wave based electronic structure calculations for correlated materials using dynamical mean-field theory and projected local orbitals*, Physical Review B **77** (20) 205112 (2008), URL <http://link.aps.org/doi/10.1103/PhysRevB.77.205112>.
- [3] Anderson, P. W.: *Localized Magnetic States in Metals*, Physical Review **124** (1) 41 (1961), URL <http://link.aps.org/doi/10.1103/PhysRev.124.41>.
- [4] Anisimov, V. I., I. A. Nekrasov, D. E. Kondakov, T. M. Rice und M. Sigrist: *Orbital-selective Mott-insulator transition in $Ca_{2-x}Sr_xRuO_4$* , The European Physical Journal B - Condensed Matter and Complex Systems **25** (2) 191 (2002), ISSN 1434-6028, 1434-6036, URL <http://link.springer.com/article/10.1140/epjb/e20020021>.
- [5] Anisimov, V. I., A. I. Poteryaev, M. A. Korotin, A. O. Anokhin und G. Kotliar: *First-principles calculations of the electronic structure and spectra of strongly correlated systems: dynamical mean-field theory*, Journal of Physics: Condensed Matter **9** (35) 7359 (1997), ISSN 0953-8984, URL <http://stacks.iop.org/0953-8984/9/i=35/a=010>.
- [6] Antipov, A. E., I. S. Krivenko, V. I. Anisimov, A. I. Lichtenstein und A. N. Rubtsov: *Role of rotational symmetry in the magnetism of a multiorbital model*, Physical Review B **86** (15) 155107 (2012), URL <http://link.aps.org/doi/10.1103/PhysRevB.86.155107>.

- [7] Aoki, H., N. Tsuji, M. Eckstein, M. Kollar, T. Oka und P. Werner: *Nonequilibrium dynamical mean-field theory and its applications*, Reviews of Modern Physics **86** (2) 779 (2014), URL <http://link.aps.org/doi/10.1103/RevModPhys.86.779>.
- [8] Ariando, X. Wang, G. Baskaran, Z. Q. Liu, J. Huijben, J. B. Yi, A. Anadi, A. R. Barman, A. Rusydi, S. Dhar, Y. P. Feng, J. Ding, H. Hilgenkamp und T. Venkatesan: *Electronic phase separation at the $\text{LaAlO}_3/\text{SrTiO}_3$ interface*, Nature Communications **2** 188 (2011), URL <http://www.nature.com/ncomms/journal/v2/n2/full/ncomms1192.html>.
- [9] Asai, Y.: *Elementary-spin-excitation spectrum of undoped and doped single-band Hubbard models*, Physical Review B **49** (14) 10013 (1994), URL <http://link.aps.org/doi/10.1103/PhysRevB.49.10013>.
- [10] Battiato, M., K. Carva und P. M. Oppeneer: *Superdiffusive Spin Transport as a Mechanism of Ultrafast Demagnetization*, Physical Review Letters **105** (2) 027203 (2010), URL <http://link.aps.org/doi/10.1103/PhysRevLett.105.027203>.
- [11] Beaurepaire, E., J.-C. Merle, A. Daunois und J.-Y. Bigot: *Ultrafast Spin Dynamics in Ferromagnetic Nickel*, Physical Review Letters **76** (22) 4250 (1996), URL <http://link.aps.org/doi/10.1103/PhysRevLett.76.4250>.
- [12] Belemuk, A. M., N. M. Chtchelkatchev und A. V. Mikheyenkov: *Effective orbital ordering in multiwell optical lattices with fermionic atoms*, Physical Review A **90** (2) 023625 (2014), URL <http://link.aps.org/doi/10.1103/PhysRevA.90.023625>.
- [13] Bert, J. A., B. Kalisky, C. Bell, M. Kim, Y. Hikita, H. Y. Hwang und K. A. Moler: *Direct imaging of the coexistence of ferromagnetism and superconductivity at the $\text{LaAlO}_3/\text{SrTiO}_3$ interface*, Nature Physics **7** (10) 767 (2011), ISSN 1745-2473, URL <http://www.nature.com/nphys/journal/v7/n10/full/nphys2079.html>.
- [14] Bi, F., M. Huang, S. Ryu, H. Lee, C.-W. Bark, C.-B. Eom, P. Irvin und J. Levy: *Room-temperature electronically-controlled ferromagnetism at the $\text{LaAlO}_3/\text{SrTiO}_3$ interface*, Nature Communications **5** 5019

- (2014), URL <http://www.nature.com/ncomms/2014/140925/ncomms6019/abs/ncomms6019.html>.
- [15] Bloch, I., J. Dalibard und W. Zwerger: *Many-body physics with ultracold gases*, *Reviews of Modern Physics* **80** (3) 885 (2008), URL <http://link.aps.org/doi/10.1103/RevModPhys.80.885>.
- [16] Boehnke, L., H. Hafermann, M. Ferrero, F. Lechermann und O. Parcollet: *Orthogonal polynomial representation of imaginary-time Green's functions*, *Physical Review B* **84** (7) 075145 (2011), URL <http://link.aps.org/doi/10.1103/PhysRevB.84.075145>.
- [17] Brinkman, A., M. Huijben, M. van Zalk, J. Huijben, U. Zeitler, J. C. Maan, W. G. van der Wiel, G. Rijnders, D. H. A. Blank und H. Hilgenkamp: *Magnetic effects at the interface between non-magnetic oxides*, *Nature Materials* **6** (7) 493 (2007), ISSN 1476-1122, URL <http://www.nature.com/nmat/journal/v6/n7/full/nmat1931.html>.
- [18] Bulut, N., D. J. Scalapino und S. R. White: *Comparison of Monte Carlo and diagrammatic calculations for the two-dimensional Hubbard model*, *Physical Review B* **47** (5) 2742 (1993), URL <http://link.aps.org/doi/10.1103/PhysRevB.47.2742>.
- [19] Bünemann, J. und F. Gebhard: *Equivalence of Gutzwiller and slave-boson mean-field theories for multiband Hubbard models*, *Physical Review B* **76** (19) 193104 (2007), URL <http://link.aps.org/doi/10.1103/PhysRevB.76.193104>.
- [20] Calabrese, P. und J. Cardy: *Time Dependence of Correlation Functions Following a Quantum Quench*, *Physical Review Letters* **96** (13) 136801 (2006), URL <http://link.aps.org/doi/10.1103/PhysRevLett.96.136801>.
- [21] Capelle, K. und L. N. Oliveira: *Dimensional scaling estimate of the energy of a large system from that of its building blocks: Hubbard model and Fermi liquid*, *Physical Review B* **73** (11) 113111 (2006), URL <http://link.aps.org/doi/10.1103/PhysRevB.73.113111>.

- [22] Castellani, C., C. R. Natoli und J. Ranninger: *Magnetic structure of V_2O_3 in the insulating phase*, Physical Review B **18** (9) 4945 (1978), URL <http://link.aps.org/doi/10.1103/PhysRevB.18.4945>.
- [23] Caviglia, A. D., S. Gariglio, N. Reyren, D. Jaccard, T. Schneider, M. Gabay, S. Thiel, G. Hammerl, J. Mannhart und J.-M. Triscone: *Electric field control of the $LaAlO_3/SrTiO_3$ interface ground state*, Nature **456** (7222) 624 (2008), ISSN 0028-0836, URL <http://www.nature.com/nature/journal/v456/n7222/abs/nature07576.html>.
- [24] Chan, C.-K., P. Werner und A. J. Millis: *Magnetism and orbital ordering in an interacting three-band model: A dynamical mean-field study*, Physical Review B **80** (23) 235114 (2009), URL <http://link.aps.org/doi/10.1103/PhysRevB.80.235114>.
- [25] Christoph Piefke: *Rotationally Invariant Slave-Boson Mean-Field Formalism (RISB-MF) - extension of the method and application to strongly correlated materials*, Diplomarbeit, Hamburg (2010).
- [26] Coomer, F. C., V. Bondah-Jagalu, K. J. Grant, A. Harrison, G. J. McIntyre, H. M. Rønnow, R. Feyerherm, T. Wand, M. Meißner, D. Visser und D. F. McMorrow: *Neutron diffraction studies of nuclear and magnetic structures in the $S = 1/2$ square Heisenberg antiferromagnets $(d_6 - 5CAP)_2 CuX_4$ ($X = Br$ and Cl)*, Physical Review B **75** (9) 094424 (2007), URL <http://link.aps.org/doi/10.1103/PhysRevB.75.094424>.
- [27] de'Medici, L., A. Georges und S. Biermann: *Orbital-selective Mott transition in multiband systems: Slave-spin representation and dynamical mean-field theory*, Physical Review B **72** (20) 205124 (2005), URL <http://link.aps.org/doi/10.1103/PhysRevB.72.205124>.
- [28] Drchal, V., V. Janiš und J. Kudrnovský: *Dynamical electron correlations in weakly interacting systems: TB-LMTO approach to metals and random alloys*, Physical Review B **60** (23) 15664 (1999), URL <http://link.aps.org/doi/10.1103/PhysRevB.60.15664>.
- [29] Eckstein, M., M. Kollar und P. Werner: *Thermalization after an Interaction Quench in the Hubbard Model*, Physical Review Letters **103** (5) 056403 (2009), URL <http://link.aps.org/doi/10.1103/PhysRevLett.103.056403>.

- [30] Eckstein, M., M. Kollar und P. Werner: *Interaction quench in the Hubbard model: Relaxation of the spectral function and the optical conductivity*, Physical Review B **81** (11) 115131 (2010), URL <http://link.aps.org/doi/10.1103/PhysRevB.81.115131>.
- [31] Erskine, J. L. und E. A. Stern: *Calculation of the M_{23} magneto-optical absorption spectrum of ferromagnetic nickel*, Physical Review B **12** (11) 5016 (1975), URL <http://link.aps.org/doi/10.1103/PhysRevB.12.5016>.
- [32] Fitzsimmons, M. R., N. W. Hengartner, S. Singh, M. Zhernenkov, F. Y. Bruno, J. Santamaria, A. Brinkman, M. Huijben, H. J. A. Molegraaf, J. de la Venta und I. K. Schuller: *Upper Limit to Magnetism in $\text{LaAlO}_3/\text{SrTiO}_3$ Heterostructures*, Physical Review Letters **107** (21) 217201 (2011), URL <http://link.aps.org/doi/10.1103/PhysRevLett.107.217201>.
- [33] Frésard, R. und G. Kotliar: *Interplay of Mott transition and ferromagnetism in the orbitally degenerate Hubbard model*, Physical Review B **56** (20) 12909 (1997), URL <http://link.aps.org/doi/10.1103/PhysRevB.56.12909>.
- [34] Gorshkov, A. V., M. Hermele, V. Gurarie, C. Xu, P. S. Julienne, J. Ye, P. Zoller, E. Demler, M. D. Lukin und A. M. Rey: *Two-orbital $SU(N)$ magnetism with ultracold alkaline-earth atoms*, Nature Physics **6** (4) 289 (2010), ISSN 1745-2473, URL <http://www.nature.com/nphys/journal/v6/n4/abs/nphys1535.html>.
- [35] Greengard, L. und J. Lee: *Accelerating the Nonuniform Fast Fourier Transform*, SIAM Review **46** (3) 443 (2004), ISSN 0036-1445, URL <http://epubs.siam.org/doi/abs/10.1137/S003614450343200X>.
- [36] Greif, D., T. Uehlinger, G. Jotzu, L. Tarruell und T. Esslinger: *Short-Range Quantum Magnetism of Ultracold Fermions in an Optical Lattice*, Science **340** (6138) 1307 (2013), ISSN 0036-8075, 1095-9203, URL <http://www.sciencemag.org/content/340/6138/1307>.
- [37] Greiner, M., O. Mandel, T. Esslinger, T. W. Hänsch und I. Bloch: *Quantum phase transition from a superfluid to a Mott insulator in a gas of ultracold atoms*, Nature **415** (6867) 39 (2002), ISSN 0028-0836, URL <http://www.nature.com/nature/journal/v415/n6867/full/415039a.html>.

- [38] Greiner, W., L. Neise und H. Stöcker: *Theoretische Physik: ein Lehr- und Übungsbuch für Anfangssemester ; mit zahlreichen Beispielen und Aufgaben mit ausführlichen Lösungen. Ergänzungsband: Quantentheorie : spezielle Kapitel*, Harri Deutsch Verlag (1989), ISBN 978-3-8171-1073-5.
- [39] Grieger, D.: *Charge self-consistency in an LDA+DMFT framework*, Dissertation, Hamburg (2013).
- [40] Grieger, D.: *private communication* (2015).
- [41] Grieger, D. und M. Fabrizio: *Low-temperature magnetic ordering and structural distortions in vanadium sesquioxide V_2O_3* , Physical Review B **92** (7) 075121 (2015), URL <http://link.aps.org/doi/10.1103/PhysRevB.92.075121>.
- [42] Grieger, D. und F. Lechermann: *Effect of chromium doping on the correlated electronic structure of V_2O_3* , Physical Review B **90** (11) 115115 (2014), URL <http://link.aps.org/doi/10.1103/PhysRevB.90.115115>.
- [43] Gull, E., A. J. Millis, A. I. Lichtenstein, A. N. Rubtsov, M. Troyer und P. Werner: *Continuous-time Monte Carlo methods for quantum impurity models*, Reviews of Modern Physics **83** (2) 349 (2011), URL <http://link.aps.org/doi/10.1103/RevModPhys.83.349>.
- [44] Hairer, Ernst, Nørsett, Syvert P. und Wanner, Gerhard: *Solving Ordinary Differential Equations I* (1993), URL <http://www.springer.com/mathematics/analysis/book/978-3-540-56670-0>.
- [45] Hart, R. A., P. M. Duarte, T.-L. Yang, X. Liu, T. Paiva, E. Khatami, R. T. Scalettar, N. Trivedi, D. A. Huse und R. G. Hulet: *Observation of antiferromagnetic correlations in the Hubbard model with ultracold atoms*, Nature **519** (7542) 211 (2015), ISSN 0028-0836, URL <http://www.nature.com/nature/journal/v519/n7542/abs/nature14223.html>.
- [46] Held, K., G. Keller, V. Eyert, D. Vollhardt und V. I. Anisimov: *Mott-Hubbard Metal-Insulator Transition in Paramagnetic V_2O_3 : An LDA+DMFT(QMC) Study*, Physical Review Letters **86** (23) 5345 (2001), URL <http://link.aps.org/doi/10.1103/PhysRevLett.86.5345>.

- [47] Held, K. und D. Vollhardt: *Microscopic conditions favoring itinerant ferromagnetism: Hund's rule coupling and orbital degeneracy*, The European Physical Journal B - Condensed Matter and Complex Systems **5** (3) 473 (1998), ISSN 1434-6028, 1434-6036, URL <http://link.springer.com/article/10.1007/s100510050468>.
- [48] Hubbard, J.: *Electron Correlations in Narrow Energy Bands*, Proceedings of the Royal Society of London. Series A. Mathematical and Physical Sciences **276** (1365) 238 (1963), ISSN 1364-5021, 1471-2946, URL <http://rspa.royalsocietypublishing.org/content/276/1365/238>.
- [49] Hwang, H. Y., Y. Iwasa, M. Kawasaki, B. Keimer, N. Nagaosa und Y. Tokura: *Emergent phenomena at oxide interfaces*, Nature Materials **11** (2) 103 (2012), ISSN 1476-1122, URL <http://www.nature.com/nmat/journal/v11/n2/abs/nmat3223.html>.
- [50] Igarashi, J.-i. und T. Nagao: *1/S-expansion study of spin waves in a two-dimensional Heisenberg antiferromagnet*, Physical Review B **72** (1) 014403 (2005), URL <http://link.aps.org/doi/10.1103/PhysRevB.72.014403>.
- [51] Igarashi, J.-i. und A. Watabe: *Dynamics of a two-dimensional Heisenberg antiferromagnet at zero temperature*, Physical Review B **43** (16) 13456 (1991), URL <http://link.aps.org/doi/10.1103/PhysRevB.43.13456>.
- [52] Ikeda, S. I. und N. Shirakawa: *Magnetic and transport properties of perovskite-related strontium molybdates*, Physica C: Superconductivity **341–348**, Part 2 785 (2000), ISSN 0921-4534, URL <http://www.sciencedirect.com/science/article/pii/S0921453400006924>.
- [53] Ikeda, S.-I., N. Shirakawa, H. Bando und Y. Ootuka: *Orbital-Degenerate Paramagnetic Metal Sr_2MoO_4 : An Electronic Analogue to Sr_2RuO_4* , Journal of the Physical Society of Japan **69** (10) 3162 (2000), ISSN 0031-9015, 1347-4073, URL <http://journals.jps.jp/doi/abs/10.1143/JPSJ.69.3162>.
- [54] Imada, M., A. Fujimori und Y. Tokura: *Metal-insulator transitions*, Reviews of Modern Physics **70** (4) 1039 (1998), URL <http://link.aps.org/doi/10.1103/RevModPhys.70.1039>.

- [55] Inaba, K. und A. Koga: *Phase diagrams of the two-orbital Hubbard model with different bandwidths*, Physical Review B **73** (15) 155106 (2006), URL <http://link.aps.org/doi/10.1103/PhysRevB.73.155106>.
- [56] Ishida, K., H. Mukuda, Y. Kitaoka, K. Asayama, Z. Q. Mao, Y. Mori und Y. Maeno: *Spin-triplet superconductivity in Sr_2RuO_4 identified by ^{17}O Knight shift*, Nature **396** (6712) 658 (1998), ISSN 0028-0836, URL <http://www.nature.com/nature/journal/v396/n6712/full/396658a0.html>.
- [57] Jördens, R., N. Strohmaier, K. Günter, H. Moritz und T. Esslinger: *A Mott insulator of fermionic atoms in an optical lattice*, Nature **455** (7210) 204 (2008), ISSN 0028-0836, URL <http://www.nature.com/nature/journal/v455/n7210/full/nature07244.html>.
- [58] Kalabukhov, A., R. Gunnarsson, J. Börjesson, E. Olsson, T. Claeson und D. Winkler: *Effect of oxygen vacancies in the $SrTiO_3$ substrate on the electrical properties of the $LaAlO_3/SrTiO_3$ interface*, Physical Review B **75** (12) 121404 (2007), URL <http://link.aps.org/doi/10.1103/PhysRevB.75.121404>.
- [59] Kalisky, B., J. A. Bert, C. Bell, Y. Xie, H. K. Sato, M. Hosoda, Y. Hikita, H. Y. Hwang und K. A. Moler: *Scanning Probe Manipulation of Magnetism at the $LaAlO_3/SrTiO_3$ Heterointerface*, Nano Letters **12** (8) 4055 (2012), ISSN 1530-6984, URL <http://dx.doi.org/10.1021/nl301451e>.
- [60] Keller, G., K. Held, V. Eyert, D. Vollhardt und V. I. Anisimov: *Electronic structure of paramagnetic V_2O_3 : Strongly correlated metallic and Mott insulating phase*, Physical Review B **70** (20) 205116 (2004), URL <http://link.aps.org/doi/10.1103/PhysRevB.70.205116>.
- [61] Khaliullin, G. und S. Maekawa: *Orbital Liquid in Three-Dimensional Mott Insulator: $LaTiO_3$* , Physical Review Letters **85** (18) 3950 (2000), URL <http://link.aps.org/doi/10.1103/PhysRevLett.85.3950>.
- [62] Kimel, A. V., B. A. Ivanov, R. V. Pisarev, P. A. Usachev, A. Kirilyuk und T. Rasing: *Inertia-driven spin switching in antiferromagnets*, Nature Physics **5** (10) 727 (2009), ISSN 1745-2473, URL <http://www.nature.com/nphys/journal/v5/n10/abs/nphys1369.html>.

- [63] Kimel, A. V., A. Kirilyuk, A. Tsvetkov, R. V. Pisarev und T. Rasing: *Laser-induced ultrafast spin reorientation in the antiferromagnet $TmFeO_3$* , Nature **429** (6994) 850 (2004), ISSN 0028-0836, URL <http://www.nature.com/nature/journal/v429/n6994/full/nature02659.html>.
- [64] Kimel, A. V., A. Kirilyuk, P. A. Usachev, R. V. Pisarev, A. M. Balbashov und T. Rasing: *Ultrafast non-thermal control of magnetization by instantaneous photomagnetic pulses*, Nature **435** (7042) 655 (2005), ISSN 0028-0836, URL <http://www.nature.com/nature/journal/v435/n7042/full/nature03564.html#B6>.
- [65] Kirschner, J., D. Rebenstorff und H. Ibach: *High-Resolution Spin-Polarized Electron-Energy-Loss Spectroscopy and the Stoner Excitation Spectrum in Nickel*, Physical Review Letters **53** (7) 698 (1984), URL <http://link.aps.org/doi/10.1103/PhysRevLett.53.698>.
- [66] Koga, A., Y. Imai und N. Kawakami: *Stability of a metallic state in the two-orbital Hubbard model*, Physical Review B **66** (16) 165107 (2002), URL <http://link.aps.org/doi/10.1103/PhysRevB.66.165107>.
- [67] Koga, A., N. Kawakami, T. M. Rice und M. Sigrist: *Orbital-Selective Mott Transitions in the Degenerate Hubbard Model*, Physical Review Letters **92** (21) 216402 (2004), URL <http://link.aps.org/doi/10.1103/PhysRevLett.92.216402>.
- [68] Kondo, J.: *Resistance Minimum in Dilute Magnetic Alloys*, Progress of Theoretical Physics **32** (1) 37 (1964), ISSN 0033-068X, 1347-4081, URL <http://ptp.oxfordjournals.org/content/32/1/37>.
- [69] Koopmans, B., G. Malinowski, F. Dalla Longa, D. Steiauf, M. Fähnle, T. Roth, M. Cinchetti und M. Aeschlimann: *Explaining the paradoxical diversity of ultrafast laser-induced demagnetization*, Nature Materials **9** (3) 259 (2010), ISSN 1476-1122, URL <http://www.nature.com/nmat/journal/v9/n3/abs/nmat2593.html>.
- [70] Kramers, H. A.: *L'interaction Entre les Atomes Magnétogènes dans un Cristal Paramagnétique*, Physica **1** (1-6) 182 (1934), ISSN 0031-8914, URL <http://www.sciencedirect.com/science/article/pii/S0031891434900239>.

- [71] Krauß, M., T. Roth, S. Alebrand, D. Steil, M. Cinchetti, M. Aeschlimann und H. C. Schneider: *Ultrafast demagnetization of ferromagnetic transition metals: The role of the Coulomb interaction*, Physical Review B **80** (18) 180407 (2009), URL <http://link.aps.org/doi/10.1103/PhysRevB.80.180407>.
- [72] Kugel, K. und D. Khomskii: *Crystal structure and magnetic properties of substances with orbital degeneracy*, JETP **37** (4) 725 (1973).
- [73] Langevin, P.: *Sur la théorie du magnétisme*, J. Phys. Theor. Appl. **4** (1) 678 (1905), URL <https://hal.archives-ouvertes.fr/jpa-00241050>.
- [74] Le Guyader, L., A. Kleibert, F. Nolting, L. Joly, P. M. Derlet, R. V. Pisarev, A. Kirilyuk, T. Rasing und A. V. Kimel: *Dynamics of laser-induced spin reorientation in Co/SmFeO₃ heterostructure*, Physical Review B **87** (5) 054437 (2013), URL <http://link.aps.org/doi/10.1103/PhysRevB.87.054437>.
- [75] Lechermann, F., S. Biermann und A. Georges: *Interorbital Charge Transfers and Fermi-Surface Deformations in Strongly Correlated Metals: Models, BaVS₃ and Na_xCoO₂*, Progress of Theoretical Physics Supplement **160** 233 (2005), ISSN 0375-9687, URL <http://ptps.oxfordjournals.org/content/160/233>.
- [76] Lechermann, F., L. Boehnke, D. Grieger und C. Piefke: *Electron correlation and magnetism at the LaAlO₃/SrTiO₃ interface: A DFT+DMFT investigation*, Physical Review B **90** (8) 085125 (2014), URL <http://link.aps.org/doi/10.1103/PhysRevB.90.085125>.
- [77] Lechermann, F., A. Georges, G. Kotliar und O. Parcollet: *Rotationally invariant slave-boson formalism and momentum dependence of the quasiparticle weight*, Physical Review B **76** (15) 155102 (2007), URL <http://link.aps.org/doi/10.1103/PhysRevB.76.155102>.
- [78] Lee, J.-Y. und L. Greengard: *The type 3 nonuniform FFT and its applications*, Journal of Computational Physics **206** (1) 1 (2005), ISSN 0021-9991, URL <http://www.sciencedirect.com/science/article/pii/S002199910400511X>.
- [79] Li, L., C. Richter, J. Mannhart und R. C. Ashoori: *Coexistence of magnetic order and two-dimensional superconductivity at LaAlO₃/SrTiO₃ interfaces*, Na-

- ture Physics **7** (10) 762 (2011), ISSN 1745-2473, URL <http://www.nature.com/nphys/journal/v7/n10/abs/nphys2080.html>.
- [80] Lichtenstein, A. I., M. I. Katsnelson und G. Kotliar: *Finite-Temperature Magnetism of Transition Metals: An ab initio Dynamical Mean-Field Theory*, Physical Review Letters **87** (6) 067205 (2001), URL <http://link.aps.org/doi/10.1103/PhysRevLett.87.067205>.
- [81] Lieb, E.: *The Hubbard Model: Some Rigorous Results and Open Problems*, arXiv:cond-mat/9311033 (1993), xI Int. Cong. MP, Int. Press (1995) 392-412, URL <http://arxiv.org/abs/cond-mat/9311033>.
- [82] Lieb, E. H. und F. Y. Wu: *Absence of Mott Transition in an Exact Solution of the Short-Range, One-Band Model in One Dimension*, Physical Review Letters **20** (25) 1445 (1968), URL <http://link.aps.org/doi/10.1103/PhysRevLett.20.1445>.
- [83] Liebsch, A.: *Mott Transitions in Multiorbital Systems*, Physical Review Letters **91** (22) 226401 (2003), URL <http://link.aps.org/doi/10.1103/PhysRevLett.91.226401>.
- [84] Lin, C. und A. A. Demkov: *Electron Correlation in Oxygen Vacancy in SrTiO₃*, Physical Review Letters **111** (21) 217601 (2013), URL <http://link.aps.org/doi/10.1103/PhysRevLett.111.217601>.
- [85] Lin, C. und A. A. Demkov: *Consequences of Oxygen-Vacancy Correlations at the SrTiO₃ Interface*, Physical Review Letters **113** (15) 157602 (2014), URL <http://link.aps.org/doi/10.1103/PhysRevLett.113.157602>.
- [86] Lüscher, A. und A. M. Läuchli: *Exact diagonalization study of the antiferromagnetic spin- $\frac{1}{2}$ Heisenberg model on the square lattice in a magnetic field*, Physical Review B **79** (19) 195102 (2009), URL <http://link.aps.org/doi/10.1103/PhysRevB.79.195102>.
- [87] Marcus, P. M. und V. L. Moruzzi: *Stoner model of ferromagnetism and total-energy band theory*, Physical Review B **38** (10) 6949 (1988), URL <http://link.aps.org/doi/10.1103/PhysRevB.38.6949>.

- [88] McKeown Walker, S., A. de la Torre, F. Bruno, A. Tamai, T. Kim, M. Hoesch, M. Shi, M. Bahramy, P. King und F. Baumberger: *Control of a Two-Dimensional Electron Gas on SrTiO₃(111) by Atomic Oxygen*, Physical Review Letters **113** (17) 177601 (2014), URL <http://link.aps.org/doi/10.1103/PhysRevLett.113.177601>.
- [89] McWhan, D. B., A. Menth, J. P. Remeika, W. F. Brinkman und T. M. Rice: *Metal-Insulator Transitions in Pure and Doped V₂O₃*, Physical Review B **7** (5) 1920 (1973), URL <http://link.aps.org/doi/10.1103/PhysRevB.7.1920>.
- [90] McWhan, D. B. und J. P. Remeika: *Metal-Insulator Transition in (V_{1-x}Cr_x)₂O₃*, Physical Review B **2** (9) 3734 (1970), URL <http://link.aps.org/doi/10.1103/PhysRevB.2.3734>.
- [91] McWhan, D. B., J. P. Remeika, T. M. Rice, W. F. Brinkman, J. P. Maita und A. Menth: *Electronic Specific Heat of Metallic Ti-Doped V₂O₃*, Physical Review Letters **27** (14) 941 (1971), URL <http://link.aps.org/doi/10.1103/PhysRevLett.27.941>.
- [92] de' Medici, L., J. Mravlje und A. Georges: *Janus-Faced Influence of Hund's Rule Coupling in Strongly Correlated Materials*, Physical Review Letters **107** (25) 256401 (2011), URL <http://link.aps.org/doi/10.1103/PhysRevLett.107.256401>.
- [93] Meevasana, W., P. D. C. King, R. H. He, S.-K. Mo, M. Hashimoto, A. Tamai, P. Songsiriritthigul, F. Baumberger und Z.-X. Shen: *Creation and control of a two-dimensional electron liquid at the bare SrTiO₃ surface*, Nature Materials **10** (2) 114 (2011), ISSN 1476-1122, URL <http://www.nature.com/nmat/journal/v10/n2/full/nmat2943.html>.
- [94] Michael Potthoff: *Quantentheorie der Vielteilchensysteme I* (2011), URL http://hp.physnet.uni-hamburg.de/group_vts/vqtv1011/qtv1011.html.
- [95] Michaeli, K., A. C. Potter und P. A. Lee: *Superconducting and Ferromagnetic Phases in SrTiO₃/LaAlO₃ Oxide Interface Structures: Possibility of Finite Momentum Pairing*, Physical Review Letters **108** (11) 117003 (2012), URL <http://link.aps.org/doi/10.1103/PhysRevLett.108.117003>.

- [96] Moeckel, M. und S. Kehrein: *Interaction Quench in the Hubbard Model*, Physical Review Letters **100** (17) 175702 (2008), URL <http://link.aps.org/doi/10.1103/PhysRevLett.100.175702>.
- [97] Moeckel, M. und S. Kehrein: *Real-time evolution for weak interaction quenches in quantum systems*, Annals of Physics **324** (10) 2146 (2009), ISSN 0003-4916, URL <http://www.sciencedirect.com/science/article/pii/S0003491609000712>.
- [98] Moriya, T.: *Spin Fluctuations in Itinerant Electron Magnetism*, Springer Series in Solid-State Sciences, Bd. 56, Springer Berlin Heidelberg, Berlin, Heidelberg (1985), ISBN 978-3-642-82501-9 978-3-642-82499-9, URL <http://link.springer.com/10.1007/978-3-642-82499-9>.
- [99] Mravlje, J., M. Aichhorn und A. Georges: *Origin of the High Néel Temperature in SrTcO₃*, Physical Review Letters **108** (19) 197202 (2012), URL <http://link.aps.org/doi/10.1103/PhysRevLett.108.197202>.
- [100] Nakagawa, N., H. Y. Hwang und D. A. Muller: *Why some interfaces cannot be sharp*, Nature Materials **5** (3) 204 (2006), ISSN 1476-1122, URL <http://www.nature.com/nmat/journal/v5/n3/full/nmat1569.html>.
- [101] Nambu, Y.: *Quasi-Particles and Gauge Invariance in the Theory of Superconductivity*, Physical Review **117** (3) 648 (1960), URL <http://link.aps.org/doi/10.1103/PhysRev.117.648>.
- [102] Negele, J. W. und H. Orland: *Quantum many-particle systems*, Westview Press (1998), ISBN 978-0-7382-0052-1.
- [103] Nolting, W. und A. Ramakanth: *Quantum Theory of Magnetism*, Springer Science & Business Media (2009), ISBN 978-3-540-85416-6.
- [104] Ohtomo, A. und H. Y. Hwang: *A high-mobility electron gas at the LaAlO₃/SrTiO₃ heterointerface*, Nature **427** (6973) 423 (2004), ISSN 0028-0836, URL <http://www.nature.com/nature/journal/v427/n6973/full/nature02308.html>.
- [105] Ortega-San-Martin, L., A. J. Williams, J. Rodgers, J. P. Attfield, G. Heymann und H. Huppertz: *Microstrain Sensitivity of Orbital and Electronic Phase*

- Separation in SrCrO₃*, Physical Review Letters **99** (25) 255701 (2007), URL <http://link.aps.org/doi/10.1103/PhysRevLett.99.255701>.
- [106] Pan, L. und D. B. Bogy: *Data storage: Heat-assisted magnetic recording*, Nature Photonics **3** (4) 189 (2009), ISSN 1749-4885, URL <http://www.nature.com/nphoton/journal/v3/n4/full/nphoton.2009.40.html>.
- [107] Parcollet, O., M. Ferrero, T. Ayrál, H. Hafermann, I. Krivenko, L. Messio und P. Seth: *TRIQS: A toolbox for research on interacting quantum systems*, Computer Physics Communications **196** 398 (2015), ISSN 0010-4655, URL <http://www.sciencedirect.com/science/article/pii/S0010465515001666>.
- [108] Pavarini, E., S. Biermann, A. Poteryaev, A. I. Lichtenstein, A. Georges und O. K. Andersen: *Mott Transition and Suppression of Orbital Fluctuations in Orthorhombic 3d¹ Perovskites*, Physical Review Letters **92** (17) 176403 (2004), URL <http://link.aps.org/doi/10.1103/PhysRevLett.92.176403>.
- [109] Pavarini, E., E. Koch und U. Schollwöck: *Emergent Phenomena in Correlated Matter: Autumn School organized by the Forschungszentrum Jülich and the German Research School for Simulation ... Jülich 23 - 27 September 2013*, Forschungszentrum Jülich (2013), ISBN 978-3-89336-884-6.
- [110] Pavlenko, N., T. Kopp und J. Mannhart: *Emerging magnetism and electronic phase separation at titanate interfaces*, Physical Review B **88** (20) 201104 (2013), URL <http://link.aps.org/doi/10.1103/PhysRevB.88.201104>.
- [111] Pavlenko, N., T. Kopp, E. Y. Tsymbal, G. A. Sawatzky und J. Mannhart: *Magnetic and superconducting phases at the LaAlO₃/SrTiO₃ interface: The role of interfacial Ti 3d electrons*, Physical Review B **85** (2) 020407 (2012), URL <http://link.aps.org/doi/10.1103/PhysRevB.85.020407>.
- [112] Pentcheva, R. und W. E. Pickett: *Charge localization or itineracy at LaAlO₃/SrTiO₃ interfaces: Hole polarons, oxygen vacancies, and mobile electrons*, Physical Review B **74** (3) 035112 (2006), URL <http://link.aps.org/doi/10.1103/PhysRevB.74.035112>.
- [113] Perfetti, L., P. A. Loukakos, M. Lisowski, U. Bovensiepen, H. Berger, S. Biermann, P. S. Cornaglia, A. Georges und M. Wolf: *Time Evolution of the Electronic Structure of 1T-TaS₂ through the Insulator-Metal Transition*, Physical

- Review Letters **97** (6) 067402 (2006), URL <http://link.aps.org/doi/10.1103/PhysRevLett.97.067402>.
- [114] Poteryaev, A. I., J. M. Tomczak, S. Biermann, A. Georges, A. I. Lichtenstein, A. N. Rubtsov, T. Saha-Dasgupta und O. K. Andersen: *Enhanced crystal-field splitting and orbital-selective coherence induced by strong correlations in V_2O_3* , Physical Review B **76** (8) 085127 (2007), URL <http://link.aps.org/doi/10.1103/PhysRevB.76.085127>.
- [115] Rapp, A., S. Mandt und A. Rosch: *Equilibration Rates and Negative Absolute Temperatures for Ultracold Atoms in Optical Lattices*, Physical Review Letters **105** (22) 220405 (2010), URL <http://link.aps.org/doi/10.1103/PhysRevLett.105.220405>.
- [116] Reyren, N., S. Thiel, A. D. Caviglia, L. F. Kourkoutis, G. Hammerl, C. Richter, C. W. Schneider, T. Kopp, A.-S. Rüetschi, D. Jaccard, M. Gabay, D. A. Müller, J.-M. Triscone und J. Mannhart: *Superconducting Interfaces Between Insulating Oxides*, Science **317** (5842) 1196 (2007), ISSN 0036-8075, 1095-9203, URL <http://www.sciencemag.org/content/317/5842/1196>.
- [117] Rodriguez, E. E., F. Poineau, A. Llobet, B. J. Kennedy, M. Avdeev, G. J. Thorogood, M. L. Carter, R. Seshadri, D. J. Singh und A. K. Cheetham: *High Temperature Magnetic Ordering in the 4d Perovskite $SrTcO_3$* , Physical Review Letters **106** (6) 067201 (2011), URL <http://link.aps.org/doi/10.1103/PhysRevLett.106.067201>.
- [118] Ron, A., E. Maniv, D. Graf, J.-H. Park und Y. Dagan: *Anomalous Magnetic Ground State in an $LaAlO_3/SrTiO_3$ Interface Probed by Transport through Nanowires*, Physical Review Letters **113** (21) 216801 (2014), URL <http://link.aps.org/doi/10.1103/PhysRevLett.113.216801>.
- [119] Rosch, A., D. Rasch, B. Binz und M. Vojta: *Metastable Superfluidity of Repulsive Fermionic Atoms in Optical Lattices*, Physical Review Letters **101** (26) 265301 (2008), URL <http://link.aps.org/doi/10.1103/PhysRevLett.101.265301>.
- [120] Sakai, S., R. Arita, K. Held und H. Aoki: *Quantum Monte Carlo study for multiorbital systems with preserved spin and orbital rotational symmetries*,

- Physical Review B **74** (15) 155102 (2006), URL <http://link.aps.org/doi/10.1103/PhysRevB.74.155102>.
- [121] Sandri, M.: *The Gutzwiller Approach to out-of-equilibrium correlated fermions*, Dissertation, SISSA, Trieste, Italy (2014), URL <http://urania.sissa.it/xmlui/handle/1963/3/browse?value=Sandri%2C+Matteo&type=author>.
- [122] Sandri, M., M. Capone und M. Fabrizio: *Finite-temperature Gutzwiller approximation and the phase diagram of a toy model for V_2O_3* , Physical Review B **87** (20) 205108 (2013), URL <http://link.aps.org/doi/10.1103/PhysRevB.87.205108>.
- [123] Sandri, M. und M. Fabrizio: *Nonequilibrium dynamics in the antiferromagnetic Hubbard model*, Physical Review B **88** (16) 165113 (2013), URL <http://link.aps.org/doi/10.1103/PhysRevB.88.165113>.
- [124] Scazza, F., C. Hofrichter, M. Höfer, P. C. De Groot, I. Bloch und S. Fölling: *Observation of two-orbital spin-exchange interactions with ultracold $SU(N)$ -symmetric fermions*, Nature Physics **10** (10) 779 (2014), ISSN 1745-2473, URL <http://www.nature.com/nphys/journal/v10/n10/abs/nphys3061.html>.
- [125] Schiró, M. und M. Fabrizio: *Time-Dependent Mean Field Theory for Quench Dynamics in Correlated Electron Systems*, Physical Review Letters **105** (7) 076401 (2010), URL <http://link.aps.org/doi/10.1103/PhysRevLett.105.076401>.
- [126] Schiró, M. und M. Fabrizio: *Quantum quenches in the Hubbard model: Time-dependent mean-field theory and the role of quantum fluctuations*, Physical Review B **83** (16) 165105 (2011), URL <http://link.aps.org/doi/10.1103/PhysRevB.83.165105>.
- [127] Schneider, U., L. Hackermüller, S. Will, T. Best, I. Bloch, T. A. Costi, R. W. Helmes, D. Rasch und A. Rosch: *Metallic and Insulating Phases of Repulsively Interacting Fermions in a 3D Optical Lattice*, Science **322** (5907) 1520 (2008), ISSN 0036-8075, 1095-9203, URL <http://www.sciencemag.org/content/322/5907/1520>.

- [128] Seibold, G., F. Becca, P. Rubin und J. Lorenzana: *Time-dependent Gutzwiller theory of magnetic excitations in the Hubbard model*, Physical Review B **69** (15) 155113 (2004), URL <http://link.aps.org/doi/10.1103/PhysRevB.69.155113>.
- [129] Seibold, G. und J. Lorenzana: *Time-Dependent Gutzwiller Approximation for the Hubbard Model*, Physical Review Letters **86** (12) 2605 (2001), URL <http://link.aps.org/doi/10.1103/PhysRevLett.86.2605>.
- [130] Sherman, A. und M. Schreiber: *Magnetic excitations of a doped two-dimensional antiferromagnet*, Physical Review B **48** (10) 7492 (1993), URL <http://link.aps.org/doi/10.1103/PhysRevB.48.7492>.
- [131] Singh, R. R. P. und M. P. Gelfand: *Spin-wave excitation spectra and spectral weights in square lattice antiferromagnets*, Physical Review B **52** (22) R15695 (1995), URL <http://link.aps.org/doi/10.1103/PhysRevB.52.R15695>.
- [132] Steiauf, D. und M. Fähnle: *Elliott-Yafet mechanism and the discussion of femtosecond magnetization dynamics*, Physical Review B **79** (14) 140401 (2009), URL <http://link.aps.org/doi/10.1103/PhysRevB.79.140401>.
- [133] Stoner, E. C.: *Collective Electron Ferromagnetism*, Proceedings of the Royal Society of London. Series A. Mathematical and Physical Sciences **165** (922) 372 (1938), ISSN 1364-5021, 1471-2946, URL <http://rspa.royalsocietypublishing.org/content/165/922/372>.
- [134] Sulpizio, J. A., S. Ilani, P. Irvin und J. Levy: *Nanoscale Phenomena in Oxide Heterostructures*, Annual Review of Materials Research **44** (1) 117 (2014), URL <http://dx.doi.org/10.1146/annurev-matsci-070813-113437>.
- [135] Syljuåsen, O. F.: *Numerical evidence for unstable magnons at high fields in the Heisenberg antiferromagnet on the square lattice*, Physical Review B **78** (18) 180413 (2008), URL <http://link.aps.org/doi/10.1103/PhysRevB.78.180413>.
- [136] Taie, S., Y. Takasu, S. Sugawa, R. Yamazaki, T. Tsujimoto, R. Murakami und Y. Takahashi: *Realization of a $SU(2) \times SU(6)$ System of Fermions in a Cold Atomic Gas*, Physical Review Letters **105** (19) 190401 (2010), URL <http://link.aps.org/doi/10.1103/PhysRevLett.105.190401>.

- [137] Thiel, S., G. Hammerl, A. Schmehl, C. W. Schneider und J. Mannhart: *Tunable Quasi-Two-Dimensional Electron Gases in Oxide Heterostructures*, Science **313** (5795) 1942 (2006), ISSN 0036-8075, 1095-9203, URL <http://www.sciencemag.org/content/313/5795/1942>.
- [138] Tsuji, N., M. Eckstein und P. Werner: *Nonthermal Antiferromagnetic Order and Nonequilibrium Criticality in the Hubbard Model*, Physical Review Letters **110** (13) 136404 (2013), URL <http://link.aps.org/doi/10.1103/PhysRevLett.110.136404>.
- [139] Vahaplar, K., A. M. Kalashnikova, A. V. Kimel, D. Hinzke, U. Nowak, R. Chantrell, A. Tsukamoto, A. Itoh, A. Kirilyuk und T. Rasing: *Ultrafast Path for Optical Magnetization Reversal via a Strongly Nonequilibrium State*, Physical Review Letters **103** (11) 117201 (2009), URL <http://link.aps.org/doi/10.1103/PhysRevLett.103.117201>.
- [140] Van Vleck, J. H.: *The theory of electric and magnetic susceptibilities*, Oxford (1932).
- [141] Vaugier, L., H. Jiang und S. Biermann: *Hubbard U and Hund exchange J in transition metal oxides: Screening versus localization trends from constrained random phase approximation*, Physical Review B **86** (16) 165105 (2012), URL <http://link.aps.org/doi/10.1103/PhysRevB.86.165105>.
- [142] Venus, D. und J. Kirschner: *Momentum dependence of the Stoner excitation spectrum of iron using spin-polarized electron-energy-loss spectroscopy*, Physical Review B **37** (4) 2199 (1988), URL <http://link.aps.org/doi/10.1103/PhysRevB.37.2199>.
- [143] Verner, J.: *Numerically optimal Runge–Kutta pairs with interpolants*, Numerical Algorithms **53** (2) 383 (2010), ISSN 1017-1398, URL <http://www.springerlink.com/content/k556316701468761/abstract/>.
- [144] Wang, W.-S., X.-M. He, D. Wang, Q.-H. Wang, Z. D. Wang und F. C. Zhang: *Finite-temperature Gutzwiller projection for strongly correlated electron systems*, Physical Review B **82** (12) 125105 (2010), URL <http://link.aps.org/doi/10.1103/PhysRevB.82.125105>.

- [145] Warusawithana, M. P., C. Richter, J. A. Mundy, P. Roy, J. Ludwig, S. Paeltel, T. Heeg, A. A. Pawlicki, L. F. Kourkoutis, M. Zheng, M. Lee, B. Mulcahy, W. Zander, Y. Zhu, J. Schubert, J. N. Eckstein, D. A. Muller, C. S. Hellberg, J. Mannhart und D. G. Schlom: *LaAlO₃ stoichiometry is key to electron liquid formation at LaAlO₃/SrTiO₃ interfaces*, Nature Communications **4** 2351 (2013), URL http://www.nature.com/ncomms/2013/130822/ncomms3351/full/ncomms3351.html?WT.ec_id=NCOMMS-20130828.
- [146] Weber, W., J. Bünemann und F. Gebhard: *On the Way to a Gutzwiller Density Functional Theory*, in P. K. Baberschke, P. W. Noltling und P. M. Donath (Hg.), *Band-Ferromagnetism*, Nr. 580 in Lecture Notes in Physics, S. 9–26, Springer Berlin Heidelberg (2001), ISBN 978-3-540-42389-8, URL http://link.springer.com/chapter/10.1007/3-540-44610-9_2.
- [147] Weiss, P.: J. Phys. Radium **6**, 661 (1907).
- [148] Werner, P., E. Gull und A. J. Millis: *Metal-insulator phase diagram and orbital selectivity in three-orbital models with rotationally invariant Hund coupling*, Physical Review B **79** (11) 115119 (2009), URL <http://link.aps.org/doi/10.1103/PhysRevB.79.115119>.
- [149] Werner, P. und A. J. Millis: *High-Spin to Low-Spin and Orbital Polarization Transitions in Multiorbital Mott Systems*, Physical Review Letters **99** (12) 126405 (2007), URL <http://link.aps.org/doi/10.1103/PhysRevLett.99.126405>.
- [150] Werner, P., N. Tsuji und M. Eckstein: *Nonthermal symmetry-broken states in the strongly interacting Hubbard model*, Physical Review B **86** (20) 205101 (2012), URL <http://link.aps.org/doi/10.1103/PhysRevB.86.205101>.
- [151] White, S. R.: *Formation of gaps in the two-dimensional half-filled Hubbard model*, Physical Review B **46** (9) 5678 (1992), URL <http://link.aps.org/doi/10.1103/PhysRevB.46.5678>.
- [152] White, S. R., D. J. Scalapino, R. L. Sugar, E. Y. Loh, J. E. Gubernatis und R. T. Scalettar: *Numerical study of the two-dimensional Hubbard model*, Physical Review B **40** (1) 506 (1989), URL <http://link.aps.org/doi/10.1103/PhysRevB.40.506>.

- [153] Wirth, G., M. Ölschläger und A. Hemmerich: *Evidence for orbital superfluidity in the P-band of a bipartite optical square lattice*, Nature Physics **7** (2) 147 (2011), ISSN 1745-2473, URL <http://www.nature.com/nphys/journal/v7/n2/abs/nphys1857.html>.
- [154] Woodward, F. M., A. S. Albrecht, C. M. Wynn, C. P. Landee und M. M. Turnbull: *Two-dimensional $S = \frac{1}{2}$ Heisenberg antiferromagnets: Synthesis, structure, and magnetic properties*, Physical Review B **65** (14) 144412 (2002), URL <http://link.aps.org/doi/10.1103/PhysRevB.65.144412>.
- [155] Woynarovich, F.: *Spin excitations in a Hubbard chain*, Journal of Physics C: Solid State Physics **16** (27) 5293 (1983), ISSN 0022-3719, URL <http://stacks.iop.org/0022-3719/16/i=27/a=013>.
- [156] Zener, C.: *Interaction Between the d Shells in the Transition Metals*, Physical Review **81** (3) 440 (1951), URL <http://link.aps.org/doi/10.1103/PhysRev.81.440>.
- [157] Zener, C.: *Interaction between the d-Shell in the Transition Metals. II. Ferromagnetic Compounds of Manganese with Perovskite Structure*, Physical Review **82** (3) 403 (1951), URL <http://link.aps.org/doi/10.1103/PhysRev.82.403>.
- [158] Zhitomirsky, M. E. und A. L. Chernyshev: *Instability of Antiferromagnetic Magnons in Strong Fields*, Physical Review Letters **82** (22) 4536 (1999), URL <http://link.aps.org/doi/10.1103/PhysRevLett.82.4536>.
- [159] Ziegler, W., H. Endres und W. Hanke: *Friedel oscillations induced by non-magnetic impurities in the two-dimensional Hubbard model*, Physical Review B **58** (8) 4362 (1998), URL <http://link.aps.org/doi/10.1103/PhysRevB.58.4362>.
- [160] Zlatić, V. und A. Hewson: *New Materials for Thermoelectric Applications: Theory and Experiment*, Springer (2012), ISBN 978-94-007-4984-9.

Eidesstattliche Erklärung

Declaration on oath

Hiermit erkläre ich an Eides statt, dass ich die vorliegende Dissertationsschrift selbst verfasst und keine anderen als die angegebenen Quellen und Hilfsmittel benutzt habe.

I hereby declare, on oath, that I have written the present dissertation by my own and have not used other than the acknowledged resources and aids.

Hamburg, den 21. Februar 2016 Malte Behrmann